



SHOCK DAY COMPENDIUM

MAY 2025

FOREWORD

SHOCK DAY

An impact occurs when two or more objects collide. The response of the objects to the collision depends on their individual masses, their geometries, the materials that comprise them, the directionality of impact, their velocities at impact, and more. During impact both energy and momentum are transferred between these objects typically resulting in their rapid acceleration or deceleration. This acceleration or deceleration is defined as mechanical shock. Alternately, explosives or explosive actuators can provide a rapid energy deposition to a structure resulting in pyroshock. Pyroshock can be defined as the decaying, oscillatory response of a structure to high-amplitude and high-frequency excitation (e.g., explosive events).

Objects encountering shock loading are susceptible to failure. Depending on its severity in terms of amplitude and duration, the measurement of a shock event can be a significant challenge. Not only must the appropriate accelerometer be selected, but its mounting; cable type, impedance and tie down; signal conditioning; filtering; and signal digitization and recording must be optimized. In addition, the noise floor and the dynamic characteristics of the measurement system must be documented to evaluate the validity of the recorded signal.

The following publications and testing provide guidance and educational resources to its customers. They are presented in a sequel to compliment our “Measuring Mechanical & Pyro Shock” Training Course. The goal of the training is to provide customer guidance in both optimizing accelerometer selection and measurement system design to enable the acquisition of meaningful shock data. Laboratory and field test results will be displayed throughout the event.

TABLE OF CONTENTS

TN-24	Selecting Accelerometers for and Assessing Data from Mechanical Shock Measurements
TN-11	Shock and Blast Measurement - Rise Time Capability of Measurement Systems
TN-23	Pyroshock Explained
TN-19	The Shock Spectrum: What Is It?
TN-25	How High in Frequency are Accelerometer Measurements Meaningful
TN-33	The Instrumentation Cable: Critical but Often Neglected
TN-17	Accelerometer Selection Considerations: Charge and ICP® Integrated Circuit Piezoelectric
TN-29	Guidance for the Filtering of Dynamic Force, Pressure, Acceleration (and Other) Signals
AR-101	Validating the Data Before the Structural Model
AR-98	Acquiring Meaningful Test Data on Purpose
WP-45	Accelerating Sensing Technologies for Severe Mechanical Shock
WP-60	Evaluation of Accelerometers for Pyroshock Performance in a Harsh Field Environment
WP-61	Causes of Zero Shift in Acceleration Data Acquired While Measuring Severe Shock
WP-85	MEMS Shock Accelerometers

A large, intense fireball or explosion in the sky, with a ship's gun barrel visible in the foreground. The fireball is bright orange and yellow, with a dark, smoky plume rising from it. The ship's gun barrel is dark and extends from the right side of the frame towards the center. The background is a clear blue sky with some light clouds.

TECH NOTE #24

This T/N provides a brief introduction to mechanical shock and the accelerometer types that measure it. More important, it provides design guidance based on the measurement system's low frequency time constant (where applicable), the system's upper frequency -3dB location, and the accelerometer's resonant frequency. Note that the circuit's time constant and its -3dB low frequency are directly related. This guidance is useful for both initial pretest planning and subsequent data assessment. While the design rules provided are based in mathematics, they are presented here in an easy to apply form.



TN-24

Selecting Accelerometers for and Assessing Data From Mechanical Shock Measurements

Written By

Patrick L. Walter, Ph. D.

Selecting Accelerometers for and Assessing Data from Mechanical Shock Measurements

Patrick L. Walter, Ph. D.

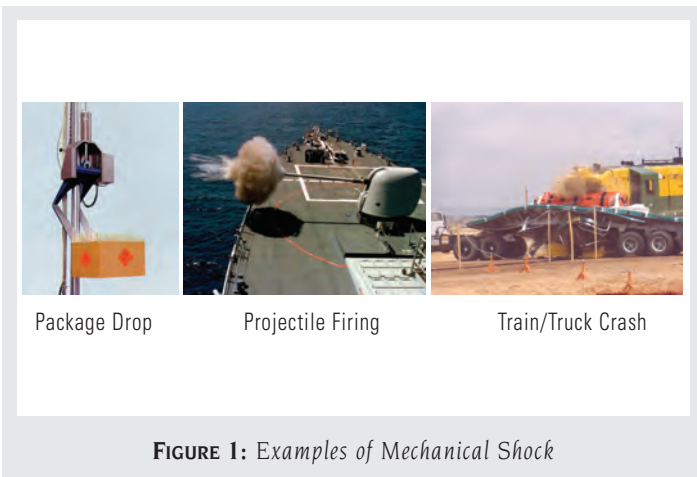
Measurement Specialist/PCB Piezotronics, Inc.
Depew, NY 14043

Engineering Faculty/Texas Christian University
Fort Worth, TX 76129

After first clarifying what mechanical shock is and why we measure it, basic requirements are provided for all measurement systems that process transient signals. High- and low-frequency dynamic models for the measuring accelerometer are presented and justified. These models are then used to investigate accelerometer responses to mechanical shock. The results enable “rules of thumb” to be developed for shock data assessment and proper accelerometer selection. Other helpful considerations for measuring mechanical shock are also provided.

Mechanical Shock: The definition of mechanical shock is, “a nonperiodic excitation of a mechanical system, that is characterized by suddenness and severity, and usually causes significant relative displacements in the system.”¹ The definition of suddenness and severity is dependent upon the system encountering the shock. For example, if the human body is considered a mechanical system, a shock pulse of duration of 0.2 seconds into the feet of a vertical human, due to impact resulting from a leap or a jump, would be sudden. This is because vertical humans typically have a resonant frequency of about 4 Hz. The amplitude of the shock would further characterize its severity. By contrast, for most engineering components, this same shock would be neither sudden nor severe.

The effects of mechanical shock are so important that the International Organization for Standardization (ISO) has a standing committee, TC 108, dealing with shock and vibration; a Shock and Vibration Handbook¹ has been published and routinely updated by *The McGraw-Hill Companies* since 1961; and the U.S. Department of Defense has sponsored a focused symposium on this subject at least annually since 1947.² Figure 1 provides several examples of components or systems experiencing mechanical shock.



Mechanical shock can be specified in either the time, and/or frequency domains, or by its associated shock-response spectrum.³ Figure 2 is an example of a shock pulse specified in the time domain. This pulse is used as an input to test sleds, to enable qualification of head and neck constraint systems for National Association for Stock Car Auto Racing (NASCAR) crashes.⁴ Its duration of approximately 63 msec. produces 68 g's at 43.5 mph.

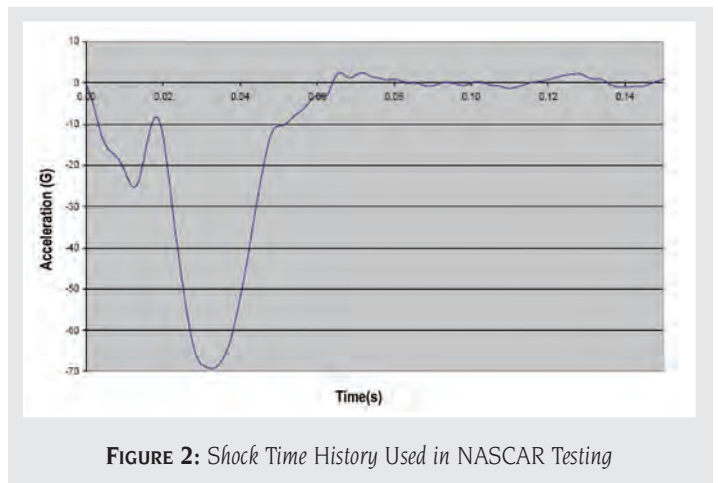


Figure 3 on the following page shows an example of a mechanical shock described by its amplitude in the frequency domain. This representation is particularly useful in linear analysis, when system transfer function is of interest (e.g., mechanical impedance, mobility and transmissibility). It provides knowledge of input-excitation frequencies to the mechanical system being characterized.

Figure 4 is an example of a shock-response spectrum. The shock response spectrum (SRS) is one method to enable the shock input to a system or component to be described, in terms of its damage potential. It is very useful in generating test specifications.

Obviously, accurate measurement of mechanical shock is a subject of great importance to designers.

Measurement System Requirements: There are a number of general measurement requirements that must be dealt with in measuring any transient signal that has an important time-history. The more significant of these requirements are listed below:

1. The frequency response of a measuring system must have flat amplitude-response and linear phase-shift over its response range of interest.⁵

2. The data sampling rate must be at least twice the highest data frequency of interest.
 - a. Properly selected data filters must constrain data signal content, so that data doesn't exceed this highest frequency.
 - b. If significant high frequency content is present in the signal, and its time history is of interest, data sampling should occur at 10 times this highest frequency.
3. The data must be validated to have an adequate signal-to-noise ratio.^{6,7,8}

It is assumed that the test engineer has satisfied the aforementioned requirements, so that this paper may focus on accelerometer selection.

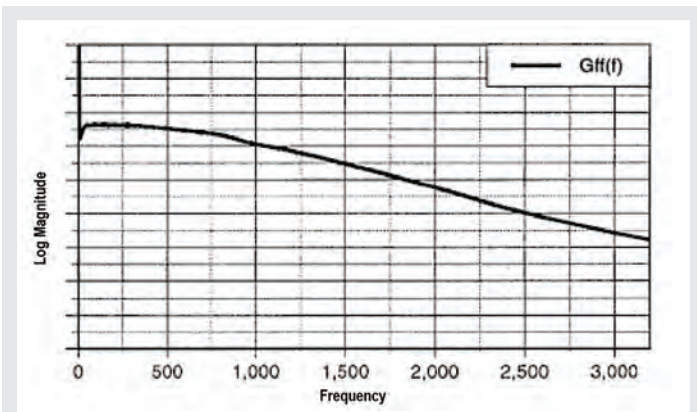


FIGURE 3: Frequency Spectrum of a Shock Used to Excite a Structure

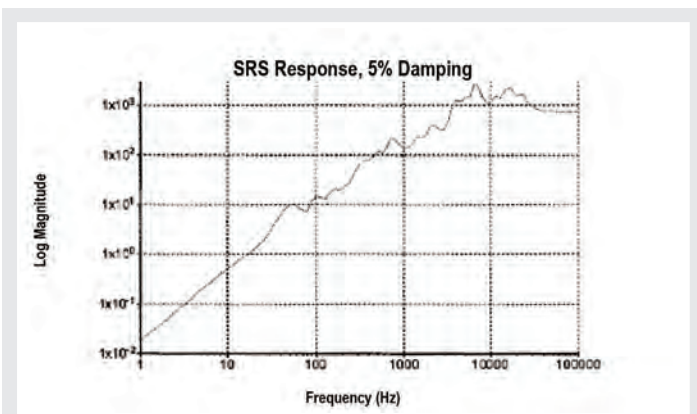


FIGURE 4: Shock Response Spectrum of Acceleration Pulses Due to Gun Fire

Accelerometer Mechanical and Electrical Models: Two types of accelerometer sensing technologies used for mechanical shock measurements are piezoelectric and piezoresistive. Piezoelectric accelerometers contain elements that are subjected to strain under acceleration-induced loads. This strain displaces electrical charges within the elements and charges accumulate on opposing electroded surfaces. A majority of modern piezoelectric accelerometers have integral signal-conditioning electronics (ICP® or IEPE), although such “on-board” signal conditioning is not mandated. When measuring mechanical shock, ICP® signal conditioning enhances the measurement system’s signal-to-noise ratio.

Today, the term “piezoresistive” implies that an accelerometer’s sensing flexure is manufactured from silicon, as a microelectro mechanical system (MEMS). MEMS shock accelerometers typically provide an electrical output due to resistance changes produced by acceleration-induced strain of doped semiconductor elements in a seismic flexure. These doped semiconductor elements are electrically configured into a Wheatstone bridge. Both of these preceding technologies will be discussed further in a subsequent section of this paper.

Accelerometers themselves are mechanical structures. They have multiple mechanical resonances⁹ associated with their seismic flexure, external housing, connector and more. If accelerometer structures are properly designed and mounted, their response at high frequencies becomes limited by the lowest mechanical resonance of their seismic flexure. Because of this limiting effect, accelerometer frequency response can be specified as if it has a single resonant frequency. Figure 5 pictorially shows a mechanical flexure in a piezoresistive accelerometer. Figure 6 on the following page shows a piezoelectric accelerometer cut away. In Figure 6, the annular piezoelectric crystal acts as a shear spring with its concentric outer mass shown. Thus a simple, spring-mass dynamic model for an accelerometer is typically provided as shown in Figure 7.

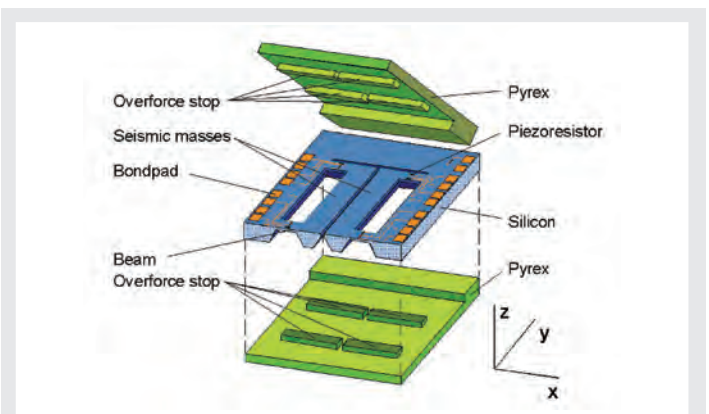


FIGURE 5: Mechanical Flexure for a MEMS Accelerometer

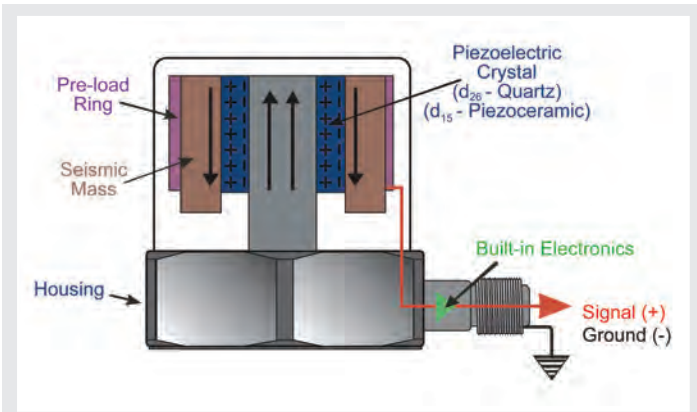


FIGURE 6: Cut Away of a Shear-Mode Piezoelectric Accelerometer

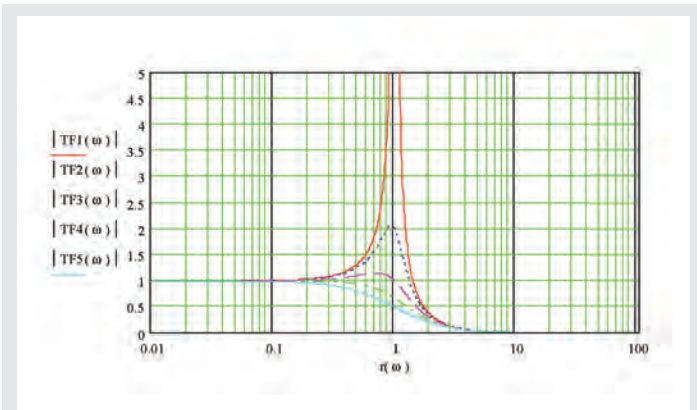


Figure 7: Simple Spring-Mass Accelerometer Model

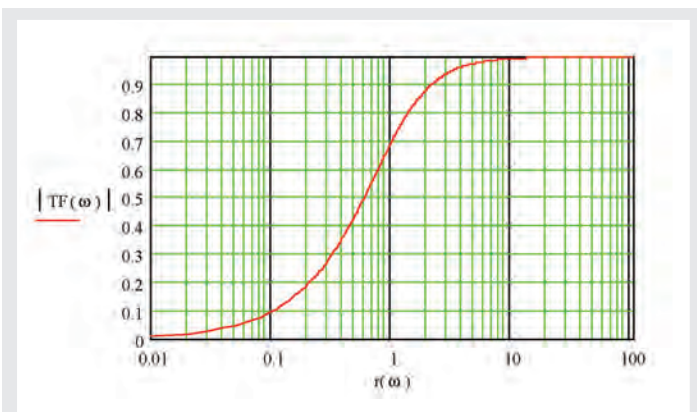


FIGURE 8: Low-Frequency Response of Piezoelectric Accelerometer

The various curves in Figure 7 represent different values of damping. These curves are normalized to the natural frequency ω_n : $r(\omega) = \omega/\omega_n$. For low damping values, the natural and resonant frequencies may be considered synonymous. For a shock accelerometer to have a high natural frequency ($\omega_n = (k/m)^{1/2}$), and, as a byproduct, a broad frequency response, its flexure must be mechanically stiff (high k). Stiff flexures cannot be readily damped; therefore, shock accelerometers typically possess only internal damping of the material from which they are constructed (typical value of 0.03 critical damping is the highest curve of Figure 7).

Piezoresistive accelerometers have frequency response down to 0 Hz. Piezoelectric accelerometers do not have response to 0 Hz. At low frequencies, piezoelectric accelerometers electrically resemble a high-pass RC filter. Their -3 dB frequency is controlled by their circuit time constant ($RC = \tau$). Typically, this time constant is controlled within the aforementioned ICP[®] circuit. [Figure 8 shows this frequency response curve. The plot is normalized to the low frequency -3 dB frequency ($r(\omega) = \omega/\omega_{-3dB}$)].

Before beginning to measure any shock motion, a test engineer has to understand accelerometer theory, mounting techniques, cable considerations, and more. Fortunately, this information is readily and effectively available in an IEST document, entitled RP-DTE011.1: *Shock and Vibration Transducer Selection*. In going forward, we will assume a properly mounted and signal-conditioned accelerometer is in use. This enables us to focus on understanding measurement limitations on shock pulses imposed by the high- and low-frequency response constraints of an accelerometer. Conversely, it enables one to establish frequency response requirements for an accelerometer measuring mechanical shock.

High-Frequency Limitations: The key to selecting a shock accelerometer, based on its high-frequency performance, is knowledge of its resonant frequency. This resonant frequency f_n (in Hz) is related to its equivalent value ω_n (in radians/second) as: $\omega_n = 2\pi f_n$. Typically, an accelerometer shouldn't be used above one-fifth its resonant frequency. At that point on the graph, device sensitivity, as a function of frequency, is 4% higher than its value near 0 Hz. Since shock pulses are composites of all frequencies, the total error due to this sensitivity increase will always be much smaller than 4%.

Conversely, if the shock pulse is analyzed in the frequency domain, and if considerable frequency content is found above one-fifth of an accelerometer's resonant frequency, increasingly greater errors will exist in the data. (This comes as no surprise, since the accelerometer is operating outside of its flat frequency-response range). Operation within the flat frequency-response range has been previously stated as a requirement for all measurement systems and their components.

Since most shock pulses are first viewed in the time domain, it is important to establish a relationship as to the credibility of the observed shock pulse based upon knowledge of resonant frequency

of the accelerometer. The natural period T_n of the accelerometer will be defined as $T_n = 1/f_n$. For example, if an accelerometer has a resonant frequency of 50 kHz, its natural period $T_n = 20\mu$ sec. Natural period T_n is introduced at this time, because “rules of thumb” will next be provided based on this natural period.

Figures 9A – c are very informative, in that they portray responses of symmetric shock-pulse inputs (of varying durations T) to an accelerometer, as a function of an accelerometer’s natural period. What all of these plots show is that at T/T_n equal to 5, the peak error of the measured shock pulse is always less than 10%, and for T/T_n equal to 10, almost perfect reproduction is achieved. Thus, the “rule of thumb” when selecting an accelerometer or assessing already recorded shock data, is:

$$T/T_n > 5$$

Real pulses typically do not have symmetric rise or fall times. The terms rise and fall time t_r , as used throughout this paper, refer to the 10 to 90% time from zero to, or from, the pulse peak. By analogy to the preceding rule:

$$t_r/T_n > 2.5$$

When applying these rules, a test engineer can prescribe any additional amount of conservatism thought to be needed, based upon intended use of data.

Low-Frequency Limitations: It is necessary to consider low frequencies only when selecting a piezoelectric accelerometer for mechanical shock. (As stated earlier, piezoresistive accelerometers possess a frequency response down to 0 Hz). However, if for example a piezoresistive accelerometer is AC-coupled to eliminate thermal drift, the following considerations also apply.

Figures 9A–9c: Shock Pulse Responses as a Function of Accelerometer Natural Period

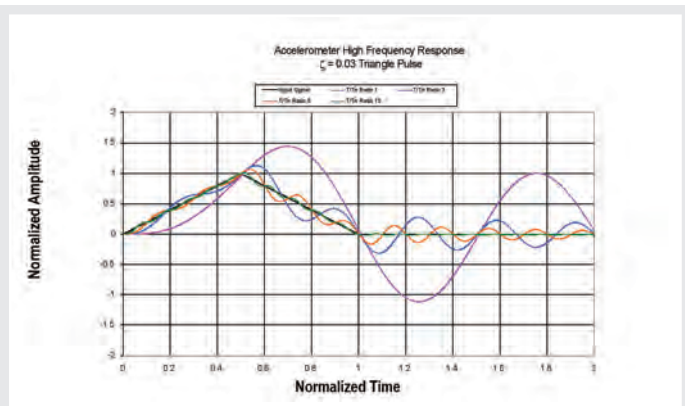


FIGURE 9A. Triangular Pulse

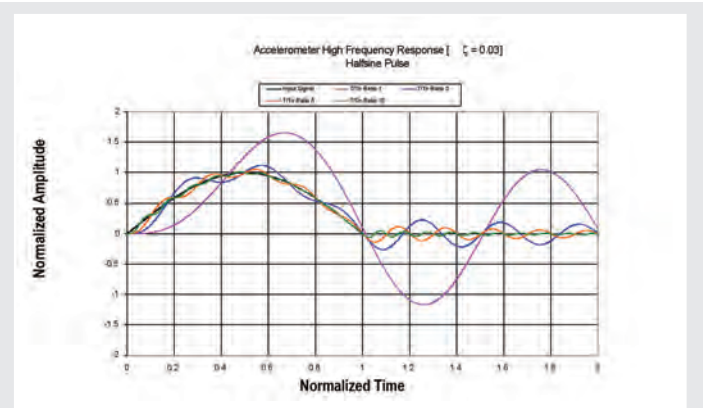


FIGURE 9B. Half-Sine Pulse

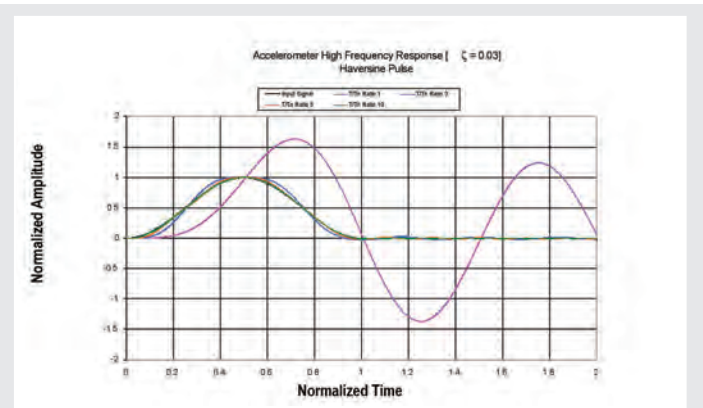


FIGURE 9C. Haversine Pulse

Figure 8 shows the low-frequency limitation of a piezoelectric accelerometer. The circuit time constant of the accelerometer is related to the low-frequency -3 dB point as: $\tau^{-1} = \omega_{-3dB}$. That is, an increased time constant provides greater low-frequency response. When looking at data in the frequency domain, a simple “rule of thumb” is:

$$f\tau > 0.5$$

This rule guarantees less than 5% attenuation in frequency content above the frequency f (in Hz). For a given time constant, this rule allows a test engineer to select the lowest frequency at which one should begin to use test data, based upon this criterion. Alternatively, it allows one to select an appropriate circuit time constant, in advance of testing.

Again, it is important to establish credibility of an observed shock pulse in the time domain, based on knowledge of the circuit time constant. This relationship will be parameterized as a function of the ratio of the time constant τ to the pulse width T . Figures 10A–10c provides these characterizations.

FIGURES 10A–10C: Shock Pulse Responses as a Function of Circuit Time Constant

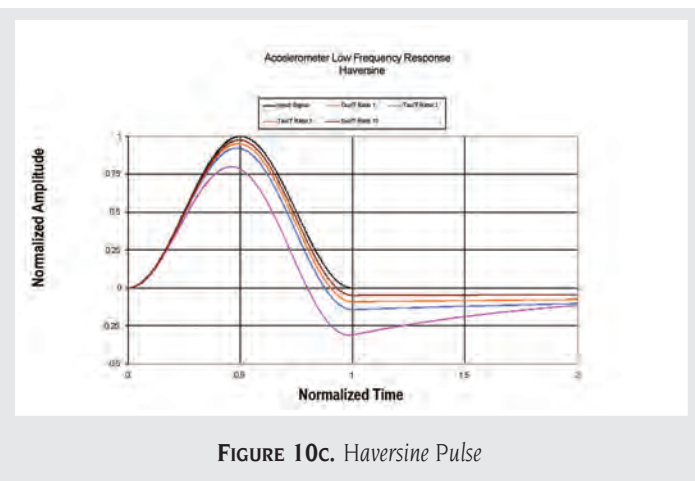
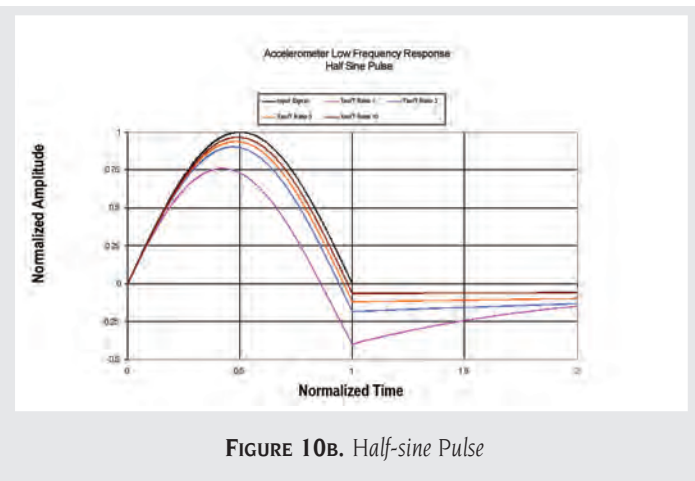
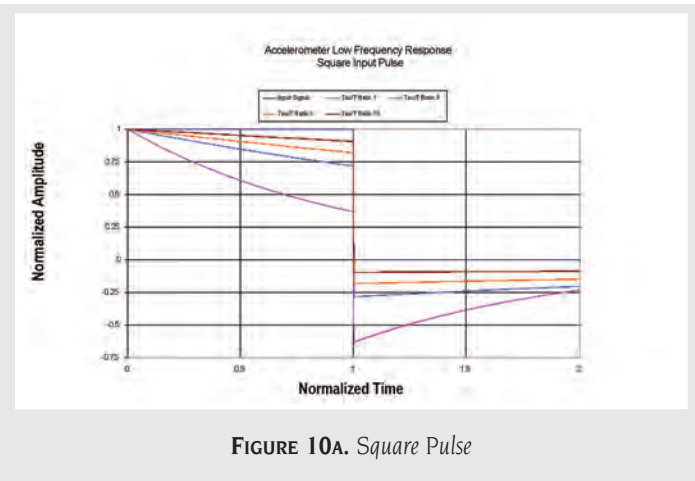


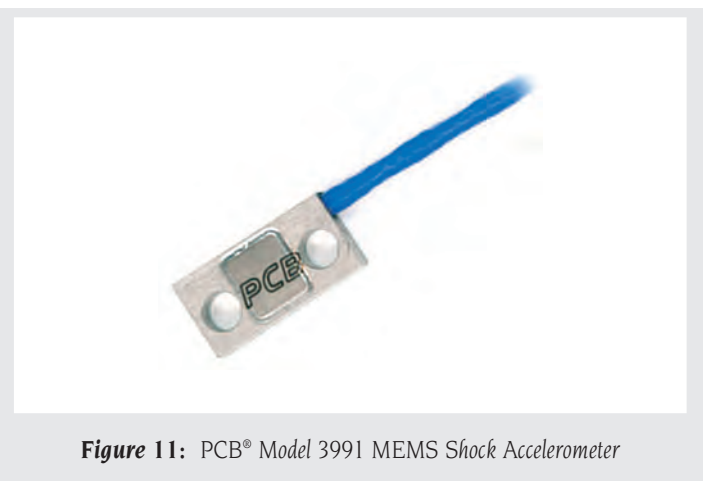
Figure 10A plots the response in the time domain of an RC circuit to a theoretical square pulse. As the ratio of time constant to pulse duration reaches 10 ($\tau/T = 10$), there remains a 10% droop (error) at the end of the pulse. This would be a worst-case assessment, since most real pulses trail off significantly before pulse termination. In Figures 10B and 10C, the Haversine and Half-sine pulses, illustrate more practical situations. This same ratio of $\tau/T = 10$ would result in a 2.4% error for the peak value determination of a Haversine pulse, and 3.4% error for a Half-sine pulse. While not shown, corresponding error for the peak of a triangular pulse would be 2.6%. Thus, a “rule of thumb” when selecting an accelerometer, or assessing already recorded shock data, is:

$$\tau/T > 10$$

Again, a test engineer can apply as much additional conservatism as an application warrants.

Other Response Considerations in Selecting Piezoelectric vs. Piezoresistive Technologies for Shock Measurements: A majority of piezoelectric accelerometers use ceramic sensing materials. At sufficiently high frequencies, the resonance of any accelerometer can be excited, but a unique characteristic of ceramic materials is that this excitation can result in a zero-shift of the signal. This remained a mystery until 1971, when the causal relationship of the zero-shift in ceramic materials was established!¹⁰ This work brought increased focus upon MEMS accelerometers for shock applications. Theoretically, MEMS accelerometers do not zero shift.

A limitation in MEMS accelerometers in shock measurement is their tremendous amplification at resonance (e.g., 1000:1), which can lead to breakage in response to high-frequency inputs (e.g., metal-to-metal impact, explosives, etc.) Figure 11 shows an example of a MEMS shock accelerometer which attempts to incorporate a small amount of squeeze film damping to minimize this problem.



High-Frequency Electronic Limitations: In order to mitigate the aforementioned zero-shift problems in piezoelectric accelerometers, certain models (e.g., PCB® Model 350) contain mechanical isolation to mitigate high-frequency stimuli. To minimize frequency-response aberrations due to this isolation, accelerometers are electrically prefiltered. Feedback components (resistors and capacitors), internal to an accelerometer and around the signal-conditioning amplifier, enable a 2-pole Butterworth filter to be developed. The high-frequency roll-off of this filter, as opposed to the resonant frequency of an accelerometer, now becomes the measurement system's upper frequency constraint.

In other instances, this same type of frequency limitation may occur outside of the accelerometer. For example, in flight test instrumentation, only 2-3 KHz maximum frequency response per channel is typically allocated. In addition, at shock levels below 2,000 g's, damped accelerometers may be used. The response of properly damped accelerometers appears as the intermediate or "flattest" of curves shown in Figure 7. This curve shows negligible gain and is attenuated approximately -3 dB at the natural frequency of the accelerometer.

The commonality of examples in the preceding two paragraphs is that amplification (i.e., gain) approaching the resonant frequency of an accelerometer no longer limits measurement system response. Instead, the limitation becomes the system's high-frequency attenuation. Due to this attenuation, another "rule of thumb" can be applied.¹¹ Here again, we base this rule on the shortest duration of the pulse's rise or fall time t_r to or from the pulse peak. By analogy to the preceding observations:

$$t_r \cdot f_{-3dB} > 0.45$$

This rule states that the rise or fall time of the shock pulse is guaranteed valid, only if the product of its duration multiplied by the high-frequency -3 dB frequency (in Hz) exceeds 0.45. Again, this rule is helpful for both pretest planning and data assessment.

Complex Pulses: As opposed to the simple pulses shown to date, real shock pulses can be quite complex (Figure 12). A question then arises as to how one applies the preceding simple "rules of thumb" to complex pulses. The answer is that we dissect the pulse for its shortest and longest, positive- or negative-going, excursions, as well as its shortest positive or negative rise-time. Since today all data are recorded in digital format, these simple rules can be readily programmed into a software data analysis package.

Cable Frequency Limitations: In ICP® circuits, if very long cables are used, cable capacitance can become an upper frequency limitation. For example, 4 mA of supply current driving 100 feet of cable supporting an ICP® circuit with cable capacitance of 30 pF/ft will begin to

attenuate full scale signals above 40 KHz¹². Other drive-current-versus-cable-operating trade-offs can be assessed using reference 12. Frequency attenuation due to cable length can usually be overcome, simply by increasing supply current.

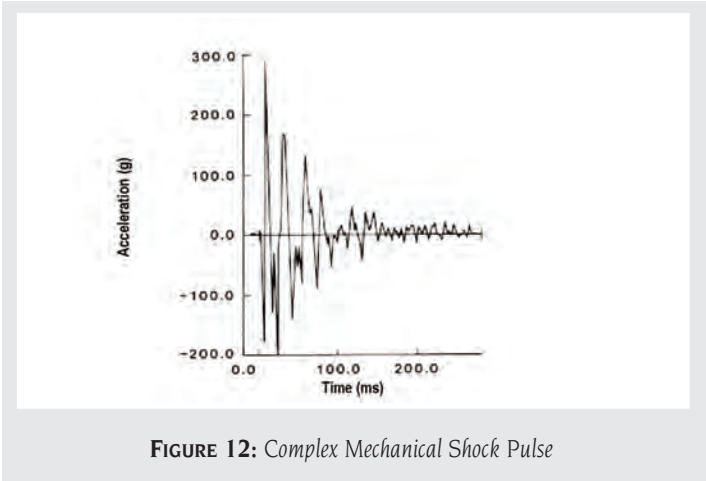


FIGURE 12: Complex Mechanical Shock Pulse

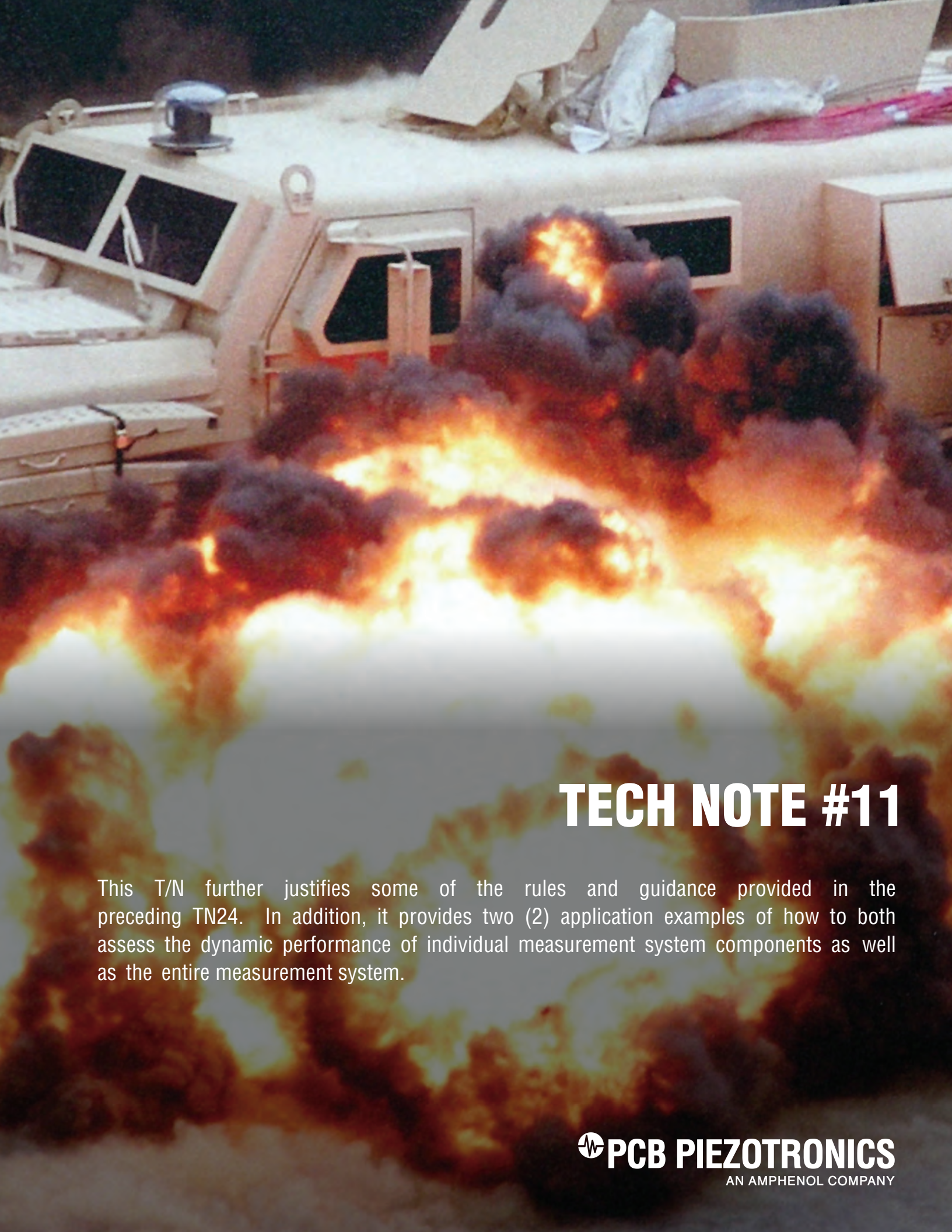
Low-Frequency Oscillations: If an ICP® accelerometer is properly selected, the effect described next should never be a consideration. However, since the effect is sometimes observed in test data where a shock pulse is excessively wide and/or the accelerometer signal-conditioning overranged, it is described for clarity.

Aside from a constant current diode, signal conditioning for ICP® circuits typically includes a coupling capacitor for blocking bias voltage on a signal return. The capacitor is always selected as to avoid impacting an accelerometer's low-frequency performance. However, the capacitor has the effect of creating a second RC time constant in the circuit. The effect of this second time constant is to transform a first-order, high-pass system into a second order one. The signal now returns to zero in anywhere from a few hundred to multiple hundreds of milliseconds with a heavily damped response.

Conclusions: This paper has presented simple "rules of thumb" to enable a test engineer to select accelerometers efficiently and accurately for mechanical shock measurements, or to assess data resulting from those measurements. Whereas "rules of thumb" are based upon theory, they result in a number of practical rules that a test engineer, designer, or data analyst can readily apply.

REFERENCES:

1. *Shock and Vibration Handbook*, edited by Cyril M. Harris and Allan G. Piersol, The McGraw-Hill Companies, 5th edition, 2002.
2. *50 Years of Shock and Vibration History*, edited by Henry C. Pusey, The Shock and Vibration Information Analysis Center (SAVIAC), 1996.
3. Walter, Patrick L., "The Shock Spectrum: What is It", Technical Note TN-19, <http://www.pcb.com/techsupport/docs/vib/>, PCB Piezotronics, Inc.
4. SFI Foundation, Inc., Specification SFI 38.1.
5. Walter, Patrick L., "Effect of Measurement System Phase Response on Shock Spectrum Computation", *Shock and Vibration Bul.*, 53, Part 1, 133-141, May 1981.
6. Walter, Patrick L., "Data Validation: A Prerequisite to Performing Data Uncertainty Analysis" PCB Piezotronics Technical Note TN-20, Proceedings International Telemetry Conference, Las Vegas, NV, October 25-27, 2005.
7. Walter, P. L., "Validating the Data Before the Structural Model", *Journal of the Society of Experimental Mechanics: Experimental Techniques*, pp 55-59, November/December 2006.
8. Walter, Patrick L., "Placebo Transducers: A Tool for Data Validation", Technical Note TN-16, <http://www.pcb.com/techsupport/docs/vib/>, PCB Piezotronics, Inc.
9. Liu, Bin, *Transducers for Sound and Vibration – The Finite Element Method Based Design*, Ph.D. thesis, Technical university of Denmark, June 2001.
10. Plumlee, Ralph H., "Zero-Shift in Piezoelectric Accelerometers," Sandia National Laboratories Research Report, SC-RR-70-755, March 1971.
11. Walter, Patrick L., "Shock and Blast Measurement – Rise Time Capability of Measurement Systems?" Technical Note TN-11, *Sound and Vibration*, January 2002.
12. Driving Long Cables, http://www.pcb.com/techsupport/tech_cables.php., PCB Piezotronics, Inc.



TECH NOTE #11

This T/N further justifies some of the rules and guidance provided in the preceding TN24. In addition, it provides two (2) application examples of how to both assess the dynamic performance of individual measurement system components as well as the entire measurement system.

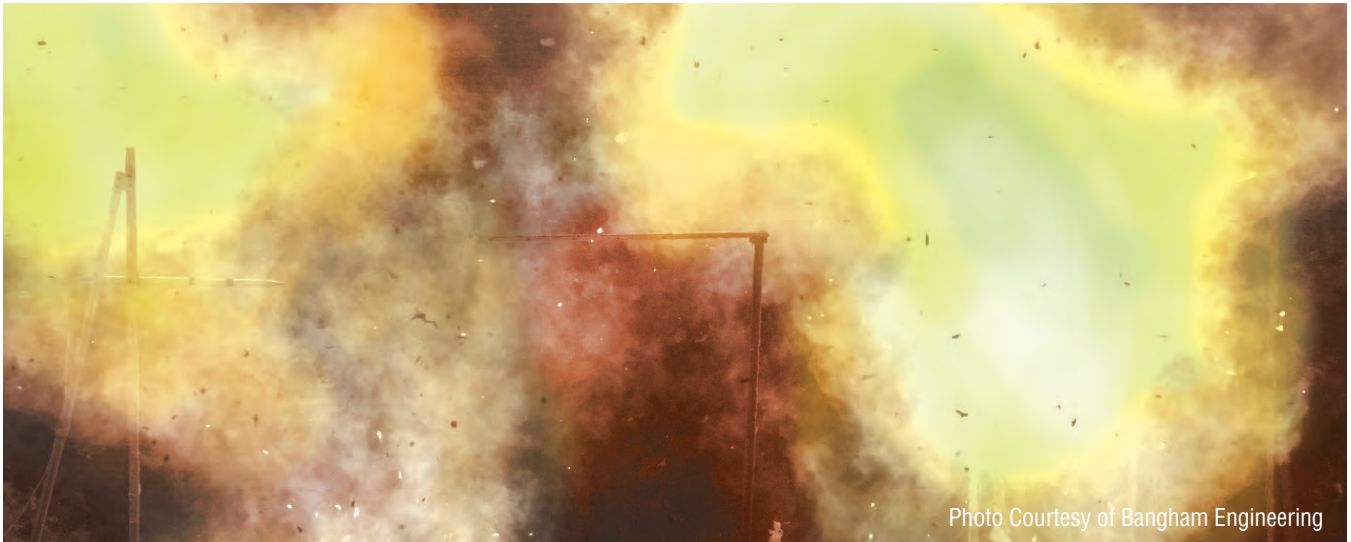


Photo Courtesy of Bangham Engineering

Blast Testing with the Hydrogen Unconfined Test Apparatus (HUCTA) in Huntsville, Alabama

TN-11

Shock and Blast Measurement- Rise Time Capability of Measurement Systems?

Written By

Patrick L. Walter, Ph. D

Shock and Blast Measurement - Rise Time Capability of Measurement Systems?

Patrick L. Walter, Ph. D.

Measurement Specialist/PCB Piezotronics, Inc.
Depew, NY 14043

Engineering Faculty/Texas Christian University
Fort Worth, TX 76129

Shock and blast loading of structures is characterized by a very rapid deposition of energy. When acquiring acceleration or pressure measurements from transducers mounted on test structures, it is often desired to quantify the rate (rise time) of this loading, the relative timing between loading and/or structural response events, or both. Regardless of which, it is important that we select transducers with adequate rise times to acquire these measurements with fidelity. Once this selection is complete, it is necessary to select measurement system components (amplifiers, filters, displays, etc ...) capable of maintaining this fidelity. However, measurement system components are typically specified in terms of the upper frequency at which they provide -3dB signal attenuation. A challenge then exists to infer the rise time capability of an entire measurement system based on the -3dB specifications of its individual components.

In 1948, Robert Walker and Henry Wallman, in chapter 2 of Vacuum Tube Amplifiers, McGraw Hill, 4th edition, worried about this same type problem when considering the rise time capability of vacuum tube pulse amplifiers. At that time, these amplifiers were being used in radar, television receivers, and communications equipment. Based on mathematics (central limit theorem), Walker and Wallman came up with the following rule. "For an amplifier made up of n stages, each of which is free from overshoot, rise times add as the sum of the square root." That is:

$$\tau = (\tau_1^2 + \tau_2^2 + \dots + \tau_n^2)^{1/2}$$

where τ is the overall rise time and the subscripted τ s are the rise times of the individual stages. For our application, the individual stages can be considered to be the various measurement system components. By combining the rise times of each of its components, we can then perform the overall assessment of the rise time capability of a given measurement system.

Fortunately, Mr. Walker and Mr. Wallman provided us with another rule: If τ is the rise time, 10 to 90 percent, of the step-function response of a low-pass amplifier without excessive overshoot and having a -3dB bandwidth f_{-3dB} , then:

$$\tau f_{-3dB} = 0.35 \text{ to } 0.45$$

This rule is very useful. It provides a relationship between measurement system component rise time and high frequency -3dB location. The form of this rule is somewhat of a surprise! The lower limit $\tau f_{-3dB} = 0.35$ can be derived exactly from the mathematics associated with a low-pass first order filter with a

time constant of $1/(2\pi f_{-3dB})$. Such a system has a high frequency roll-off of 6dB/octave, i.e., the slowest possible. However, the surprise is that no matter how steep the roll-off of a measurement system, its shortest rise time is limited to be between $0.35/f_{-3dB}$ and $0.45/f_{-3dB}$.

To witness this rule, I ran a number of tests where the step response of various low-pass Butterworth and Bessel filters were measured. These filters had -3dB frequencies between 1,500 and 15,000 Hz and roll-offs of 24dB/octave (4th order filters). In all instances the τf_{-3dB} product varied between 0.35 and 0.39. This variation was consistent with experimental error. To further investigate this rule, I calculated the impulse response of an ideal boxcar filter. While such a filter is not physically realizable because its step response would have to start before time = 0, its rise time and -3dB relationship were shown to be $\tau f_{-3dB} = 0.44$. This value correlates very well with the 0.45 value postulated in 1948.

Before providing some application examples, one final rule will be provided. Many transducers behave as resonant systems. If the rise time they encounter in service is too short, their resonant frequency is excited and superposed on the recorded data. To preclude significant resultant overshoot from occurring, a rule of thumb for these type transducers is:

$$\tau f_n \geq 2.5$$

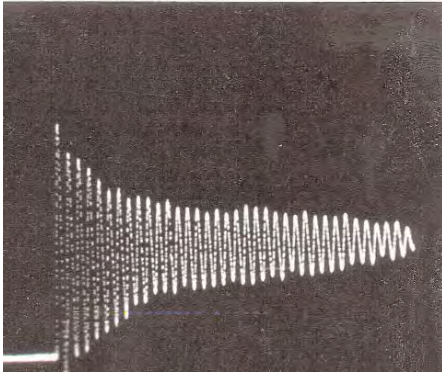
where τ is the 10-90 percent rise time as before and f_n is the resonant frequency of the transducer.

The following figures provide the response of two types of pressure transducers to submicrosecond rise time pressures. The first transducer behaves as a resonant system and the second transducer pair as a nonresonant system (PCB Model 134A pressure bar).

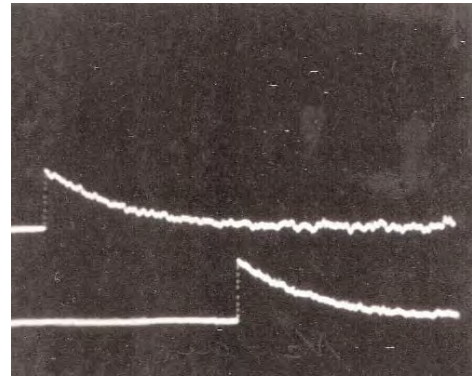
Now that the requisite "rules of thumb" have been provided, two application examples of them are presented.

Example 1:

A nonresonant pressure transducer has a 1 microsecond (μ s) rise time. Its signal passes through an amplifier with a -3dB frequency of 250 kHz. The signal is filtered before digitization by a filter with a -3dB frequency of 100 kHz. After digitization, the signal is displayed on a recorder with a 1 MHz capability. Is the system capable of measuring pressure rise times of 3 μ s?



Resonant transducer response to submicrosecond step input



Nonresonant transducer pair response to submicrosecond rise time inputs

Determination:

Transducer rise time (given):	1 μs
Amplifier rise time: ($\tau_{f_{-3\text{dB}}} = 0.45$ for most conservative value)	1.8 μs
Filter rise time: ($\tau_{f_{-3\text{dB}}} = 0.45$ for most conservative value)	4.5 μs
Recorder rise time: ($\tau_{f_{-3\text{dB}}} = 0.45$ for most conservative value)	0.45 μs
System rise time: (square root of the sum of the squares)	4.97 μs

Answer: No. The measurement system rise time is 4.97 μs , which is longer than the 3 μs rise time it is desired to measure.

Example 2:

A piezoelectric accelerometer has a fundamental resonant frequency of 50 kHz. It is desired to record a shock pulse with a rise time that may be as short as 50 μs . A charge amplifier is available with a -3dB frequency of 100 kHz. A digital recorder has an associated -3dB frequency of 1 MHz. Are these measurement system components adequate for their intended use?

Determination:

Transducer rise time: ($\tau_{f_n} = 2.5$ to determine shortest)	50 μs
Amplifier rise time: ($\tau_{f_{-3\text{dB}}} = 0.45$ for most conservative value)	4.5 μs
Recorder rise time: ($\tau_{f_{-3\text{dB}}} = 0.45$ for most conservative value)	0.45 μs
System rise time: (square root of the sum of the squares)	50.2 μs

Answer: No. The measurement system rise time is 50.2 μs , which does not provide design margin relative to the 50 μs it is desired to measure. The observed rise time should be approximately 5-times the system rise time to be unaffected. Therefore, it would be preferable to acquire an accelerometer with a fundamental resonance above 250 kHz.

Hopefully, these two examples have helped to illustrate how to apply these "rules of thumb" to assess the capability of measurement system components, and thus the overall measurement system, in order to acquire fast rise time data.



TECH NOTE #23

This T/N introduces pyroshock and explains its relevance. Terms such as near field and far field are often heard when describing pyroshock. The physics that supports this distinction is explained. The influence of accelerometer zero shift on shock spectra is briefly mentioned.



TN-23

Pyroshock Explained

Written By

Patrick L. Walter, Ph. D.

PYROSHOCK EXPLAINED

Patrick L. Walter, Ph. D

Measurement Specialist, PCB Piezotronics, Inc.
Depew, NY 14043

Engineering Faculty, Texas Christian University
Fort Worth, TX 76129

This Tech Note provides an introduction to the mechanical environment of pyroshock. Specifically, it (1) defines pyroshock, (2) identifies those situations where pyroshock can induce equipment failure, (3) explains the response of structural systems to pyroshock, and (4) discusses uniqueness in the shock spectra (see PCB® Tech Note 19) associated with pyroshock. Since the importance of pyroshock became recognized in the late 1960s, many articles^{1,2} have been written about it and some test standards³ generated.

Pyroshock is the decaying, oscillatory response of a structure to high-amplitude and high frequency mechanical excitation. The frequencies that comprise this oscillatory response can extend to thousands of Hertz and beyond. They are a subset of the resonant frequencies of the structure.

The aerospace industry was the first to recognize the potentially destructive effect of pyroshock. The firing of explosive bolts, nuts, pins, cutters, and other similar devices initiated this pyroshock. Subsequently, it was recognized that other environments (e.g., the sudden release of strain energy and metal-to-metal impact), although not initiated by explosive devices, produced effects similar to pyroshock.

Originally, the high frequencies associated with pyroshock were believed to be benign; i.e., they did not have the potential to cause damage. For example, a rocket guidance system typically contains an inertial measuring unit (gyros and precision accelerometers) mounted with elastomeric materials to mechanically isolate it from pyroshock. Similarly, massive structures have low resonant frequencies, which effectively isolate them from pyroshock. However, over the years, electrical and optical components have become increasingly more miniature. Because of this miniaturization,

the mechanical resonant frequencies of these components have increased, making them susceptible to damage by pyroshock.

Pyroshock is categorized in the literature as near-field and far-field. This categorization is really a division of thought process and can be explained by the following example⁴. Consider the center of a 1-centimeter thick aluminum plate (Figure 1), which is explosively loaded. One-dimensional strain will be achieved in this center portion until relief waves propagate from the edge of the plate into this region. We will initially focus just on this central region.

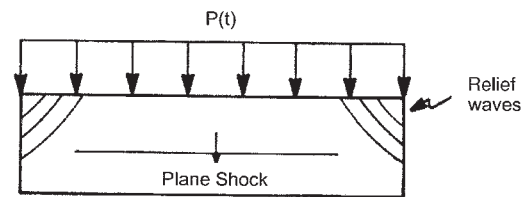


Figure 1: Plane wave propagating through material

Figure 2 describes the interaction between the explosive and the plate. It shows the left going pressure-particle velocity curve for the explosion products of TNT, along with the pressure-particle velocity relationship for aluminum. State (2) represents the pressure and particle velocity initially imparted to the loaded surface of the plate. State (3) occurs after a shock wave has traversed the plate thickness and arrived at its front surface. At state (4), a rarefaction has traversed back to the loaded surface and again interacted with the detonation products, similar to states (6), (8), etc. These reflections occur until the plate is traveling with zero internal pressure and uniform particle velocity.

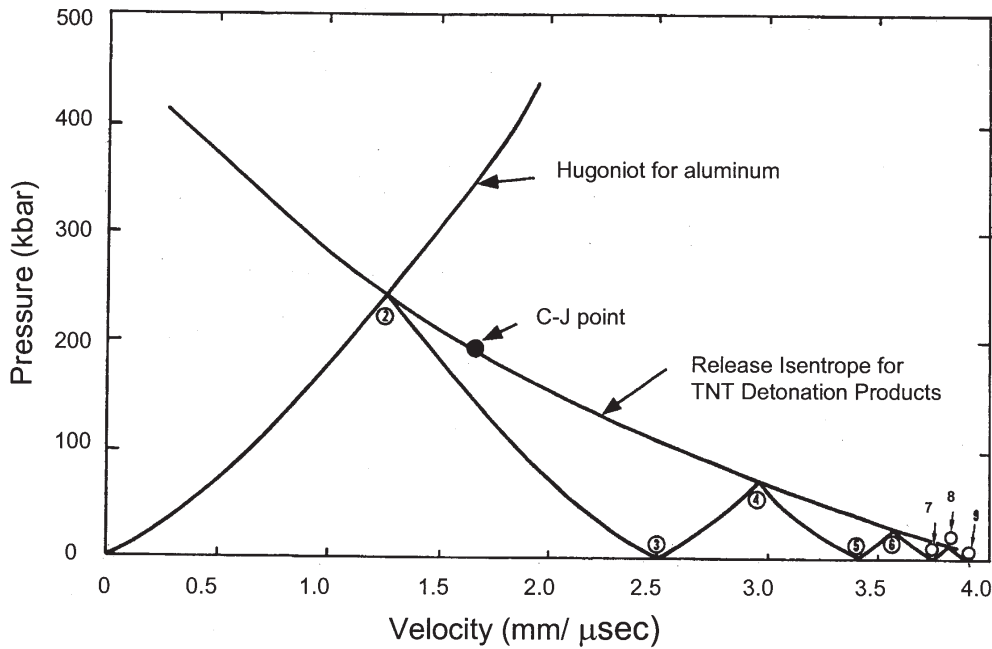


Figure 2:
Pressure versus particle velocity for explosively loaded aluminum plate

Figure 3 illustrates this same process but in the context of a position-time plot. At state (2), the loaded surface begins to move, and at state (3) the unloaded front surface begins to move. At state (4), the loaded surface attains a new velocity, and so on. Figure 4 shows the velocity-time response of the

loaded surface, which is the time derivative of Figure 3. Similarly, Figure 5 shows the acceleration-time response of the loaded surface, which is the time derivative of Figure 4.

Note that these time-response determinations have all been for the loaded surface of the plate. This is the surface that directly interacts with the explosive. The front surface of the plate, the unloaded surface, will have a very similar response, only time-delayed about 1 μ s. For this example, the just described complex response of the central region of the plate ends after about 12 μ s and can be considered near-field pyroshock.

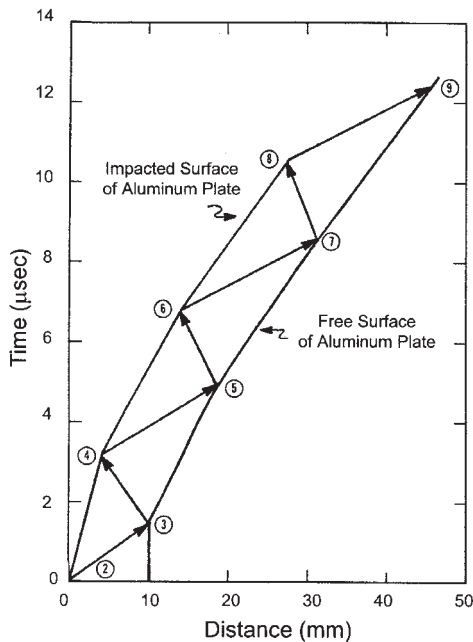


Figure 3: Time versus position for explosively loaded aluminum plate

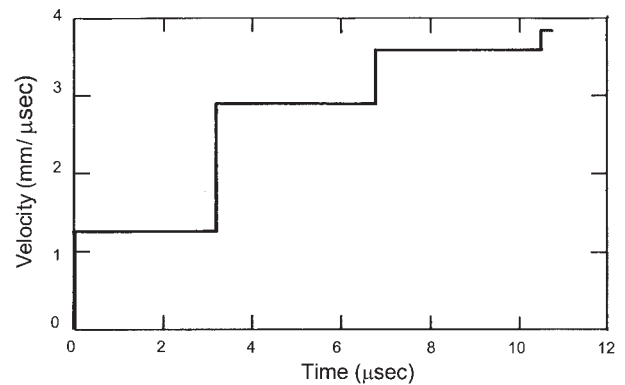


Figure 4: Velocity versus time of loaded surface of aluminum plate

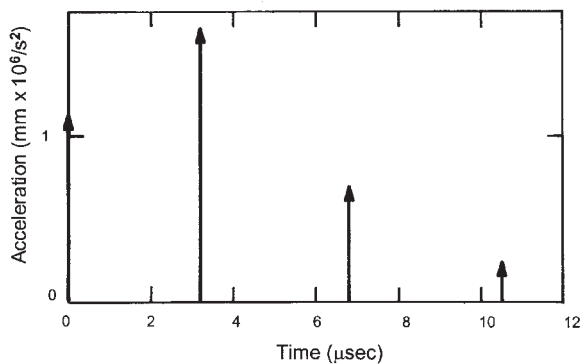


Figure 5: Acceleration versus time of loaded surface of aluminum plate

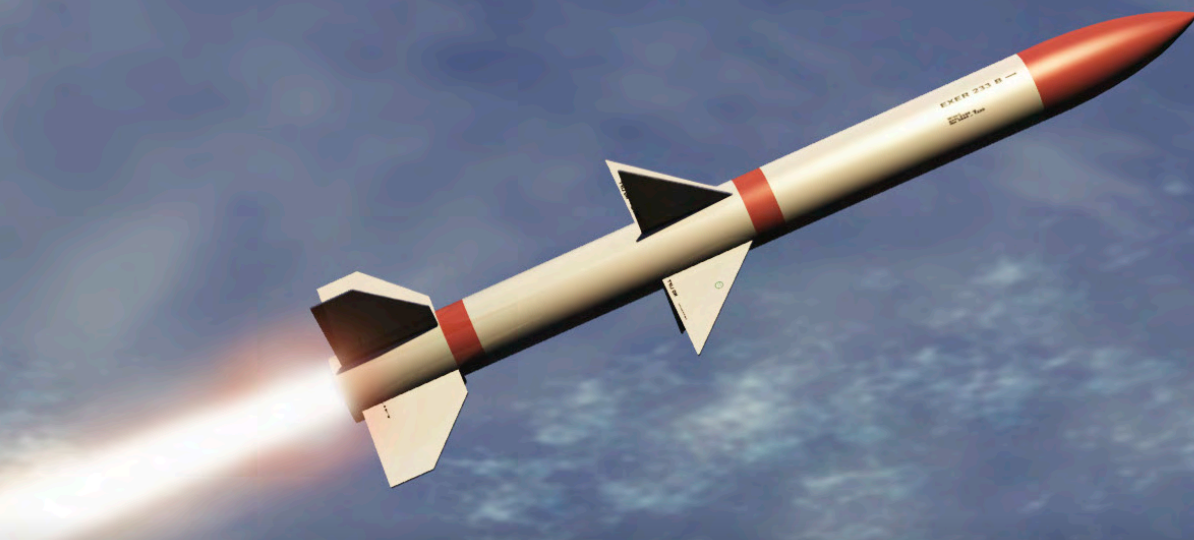
Other than briefly at the center of the plate, one-dimensional strain is not achieved. The motion of the plate extremities is governed by three-dimensional strain. In addition, practical engineering structures have joints and interfaces. Complex geometries and various materials, along with these joints and interfaces, initiate multiple wave reflections. Material properties can also be rate sensitive. The motion in the extremities of an explosively loaded structure lasts for a much longer time period than it takes the

waves traversing back and forth in the central portion of the plate to settle down. This longer time motion is modeled by treating the system as an assembly of discrete springs and masses. The motion in these extremities describes far-field pyroshock.

The damage potential associated with a specific pyroshock event can be replicated to a test item in the laboratory by developing an acceleration-time stimulus whose shock spectra envelopes that which the item encounters in service. Carefully tuned bars, beams, plates, and more complex structures are used to achieve this simulation. They are excited by mechanical impact or even explosive loading³.

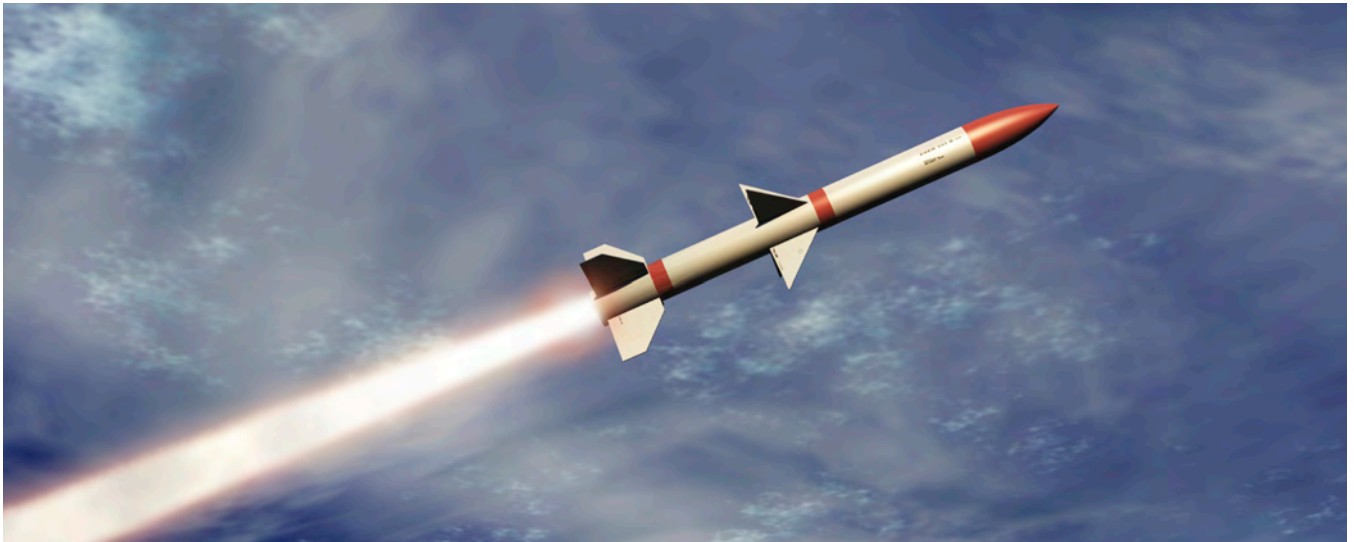
Ideally the shock spectra associated with pyroshock has a low frequency slope of between 6 and 12 dB/octave. Reference 5 provides the mathematical basis for this observation. It is not uncommon for a lesser slope to be observed in processed data. When this occurs, typically the measuring accelerometer is blamed. While a very small zero shift originating in the accelerometer can produce this error, it can also be attributed to an improperly defined signal zero reference level⁵, truncation of the signal during recording⁵, or even aliasing⁶ of the signal due to an inadequate sampling rate.

-
1. Davie, N. T. and Bateman, V. I., Part II, Pyroshock Testing, Harris' Shock and Vibration Handbook, edited by Harris and Piersol, McGraw Hill, 5th Edition, 2002.
 2. Zimmerman, Roger W., Pyroshock – Bibliography, 39th Annual Meeting IEST, Las Vegas, NV, May 2-7 1993.
 3. IEST-RP-DTE032.1: PYROSHOCK TESTING TECHNIQUES. Design, Test, and Evaluation Division, Institute of Environmental Sciences and Technology, 20 pages, Document No. D032, 2002.
 4. Walter, Patrick L., Lessons Learned in Applying Accelerometers to Nuclear Effects Testing, Proceedings 74th Shock and Vibration Symposium, San Diego, CA, October 2003.
 5. Smallwood, David O., Shock Response Spectrum at Low Frequencies, The Shock and Vibration Bulletin, SAVIAC, Volume 1, 279-288, 1986.
 6. Edwards, Tim, Errors in Numerical Integration Due to Band Limiting and Sampling Rate, Proceedings 75th Shock and Vibration Symposium, Virginia Beach, VA, October 2004.



TECH NOTE #19

This T/N provides a brief explanation of the shock spectrum. The shock spectrum is a method to enable replication of the damage potential of a measured complex shock on a unit under test (UUT) with another shock that can more easily be synthesized. The basis of the Shock Response Spectrum (SRS) and its application is illustrated through a simple pictorial example.



TN-19

The Shock Spectrum: What Is It?

Written By
Patrick L. Walter, Ph. D.

The Shock Spectrum: What Is It?

Patrick L. Walter, Ph. D

Measurement Specialist, PCB Piezotronics, Inc.
Depew, NY 14043

Engineering Faculty, Texas Christian University
Fort Worth, TX 76129

Mechanical shock loads that are imparted to electrical and mechanical systems can degrade the performance of these systems or even induce failure. It is therefore desirable to develop a methodology to guarantee the reliability of the more critical of these systems when they are subjected to transient mechanical loading. This methodology is provided in Figure 1. A hypothetical example of the application of this methodology follows.

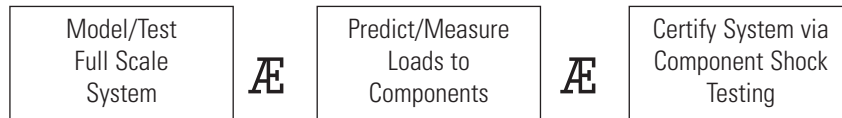


Figure 1: Methodology for Attaining Structural Reliability under Transient Loading

Assume that we want to assure the reliability of a guidance component within a missile system such as shown in Figure 2. We would either model the system analytically, or, preferably, perform a few test flights. We would subsequently model, or, again, preferably measure, the transient acceleration loads imparted to the guidance component at its mounting support. Assuming that the component functioned properly, we could set up a program to perform additional flight tests routinely in such a way as to maintain an ongoing assessment of the component's reliability.



Figure 2: Theater Defense Missile (Lockheed Martin Missiles and Fire Control)

However, such testing would quickly become too expensive. Therefore, to instill ongoing confidence that the component

will function properly after encountering mechanical shock loading in its use environment, the design engineer needs a laboratory test method.

A problem exists in the preceding example since the transient acceleration-time histories that were measured at the component mount are unique to the missile system launch-and-flight environment. These time-histories typically cannot be replicated using laboratory shock equipment. The challenge is then to create in the test laboratory a qualification shock environment for the guidance component that exceeds the component's operational environment in some sense. The shock response spectrum (SRS), first presented by Biot¹ in 1933, is a widely accepted tool used to develop these laboratory tests.

We assume that the component of interest can be modeled by a continuous series of single-degree-of-freedom (SDOF), second-order systems (oscillators), each increasing in natural frequency ($f_n = [1/(2\pi)]\sqrt{k/m}$). Figure 3 represents this independent set of oscillators. Their increase in natural frequency is pictorially represented by a decreasing mass size from left to right. By convention, we assign to each oscillator a ratio of critical viscous damping of $\xi = 0.03$. Figure 4 provides enhanced definition of one of these oscillators.

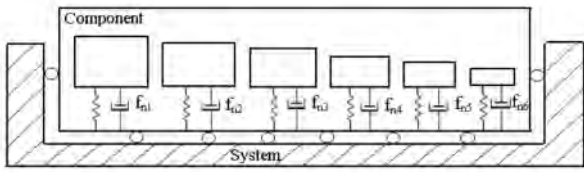


Figure 3: Component Represented by SDOF Oscillator Array

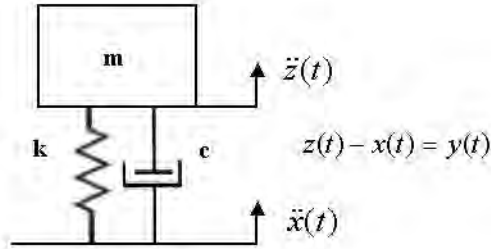


Figure 4: Individual Oscillator with Coordinates Defined

Focusing on the missile in Figure 2, we will conjecture that at release from its launch canister we measure an acceleration input to a guidance component as in Figure 5. We will then analytically input this acceleration $[\ddot{x}(t)]$ into the base of one of the oscillators (Assume #1). We will then calculate the maximum absolute acceleration time history response (Figure 6a) of oscillator #1 to $\ddot{x}(t)$ and eventually plot this point at frequency f_{n1} . This plotted response point will be $\ddot{z}(t) = \ddot{y}(t) + \ddot{x}(t)$. We will then advance to oscillator #2, perform the same calculation (Figure 6b), and plot the result at frequency f_{n2} . As the oscillators become more and more stiff ($f_n = \infty$), they will eventually follow $x(t)$ exactly, and the maximum response (Figure 6c) will be the same as the maximum peak value in Figure 5.

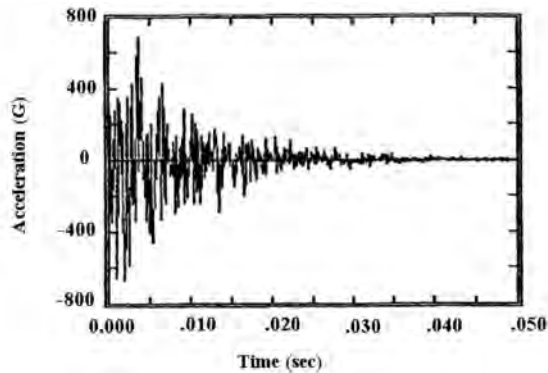


Figure 5: Component Input

Figure 7 is then the envelope resulting from plotting the individual responses of an infinite set of oscillators to the acceleration input of Figure 5. This plot of the maximum absolute value of each acceleration response $\ddot{z}(t)$ for each oscillator as a function of frequency f_n represents the most common two-dimensional shock spectrum. In some instances, where a more appropriate component failure model holds, the maximum absolute velocity or displacement spectrum might be plotted as an alternative. As long as the guidance component can be modeled as Figure 3, and its damage can be related to its peak response experienced as a result of the shock, the shock spectrum provides an indication of the damage potential of the shock being analyzed.

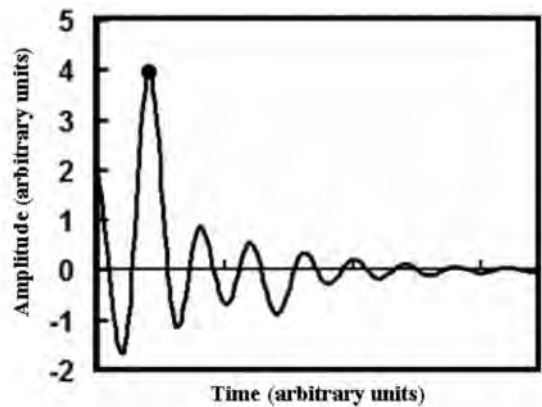


Figure 6a: Oscillator #1 response at $f_{n1} = f(1)$

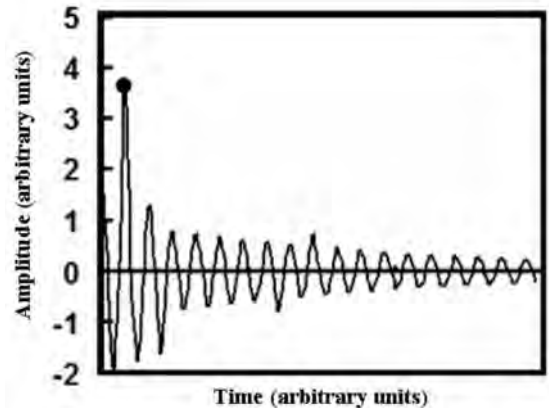


Figure 6b: Oscillator #2 response at $f_{n2} = f(2)$

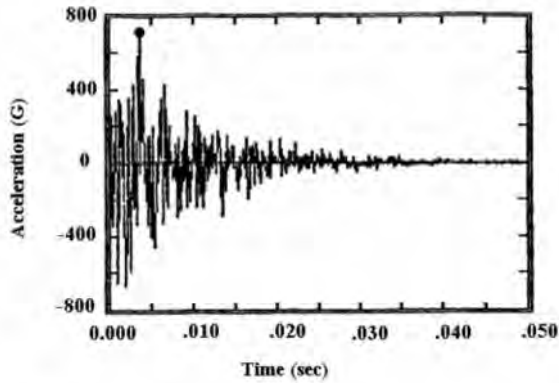


Figure 6c: Oscillator response at $f_{n\infty} = f(\infty)$

Figure 6: Example of Response of Individual Oscillators in Figure 3 to Component Input in Figure 5

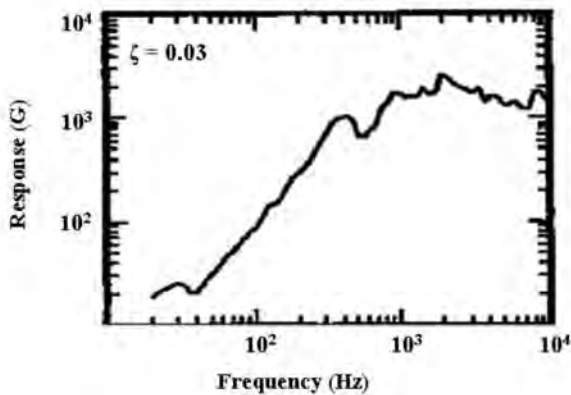


Figure 7: Envelope of Maximum Response vs. Frequency of an Infinite Number of Oscillators to the Shock in Figure 5

The next challenge is to establish an equivalent qualification-shock for the test laboratory. The commonly made assumption is that any qualification shock is acceptable as long as its shock spectrum fully encompasses the measured field environment. Haversine shapes are classical pulses that are called out in shock testing and that can be approximated on laboratory shock machines. A haversine pulse of amplitude A and period T would analytically be expressed as:

$$\ddot{x}(t) = (A/2)[1 - \cos(2\pi t/T)], \quad 0 \leq t \leq T \quad (1)$$

We want to select a haversine pulse whose shock spectrum will encompass but not greatly exceed that of the field shock (per Figure 7). Figure 8a shows such a pulse and Figure 8b shows how its shock spectrum envelops the shock spectrum of the field pulse. Thus, for our example, a 2000G-amplitude haversine pulse of 0.5 milliseconds (0.0005 seconds) duration will become the qualification shock for our guidance component. Since Figure 5 has both positive and negative halves, the haversine pulse needs to be applied in the test laboratory in both directions.

Much more could be written about the shock spectrum technique and variations associated with it. The technique satisfies the requirement to provide a simple means to characterize a shock environment, and, since it is an enveloping technique, it also enables different shock events to be combined into a single environment. However, it remains controversial because acceleration pulses that differ greatly in amplitude, frequency content, and duration can produce equivalent shock spectra. For example, the previous haversine pulse can be seen to have a finite velocity change associated with it while the field pulse does not.

Nevertheless, in spite of any controversy associated with the shock spectrum method, it remains firmly entrenched as the principal tool for laboratory shock testing, and, as such, the method is a key element in the process of assuring system reliability in field applications.

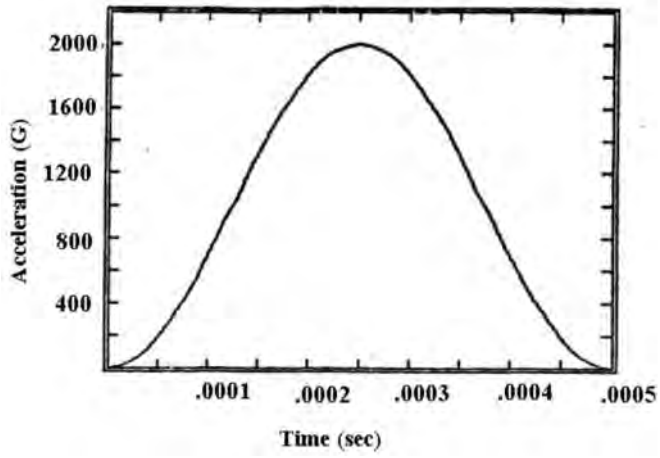


Figure 8(a)

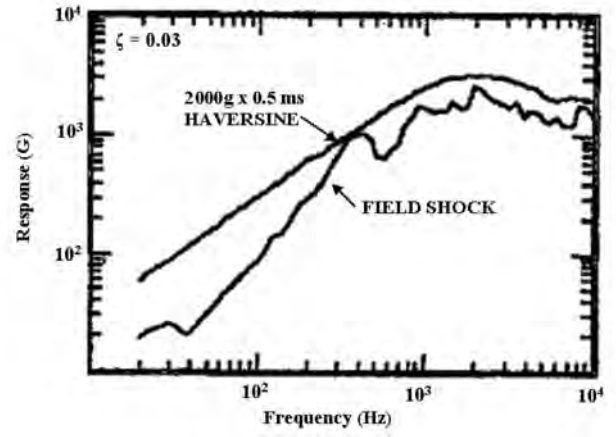


Figure 8(b)

Figure 8: Haversine Pulse and Enveloped Shock Spectrum of Field Shock

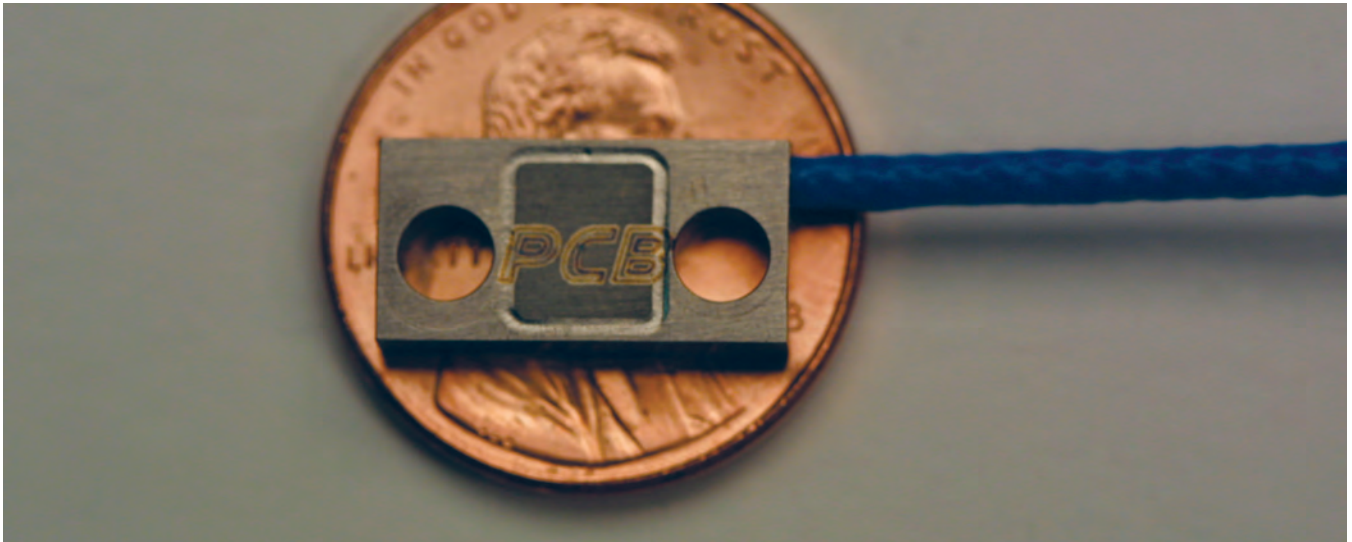
REFERENCE

1. Biot, M. A., "Theory of Elastic Systems Vibrating Under Transient Impulse With an Application to Earthquake Proof Buildings", Proceedings of the National Academy of Sciences, Vol. 19, No. 2, 1933, pp. 262-268.



TECH NOTE #25

This TN attempts to answer the question as to the upper frequency limit that accelerometer data should be viewed as credible. Severe shock (e.g. pyro) often has associated with it very high frequency content. This is evidenced by the fact that the resonant frequency of the measuring accelerometer is often excited. The fact that these high frequencies are present does not mean that they have significant damage potential to the test item (UIT). However, a reasonable question is: how high in frequency is the output of an accelerometer an accurate portrayal of its input?



TN-25

How High in Frequency Are Accelerometer Measurements Meaningful

Written By
Patrick L. Walter, Ph. D.

How High in Frequency Are Accelerometer Measurements Meaningful

Patrick L. Walter, Ph. D.

Senior Measurement Specialist, PCB Piezotronics, Inc.
Depew, NY 14043

Professor of Engineering, Texas Christian University
Fort Worth, TX 76129

Almost all piezoelectric accelerometers in the current market place have a fundamental sensor resonance below 100 KHz. In 1983 Endevco Corporation designed a series of MEMS (Micro Electro-Mechanical Systems) accelerometers [1]. These silicon-based piezoresistive accelerometers enabled sensor resonances of 100s of KHz to above 1 MHz. The original intent of this design (Model 7270) was to create an accelerometer with a resonant frequency high enough that it would not be excited in metal-to-metal impact or explosive environments. These types of environments are generally described by the term pyrotechnic shock (pyroshock). Unfortunately, in spite of the advantage provided by the high resonant frequencies of these accelerometers, the extremely low intrinsic damping of silicon acts as a counterbalance. The result of this low damping is often over-ranging and breakage of the accelerometers when they are subjected to pyroshock [1]. In order to support the development of a series of more robust MEMS accelerometers, this paper answers the question: How high in frequency response are accelerometer measurements meaningful?

Introduction

In 2008, a new MEMS shock accelerometer (PCB Piezotronics Model 3991) was designed and introduced into the market place. While this accelerometer has the same foot print as the Endevco 7270, its most significant differences are its contained damping (~ 0.05 of critical viscous, $Q=10$) and over-range stops [2]. The goal of the damping is to reduce the "Q" of the sensor at its resonant frequency. This lowered "Q" should lessen the fragility and associated over-range issues associated with MEMS accelerometers in high frequency (e. g., pyroshock) environments. To enable damping to be achieved, the compliance of the sensing element of the Model 3991 had to be increased (i. e., its stiffness had to be decreased). This initiated the discussion, which is the subject of this paper: How high in frequency are accelerometer measurements meaningful? The author contributed to this discussion by opining that 20 KHz was a realistic upper limit. This paper provides the basis for this opinion.

Actually, the author had encountered this discussion twice before. In the early 1970s, at a Transducer Workshop sponsored by the DoD National Test Ranges, a need was expressed for accelerometers capable of measuring to 100 KHz to support shock wave physics experiments. At that time, no accelerometer capable of this measurement could even be

conceptualized. In 1976, at Sandia National Laboratories, the request for an extremely high frequency acceleration measurement was again presented to the author. The goal was to characterize the structural input to hypersonic vehicles flying through rain storms. This input was theorized to have a power spectral density (PSD) surpassing 50 KHz in frequency content. The author performed several calculations that discouraged any attempt at measurements to support a test series.

In the ensuing years, several standards have evolved to define and support pyrotechnic shock testing [3]. These include: (1) IEST-RP-DTE032.1, Pyroshock Testing Techniques (being reviewed and updated), (2) MIL-STD-810F, Method 517 (changes currently being proposed), and (3) NASA HDBK-7003. In these standards are definitions for near field pyroshock. Respectively, in terms of amplitude and frequency content, these definitions are:

IEST-RP-DTE032.1: no magnitude specified, $> 10,000$ Hz in frequency content,
MIL-STD-810F: $> 5,000$ G in magnitude, $> 100,000$ Hz in frequency content, and
NASA HDBK-7003: $> 5,000$ G in magnitude, $> 100,000$ Hz in frequency content.

These definitions might imply that frequencies much higher than 10,000 Hz can and should be measured by surface mounted accelerometers. This implication would be incorrect and is supported by the following four (4) arguments:

1. Calibration limitations in the national system of standards preclude the verification of the performance of accelerometers above 20 KHz.
2. Structural modeling of a unit under test (UUT) to very high frequencies typically lacks adequate predictive capabilities to correlate with experimental structural measurements.
3. The physical size of accelerometers tends to provide spatial averaging of the structural response of the UUT at high frequencies.
4. At very high frequencies, the physical presence of the accelerometer modifies the response of the structure to which it is affixed.

Each of these arguments will be investigated and individually supported.

Figure 1 shows a PCB Model 3991 (geometrically identical to an Endevco 7270) sitting on top of a United States one-cent piece. The coin's dimensions are 0.75 inches or 19 mm in diameter and 0.05 inches or 1.27 mm in thickness.

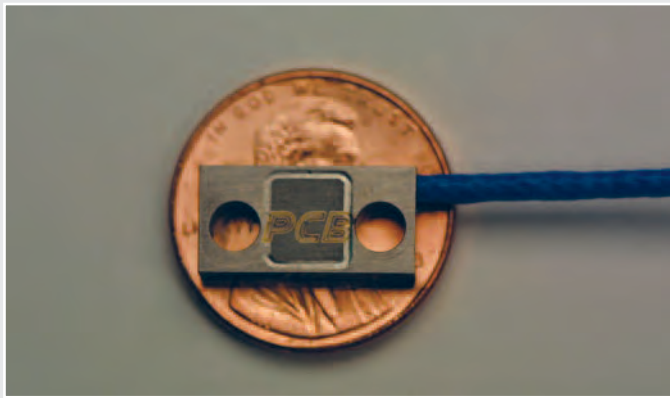


FIGURE 1: PCB Model 3991 on a United States One-Cent Coin (penny)

The resonant frequency for the first mode of vibration of the one-cent coin alone, with free edges, can be calculated to be 12,470 Hz. Its mass is approximately 2.57 grams. Envision how radically this resonant frequency would decrease due to the stiffening effect and the addition of the 1.28 gram mass of the accelerometer if it were physically attached to the coin! This observation supports the premise of this paper. That is, there is an upper frequency limit above which an accelerometer stops providing a meaningful structural response assessment of the UUT. The challenge then is to define this limit.

Calibration Limitations: Most developed countries have a centralized, government-supported, calibration service. For the United States of America this service is the National Institute of Standards and Technology (NIST). At NIST, the upper frequency limit of accelerometer calibration services is 20,000 Hz [4]. Specifically, this calibration is performed from 3 KHz to 20 KHz at constant displacement amplitude of 121.10 nm, which enables its accurate measurement. The resultant acceleration varies from about 4 G at 3 KHz to 200 G at 20 KHz. Measurement uncertainty is 1 – 3 %.

Above 20 KHz the air bearing shakers [5], typically used to provide linear motion, begin to become operationally limited. In addition, at any constant G-level, as vibration frequencies increase their associated displacements decrease, and the accuracy of laser based interferometer measurements is lessened. These interferometer measurements, along with independent frequency determinations, provide the basis for the calibration. In summary, 20 KHz represents the upper frequency limit for quantitative accelerometer calibrations both nationally and internationally.

Still focusing on the calibration issue, it should be noted that MEMS piezoresistive accelerometers typically provide between 100 and 200 mV

full-scale output. Thus, a 20,000-G accelerometer, typical of those used for pyroshock measurements, would provide signal levels between 0.02 and 0.04 mV at 4 G and between 1 and 2 mV at 200 G. These low signal levels further increase the uncertainty in the determination of the frequency-response function for an accelerometer (See Fig. 2). The red curve is the most probable response of the Model 3991 and the actual test data (blue scatter) contains uncertainty due to its low signal output. Thus, frequency-response determinations become further complicated by low signal levels from the accelerometer under test. This provides additional credibility for limiting the performance certification of accelerometers to an upper frequency of 20 KHz. Above that value, unanticipated torsional or lateral resonances internal to the accelerometer's sensing element [6], resonances in the accelerometer's case, and lead-wire attachment resonances can erroneously be interpreted as structural response of the UUT. None of these resonances would have been identified in the calibration process. Mounting anomalies can also be a further error contributor.

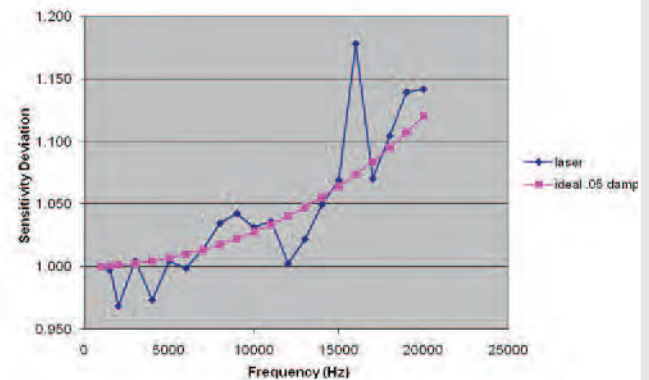


FIGURE 2: Vibration Test Results on a Model 3991

Modeling Limitations at High Frequencies: Pyroshock testing techniques first evolved in support of the aerospace community. Most UUTs associated with this community are fairly substantial in size (e.g., satellites with volumes as small as a few cubic feet up through large launch vehicles). As a byproduct, their fundamental resonant frequencies are low. However, high frequencies become of interest when assessing the response to pyroshock stimuli of smaller, contained electronics or other fragile items internal to the UUT.

Modeling the response of complex structures to high frequencies necessitates their discretization into a very large number of elements. This number of elements can be thousands, tens of thousands, or even higher. For a given structure, as the number gets larger, the element size progressively decreases. Even though the UUT may be substantial in size, the accelerometer measures the response of the element to which it is affixed. Thus, as we attempt to make an experimental correlation of structural dynamics measurements to predictive models at high frequencies, we reduce the problem to the dilemma presented in Fig 1.

One question that could be asked is: Why not include the structural characteristics of the accelerometer in the modeling? The answer is that these characteristics (particularly those of the interconnecting cable) are not well defined, and the mounting attachment can also be a variable. For example, an article in Machine Design (11/15/2002) notes that there are 75 factors that affect the tension in applying torque to a single bolt.

While this discussion of modeling limitations has not produced a definitive upper frequency limit for meaningful accelerometer measurements, it is consistent with prior discussions that such a limit must exist.

Spatial Averaging Considerations of the Measurements: Digital sampling of data requires at least two samples per cycle of a sine wave to preserve its frequency content. This requirement is based on the well-known Shannon theorem, and sampling that satisfies it is referred to as Nyquist sampling. However, if the goal of the measurement is to obtain an experimental peak value of a sinusoidal signal at that frequency, sampling must occur at not less than ten equally spaced intervals per cycle. This sampling density assures no more than a 5% peak error. This last requirement enables one to infer that the wavelength of any traveling elastic wave is particularly important in establishing the minimum accelerometer spatial mounting density required to define the upper frequency content of pyroshock or other high-frequency events. This wavelength must then contribute to defining an upper frequency limit for meaningful measurements.

The velocity of propagation of elastic waves traveling in a solid is defined by the Lamé constants [7] λ and μ . Assuming an isotropic, unbounded solid medium, the surface of a discontinuity advances through the solid with a velocity of:

$$\sqrt{((\lambda+2\mu)/\rho)} \quad (1)$$

for waves of dilation and

$$\sqrt{(\mu/\rho)} \quad (2)$$

for waves of distortion. All plane waves travel with the velocities obtained in either Eqs. (1) or (2) above. A third type wave (Rayleigh) also exists and propagates on the surface of a solid, elastic body. Its velocity is always between the two above, so the dilational and distortional waves will be evaluated as limiting cases. The Lamé constants are defined by the material properties E (Young's modulus) and ν (Poisson's ratio). Steel (E = 30,000,000 psi, $\nu = .33$) will be selected as a material to perform some representative calculations. Steel results in a calculated nominal velocity for the dilation wave (P-wave) of 245,000 inches/second. Its distortional wave (S-wave) has a calculated nominal velocity of 123,000 inches/second. Again, the Rayleigh wave has an

intermediate velocity. Using the relationship:

$$(\text{wavelength}) \times (\text{frequency}) = \text{velocity} \quad (3)$$

we can find the corresponding wavelengths for the P and S waves in steel at 20 KHz. These calculate to be nominally 12 inches for the P-wave and 6 inches for the S-wave.

One-inch is a typical minimum spacing between accelerometers mounted on a structure. Using the just-presented requirement (in the two underlined sentences just above Eq. (1)) for 10 samples/cycle to define the peak value of a sine wave within 5%, the above wavelength values (6 and 12 inches) also indicate 20 KHz to approximate a nominal upper limit at which one should expect to acquire quantitative structural dynamics measurements with accelerometers. (Note: This observation is based on the fact that 10 samples/cycle at 1-inch intervals enable the accurate definition of a wavelength 10 inches long.)

Modification of the Structural Response by the Accelerometer: Mechanical impedance can be considered to be the resistance of a structure to motion. If F is the peak harmonic input force to a structure, and V is the velocity response at a point, then the mechanical impedance at a given frequency is:

$$Z_{\text{mech}} = (F/V)e^{i\theta} \quad (4)$$

An accelerometer can be approximated as a pure mass to approximately 80% of the fundamental resonant frequency of its seismic flexure. This is because even as the seismic flexure of the accelerometer approaches resonance, if properly designed, the much larger, rigid accelerometer case that houses the flexure will dominate its response. Thus, the mechanical impedance (Z) of an accelerometer can be calculated to be:

$$Z_{\text{accel}} = (-\omega^2 m_{\text{accel}} A)/(j\omega A) = -j\omega m_{\text{accel}} \quad (5)$$

Here, ω is the angular frequency, A is the amplitude of displacement at ω , $j = \sqrt{-1}$, and the mass of the accelerometer is clearly identified. Note that the impedance of the accelerometer increases with frequency. Having made this observation, the mechanical impedance of an Endevco 7270 or PCB 3991 can easily be calculated. Two grams will approximate the mass of either accelerometer while also accounting for mounting screws and cable attachment. The magnitude of Z_{accel} then becomes 7.178×10^{-3} pound-seconds/inch at 100 Hz and 1.436 pound-seconds/inch at 20 KHz.

It is then desired to assess the effect of Z_{accel} on the response of the structure to which it is affixed. For a linear, elastic structure subjected to a constant harmonic forcing function, the presence of an accelerometer will modify the structural motion such that:

$$V_{\text{final}} = V_{\text{initial}} [Z_{\text{structure}}/(Z_{\text{structure}} + Z_{\text{accel}})] \quad (6)$$

For most complex structures, $Z_{\text{structure}}$ is undefined. Regardless, the preceding equation identifies the mechanism by which the presence of the accelerometer modifies the response of the structure.

This situation has been studied [8] for the case of an accelerometer on the end of a long, thin rod that is harmonically excited at its opposite end. This is one of the few cases where $Z_{\text{structure}}$ can be calculated. Results are:

$$Z_{\text{structure}} = -j(\sqrt{E\rho})A\sin(\omega L/\sqrt{E/\rho}). \quad (7)$$

In the above equation, all variables remain as defined earlier with the addition of A as the cross sectional area of the rod and ρ as its material density. To perform a representative calculation, consider an aluminum rod that is 9.82 inches long with a diameter of 1.00 inches. The velocity of propagation of a longitudinal wave in this rod is 196.4×10^3 inches/second. The 9.82 inch length was selected only because the propagation velocity (196.4×10^3 inches/second) is a multiple of this length allowing 20 KHz to correspond to one of the resonances of the rod. For this rod length, at 20 KHz, the magnitude of its mechanical impedance can be calculated to be 33.63 pound-seconds/inch.

If we include the effect of the accelerometer on $V_{\text{final}}/V_{\text{initial}}$ (Eq. 6), using the values we have just calculated for the accelerometer and the rod, we determine the accelerometer will modify the response of the structure by 5%. An accelerometer of larger mass (e.g. triaxial) would produce a larger degradation. While the influence of a given model of accelerometer on the response of a structure is dependent on the accelerometer's mass, its operating frequency, and the geometry and material of the structure on which it is mounted, the result of the 20 KHz calculation (just obtained) again shows consistency as an approximate upper-measurement limit.

Conclusions: The goal of any accelerometer measurement is to define the response of the structure to which it is affixed without disturbing the structure's motion. At high frequencies, differences between the true response of the structure and the measured response from the accelerometer will occur. These differences can be attributed to unidentified higher frequency resonances or mounting anomalies associated with the accelerometer, spatial averaging of frequencies due to the physical size of the accelerometer, and mass loading of the

structure to which the accelerometer is affixed. In addition, experimental verification of the modeling of structural response of the UUT becomes increasingly limited as finite element grid size is reduced. A series of arguments has been presented that indicate a realistic high frequency limit for quantitative acceleration measurements from surface mounted accelerometers to be approximately 20 KHz. Having been presented, this limit should result in the establishment of more realistic testing goals in general and specifically assist in evolving specifications for pyrotechnic shock (pyroshock).

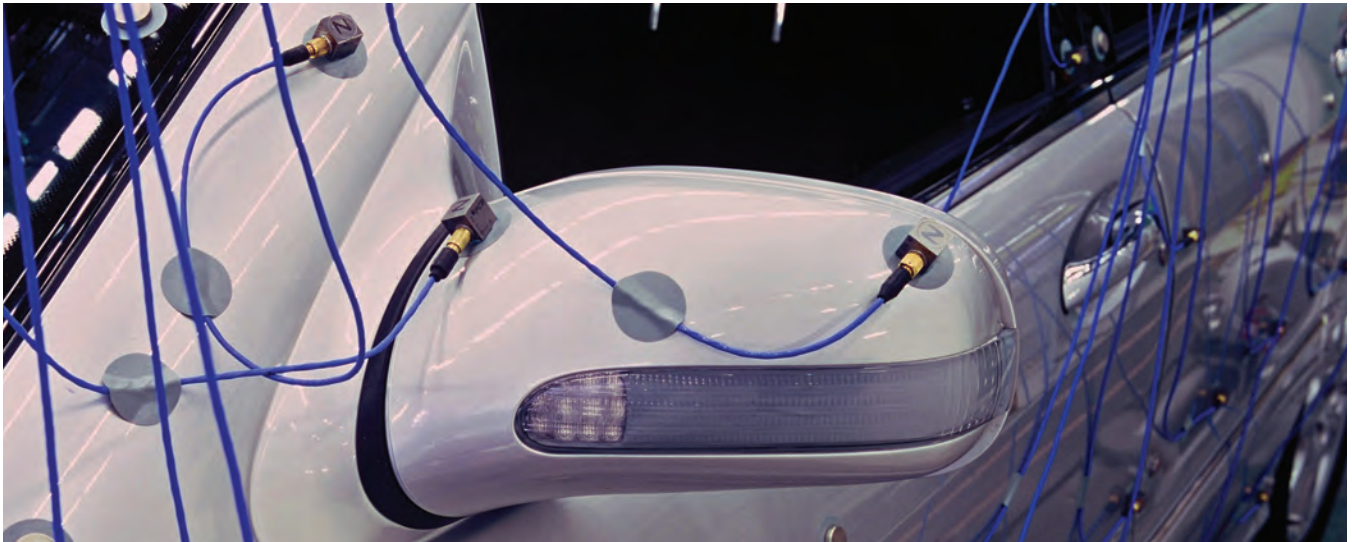
REFERENCES

1. Walter, Patrick L. "Lessons Learned in Applying Accelerometers to Nuclear Effects Testing", *The Shock and Vibration Digest*, to be published November/December 2008, Sage Science Press.
2. Sill, Robert D., "Test Results and Alternate Packaging of a Damped Piezoresistive MEMS Accelerometer", May 13-15, 2008, 52nd Annual NDIA Fuze Conference, Sparks, NV.
3. Bateman, Vesta I., "Use pyroshock definitions as guidelines – analyze your data first!", *Test*, June/July 2008, pp. 10-12.
4. <http://ts.nist.gov/MeasurementServices/Calibrations/vibration.cfm>, May 2008.
5. Dimoff, T., "Electrodynamic Vibration Standard with a Ceramic Moving Element", *Journal of Acoustic Society of America*, September 1966, Vol. 40 (3), pp 671-676.
6. Liu, Bin, *Transducers for Sound and Vibration – The Finite Element Method Based Design*, June 2001, Ph.D. dissertation, Department of Manufacturing and Engineering and Management Technical University of Denmark. June 2001.
7. Bedford, A., Drumheller, D. S., *Introduction to Elastic Wave Propagation*, 1994, John Wiley and Sons, New York.
8. Walter, Patrick L., *Limitations and Corrections in Measuring Dynamic Characteristics of Structural Systems*, 1978, Ph.D. thesis, Arizona State University, pp. 121-124.



TECH NOTE #33

This TN describes the important considerations that must be made when selecting and tying down the instrumentation cable of the accelerometer. The cable is a distributed parameter electrical system with material properties. Its potential to modify signals and act as an additive noise source are discussed.



TN-33

The Instrumentation Cable: Critical but Often Neglected

Written By
Patrick L. Walter, Ph. D.

The Instrumentation Cable: Critical but Often Neglected

Patrick L. Walter, Ph. D.

Senior Measurement Specialist
PCB Piezotronics

Professor of Engineering
Texas Christian University

ABSTRACT:

Compared to other measurement system components such as high-performance transducers, signal conditioning amplifiers, anti-aliasing filters, and high-speed and high-resolution digitizers, interconnecting cables are often viewed as lacking glamour. Their functionality is frequently considered as analogous to fluid flow in a pipe where everything that enters exits successfully. Nothing could be further from the truth! Cables are extremely important, and can be one off the largest sources of problems in instrumentation systems. Properly selected cables are necessary to enable information bearing signals from transducers to be transmitted with fidelity for recording and analysis. This paper provides guidance for selecting appropriate instrumentation cables with specific focus on signal modification that can occur when improper cables are chosen. This modification can occur due to either filtering by or signal generation within the cables or a combination of the two.

INTRODUCTION:

Typically instrumentation system designers worry about parameters such as low and high-frequency -3dB points, signal-to-noise ratios, anti-alias filter types and settings, data digitization rates, bit resolution, data post processing algorithms, and more. The interconnecting cabling, in spite of the fact that it must transmit the signal with fidelity, is often an afterthought. In instrumentation system design cable selection considerations should include, as a minimum, items such as:

- hermeticity and surety at the connector
- operating temperature range
- impedance
- shielding
- noise generation
- abrasion resistance
- strength
- weight
- compliance
 - bend radius
- outgassing (in vacuum operation)
- cost

This list could be further expanded to also encompass the cable connector. The connector is typically comprised of a large number of intricate parts. Pin chatter during vibration is just one of many observable connector malaises. This article focuses on (1) inadvertent signal filtering attributable to the cable impedance and (2) noise generation internal to the cable (see Figure 1).

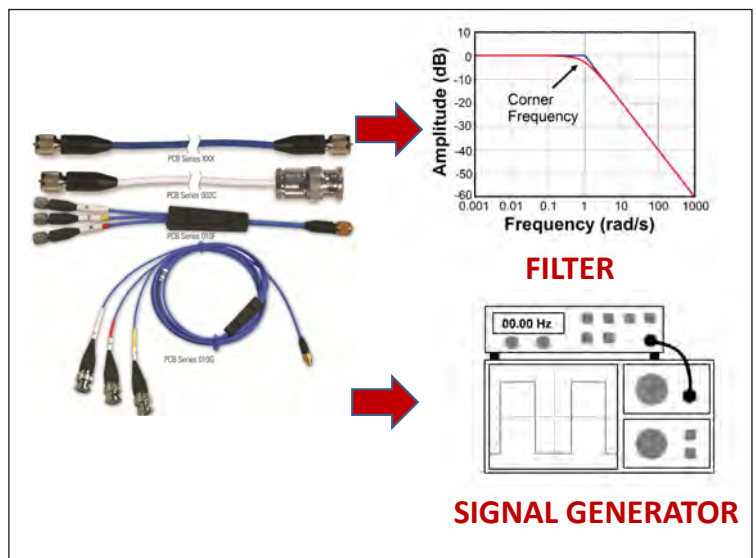


Figure 1: The cable can function as both a filter and a signal generator

TRANSDUCER SIGNALS:

Static pressure and force measurements are typically acquired by resistive bridge-type transducers. More often than not these measurements use transducers containing metal strain gages, but semiconductor gages can also be employed. Alternately, strain itself can be the measurement parameter of interest, and the metal strain gages are then affixed to the particular structure of concern and connected into a Wheatstone bridge circuit. For all of these measurements the cable must transmit without attenuation the bridge supply voltage to the appropriate input corners of the bridge circuit to preclude signal attenuation. Thus, cable resistance must be considered.

Vibration measurements are typically made with piezoelectric accelerometers at frequencies below 2,500 Hz. Today, most piezoelectric accelerometers contain integral electronics (IEPE = ICP®) operating from a 4 milliamp constant current supply. For hazardous vibration tests requiring long cable lengths, this current may have to be increased. Similarly, when using ICP® type accelerometers to measure high frequency mechanical shock (e.g., to 10,000 Hz) with intermediate to long cable lengths, higher drive currents may again be required. This higher current is necessary to overcome filtering attributable to the cable capacitance, which must be considered. In some instances (e.g., very high temperatures) the piezoelectric accelerometer may not contain these integral electronics but have them remotely placed. In this later situation other cable concerns become involved, which have yet to be discussed.

Air blast measurements are extremely demanding in terms of high frequency requirements¹. Piezoelectric or semiconductor (MEMS) technology is typically used. Wide band amplifiers are required to enable digitization of data to frequencies as high as or higher than 1 million/samples second. The associated explosive environment may require standoff transducer distances in terms of 100s to low 1000s of feet. Due to this extremely high frequency data requirement, both the cable's capacitance and inductance must be considered as they can contribute to signal distortion or modification (filtering).

FILTERING WITHIN THE CABLE:

Filtering will be defined here as any attenuation or modification of the frequency content of the output signal from the transducer attributable to the cable. To understand this effect, we will look at impedance sources exclusively associated with the cable. These are the cable resistance r per unit length, capacitance c per unit length, inductance l per unit length, and cable conductance g (leakage from one conductor to another) per unit length². Figure 2 below provides a lumped mass model of a cable segment Δx long. Input and output currents and voltages are also shown. Instrumentation cables are typically tightly bundled or are configured as twisted pair or coaxial so that conductance can usually be ignored.

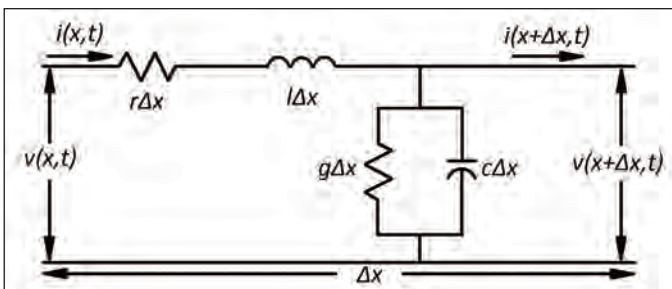


Figure 2: Lumped mass model of a cable Δx long

Bridge transducers making static measurements are the easiest to analyze with regard to cable signal attenuation and will be discussed first. Figure 3 shows that the effect of the series line resistance rL ($L = \text{cable length}$) is to limit the supply voltage E available at the bridge. Therefore the supply voltage must be increased by the ratio of $(2rL + R_{\text{bridge}}) / R_{\text{bridge}}$ to avoid signal attenuation.

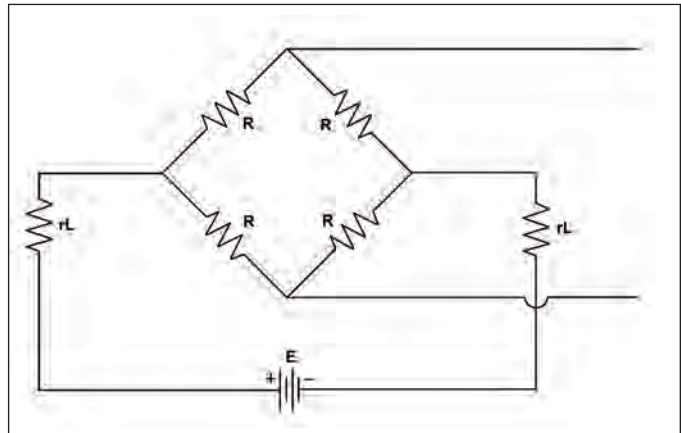


Figure 3: Series line resistance limits bridge supply voltage

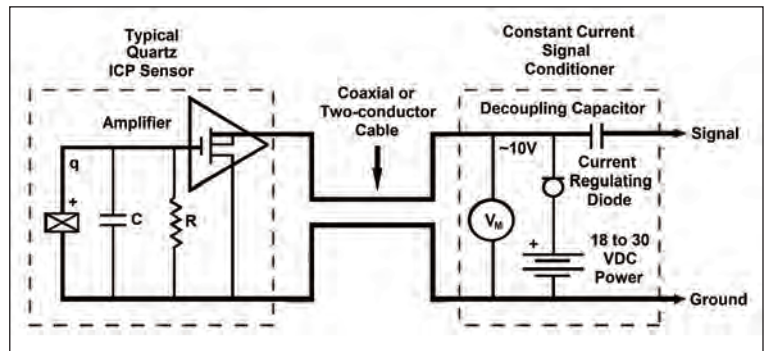


Figure 4: ICP® transducer with constant current supply

Figure 4 schematically shows an ICP® piezoelectric accelerometer and/or pressure transducer used for dynamic measurements. We will consider the effect of the coaxial or two-conductor cable between the constant current diode and the amplifier. For very long cable runs, one has to assure that there is adequate current to drive the cable capacitance. If the time varying current $i(t)$ supplied to the cable is $i(t) = (I)\sin(2\pi ft)$, then at frequencies such as are being discussed output voltage is:

$$v(t) = (1/C) \int i(t) dt = [(I / 2\pi f C) \cos(2\pi ft)]. \tag{1}$$

Here, C is the total cable capacitance cL . It can be seen that the magnitude of the measured voltage is inversely proportional to this total capacitance $C = cL$. Thus, measured signal voltage $v(t)$ decreases with increasing cable length. This same inverse relationship holds for frequency. Conversely, the voltage is directly proportional to the supply

or drive current. Depending on the upper frequency of measurement interest, for long cable runs as C increases the supply current must also be increased to preclude signal attenuation. Nomographs³ of this frequency vs. current relationship are readily available to enable this determination for any value of cable length (i.e., capacitance).

Cable capacitance in the output leads can also significantly affect the signal from the bridge transducers (metal strain gages and MEMS) of Figure 3 at frequencies greatly above 0 Hz. Signal attenuation can again occur. The effect of this capacitance $C = cL$ in parallel with the output voltage signal can be calculated as follows.

$$\text{attenuation ratio} = \frac{1}{\sqrt{1 + (2\pi f(2rL + R_{\text{bridge}})(cL))^2}} \quad (2)$$

If this attenuation ratio value is close to 1.0, no signal is lost. If, for example, this ratio calculates to a value of 0.9, the signal will be attenuated (i.e., be in error) by 10% at frequency f . The highest measurement frequency of interest should be used in this calculation.

The magnitude of the impedance of a capacitor is $1/(2\pi fC)$ and an inductor $2\pi fL$ (L here is inductance). At lower frequencies cable capacitance dominates as a concern but at higher frequencies (e.g., as encountered in high frequency mechanical shock or blast measurements) the total cable inductance $L = lL$ (2^{nd} L here is cable length) also comes into play. Figure 5 shows the measured frequency response of 400 feet of Belden⁴ non-paired #82418, 4-conductor cable, 22 AWG, fluorinated ethylene propylene insulation, Beldfoild[®] shielded, with a nominal inductance of 0.15 $\mu\text{H}/\text{foot}$ and a conductor-to-conductor capacitance of 30 pF/foot. Note the 5 different response curves measured for the same cable! Each response is associated with a different cable termination impedance. Also note that at frequencies to 50 KHz the termination impedance of the cable has no effect on its frequency response. With an infinite termination impedance (1 M Ω used here) we see resonant peaks occurring within the frequency response with the first being nominally 330 KHz. With a termination impedance of 100 Ω we notice that for this same cable the flat frequency response region is extended by a factor of 10 from 50 to 500 KHz. Obviously in this example at frequencies above 50 KHz, dependent on termination, the cable has the potential to greatly magnify or attenuate the signal it is transmitting. This effect must be understood.

Considering the infinite load case, the resonant frequency of the cable should closely approximate its natural frequency. The velocity of propagation of the signal down the cable, using the nominal values per foot of capacitance and inductance provided, is equal to²:

$$1/\sqrt{lc} = 0.47 \times 10^9 \text{ feet/second} \quad (3)$$

If the cable operates directly into a high impedance amplifier (typically $R \geq 1\text{M}\Omega$), at high frequencies reflections can occur. The first

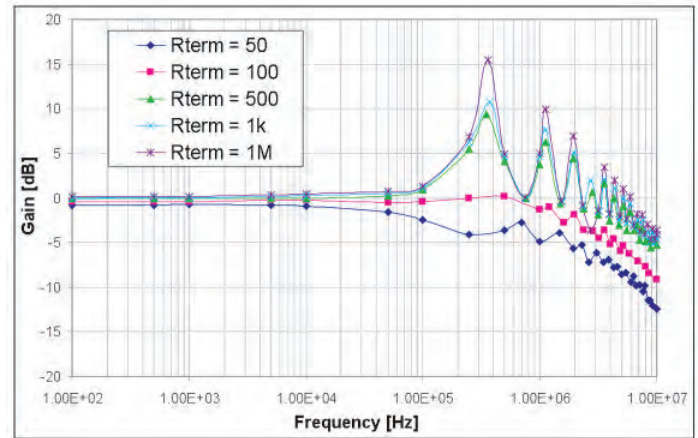


Figure 5: Frequency response of 400 feet of a specific cable

reflection will occur at a frequency (f) corresponding to a wavelength (λ) equal to four (4) times the cable length ($4L$).

As an example, assume in a test using the above specific Belden cable we observe a resonance of 100,000 (i.e., 1×10^5) Hz. The corresponding wavelength λ can be calculated as:

$$\lambda f = 4L = \text{propagation velocity or} \quad (4)$$

$$\lambda = 4L = (0.47 \times 10^9 \text{ ft./sec.}) / (1 \times 10^5 \text{ Hz}) = 4700 \text{ ft.}$$

Thus, a cable length of $(4700/4)$ or 1175 feet should be observed as the cause of the oscillations at 100,000 Hz. Signal fidelity can only be maintained to approximately 20,000 Hz ($100,000/5$) or one-fifth the frequency of this oscillation.

To test our understanding of this phenomenon redirect thinking back to the obtained, experimental frequency response of Figure 5 for 400 feet of the 4-conductor shielded Belden instrumentation cable #22 AWG. Note the resonant frequency at 330,000 Hz for the infinite load ($R = 1\text{M}\Omega$). If we calculate the fundamental wavelength for this cable, and use the above propagation velocity of 0.47×10^9 ft./sec., which is a nominal value for this cable, we get $\lambda = 4L = (0.47 \times 10^9 \text{ ft./sec.}) / (3.3 \times 10^5 \text{ Hz.}) = 1,424$ ft. or a cable length of $1,424/4 = 356$ feet, which agrees reasonably well with its known value of 400 feet.

How do we improve this frequency response? The characteristic impedance for a cable at very high frequencies is expressed as:

$$Z = \sqrt{l/c} \quad (5)$$

which for the preceding cable can be calculated to be 70.7 ohms. If the cable is terminated properly ($\sqrt{l/c} = 70.7$ ohms), there will be no reflections at high frequencies. Figure 5 shows for the test termination impedance of 100 ohms (close to 70.7 ohms) an improvement by almost a factor of 10 in frequency response flatness. Thus, when high frequencies and long cable runs are involved, the cable termination impedance matching can become very important.

SUMMARY OF CABLE FILTERING EFFECTS:

The above paragraphs have enabled us to evaluate:

1. Signal attenuation in static (0 Hz or dc) resistive bridge measurements due to cable resistance
2. Signal attenuation at high frequencies and long cable lengths in integral electronic ICP® piezoelectric transducers due to line capacitance
3. Signal attenuation at intermediate frequencies in resistive bridge (metal strain gage or MEMS) transducers due to signal line capacitance
4. Signal modification in very high frequency measurements over long lines such as high frequency mechanical shock or blast measurements due to both capacitive and inductive loading of the signal lines

The cable parameters that control this signal modification must be known and their effects evaluated to assure signal fidelity.

SIGNAL GENERATION WITHIN THE CABLE:

Signal generation within a cable (as opposed to cable pickup) occurs attributable to what is known as a triboelectric effect. This effect is important when dealing with bridge type sensors providing millivolt level signals or piezoelectric sensors (accelerometers, pressure transducers, force transducers) without contained electronics (non ICP®). For this effect to occur there must be cable motion. The triboelectric³ effect (also known as *triboelectric charging*) is a type of contact electrification in which certain materials become electrically charged after they come into contact with a different material and then become separated (such as through rubbing). The polarity and strength of the charges produced differ according to the material types, surface roughness, temperature, strain magnitude, and other parameters. Thus, this effect is not very predictable, and only broad generalizations can be made about it. One example of materials that can acquire a significant charge when rubbed together is glass rubbed with silk. Since all instrumentation cables are combinations of metal conductors, inner dielectrics, metal shields, and outer jackets of differing materials, it would be expected that any motion of the cable would result in some triboelectric effect (signal generation). This motion can be attributed to cable vibration or, in mechanical impact environments where cables are taped or securely tied down, cable compaction due to traveling stress waves underneath them. The greater the relative motion between the cable constituents, the more charge that is generated. Figure 6 shows one example of this charge generation within a coaxial cable.

Examining Figure 6, during cable vibration charge builds up due to relative motion between the shield and the dielectric due to rubbing. Subsequently the shield and dielectric separate, and the mobile charge on the shield flows into the next stage of signal conditioning resulting in additive noise superposed on the signal. One solution is to pack all the internal cable interfaces with graphite, which essentially functions as a conductive shunt when the cable materials separate, thus eliminating charge buildup.

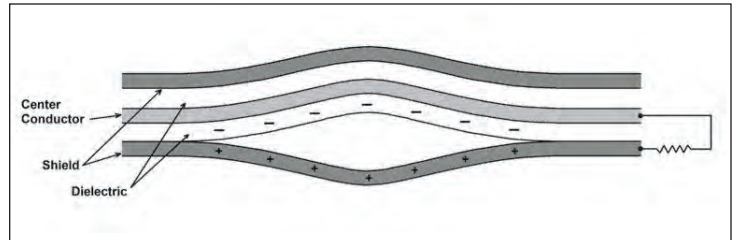


Figure 6: Charge buildup due to cable motion

Figure 7 below provides a chart of the Triboelectric Series. The farther apart materials are from one another on the table the more charge build up they generate if rubbed together.

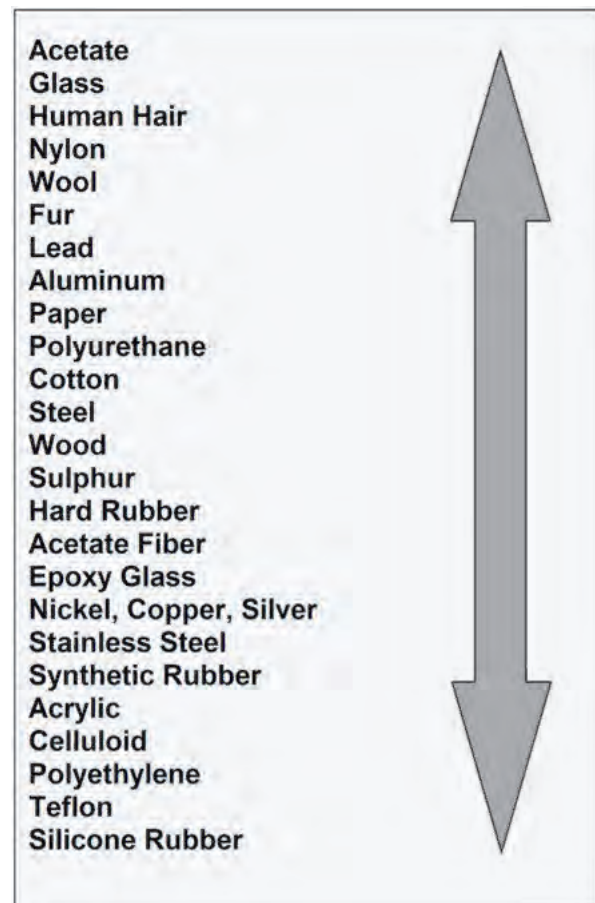


Figure 7: Triboelectric Series

The solutions to cable noise attributable to triboelectric effects are: (1) in vibratory environments minimize cable “whip”, (2) in severe mechanical impact environments avoid securing the cable to any structure in such a manner that stress waves couple into it (keep it as free as possible), and (3) use as much graphite as possible as a cable filler between cable constituents. Relating only to item (3), Figure 8 shows two cables affixed to a long, slender bar with aluminum tape. The cables were identically terminated in 350 and 1000 ohm resistors that were mechanically isolated from the bar. During the course of testing various types of tapes were used. Figure 8 shows only one of many test configurations in terms of cable routing. The bar has a 1 inch square cross section and a length/width ratio of 48:1 to assure essentially 1-dimensional wave motion. The bar was impacted numerous times on its end and cable responses were monitored.

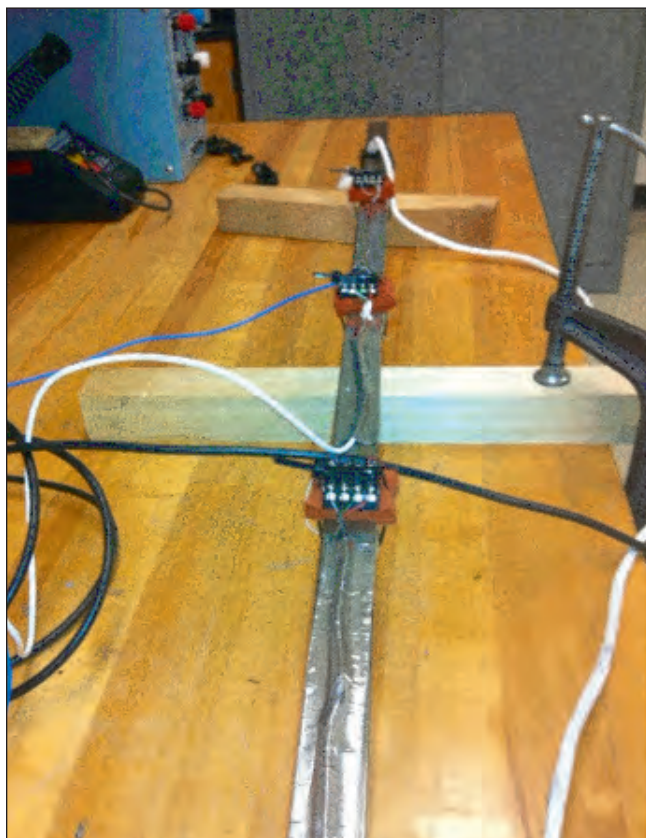


Figure 8: Longitudinal rod (Hopkinson Bar) used in cable testing

The center (white) cable is from Measurements Group (strain gage manufacturer) and the lower (black) is a special cable manufactured for the author by Calmont Wire and Cable⁵. As noted, the cables were terminated in resistive bridges that are totally strain isolated from any mechanical input. Figure 9 shows comparative test results (Calmont (purple trace) to Measurements Group (yellow trace)) when the bar is impacted on its end. Both are shielded and contain the same AWG wiring. Among other things the Calmont is packed full of graphite. The graphite has minimized signal generation.

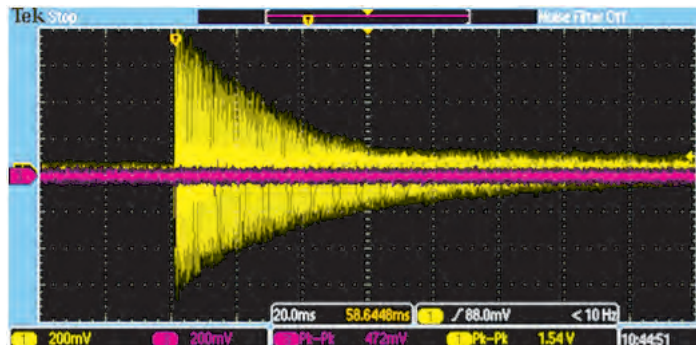


Figure 9: Relative cable triboelectric response tests

SUMMARY OF CABLE NOISE GENERATION EFFECTS:

While not predictable due to dependency on cable materials, construction, and motion, triboelectric charge generation in the cable can be a significant error contributor in measured signals. When dealing with non-ICP piezoelectric transducers, or transducers operating at millivolt signal levels, graphite cable treatment should be provided to minimize this effect. Other parameters such as cable flexibility should also be considered.

CONCLUSIONS:

Careful attention must be paid to cable selection when designing instrumentation systems. Cable operating temperature range, impedance, shield coverage, abrasion resistance, strength, weight, compliance, outgassing, and cost are among needed considerations. However, the potential for the cable to provide signal attenuation by inadvertent filtering or adding internal charge generated noise to the measured signal attributable to triboelectricity is often overlooked. Hopefully this article has provided insight into these little recognized error sources.

REFERENCES:

- (1) Walter, Patrick L., Air Blast and the Science of Dynamic Pressure Measurement, Sound and Vibration, pp.10-16, December 2004.
- (2) Magnusson, Philip C. et. al., Transmission Lines and Wave Propagation, CRC Press, ISBN 0-8493-0269-2, 2000.
- (3) Signal Conditioning Basics for ICP® & Charge Output Sensors, PCB Piezotronics Tech Support, www.pcb.com.
- (4) Belden Wire and Cable, Indianapolis, IN.
- (5) Calmont Wire and Cable, Santa Ana, CA.

Who is Patrick L Walter?



Patrick Walter graduated in 1965 with a BSME from The Pennsylvania State University and hired into a Component Test (shock, vibration, climatic, . . . and functional test) organization at Sandia National Laboratories in Albuquerque, NM. Concurrent with his employment, he completed his MSME in 1967 at the University of New Mexico. He subsequently became a Project Leader in a flight telemetry organization and was responsible for transducer calibration as well as both transducer and flight electronics development. Among other early accomplishments, he developed some of the first high shock sensing capabilities for large caliber guns and earth penetrators. In 1976, Sandia sponsored his doctoral studies at Arizona State University (ASU) with now Professor Emeritus Peter K. Stein, founder of ASU's Laboratory for Measurement System Engineering. Pat's PhD dissertation involved analyzing structural test data from the Trident I strategic missile system.

In 1978, Dr. Walter resumed full time employment at Sandia and was promoted into test management shortly thereafter. Among the many organizations/functions he supervised were Transducer Development and Calibration, Measurement Consulting, Telemetry Component Development, Telemetry System Packaging for Weapon System Stockpile Surveillance, Mass Properties, Test Facilities Development, and Precision Inertial Test System Development. In 1987 he was transferred as Supervisor Test Operations for the Kauai Test Facility, a rocket launch facility on the Pacific Missile Range Facility (PMRF), Kauai, HI. Subsequently he became responsible for developing and launching rocket systems from Sandia and NASA facilities. These rocket focused activities supported President Regan's Strategic Defense Initiative (SDI).

Post Cold War (1991-1995) Dr. Walter established a joint Sandia-Federal Aviation Administration (FAA) program as part of the FAA's congressionally mandated Aging Aircraft Program. He validated this program with the aircraft and engine OEMs, the Air Transport Association, and other organizations, and it remains contributory today on Albuquerque International Airport.

During his entire Sandia tenure (1965-1995), Dr. Walter's professional focus was on flight, field, and laboratory measurements (e.g., displacement, velocity, strain, accelerations from milli-gs to > 100,000 gs, acoustic level pressures to 10's of thousands of psi, temperature, flow, and much more) to support test and evaluation activities. His professional interests spanned the entire measurement chain: transducers, signal conditioning, acquisition systems, and end data analysis.

In 1995, Pat accepted a position in the Engineering Department at Texas Christian University (TCU). Professor Walter developed TCU's Experimental Mechanics and Structural Dynamics Laboratories and established an industry based Senior Design Program focused around test, calibration, and control activities. From 1996-2003, he consulted for Endevco Corporation, a major supplier of dynamic instrumentation. From 2003 through today he consults as Senior Measurement Specialist for PCB Piezotronics, the world's largest supplier of dynamic instrumentation. Occasionally, he also consults for various aerospace and defense contractors on test measurement applications. Through TCU's Engineering and Extended Education Departments, he has developed a Measurements Systems Engineering short course, which he teaches nationally and internationally.

Pat is a 30+ year member of both the Society of Experimental Mechanics and the International Automation Society as well as a member of the American Society of Engineering Educators. He has authored one book, numerous book chapters, and more than 100 journal articles and reports (see TCU Engineering website). During the late 1970s he chaired a working subgroup of the Telemetry Group of the National Test Ranges. In 1989, he received both a USDOE Albuquerque Office Quality Award and a joint Certificate of Appreciation Award from Sandia Labs and Allied Signal for his work on the Trident II program. In 1990 he received an Award of Excellence from the USDOE Nuclear Weapons Program, and in 1994 he received a Meritorious Achievement Award from Sandia Labs. In 1995 (upon his retirement from Sandia), he received a letter of commendation from Senator Pete Domenici, then head of the U.S. Senate Budget Committee. In 2002, Prof. Walter's TCU engineering seniors won the Design News national competition award (\$20,000). In 2006, Prof. Walter received a Commander's coin from Aberdeen Test Center (U. S. Army) and in 2008 he received Edwards AFB Instrumentation Special Recognition coin (#19). In 2008, he was awarded the Shock and Vibration Information Analysis Committee's (SAVIAC's) Lifetime Achievement Award. SAVIAC represents the Department of Defense, Department of Energy, and the Defense Treat Reduction Agency in this subject area. Most recently (2009) he was recognized as a Senior Life Member of ISA.



TECH NOTE #17

This TN highlights the advantages and disadvantages of charge versus ICP® circuits for the signal conditioning of piezoelectric accelerometers. Historically (early 1960s) all piezoelectric accelerometers were operated in a charge mode whether for shock or vibration. Today most piezoelectric accelerometers are used with contained ICP® circuits. This somewhat historic paper describes the trade-offs.



TN-17

Accelerometer Selection Considerations

Charge and ICP[®] Integrated Circuit Piezoelectric

Written By

Jim Lally, PCB Piezotronics, Inc.

ACCELEROMETER SELECTION CONSIDERATIONS

Charge and ICP® Integrated Circuit Piezoelectric

Jim Lally,
PCB Piezotronics, Inc. Depew, NY 14043

There is a broad selection of charge (PE) and Integrated Circuit Piezoelectric (ICP®) accelerometers available for a wide variety of shock and vibration measurement applications. Selection criteria should include accelerometer electrical and physical specifications, performance characteristics, and environmental and operational considerations. Comparing advantages and limitations of the two systems may be helpful in selecting an accelerometer and measurement system best suited for a specific laboratory, field, factory, underwater, shipboard or airborne application.

Introduction

This paper will review sensor selection considerations involving two general types of piezoelectric sensors. High impedance, charge output (PE) type and ICP® with a characteristic low impedance output. In addition to sensor electrical and physical characteristics, several factors play a role in the selection of an accelerometer for a specific application. These factors include environmental, operational, channel count and system compatibility.

PIEZO ELECTRIC (PE) TYPE ACCELEROMETERS

PE type accelerometers generate a high-impedance, electrostatic charge output in response to mechanical stress applied to its piezo ceramic, or crystal, sensing element. Because of its high charge sensitivity, piezo ceramics have found wide use in both charge and voltage mode accelerometers. Quartz, generally recognized as the most stable of all piezoelectric materials, is also commonly used in general purpose ICP® accelerometers, calibration transfer standards, and PE pressure and force sensors. Charge output systems have been available for about 40 years. PE accelerometers operate through low-noise cable into a high input impedance charge amplifier, which converts the charge signal into a usable low-impedance voltage signal for acquisition purposes. The charge amplifier provides for signal impedance conversion, normalization, and gain/range adjust. Options may include filtering, integration for velocity and/or displacement, and adjustment of the input time constant, which determines low frequency response. Modern charge amplifiers are designed with more effective low-noise circuits and may incorporate simplified LCD displays and digital controls. Some "dual-mode" models operate with both PE and ICP® accelerometers. The main advantage of the laboratory charge system is flexibility of adjusting and controlling the electrostatic charge output of the PE accelerometer. Miniature, solid-state charge amplifiers, generally with fixed characteristics, have been used historically for airborne applications. PE accelerometers can also operate to higher temperature than ICP® accelerometers with built-in electronics.

The main limitations of the PE charge system involve system complexity, difficulty operating, maintaining high impedance circuits in dirty adverse environments, and noise increase when

operating through long input cables. High impedance circuits are generally more susceptible to electrical interference.

INTEGRATED CIRCUIT PIEZOELECTRIC (ICP®) ACCELEROMETERS

ICP® accelerometers incorporate a built-in microelectronic charge or voltage amplifier, which functions to convert high impedance electrostatic charge from the PE sensing element into a low impedance voltage signal. In hermetic welded designs, all high impedance circuitry is sealed and electrically shielded inside the accelerometer. ICP® accelerometers were first manufactured in the mid 1960's.

ICP® accelerometers operate from a low-cost, constant-current power source over a two-wire circuit with signal/power carried over one wire and the other wire serving as ground. The cable can be ordinary coaxial or ribbon wire. Low-noise cable is not required. Constant current to operate the accelerometer comes from a separate power unit or it may be incorporated inside a readout instrument such as an FFT analyzer or Data Collector. Integrated electronic accelerometers are available under several different trademark names such as ICP® (PCB Piezotronics), Isotron® (Endevco), Delta-Tron® (B&K), and Piezotron® (Kistler) to mention a few. Although built-in electronics is a "common thread," all integrated electronic accelerometers are not necessarily interchangeable or "compatible" with each other. Some contain MOSFET circuits, others JFETS. Some use hybrid, microelectronic, charge amplifiers, others voltage followers. Although most integrated electronic accelerometers operate from 2 to 4 mA constant current, some operate from as little as 0.5 mA for low power consumption and others operate up to 20 mA for driving

long cables at high frequencies. It is recommended that ICP® sensor and power specifications be checked before assuming compatibility.

The main advantage of low-impedance operation is the capability of ICP® accelerometers to operate continuously in adverse environments, through long, ordinary, coaxial cables, without increase in noise or loss of resolution. Cost per channel is less, since low-noise cable and charge amplifiers are not required. The

main limitation involves operation at elevated temperatures, above 325 °F. ICP® accelerometers, structured with quartz sensing elements and special electronics, operate well at cryogenic temperatures. Table I is a comprehensive list of advantages and limitations of PE and ICP® accelerometers. This list was reviewed and inputs provided by outside consultants with years of experience in shock and vibration technology. The list should be considered "dynamic", subject to additional inputs relative to advantages and limitations.

TABLE I
CONSIDERATIONS FOR SELECTING PE & ICP® ACCELEROMETERS

PE SENSOR
Advantages

- Flexibility in adjusting accelerometers electrical output characteristics properly
- Wide dynamic range
- Higher temperature operation >500 °F
- Interchangeability in existing charge systems
- Extended low frequency response

Limitations

- Requires training and expertise to understand and operate high impedance circuits
- Capacitive effects from accelerometer and cable increases noise and reduces resolution
- High impedance circuitry must be kept clean and dry. (Sensor, low-noise cable and charge amplifier)
- Requires special purpose low-noise cable to minimize triboelectric noise
- High impedance systems are more susceptible to electrical and RF interference
- PE accelerometer size and sensitivity are directly related - A sensitivity/size/mass loading consideration
- Higher cost per-channel than ICP® type (due to required low-noise cable and charge amplifier)

ICP® SENSOR
Advantages

- Simplified operation-less operator attention, training and expertise
- Uses standard coaxial cable or ribbon wire
- Drives long cables without noise increase or loss of resolution
- Operates from low-cost, constant-current power source
- Connects directly to many readout instruments
- High output miniature designs reduce mass loading
- Low impedance systems have greater resistance to contamination and electrical interference
- Better system reliability
- Dynamic range typically >100,000 to 1 (>100 dB)
- Range and resolution are data sheet specifications
- Bias monitor detects cable faults - shorts or open circuits
- Can incorporate self-identification "TEDS" circuit and steep filtering
- Operates through slip rings
- Lower cost per-channel than PE type

Limitations

- Electrical characteristics, sensitivity, range, and discharge time constant are fixed within the sensor
- Limited temperature range (-320 °F to + 325 °F)
- May not be interchangeable in system if power requirement is not the same

Each of these considerations will now be reviewed in more detail for both PE and ICP® accelerometers.

ADVANTAGES OF PE ACCELEROMETERS

Flexibility- A laboratory "bench type" charge amplifier usually has controls for adjusting and modifying output signal from the PE accelerometer. At a minimum, there are controls for normalizing sensitivity, setting gain and full-scale range, and grounding. The charge amplifier may also have capability for filtering, integration, and adjustment of discharge time constant, which determines low-frequency response. Dual-mode charge amplifiers also provide constant current, which allows operation with both ICP®, and charge output PE sensors.

Dynamic Range- Typically, a high-sensitivity PE accelerometer may operate over a wide dynamic range (>100 dB.) When used with a laboratory charge amplifier, full-scale output can be set for any g level within maximum range. Dynamic range can be defined as the operating range from resolution to the maximum range that the sensor will remain in specification. However, neither dynamic range nor resolution is specified for most ceramic crystal structured PE accelerometers. Maximum range is sometimes determined by the maximum acceptable non-linearity associated with operating at a higher range. Non-linearity is often expressed as a percentage of "X" number of g's, e.g. 1% per 500 g's. Resolution is based on system noise, which is determined by amplifier gain and capacitive loading from the input cable and accelerometer on the charge amplifier input.

High Temperature Operation- Since the PE accelerometer does not contain built-in electronics, the operating temperature is limited only by the sensing element and materials used in the construction. PE accelerometers commonly operate to 500 °F. Special models are available to > 1000 °F. For best accuracy, the accelerometer should be calibrated at operating temperature.

Interchangeability- Virtually any PE accelerometer is interchangeable in a charge output system, with the exception of some models which may have very low insulation resistance at high temperatures. Special charge amplifiers are available for operation with low-resistance inputs.

Extended Low Frequency Response- Quartz force sensors are commonly used in force controlled shaker applications. When coupled into high input impedance electrostatic charge amplifiers (> 1012 ohm), quartz force sensors have discharge time constants in the order of hundreds, or thousands of seconds, imparting excellent low-frequency response and capability for static calibration.

LIMITATIONS OF PE ACCELEROMETERS

Expertise- Training and expertise are required to understand, operate and maintain charge output systems. Basic understandings of high-impedance circuitry, low-noise cables, sensor pC/g sensitivity, capacitive loading effects, system noise, setting charge amplifier controls, and keeping the system clean and moisture-free are required. Some newer charge amplifiers have digital controls, which simplify entering sensitivity and setting range.

Resolution- Although resolution for PE accelerometers may be considered infinite, resolution is not generally specified on a data sheet, since it is determined by system noise. Until capacitance values for the sensor and input cable length are determined and the amplifier gain set, resolution is not known. This can present uncertainties for low-level measurements involving long cables. Although increased cable length does not affect sensitivity, it does affect system noise and resolution. Lack of capability to drive long cables is one of the main limitations of the PE accelerometer charge output system. New, more modern charge amplifiers, with low-noise circuits, minimize this problem. "Triboelectric" noise generated as a result of input cable motion, can also degrade resolution.

Operating Environment- High-impedance PE accelerometers and charge amplifiers are best suited for operation in clean laboratory conditions. They do not operate well in adverse factory, shipboard or underwater environments. All high-impedance components, including the accelerometer, low-noise cable and charge amplifier must be kept clean and dry. Contamination of the high impedance circuit causes low resistance, loss of low frequency response, and baseline drift.

Cable and Connectors- PE accelerometers require the use of high insulation resistance, low-noise, coaxial cable. Low-noise cable has a graphite lubricant embedded in the dielectric layer to minimize friction and generation of "triboelectric" static electricity. The electrostatic charge generated by cable motion is the same as the charge generated from the piezo element. The charge amplifier cannot differentiate between the two. Cable connectors are commonly Microdot® 10-32 coaxial. Cable and connector selection are limited.

Size vs Sensitivity- Size, sensitivity, and frequency response of PE accelerometers are all directly interrelated. The larger the accelerometer, the higher the sensitivity, but lower the frequency response, and vice-versa. When a measurement application requires a miniature accelerometer for low-mass loading considerations, compromise may have to be made in selecting a larger accelerometer that provides adequate sensitivity.

Cost- PE accelerometer cost is essentially the same as an equivalent ICP® design. However, since the PE accelerometer requires the use of low-noise cable and charge amplifiers, cost per-channel is higher than an ICP® voltage output channel. Cables and amplifiers are major cost considerations in multi-channel measurement systems.

ADVANTAGES OF ICP® ACCELEROMETERS

Simplified Operation- ICP® accelerometer systems offer simplified operation requiring less operator expertise, training and attention. They provide a fixed, mV/g, low-impedance output signal that is virtually unaffected by cable type, length, and environmental operating conditions.

Resolution- The resolution of ICP® accelerometers is virtually unaffected by cable type or length. Resolution is a standard data sheet specification. Long cables can be used without increase in noise, loss of resolution, or signal attenuation. Input cables hundreds of feet long can act as an LP filter on ultra high-frequency data. However, this is usually only of concern with ICP® pressure sensors used for microsecond shock and blast wave pressure measurements.

Operating Environment- Hermetically sealed ICP® accelerometers operate well in adverse environments. They are resistant to contamination, since all the high impedance circuitry is safely sealed inside the accelerometer. Welded hermetic designs are generally more contamination resistant than epoxy sealed designs. Compatibility with adverse environments makes ICP® accelerometers the preferred choice for industrial machine health monitoring, underwater, shipboard, vehicular and field test applications.

Cable and Connectors- The low-impedance output of ICP® accelerometers allows complete flexibility in cable type and connectors. Cable and connector considerations can be important in certain applications involving high or low temperature, pressure, vacuum, corrosive fluids and where mass loading is a concern. Miniature ICP® accelerometer designs often incorporate solder terminal connections, allowing the use of lightweight flexible cable to minimize strain and mass loading effects. Industrial accelerometers use large, rugged connectors and/or vulcanized connections to achieve reliability in adverse environments. The use of standard cable and connectors in large channel-count systems promotes effective cable management and is a significant factor in cost reduction.

Size and Sensitivity- By incorporating gain in miniature ICP® accelerometers, it is possible to solve applications requiring accelerometers with low mass, high sensitivity, and high frequency response. Internal gain also improves the resolution of ceramic structured ICP® accelerometers incorporating hybrid charge

amplifiers. Some ICP® accelerometers incorporate voltage gain circuits, and although signal level is boosted for recording and/or cable driving purposes, so is the noise level.

Dynamic Range- ICP® accelerometers have a very wide dynamic range. "Limited or Fixed Dynamic Range" is sometimes cited as a "limitation" of ICP® accelerometers. Most ICP® accelerometers have greater than 100,000 to 1 (>100 dB) dynamic range. Some seismic models incorporating special low-noise circuits have >500,000 to 1 range. Both dynamic range and resolution of an ICP® sensor are known data sheet specifications. Even more significant, the ICP® system does not lose dynamic range, due to added cable length and system configuration.

Powering ICP® Accelerometers- Depending on the specific model, ICP® accelerometers may operate from 0.5 mA to 20 mA constant current at anywhere from 3 to 30 VDC. For extended dynamic range, some special models have been supplied to operate from as high as 35 VDC. As cautioned earlier, all ICP® accelerometers do not contain the same internal electrical circuit and consequently, they are not necessarily compatible with all constant current power sources. Sensor bias and supply voltage both affect dynamic range. Supply current affects cable driving capability, especially when driving high-voltage signals at high frequencies. Constant current power units are available today with battery or line power, with or without gain, and manual or computer controlled operation. ICP® sensor line power units generally supply 2 to 4 mA current. However, they are usually adjustable to 20 mA, which may be required when driving long cables at high frequencies. Many commercial readout instruments, such as FFT analyzers and Vibration Data Collectors, incorporate constant current power input for direct connection to ICP® accelerometers. Dual-mode charge amplifiers incorporate constant-current power to provide for operation with both PE and ICP® accelerometers.

Cable Fault Monitor- In ICP® two-wire sensor circuits, signal/power is carried over one wire and signal return (ground) over the other. By monitoring the characteristic DC "bias" voltage that exists on the signal/power wire, it is possible to detect cable open or short circuits. ICP® sensor power units commonly incorporate red, green, yellow color-coded meters, or LED's, to indicate normal operation or cable faults.

Operation Through Slip Rings- Certain vibration measurement applications on rotating machinery require operation through slip rings. The characteristic low-impedance output voltage from ICP® accelerometers is compatible with operation through slip rings.

"TEDS" Transducer Electronic Data Sheet- Incorporation of a "TEDS" memory circuit in ICP® accelerometers allows storing self identification information such as manufacturer's name, sensor type, model, serial number, sensitivity, calibration date, channel ID, sensor location, and other information. TEDS accelerometers

operate in a "mixed" analog or digital mode. A TEDS signal conditioner is used to access digital memory over the same wires normally used for analog measurements. Once the memory data has been accessed, the digital memory circuit can be switched out and the accelerometer can be used for normal analog operation.

Cost- Although most ICP® and PE accelerometers essentially cost the same, the per-channel cost of the ICP® system is substantially lower since special low-noise cables and charge amplifiers are not required. Savings can be substantial when comparing costs of multi-channel systems. From an operational perspective, less care, attention, and effort is required to operate and maintain low impedance systems.

LIMITATIONS OF ICP® ACCELEROMETERS

Fixed Output- Electrical characteristics, such as sensitivity, range, resolution and discharge time constant, are fixed within the ICP® accelerometer. Fixed discharge time constant is less of a limitation with accelerometers than with quartz pressure and force sensors, which can be operated in the long time constant mode for quasi-static calibration purposes.

Temperature Range- Most general purpose ICP® accelerometers have limited temperature range from about -65 °F to +250 °F. Special cryogenic models operate down to -320 °F and high temperature designs to +325 °F.

BIBLIOGRAPHY

- "General Guide to ICP® Instrumentation," PCB Technical Bulletin G-0001 Lally, R.W., "Application of Integrated-Circuits to Piezoelectric Transducers," ISA Conference & Exhibit 1967, Preprint Number P4-2-PHYMMID-67
- Goldman, Steve, "Vibration Spectrum Analysis," 2nd Ed, Industrial Press, 1999
- Lally, J.F., "Accelerometer Cable, Wiring, and Connections," PCB Recommended Practices, RP-59
- Wilson, Jon, "Dynamic & Environment Effects on Performance," SENSORS, Mar. 1999

SUMMARY

Charge amplifier systems benefit from the very wide dynamic range of PE accelerometers by offering flexibility in adjusting the electrical output characteristics such as sensitivity and range. They are well-suited for operation at high temperatures. Modern charge systems feature improved low-noise operation, simplified digital controls, and dual output operation for operation with charge or ICP® voltage mode sensors. High-impedance circuitry is not well suited for operation in adverse field or factory environments. PE accelerometer resolution may not be specified or known since noise is a system consideration determined by cable length and amplifier gain. ICP® accelerometers operate from a constant current power source, provide a high-voltage, low-impedance, fixed mV/g output. They operate through long, ordinary, coaxial cable in adverse environments without degradation of signal quality. They have limited high temperature range. ICP® sensors are simple to operate. Both resolution and operating range are defined specifications. Cost per-channel is lower compared to PE systems, since low-noise cable and charge amplifiers are not required.

Power Ground Surge

CyberPower
CPS-1220RMS

PCB PIEZOTRONICS MODEL 483C SERIES SENSOR SIGNAL CONDITIONER
1 2 3 4 5 6 7 8
00-20-4A-91-A6-5F SN 126
• OPEN
• SHORT
• OVERLOAD

PCB PIEZOTRONICS MODEL 483C SERIES SENSOR SIGNAL CONDITIONER
9 10 11 12 13 14 15 16
00-20-4A-91-4A-27 SN 127
• OPEN
• SHORT
• OVERLOAD

PCB PIEZOTRONICS MODEL 483C SERIES SENSOR SIGNAL CONDITIONER
17 18 19 20 21 22 23 24
00-20-4A-91-4A-23 SN 128
• OPEN
• SHORT
• OVERLOAD

PCB PIEZOTRONICS MODEL 483C SERIES SENSOR SIGNAL CONDITIONER
25 26 27 28 29 30 31 32
00-20-4A-91-A6-64 SN 129
• OPEN
• SHORT
• OVERLOAD

PCB PIEZOTRONICS MODEL 483C SERIES SENSOR SIGNAL CONDITIONER
33 34 35 36 37 38 39 40
00-20-4A-91-A6-65 SN 130
• OPEN
• SHORT
• OVERLOAD

PCB PIEZOTRONICS MODEL 483C SERIES SENSOR SIGNAL CONDITIONER
41 42 43 44 45 46 47 48
00-20-4A-91-4A-2D SN 131
• OPEN
• SHORT
• OVERLOAD

PCB PIEZOTRONICS MODEL 483C SERIES SENSOR SIGNAL CONDITIONER
49 50 51 52 53 54 55 56
00-20-4A-91-4A-26 SN 132
• OPEN
• SHORT
• OVERLOAD

TECH NOTE #29

This TN discusses the data filtering, which must be present in any instrumentation system measuring mechanical shock. The analog filter constrains the bandwidth of the signal from the accelerometer so that an appropriate data sampling rate can be established. This paper also describes the influence that analog filtering can have on the resultant signal and provides criteria for filter selection. In addition, digital filters are briefly discussed. While today many data acquisition systems are designed around Sigma Delta filters, the amplitude and phase characteristic of these filters must similarly be understood.



TN-29

Guidance for the Filtering of Dynamic Force, Pressure, Acceleration (and Other) Signals

Written By

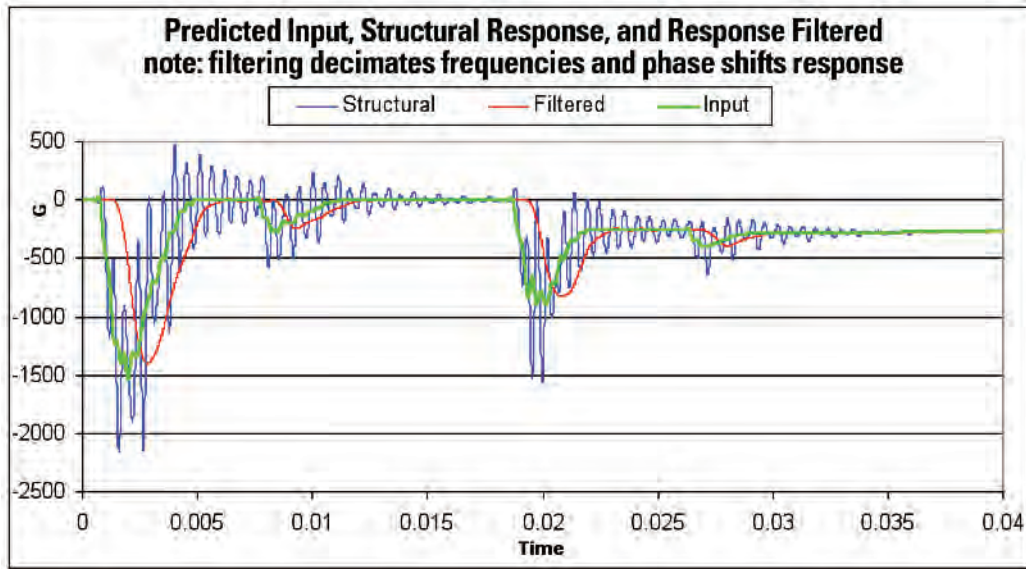
Patrick L. Walter, Ph. D.

Guidance for the Filtering of Dynamic Force, Pressure, Acceleration (and Other) Signals

Patrick L. Walter, Ph. D.

Senior Measurement Specialist, PCB Piezotronics, Inc.
Depew, NY 14043

Professor of Engineering, Texas Christian University
Fort Worth, TX 76129



Filters are frequency selective devices described by their types (low-pass, high-pass, band-pass, and band-reject), their characterization (e.g., names such as Bessel, Butterworth, Chebyshev), and their complexity (the filter order, which controls their rate of signal attenuation with frequency). When using force, pressure, or acceleration transducers to measure the loading to or response of structural systems, linear, low-pass filters are typically employed to condition their signals. These filters can perform any or all of the following functions: (1) eliminate the transducer's own, internal, high-frequency structural resonances while preserving its undistorted, low-frequency signal region of interest; (2) eliminate the possibility of aliasing where, due to inadequate sampling rate, high frequency data "folds over" and

corrupts this just mentioned low-frequency signal region; and (3) more effectively utilize the measurement system's data bandwidth and storage capacity. A brief introduction to analog filters and their associated terminology is first provided, and then this work focuses on the selection of appropriate analog, low-pass filters for any given user application. Aside from preserving the transducer's signal frequency content, guidance will be also provided towards preserving its wave shape. The principal contribution of this work to the literature will be a table that enables filters to simply and quickly be selected to support structural measurements. A limited discussion of digital filtering for data post-processing will culminate this effort.

Introduction:

If analysis of measured data is only required in the time domain, the signal simply has to be sampled fast enough to visualize the highest frequency of interest. Sampling a signal at 10 times this highest frequency will define the peak value of that frequency within 5%. This error criterion results from that fact that sampling 10 times per cycle for any frequency will miss its peak by no more than 18 degrees. The cosine of 18 degrees is 0.951.

When making dynamic measurements with force, pressure, or acceleration transducers, it is common to incorporate low-pass filters at some location in front of the digitizer in the measurement system. This filtering is implemented to: (1) eliminate the transducer's own, internal, high-frequency structural resonances while preserving its undistorted, low-frequency signal region of interest; (2) eliminate the possibility of aliasing [6] where, due to inadequate sampling rate, high frequency data "folds over" and corrupts this just mentioned low-frequency signal region; and (3) more effectively utilize the measurement system's data bandwidth and storage capacity. This last consideration is particularly important in environments such as transportation where 100s or 1000s of transducer-based data channels might be recorded during a specific test. All of these channels have to be recorded on, identified on, and accurately retrieved from data storage media.

A specific filtering technique, Sigma-Delta [15] filtering, while useful in some applications is only mentioned here in passing. This technique involves extreme oversampling, subsequent digital filtering, and then data decimation. For very large channel counts an already grievous data storage and retrieval issue can be aggravated. More important, the effective filtering is a combination of the manufacturer's front end analog filter (often first-order, low-pass) and the subsequent digital filter. This combination is not unique. We will then consider the more classical filters as will be discussed in subsequent paragraphs.

The amplitude response of an ideal, low-pass filter [1] would uniformly pass all frequencies to some upper limit and then completely eliminate frequencies above that limit. The phase response of this ideal, low-pass filter would be perfectly linear to this same upper frequency bound. Such a filter would maintain signal frequency fidelity to this upper limit while introducing only a time delay in the output signal. Wave shape of the signal over this frequency range would be preserved. The resultant time delay could be calculated from the slope of the phase (radians) versus frequency (radians/second) response. This slope is often referred to as the Group Delay or Time Delay [10] of the filter. A linear phase response results in a constant Group Delay.

Ideal filters do not exist. Figures 1a and 1b are the amplitude and phase responses for both a 6-pole Chebyshev filter and a 6-pole

Bessel filter with the same -3dB frequency. The Chebyshev best approximates the amplitude response of the ideal filter while the Bessel best approximates the ideal phase response. Thus, data filtering always involves some compromise.

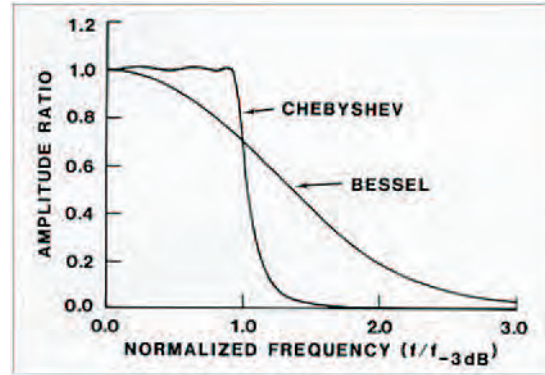


FIGURE 1A. COMPARATIVE AMPLITUDE RESPONSE

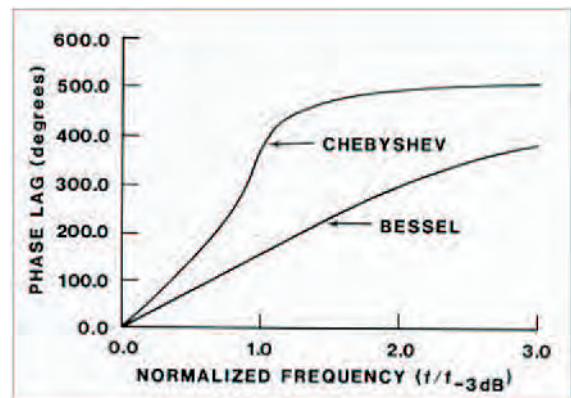


FIGURE 1B. COMPARATIVE PHASE RESPONSE

FIGURE 1. RESPONSE OF TWO DIFFERENT 6-POLE FILTER TYPES

The terminology that describes filters is often confusing. Figure 2 is a simple RLC circuit. The output measured across the capacitor is in fact a low-pass filter.

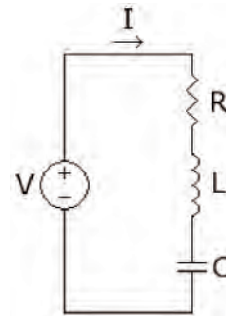


FIGURE 2. RLC CIRCUIT

The transfer function across this capacitor is [2]:

$$H(s) = (V_o/V_{in}) = 1/(LCs^2 + RCs + 1) \quad (1)$$

The degree of the denominator of $H(s)$ in this equation is $n = 2$; therefore, this is a second order filter. Solving for the roots of the denominator provides values for the poles of the filter. Each pole will provide a slope of -1 on a log amplitude versus log frequency plot, which is equivalent to -6 dB/octave or -20 dB/decade response attenuation [4]. The above $H(s)$, being 2nd order, would then produce an ultimate slope of -2 on a log amplitude versus log frequency plot, equivalent to -12 dB/octave or -40 dB/decade attenuation.

If $H(s)$ is realizable, we are able to substitute $s = j\omega$ [3] resulting in a complex function of frequency $H(j\omega)$. We typically plot this frequency response function in the form of Bode plots, i.e., amplitude and phase versus frequency plots. Figure 3 below illustrates the output across the capacitor (C) of Figure 2, verifying it to be a low-pass filter. The exact shape of the amplitude (top) and phase (lower) responses depends on the damping parameter ζ and the natural frequency ω_n . While not the focus of this work, the output across the resistor (R) in Fig. 2 would be band-pass in form and the output across the inductor (L) would be high-pass.

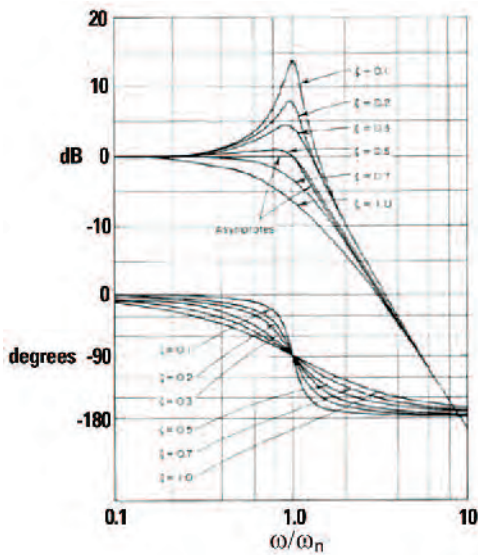


FIGURE 3. BODE PLOTS ACROSS CAPACITOR IN FIGURE 2

The bandwidth of a filter is typically specified in terms of its -3 dB frequency. For a simple, 1-pole, low-pass (RC) filter, this -3 dB frequency, in radians/second, is $1/(RC)$. That is, at the -3 dB frequency only 0.707 of the input signal is passed. For all filter configurations other than RC, the -3 dB frequency has little physical significance. However, by convention we specify filter bandwidth in terms of this -3 dB frequency.

Low and high-pass filters are primarily implemented with operational amplifiers. A generic, second order, active filter configuration [5] is shown in Fig. 4. For example, a low-pass filter can be configured by making G_2/G_4 capacitors and G_1/G_3 resistors. A 4-pole filter would require two such stages in series, a 6-pole three stages, etc. The values of G_1 , G_2 , G_3 , and G_4 for each stage would depend on the character of the specific filter desired. Each stage provides 180 degrees of phase shift; e.g. a 3-stage or 6-pole filter would have an associated 3×180 or 540 degrees of total phase shift.

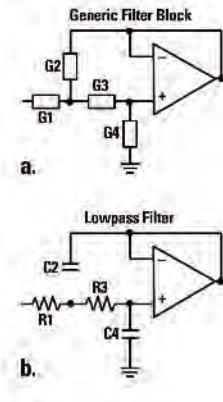


FIGURE 4. 2-POLE GENERIC LOW-PASS ACTIVE FILTER

Filter Characterizations:

There are four classic analog filter characterizations: Butterworth, Chebyshev, Elliptic and Bessel. The Elliptic will be mentioned but for reasons presented below the other three (3) will be characterized in great detail.

Butterworth [11]: The first and probably best-known filter approximation is the Butterworth or maximally-flat amplitude response. It exhibits a nearly flat pass band with no ripple. Its roll-off is smooth and monotonic. It has a reasonably linear phase response.

Chebyshev [12]: The Chebyshev response follows a mathematical strategy for achieving a faster roll-off by allowing ripple in the amplitude response. As the ripple increases (bad), the roll-off becomes sharper (good). The Chebyshev response is an optimal trade-off between these two parameters. Chebyshev filters, where the ripple is only allowed in the pass band, are called type 1 filters. Chebyshev filters that have ripple only in the stop band are called type 2 filters, but they are seldom used. Chebyshev filters have a relatively nonlinear phase response.

Bessel [13]: The Bessel filter has nearly perfect phase linearity in the pass band. However, its amplitude roll-off is slower than either the Butterworth or Chebyshev filter for an equivalent order (number of poles).

Elliptic [14] often called Cauer: The cut-off slope of an elliptic filter is steeper than that of a Butterworth, Chebyshev, or Bessel, but the amplitude response has ripple in both the pass band and the stop band. In addition, its phase response is highly nonlinear. If the primary concern is to pass frequencies falling below a certain frequency limit and reject frequencies above that limit, regardless of phase shifts or ringing, the elliptic response will optimally perform that function. However, we will ignore this filter because its highly nonlinear phase greatly distorts complex time signals.

Selection Criteria:

The establishment of low-pass filter selection criteria has to consider two requirements. One requirement dictates that at a preselected upper frequency limit the filter must attenuate the signal by some specified amount. The second requirement dictates that over some range of frequencies below this limit the filter must maintain both flat amplitude and linear phase response to preserve signal wave shape.

Specific requirements must be generated in order to establish these criteria. To initiate this discussion, these requirements will be specified as: (1) 95 percent (26dB) signal attenuation by some selected upper frequency limit and (2) both flat amplitude within 5 percent and linear phase within 5 degrees over some specified range of lower frequencies. Although the final outcome of this study will allow us to apply flexibility to these criteria, their justification as a starting point will subsequently be provided.

Right (Fig. 5) are three color coded plots for four configurations of 4-pole, low-pass filters. All of these filters are normalized to provide 95% amplitude attenuation (see top plot) at a frequency value of 1.0. The three groupings of plots respectively are amplitude versus frequency, phase (0 to 360 degrees) versus frequency, and time or group delay versus frequency. Within a specific grouping, from top to bottom, is a 0.5 dB type 1 Chebyshev (green), 0.1 dB type 1 Chebyshev (dashed magenta), Butterworth (red), and Bessel (dotted blue) characterization. For all plots in this figure both the vertical axes (ordinates) and horizontal axes (abscissas) are shown on a linear scale.

Looking at the plots of Fig. 5, several facts are apparent. First, for the 4-pole filters, Fig. 5 (top) shows that the amplitude response of the Chebyshev filters are much more frequency selective than the others. As predicted, the Butterworth is intermediate in selectivity and the Bessel is the least selective. Figure 5 (center) does not clearly delineate phase linearity or lack thereof. However, the more constant group delay in the bottom plot of Fig. 5 for the Bessel filter shows it to have the most linear phase, the Butterworth intermediate, and the Chebyshev filters to have the most nonlinear phase characteristics.

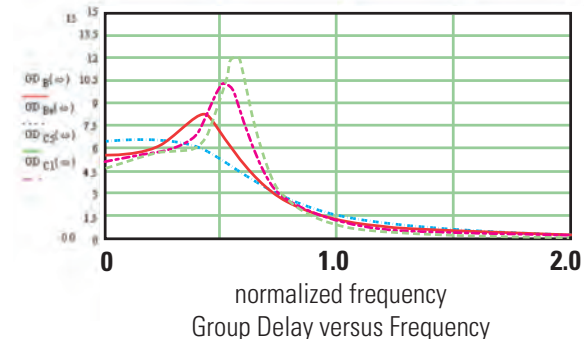
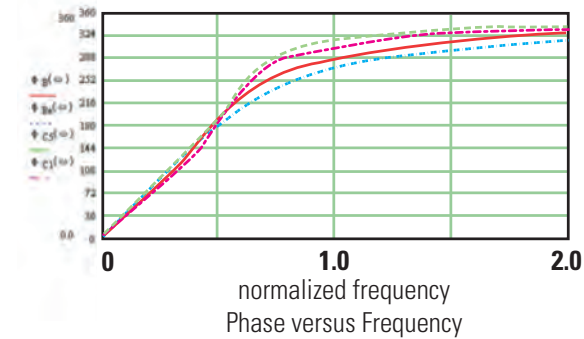
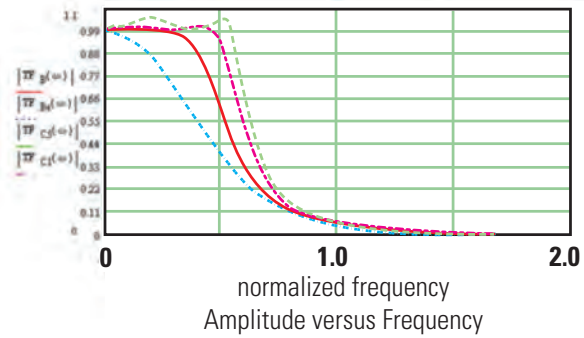


FIGURE 5. AMPLITUDE, PHASE, AND GROUP DELAY FOR VARIOUS 4-POLE, LOW-PASS FILTER CONFIGURATIONS

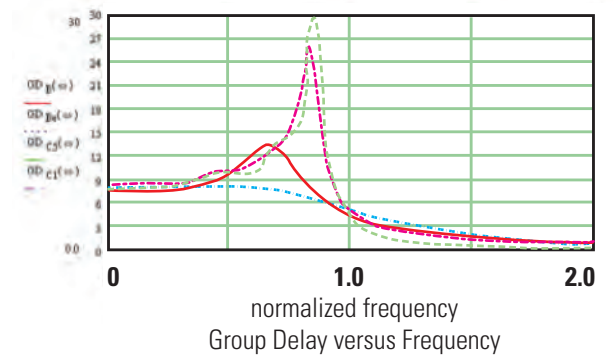
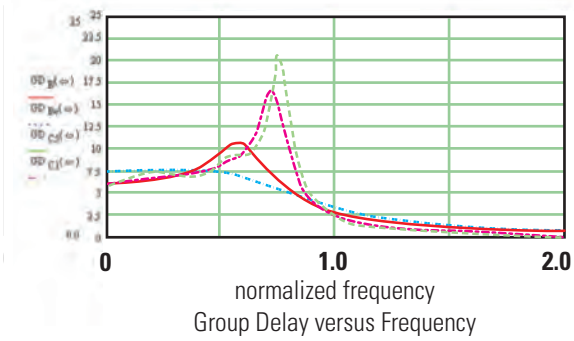
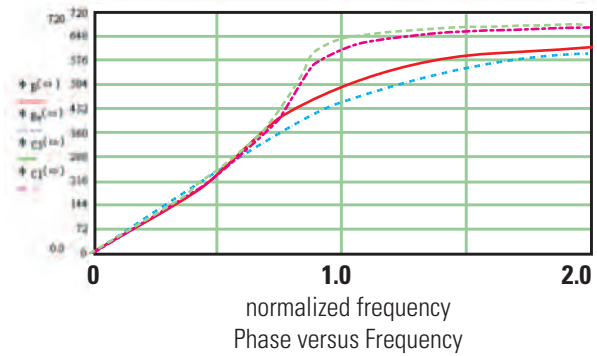
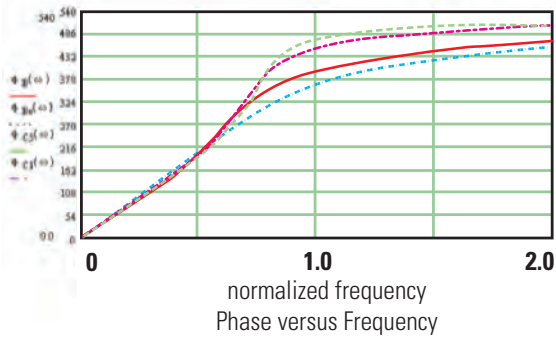
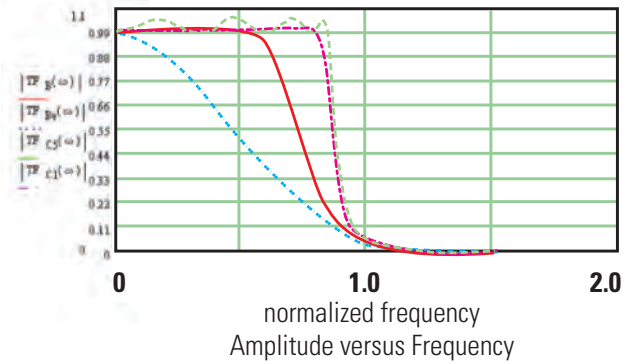
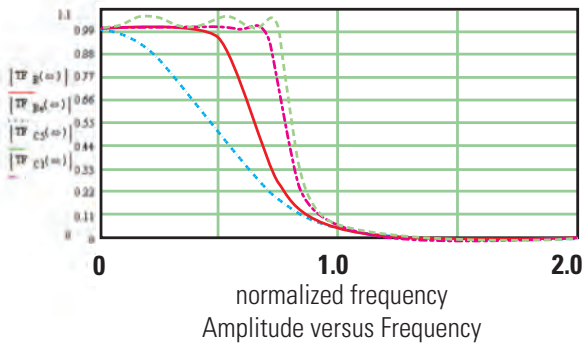


FIGURE 6. AMPLITUDE, PHASE, AND GROUP DELAY FOR VARIOUS 6-POLE, LOW-PASS FILTER CONFIGURATIONS

FIGURE 7. AMPLITUDE, PHASE, AND GROUP DELAY FOR VARIOUS 8-POLE, LOW-PASS FILTER CONFIGURATIONS

Figures 6 and 7 repeat this same sequence of plots for 6-pole and 8-poles versions of these same filters. The same trends as in Fig. 5 are observed to occur.

Having presented these global observations, what is required is to provide the test engineer or technician with a quick and simple tool to select an appropriate filter for his/her application. The tables in the appendix parameterize these plots to facilitate this selection process. The tables will next be explained along with application examples and a methodology to implement them and even increase their flexibility.

Tables Explanation and Implementation

Among other things, the successful design of an instrumentation system has to include: (1) the sampling rate of the existing digitizer or that rate which will ultimately be required, (2) the data bandwidth required or that which will result as a byproduct of filter selection, and (3) the existing available filter characteristic and order or that which will ultimately be required for compatibility with the data sampling rate. Considering only item (3), specific filters characteristics tabulated in the appendix include Chebyshev type 1 with 0.5 dB ripple in its pass band, Butterworth, and Bessel. For completeness, data are tabulated for 2, 4, 6, and 8 poles. However, pragmatically only 4, 6, and 8 poles attenuate or roll-off fast enough to be considered as practical anti-aliasing filters.

To enter the tables we either have to start with an initial requirement on amplitude "flatness" or constancy and/or a maximum acceptable phase nonlinearity. The first sheet (no.1) allows us to enter with an amplitude flatness requirement and the second (no.2) with a maximum phase nonlinearity requirement. The following examples will illustrate their use.

Example 1: Assume that we need to preserve the frequency content of a signal to 2000 Hz while also minimizing its wave shape distortion over this same bandwidth. We decide that maintaining frequency response flat within 5% and phase response linear (based on the filter's initial phase-frequency slope) within 5 degrees over this frequency range will satisfy both these requirements. We have 4-pole (i.e., 4th order) 0.5 dB Chebyshev, Butterworth, and Bessel filters available to select from. The goal is to determine which of these filter characteristics best satisfies our requirements while minimizing our sampling rate, thereby also minimizing the quantity of data we have to store.

Solution: Looking at sheet no.1, we enter at the top with the column "flat to 5%" and observe when satisfying the required criteria with 4th order filters the Butterworth can get us to within 35.82% of its 95% attenuation frequency, the Bessel to within 12.91%, and the Chebyshev to within 16.07%. Now we have to determine how well phase linearity is maintained over these same frequency ranges. We go to the bottom part of this same sheet in the 5% column and find that the corresponding phase nonlinearity is 13.31 degrees for the Butterworth, -0.000 degrees for the Bessel, and 3.04 degrees for the Chebyshev. Thus, both the Bessel and the Chebyshev have satisfied our criteria, but the Butterworth has not yet accomplished this. Since the Butterworth is limited in this application by its phase nonlinearity, we enter sheet no. 2 at the top with "5 degrees" max phase nonlinearity. We see that the 4-pole Butterworth can get us to 27.16% of the 95% attenuation frequency while satisfying this 5 degree requirement. We go to the bottom part of this sheet under the 5 degrees column and confirm the Butterworth is flat over this region within exactly 0.59%. Thus both criteria are satisfied. The conclusion is the Bessel satisfies

our starting criteria to 12.91% of its 95% attenuation frequency, the Chebyshev to 16.07% and the Butterworth to 27.16%. Thus, given our selection choices, the Butterworth is the most optimum and can perform within our 5% amplitude requirement and our maximum 5% phase nonlinearity criteria while providing 95% amplitude attenuation at (2000Hz/2716) or 7364 Hz. The minimum sampling rate required would be 14728 samples/second based on the Nyquist sampling criterion. The sampling rate required for the Bessel would be higher (2000/.1291) x 2 or 30984 samples/second as would the Chebyshev (2000/.1607) x 2 or 24891 samples/second based on this same criterion. *While this example doesn't prove it conclusively, it can be shown that when the goal is to both optimize amplitude "flatness" and phase linearity while minimizing sampling rate the Butterworth will always be the better performing filter among the three being evaluated. It should also be noted that neither 5% deviation from amplitude flatness or 5 degrees deviation from phase linearity imply large errors in the time history. These errors only occur only at the maximum frequency in the signal spectrum of interest. Signals other than a sine wave are typically complex and contain multiple frequencies. Thus, the composite signal error, while dependent on the specific wave shape, would typically be very small.*

Example 2: We will again work the same problem as Example 1 above but this time require amplitude response flat within 2% and phase linearity (based on initial phase-frequency slope) within 2 degrees to 2000 Hz from our 4-pole Butterworth filter.

Solution: Looking at sheet no.1, we enter at the top with the column "flat to 2%" and observe while satisfying this criterion the Butterworth can get us to within 31.75% of its 95% attenuation frequency. However, the lower portion of this sheet in the 2% column shows that our phase will be 8.68 degrees from linearity (> the 2 degrees allowed). We therefore enter sheet no. 2 at the top with "2 degrees" phase linearity. We see that the 4-pole Butterworth can get us to 20.74% of the 95% attenuation frequency at the 2 degree phase nonlinearity point. We then go to the bottom part of this sheet under the 2 degrees column to confirm the Butterworth is flat over this region to exactly 0.068%. Thus, this Butterworth can perform within our 2% amplitude requirement and our 2% maximum phase nonlinearity criteria and provide 95% amplitude attenuation at (2000Hz/.2074) or 9643 Hz. The minimum sampling rate required would be 19286 samples/second based on the Nyquist criterion. Obviously this rate would be rounded to a more even number (e.g., 20,000 samples/second). We will expand this example further by referring to sheet no. 3. Sheet no. 3 shows that the -3dB point for this filter would be 9643 x .473 or 4561 Hz. Thus a 4-pole Butterworth with a -3dB frequency at 4561 Hz would satisfy the amplitude and phase requirements of this example and provide 95% attenuation at 9643 Hz. Again, a more convenient -3dB value could be selected by applying whatever value of conservatism the customer desired.

Example 3: We have a digitizer with a sampling rate of 250,000 samples per second. Signal frequency content is to be optimized and wave shape reproduction is important. What filter type and -3dB point should we specify to best satisfy this requirement?

Solution: By now we recognize that among the filters characterized the Butterworth has the optimum performance when considering both its amplitude and phase characteristics. It can also be inferred that higher orders filters offer better overall performance than lower order filters. We will go directly to the 8th order Butterworth with requirements (justified earlier) for frequency response flat within 5% and maximum phase nonlinearity (based on initial phase-frequency slope) of 5 degrees over our frequency range, which has yet to be determined. This problem can be worked both ways but the Butterworth filter characteristic will become limited by nonlinear phase before it deviates from flat amplitude response. Therefore we will go directly to sheet no. 2 with "5 degrees phase linearity" and see that we can operate to 34.8% of the 95% attenuation frequency while satisfying this requirement. We next go to the bottom part of this sheet under the 5 degrees column to confirm the Butterworth is flat over this region to exactly 0.001%. If we specify 95% (26 dB) attenuation at the Nyquist frequency (250,000/2) or 125,000 Hz, we can optimize our filter selection with an 8th order (8-pole) Butterworth and satisfy our requirements to 125,000 x .348 or 43,500 Hz. From sheet no. 3 the -3dB filter value would be 125,000 x 0.687 or 85,875 Hz. Again, a close but more convenient value could be selected. *By contrast, if we had considered an 8th order Bessel, sheet no. 1 shows it would become limited by its 5% amplitude deviation at 14.74% of the 95% attenuation frequency. We could check the phase in sheet no.1, but Bessel filters are always limited by their amplitude deviation from flatness. Thus, for the same sampling rate the Bessel filter in this instance affords only (.147/.348) or 42% of the bandwidth provided by the Butterworth.*

Why is 95% Attenuation at the Nyquist Frequency Generally Enough?

First, there is no hard and fast rule on how much attenuation is required at the Nyquist frequency. An absolute answer could only be based on apriori knowledge of the signal, a specific filter characteristic and order, and the allowable aliasing error contribution. Let's look at Example 3 as a basis for discussion since an 8th order Butterworth filter has a relative sharp roll-off or attenuation curve. Let's round off the -3dB frequency of the filter in this example to 86,000 Hz. Note that 86,000 subtracted from the Nyquist frequency (125,000 - 86,000) is 39,000 Hz. Let's then assume that we have data signal frequency content at 125,000 + 39,000 or 164,000 Hz. This spectral content would be folded back or aliased to 86,000 Hz (the filter's -3dB frequency). A simple calculation shows that at 164,000/86,000 or 1.91 times the -3dB point of this filter less than 0.6% of this 164,000 Hz signal content

is folded back or aliased to the filter's -3dB point. This aliased frequency content would be added to the spectral content at 86,000 Hz which is already in error by virtue of being attenuated by 29.3% (-3dB). In this example the error contribution due to aliasing would be inconsequential relative to the 29.3% existing error due to filter signal attenuation. This is typically the case.

Pyroshock:

Pyroshock is a unique type of high frequency mechanical shock mentioned here only because a currently proposed revision to a specific military standard 810G [9] requires approximately 50 dB attenuation from the filter at the Nyquist frequency of the sampled data. Whether this value is overly conservative or not can be debated, but 50dB corresponds to an attenuation of 1 part in 316 (1/316th). The tables in the appendix can still be used effectively. For an 8th order Butterworth this amount of attenuation occurs at 2.05 times the -3dB frequency or 1.41 times the frequency where 95% attenuation occurs in this filter. Thus, if you use the developed tables for the 8th order Butterworth, perform the standard calculations based on 95% or 26dB attenuation at the Nyquist frequency, and increase the resultant sampling rate by 45% $[(2.05 - 1.41) / 1.41] \times 100$, military standard 810G will be satisfied. For a 4th order Butterworth an analogous calculation would show the sampling rate needs to be increased by 100%.

Subsequent Digital Filtering:

First, it should be clearly stated that if analog data become aliased during the measurement process, no amount of subsequent digital filtering can correct this situation. Digital filtering is only used to further limit the data bandwidth after valid data are initially recorded. Only a brief discussion of digital filtering is provided here. This discussion is further limited to Butterworth characteristic digital filters since these are routinely available in commercial software packages such as MATLAB® and LabView®. Other digital filter types are available.

The previous work has thus far enabled the recording of a signal with a given data bandwidth that can be certified to be within known bounds of amplitude flatness and phase linearity. However, for any complex signal, signal content still exists above this bandwidth. For example, signal content exists at the -3dB point of the measurement system, which is 29.3% reduced from its true value. Higher frequencies result in further attenuation and increased phase nonlinearities. If it is desired to further constrain signal content to a specific upper frequency bound, subsequent digital filtering can help.

Zero phase digital filters can be achieved. The analogous resultant analog filter characteristics would be equivalent to:

$$[H(j\omega)H^*(j\omega)] = |H(j\omega)|^2 \quad (2)$$

where the * denotes a complex conjugate. An equivalent digital filter would have no phase shift and an amplitude response which is the square of that of the analog filter. For example, an 8-pole digital Butterworth filter, when requested with a zero phase option, would produce a 16-pole roll off. This is equivalent to 96dB/octave or 320dB/decade attenuation. Thus it is possible to closely limit any recorded data bandwidth to a selected upper bound by eliminating the higher frequencies in the signal where distortion is occurring. Digitally this is achieved by passing the sampled data through the digital Butterworth filter [7,8], passing the reversed output data through the filter a second time, and reversing the order of this output a final time.

There are other unique features of this filter, but it is easiest to assess its effectiveness in application. Assume that data are recorded, as in example #2, with amplitude response flat within 2% and phase linearity (based on initial phase-frequency slope) within 2 degrees to 2000 Hz using our 4-pole Butterworth filter. Next, assume it is desired to limit data frequency content as much as possible to 2000 Hz to enable model correlation. I can first perform a Fourier transform on this data and note its spectral content. I can now pass this digitized record through a high order, zero phase, digital Butterworth filter and progressively iterate its -3dB frequency lower in value. When spectral content at 2000 Hz just begins to become influenced, the iterations are stopped. The extreme attenuation achievable in the zero phase digital filter will eliminate the majority of the signal content above 2000 Hz without introducing amplitude or phase distortion over the data bandwidth of interest

Conclusion:

While analog filters are often integrated into measurement systems, their selection process lacks precise guidelines. The work presented here has:

1. explained the technical basis of analog filters,
2. proposed a set of guidelines for filter implementation,
3. provided justification for these guidelines,
4. provided a set of parameterized tables to greatly simplify guideline implementation,
5. enabled enough flexibility in these tables to allow a designer to modify these guidelines,
6. provided typical application examples, and
7. described the complimentary role that digital filtering can play once meaningful data are acquired.

It is hoped this effort will greatly simplify the filter selection and/or design process for the measurement engineer.

Acknowledgement: These tables were generated under my direction a number of years ago by Mr. Manoj Gopalan, a former TCU student. His efforts are appreciated. I have made a number of checks on their accuracy and they have been displayed and validated for efficacy in numerous TCU Continuing Education programs.

REFERENCES

- [1] Sedra, Adel S., Smith, Kenneth C., Microelectronic Circuits, 5th ed., Oxford University Press, 2004, pp. 1085.
- [2] Ibid., pp. 1101 – 1108.
- [3] Ibid., pp. 33.
- [4] Ibid., pp. 90.
- [5] Ibid., pp. 1132.
- [6] Proakis, John C., Manolakis, Dimitris G., Digital Signal Processing, 4th ed., Pearson, 2007, pp. 389-394.
- [7] Ibid., pp. 717-720
- [8] Walter, Patrick L., Rodeman, Ronald, Characterization of Digital Filters Used in Sandia Laboratories Test Data Analysis Division, Sandia Laboratories Technical Report SAND79-1230, October 1979.
- [9] MIL-STD-810G, Department of Defense Test Method Standard: Environmental Engineering Considerations and Laboratory Tests, October 31, 2008.
- [10] Schaumann, Rolf, Haiqiao, Xiao, Van Valkenburg, Mac E., Design of Analog Filters, 2nd ed., Oxford University Press, 2010, pp. 363-366.
- [11] Ibid., pp. 276-290.
- [12] Ibid., pp. 300-311.
- [13] Ibid., pp. 430-439.
- [14] Ibid., pp. 323-355.
- [15] Memon, Tayab, Beckett, Paul, Sadik, Amin Z., Sigma-Delta Modulation Based Digital Filter Design Techniques in FPGA, ISRN Electronics Volume 2012, Article ID 538597, 2012, 10 pages.

APPENDIX

FILTER SELECTION TABLES

SHEET 1

Filters Sorted By Flat Amplitude

All Filters Scaled to have 95% Attenuation at $\omega = 1$

Filter Type	Order	Flat to within			
		10%	5%	2%	1%
Butterworth	2nd	15.57	12.83	10.08	8.45
Butterworth	4th	39.46	35.82	31.75	29.06
Butterworth	6th	53.8	50.43	46.54	43.87
Butterworth	8th	62.82	59.85	56.35	53.91
Bessel	2nd	10.03	7.11	4.51	3.2
Bessel	4th	18.39	12.91	8.13	5.74
Bessel	6th	20.67	14.47	9.09	6.42
Bessel	8th	21.08	14.74	9.26	6.53
0.5dB Chebyshev	2nd	21.23	10.03	5.67	3.93
0.5dB Chebyshev	4th	57.67	16.07	8.81	6.06
0.5dB Chebyshev	6th	76.24	14.62	7.97	5.48
0.5dB Chebyshev	8th	85.29	12.4	6.75	4.63

Filter Type	Order	Corresponding Phase Non Linearity			
		10%	5%	2%	1%
Butterworth	2nd	5.957	3.921	2.134	1.317
Butterworth	4th	18.475	13.311	8.687	6.34
Butterworth	6th	31.875	24.615	17.821	14.139
Butterworth	8th	46.019	37.152	28.601	23.778
Bessel	2nd	-0.2917	-0.056	-0.0060414	-0.00109414
Bessel	4th	-0.0025	-0.000114	-0.00000195	0
Bessel	6th	-0.0000067	0	0	0
Bessel	8th	0	0	0	0
0.5dB Chebyshev	2nd	22.1705	3.3499	0.6133	0.204
0.5dB Chebyshev	4th	61.9076	3.038	0.557	0.185
0.5dB Chebyshev	6th	111.551	2.854	0.527	0.176
0.5dB Chebyshev	8th	166.682	2.761	0.512	0.171

SHEET 2

Filters Sorted By Linear Phase

All Filters Scaled to have 95% Attenuation at $\omega = 1$

Filter Typez	Order	Phase Linear to within			
		10°	5°	2°	1°
Butterworth	2nd	38.24	14.29	9.84	7.66
Butterworth	4th	33.03	27.16	20.74	16.75
Butterworth	6th	40.02	32.86	24.82	19.9
Butterworth	8th	42.77	34.8	26.11	20.88
Bessel	2nd	23.17	19.23	15.38	13.12
Bessel	4th	54.79	48.61	42.24	38.3
Bessel	6th	74.31	67.82	60.97	56.65
Bessel	8th	87.25	80.92	74.16	69.84
0.5dB Chebyshev	2nd	14.78	11.51	8.43	6.68
0.5dB Chebyshev	4th	26.82	19.51	13.78	10.78
0.5dB Chebyshev	6th	26.31	18.35	12.78	9.96
0.5dB Chebyshev	8th	23.48	15.86	10.97	8.53

Filter Type	Order	Corresponding Amplitude Attenuation			
		10°	5°	2°	1°
Butterworth	2nd	67.605	7.4	1.819	0.678
Butterworth	4th	2.712	0.586	0.068	0.012
Butterworth	6th	0.335	0.032	0.001105	0.0000889
Butterworth	8th	0.025	0.000837	0	0
Bessel	2nd	43.554	33.178	22.681	16.897
Bessel	4th	66.994	57.554	46.543	39.519
Bessel	6th	80.886	73.881	64.924	58.679
Bessel	8th	89.016	84.232	77.672	72.791
0.5dB Chebyshev	2nd	-5.166	-5.708	-3.936	-2.681
0.5dB Chebyshev	4th	-4.692	-5.821	-4.131	-2.834
0.5dB Chebyshev	6th	-4.005	-5.881	-4.255	-2.929
0.5dB Chebyshev	8th	-3.427	-5.904	-4.322	-2.979

SHEET 3

Relationship between 3dB points and 95% attenuation points

Filter Type	Order	Ratio of 3dB Point to 95% attenuation point
Butterworth	2nd	0.22375
Butterworth	4th	0.47302
Butterworth	6th	0.60709
Butterworth	8th	0.68776
Bessel	2nd	0.17781
Bessel	4th	0.32317
Bessel	6th	0.36861
Bessel	8th	0.37784
0.5dB Chebyshev	2nd	0.26073
0.5dB Chebyshev	4th	0.61124
0.5dB Chebyshev	6th	0.78286
0.5dB Chebyshev	8th	0.86580



ARTICLE REPRINT #101

This AR describes a technique to ascertain the noise floor of the measurement system. When measuring severe shock, there can be a combination of chemical, optical, mechanical electrical, thermal, magnetic, acoustic, and nuclear energy sources present. Each of the stimuli from these energy sources can influence the signal from the accelerometer. This paper describes how to ascertain what portion of the signal is acceleration and what portion is noise.

VALIDATING THE DATA BEFORE THE STRUCTURAL MODEL

A number of requirements must be fulfilled before measurement uncertainty analysis of signals from transducers is justified. These requirements include good measurement system design practices such as adequate low- and high-frequency response and data-sampling rates, appropriate anti-aliasing filter selection,¹ proper grounding and shielding, and many more. Numerous textbooks contain procedures for performing uncertainty analysis² to assign accuracy bounds to measured data. These bounds can easily be established if the measurement system operates in a fixed environment. However, many testing environments vary as a function of both space and time. These variations, which often are not quantified or even identified, can invalidate any uncertainty analysis performed. For example, consider an explosively loaded structure. Aside from the air-blast-induced loads, as a minimum, the structure encounters severe thermal transients, ionization products of the detonation, particle impingement, and induced accelerations and strains.

The intent of this paper is to outline procedures for data validation in test environments. Data validation is essential before data uncertainty analysis can be performed. Most authors of uncertainty analysis textbooks do not acknowledge this fact.

The goal of transducer-based (force, pressure, acceleration, strain, etc.) measurements during testing is either to verify predicted structural loading and response or to identify if established structural limits have been exceeded. Data assessment depends on structural, acoustic, or other relevant analysis to establish acceptable data bounds. A measurement system must then be designed and calibrated specifically for the appropriate physical measurements.

Because all the attributes of the test environment may not be known, data validation³ channels must also be allocated to the test. If these validation channels indicate that the measured data have not been compromised, data uncertainty bounds can be assigned. Figure 1 illustrates this entire sequence of events. The goal of this paper is to clarify the manner in which this data validation process should be implemented.

The front end of any physical measurement system is the transducer. Transducer responses can be categorized as (1) non-self-generating (e.g., a bridge with variable resistance, capacitance, or inductance elements that require external power) or (2) self-generating (piezoelectric, thermoelectric, photoelectric, magnetoelectric, etc.).

Having established these two types of responses, it must be recognized that both types are susceptible to two classes of environmental inputs: desired and undesired. (For example, the *desired*

environmental input to an accelerometer is clearly acceleration.) Thus, one can conclude that for every measurement system, there exists four response-input combinations (Fig. 2).

The table of Fig. 2 enables a definition for the signal output from a measurement system to be established. Signal will be defined as the correct response type to the desired environmental input. For example, consider the case of a piezoresistive accelerometer. For this example, the non-self-generating response (resistance change) to the desired environment (acceleration) is the signal. It is the object of the measurement.

The non-self-generating response to the undesired environments, as well as the self-generating response to both the desired and the undesired environments, will be denoted as noise. Examples of these noise effects could include resistance changes due to temperature as opposed to acceleration and self-generated outputs due to thermoelectric effects in the transducer wiring. Figure 3 diagrammatically illustrates the paths associated with these four combinations, path 4 being signal, and paths 1, 2, and 3 being noise. This example can be generalized to any bridge-type transducer.

Numerous technical agencies such as the International Society for Measurement and Control (ISA) have published specifications and test guides for various types of transducers. One such publication is the "Guide for Specifications and Tests for Piezoelectric Acceleration Transducers for Aero-Space Testing" (ISA-RP37.2-1982⁴). This document includes specifications to minimize the response of accelerometers to the *undesired* environmental inputs of steady-state and transient temperature, base strain, acoustic pressure, magnetic fields, humidity, radio interference, and nuclear radiation.

In any measurement system, the goal is to assure that the path defined as signal is the only one that is present to any significant extent. Some question may arise as to how to implement this verification. An acceptable method for the preceding example would be to field three accelerometers in close proximity. The first accelerometer could be mounted without electrical power applied to document paths 1 and 3. Note that without power, paths 2 and 4 are not possible. The second accelerometer could have power applied but be mounted on a piece of foam (or suspended in air) to isolate it from the acceleration environment, resulting in documentation of paths 1 and 2. Note that without the desired environment (acceleration) present, paths 3 and 4 are not possible. The third accelerometer could be mounted with power properly applied to measure the acceleration environment. If the first two accelerometers produced no output, paths 1, 2, and 3 would be documented not to be present and the output from the third accelerometer would be path 4, which is the noise-free signal. Valid data, that is, data worthy of subsequent uncertainty analysis, would have been acquired!

The same strategy applies to impedance-type force and pressure transducers. Simply install three force or pressure transducers

P.L. Walter (SEM member) is a senior design lecturer in the Department of Engineering at Texas Christian University, Fort Worth, TX, and a measurement specialist with PCB Piezotronics, Depew, NY.

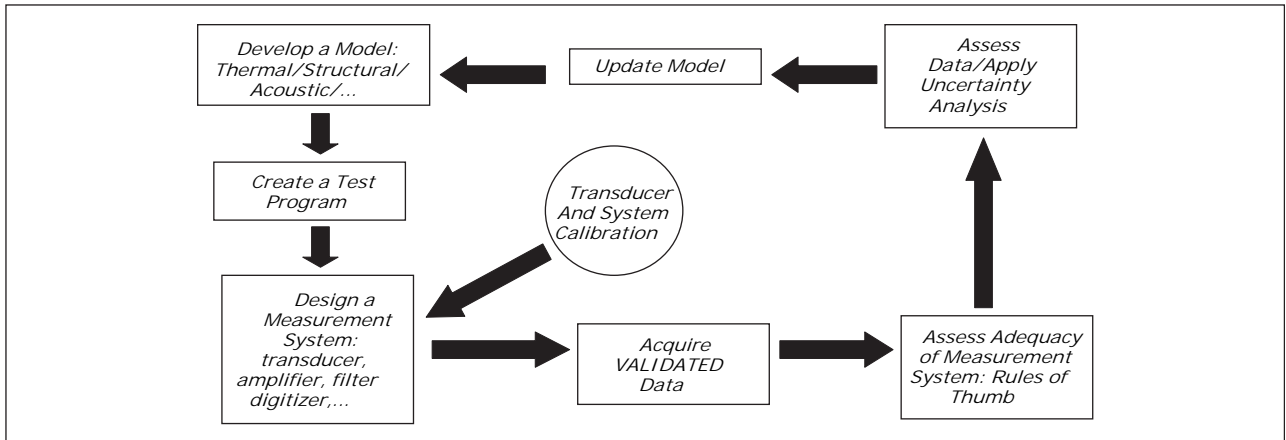


Fig. 1: Analysis, test, measure, and data validation synergies

Response Type	Environmental Input
Non-self generating	Desired
Self-generating	Undesired

Fig. 2: Four transducer response combinations

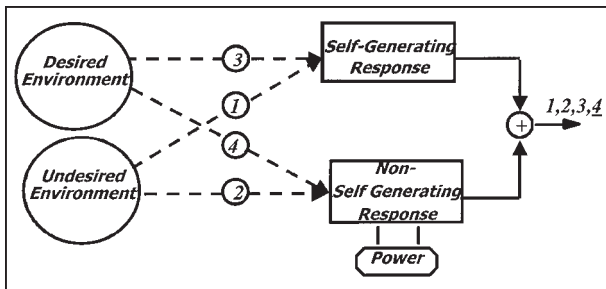


Fig. 3: Non-self-generating transducer model

in close proximity. Apply power to one, do not apply power to the second, and apply power but isolate the third from its intended force or pressure environment. For example, a pressure transducer could be mounted in a “blind hole” to ensure its diaphragm is not exposed to pressure. It would still be exposed to vibration, strain, electromagnetic fields, and other undesired environments to which it could potentially respond.

The efficacy of these noise documentation techniques is shown in the following example. Figure 4a and 4b shows launch acceleration acquired from resistive bridge accelerometers within a projectile in a gun environment.⁵

Figure 4a is data acquired from a legacy measurement system, which had been verified to be trustworthy through successful testing over many years. Figure 4b represents concurrent data from the initial test performed using a new, higher frequency measurement system. The initial results look encouraging. However, Fig. 5 shows the results from recording a separate data channel with no power applied to the associated accelerometer. Any signal present in Fig. 5 represents paths 1–3, which are noise. When scaled, it can be shown that the peak noise signal in Fig. 5 is more than 20% of the signal in Fig. 4b. Because no power is on the accelerometer bridge, this signal is entirely attributable to some

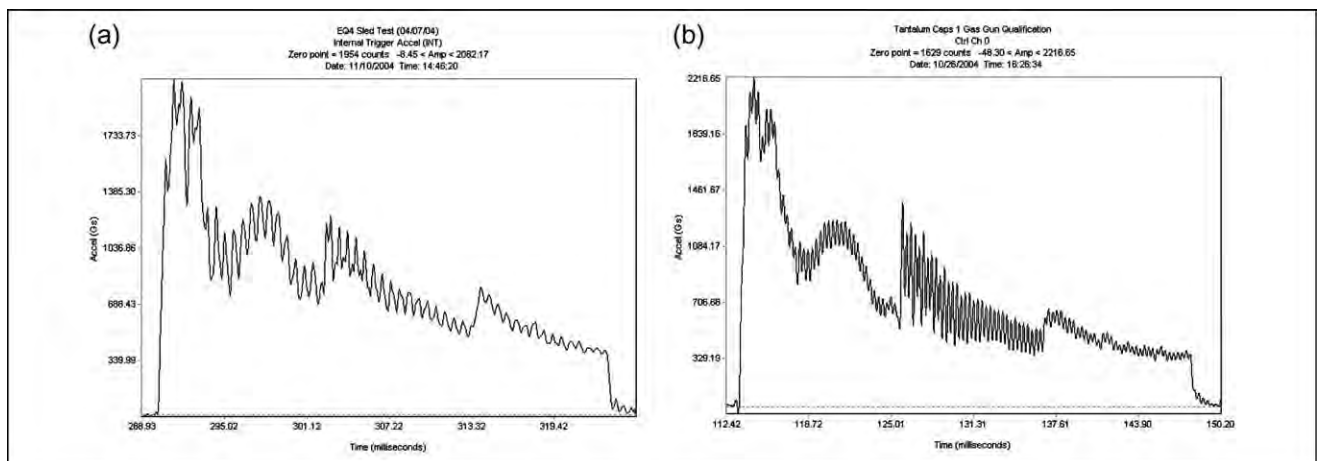


Fig. 4: Gun launch acceleration time measurement. (a) Legacy system, (b) proposed new system

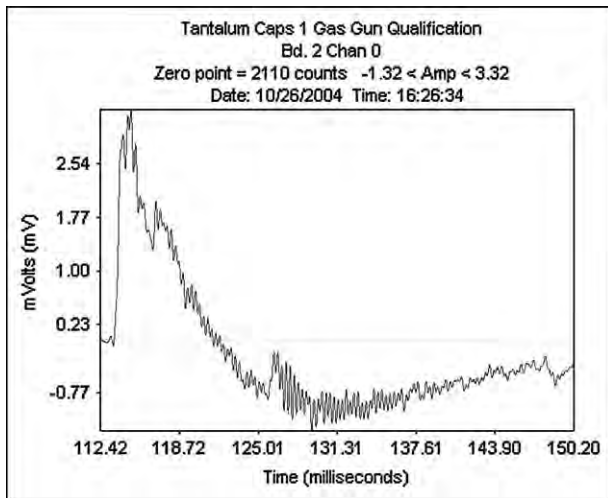


Fig. 5: Paths 1-3 documentation for proposed new system

error source. Investigation showed its cause to be shock sensitivity of capacitors within the new measurement system. No pretest uncertainty analysis would have encompassed this error. Worse yet, if data validation had not been performed, the similarities between Fig. 4a and 4b might have encouraged the adoption of the proposed new system without design corrections.

While the foregoing, projectile-related example was provided for a non-self-generating transducer, the next example is for a self-generating transducer. We will use the example of a piezoelectric accelerometer measuring acceleration. For piezoelectric transducers, “placebo” (Institute of Environmental Sciences and Technology [IEST]-RP-DTE011.1) transducers enable data validation to be accomplished. The referenced IEST standard defines a placebo transducer as “identical to a ‘live’ unit in every parameter except for mechanical sensitivities.” The placebo transducer should respond only to extraneous “environmental factors.” Ideally, its output would be zero. Any signal output from it would indicate that the signals from the “live” transducers could be corrupted.

The manufacture of placebo transducers will now be clarified. Figure 6 shows a boule of quartz from which piezoelectric elements are cut in order to be integrated into transducers for force, pressure, and acceleration. The boule possesses dif-



Fig. 7: Poling ceramics

ferent piezoelectric properties for cuts in different directions, as illustrated by the equation set (Eq. 1) below.⁶ While the details of the system of equations are not important for this discussion, note that the third equation in the set shows a direction (i.e., the z-axis) that produces no piezoelectric output. Cuts along this axis provide the quartz for the placebo transducers.

$$\begin{aligned} P_{xx} &= d_{11}\sigma_{xx} - d_{11}\sigma_{yy} + 0\sigma_{zz} + d_{14}\tau_{yz} + 0\tau_{zx} + 0\tau_{xy} \\ P_{yy} &= 0\sigma_{xx} + 0\sigma_{yy} + 0\sigma_{zz} + 0\tau_{yz} - d_{14}\tau_{zx} - 2d_{11}\tau_{xy} \\ P_{zz} &= 0\sigma_{xx} + 0\sigma_{yy} + 0\sigma_{zz} + 0\tau_{yz} + 0\tau_{zx} + 0\tau_{xy} \end{aligned} \quad (1)$$

where “P” is a piezoelectric directional constant, “d” is a piezoelectric coefficient, and “σ” and “τ” are a stress components.

As opposed to piezoelectric transducers for pressure and force, which almost exclusively use quartz, many accelerometers use ceramic-based materials for their sensing elements. These ceramics result from complex manufacturing processes. The commonality of the ceramic processing is as follows: in order to behave in a piezoelectric manner, the ceramics must have a high poling voltage placed across their electrodes at a high temperature during the final stages of their manufacture (as illustrated in Fig. 7). If this poling is intentionally skipped, an inert sensing element is produced, and it can be used in a placebo transducer. Neither the z-cut quartz nor the unpoled ceramic placebo transducers can produce a piezoelectric output.

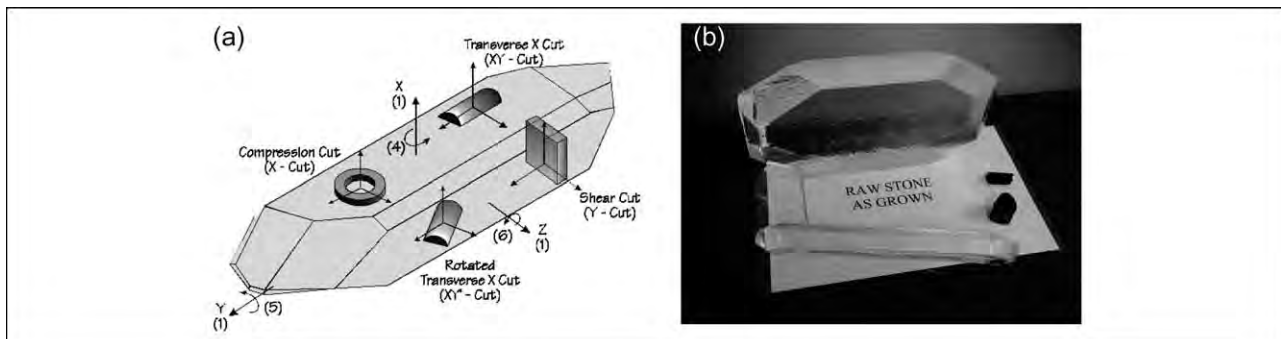


Fig. 6: Axes definition of quartz with grown boule. (a) Axes definitions, (b) grown quartz

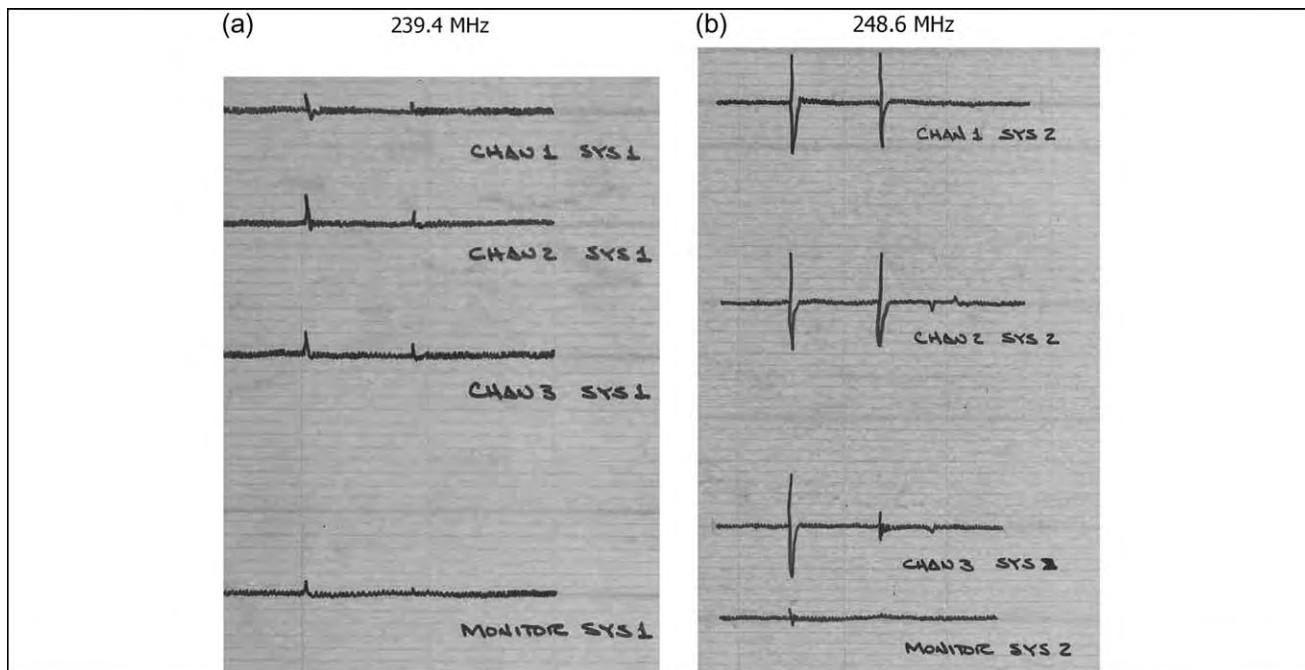


Fig. 8: Telemetered acceleration data. (a) Transmitter 1, (b) transmitter 2

However, they do respond the same as a live transducer to the undesired environmental factors described previously.

The value of integrating placebo transducers into a test is illustrated in Fig. 8a and 8b, which involves telemetered data.^{7,8} The uppermost three of the four records in each figure are from live accelerometers and the bottom record is from a placebo accelerometer. Each set of four accelerometers was assigned to a specific telemetry transmitter, the frequencies of which are shown. Data recorded during a test using these accelerometer sets were subsequently noted to be anomalous. After the test, the set of accelerometers on the 239.4-MHz transmitter was removed from the system, mounted to a metal plate, and impacted with results shown in Fig. 8. The live accelerometers recorded data, as did the placebo! More surprising, signals were emitted from all the accelerometers (live as well as placebo) on the 248.6-MHz channel, even though those accelerometers were not impacted. A ground loop was found to be the culprit, and bad data were not accepted as good. Design corrections to the measurement system were subsequently performed and erroneous data were not accepted, thanks to the validation channels incorporated into the test.

While the above example has again focused on acceleration data, placebo transducers are equally useful in dynamic testing irrespective of whether force, pressure, acceleration, or other measurements are required. For example, strain measurements depend on resistive elements in a bridge circuit, and validation techniques for non-self-generating transducers apply.

CONCLUSIONS

The data validation process has been illustrated by the preceding material. Several methods have been shown by which to perform data validation. The value of data validation in documenting erroneous signals has also been shown by actual

test examples. When measurement systems are required to operate in situations where their environmental boundaries are not fixed, validation channels should always be provided. The final configuration and utility of these channels is limited only by the inventiveness of the instrumentation engineer. Without validation channels, in situations where the environment of the measuring transducers varies with time and/or location, data accuracy bounds based on uncertainty analysis remain questionable.

ACKNOWLEDGMENTS

Prof. Emeritus Peter K. Stein initiated my journey down the road of data validation as a structured process, and Jim Lally, CEO of PCB Piezotronics, saw the early utility of and then manufactured placebo transducers.

References

1. Walter, P.L., "Optimizing Flight Shock and Vibration Measurement by RF Links," *International Telemetry Conference*, San Diego, CA (1998).
2. Coleman, H.W., and Steele, W.G., *Experimentation and Uncertainty: Analysis for Engineers*, John Wiley and Sons, New York (1999).
3. Stein, P.K., *The Unified Approach to the Engineering of Measurement Systems*, Stein Engineering Services, Phoenix, AZ (1992).
4. *Standards and Recommended Practices for Instrumentation and Control*, 10th Edition, Vol. 1, Instrument Society of America, Research Triangle Park, NC (1989).
5. Partridge, M.E., "Sandia National Laboratories," Personal Communication to author, November 16, 2004.
6. Neubert, H.K.P., *Instrument Transducers*, 2nd Edition, Clarendon Press, Oxford (1975).
7. Walter, P.L., "Placebo Transducers: A Tool for Data Validation," Technical Note 16, PCB Piezotronics, Depew, NY (2005).
8. Walter, P.L., "Air Blast and the Science of Dynamic Pressure Measurements," *Sound and Vibration*, pp. 10-16 (2004). ■



ARTICLE REPRINT #98

This AR is of great importance in that it summarizes all the lessons that were hopefully learned in the heretofore presented material. It provides the requisite sequence of events that must occur to develop an instrumentation plan. It begins with the test objectives, organizes test system design and preparation, and culminates with data comparison and reporting.

Acquiring Meaningful Test Data on Purpose

Patrick L. Walter, Contributing Editor

Large-scale, instrumented testing, such as crash, flight (see Figure 1), explosive, drop, and more, can be very expensive to perform and difficult to repeat. It is not uncommon that after test completion a group of stakeholders (test engineers, test requesters, analysis personnel, calibration staff, and others) spend a lot of time “scratching their heads” trying to figure out what the resultant data are telling them.

As the data significance is being pondered, one hears questions being raised regarding sensor-mounting techniques, data-channel noise floor, data-channel bandwidth, extraneous environmental effects, and more. The fact that these questions are being asked after the test has been completed indicates that the pretest instrumentation planning was not performed in a methodical manner.

A requisite sequence of events to develop a successful instrumentation plan follows:

1. Clearly identify why the test is being run. What is its goal? Physics-based predictions or models must exist to justify the measurements requested. It is not unusual when discussing a test for someone to say as an afterthought, “let’s add some instrumentation to the test.” The instrumentation should be the first part of the test plan, *not* an afterthought.

2. The physics-based analysis of item 1 should result in the specification of the specific measurands (strain, acceleration, pressure, force, angular rate, temperature, heat flux, flow, etc.) that need to be acquired. It should also, as a minimum, provide guidance as to sensor types, sensor mounting densities, measurement directions, anticipated amplitudes, and required data bandwidth.

3. All sensors respond to other measurands (environments) in addition to the one they are intended to measure. The manufacturer’s specification sheets clearly indicate this fact. Additional data channels should always be incorporated into the test planning to monitor the instrumentation system noise floor in application. If properly implemented, these additional channels will document system noise attributable to other inputs to the instrumentation system aside from the desired measurand(s). The sensors dedicated to this purpose are called “placebo” sensors. They should have signal conditioning identical to any similar channel, except that they are configured to not respond to the measurand of interest.

4. The sensor must next be coupled or interfaced to the test item. The goal is to acquire a measurement as if the sensor was not there to transfer energy from the process being measured. The mass loading and



Figure 1. Typical commercial airliner outfitted for flight testing.

stiffening of a structure by accelerometers, the effects of cavities or voids in front of pressure transducers, and the mechanical compliance of load cells are but a few examples of undesired modification of the process being measured.

5. The sensor’s cable must be carefully selected. The cable has resistance, capacitance, and inductance. If its influences are not understood and accounted for, it can attenuate signals and induce unwanted filtering. It can also be a signal source attributable to cable-induced triboelectric effects. In addition, if not properly shielded, it can also couple undesired electromagnetic and electrostatic fields into the signal. Wear, bend radius, and thermal capabilities are but a few additional cable selection considerations.

6. The analog signal conditioning must be selected to be compatible with the sensor and its associated cable. Over the bandwidth that the physics-based data are desired, not only should the bandwidth of the analog portion of the instrumentation system be flat (constant) but if data time histories are of interest, system phase response must also be linear.

7. The instrumentation system must be verified to be linear in its input-output relationship; this differs from phase linearity. Assuming dynamic measurements are being made, these input-output linearity checks must be performed to encompass the entirety of the data frequency range. If the instrumentation system becomes dynamically over-ranged in application (driven nonlinear), extraneous frequencies are generated within it, and these frequencies contaminate the data.

8. The analog filter, when necessary, is typically the final modifier of the analog signal before digitization. Terms such as filter type (Chebyshev, Bessel, Butterworth, etc.) must be understood as well as the degree of attenuation that the filter provides. The latter information is provided by the number of filter poles, filter order, attenuation in dB/octave, attenuation in dB/decade, or some analogous specification.

9. In today’s world, data are typically digitized for storage and analysis. The data-sampling rate must be compatible with the analog portion of the system. This is typically controlled or constrained by the aforementioned analog filter, whose effect on the data must be understood. With modern technology, data are often acquired with sigma-delta type systems containing an integral digital filter whose characteristics must equally be understood. Digital system resolution (number of effective bits) must be considered relative to the subsequent data processing. For example, successful data integration is very dependent on the ability to define a true zero, which can only be quantified within the limits of \pm one-half bit in a digital system.

10. Before test, the sensor must be calibrated and perhaps have its response evaluated to anticipated extraneous measurands. Then the entire measurement system must be calibrated end to end.

11. Throughout this entire planning process, the end use of the data must be considered. As noted previously, data integration requires an increased focus on bit resolution. Also of note, if the recorded data are to be integrated, less high-frequency response is required than if differentiation

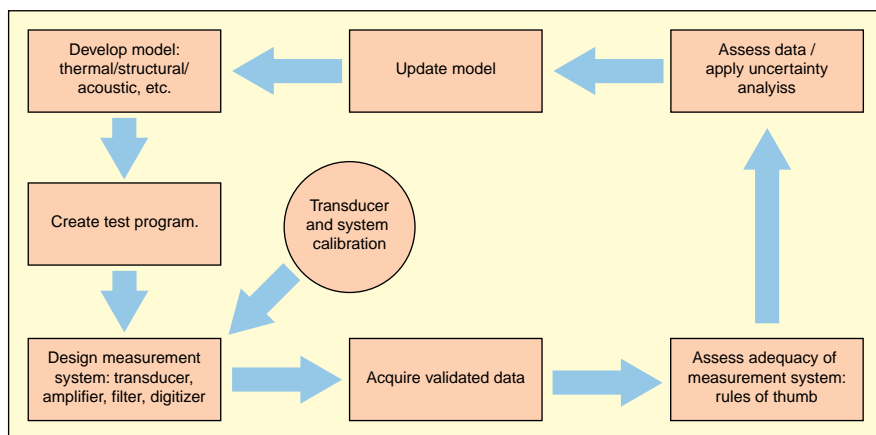


Figure 2. Schematic diagram of the dynamic data acquisition process.

is to occur. If only data frequency content is of interest, theoretically we only need to sample to twice the highest frequency contained in it. If we want to visually see this highest frequency, we should sample to a minimum of 10× its value. For random signals to be subjected to power spectral density (PSD) analysis, maintaining instrumentation system phase response becomes less important. These are but a few examples of how the ultimate data usage should guide measurement system design.

12. Finally, after comparison with pretest predictions, the data need to be carefully plotted for future reference, and the instrumentation system that recorded them must be carefully documented. The assessment of future test item improvements or the development of the next generation of test items depends on performance comparison to prior test results.

Now, having presented the sequence, it might seem overwhelming. However, it just requires a transformation in thinking. In our formal technical education process, we were typically presented with a system and asked how it would respond to a given input. That is called analysis, which can be summarized as follows:

$$\text{Input} \Rightarrow \text{System} = ?$$

Measurement is just the opposite. We typically measure an electrical parameter output (current, voltage) and try to infer the system input (temperature, pressure, acceleration, strain, etc. as denoted before).


$$? \Rightarrow \text{System} = \text{Output}$$

Two things are obvious here:

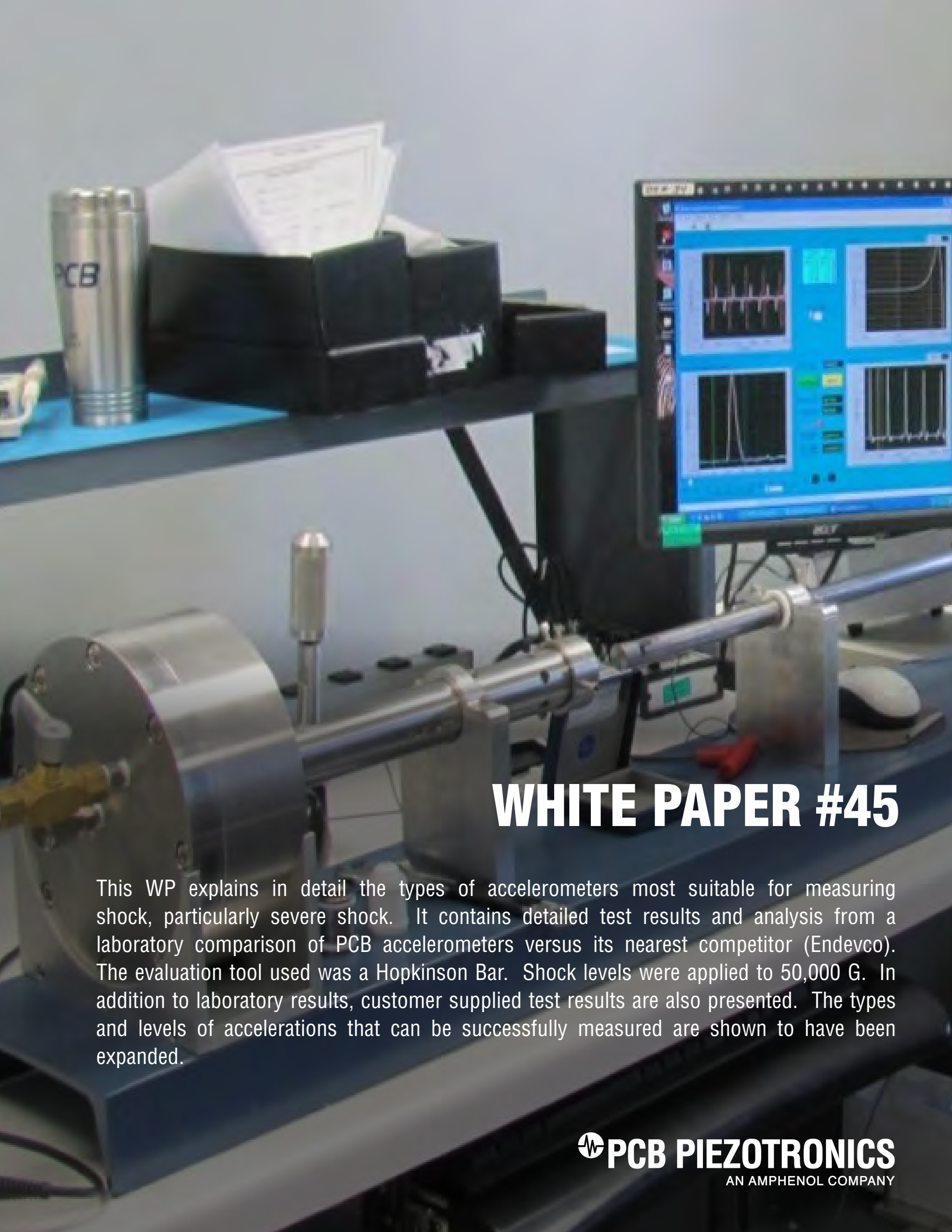
- Unless the instrument system is appropriately designed and characterized, we cannot infer its input. Note that the instrumentation input is the object of the test. We measure its output. Grabbing components “off the shelf” and “sticking them together” rarely produces good test measurements.
- We all have the knowledge base to understand instrumentation. It just involves reorganizing lessons taught to us previously. *Independent of the amount of physics based analysis performed on a test item, if the item is properly instrumented, the truth is always in the data.*

Figure 2 illustrates a synopsis of the process just described. Without an orderly instrumentation system design process, the only guarantee that I can provide to you is that you will record something. It may be the cable breaking, a pressure transducer responding to dynamic strain or transient or steady-state temperature, a strain gage in a transient thermal environment behaving as a thermocouple, an accelerometer responding to base strain, etc. I can continue this list *ad infinitum*.

This takes us right back to where I started with the second sentence of this editorial: *It is not uncommon that after test completion a group of stake holders (test engineers, test requesters, analysis personnel, calibration staff, and others) spend a lot of time “scratching their heads” trying to figure out what the resultant data are telling them.*

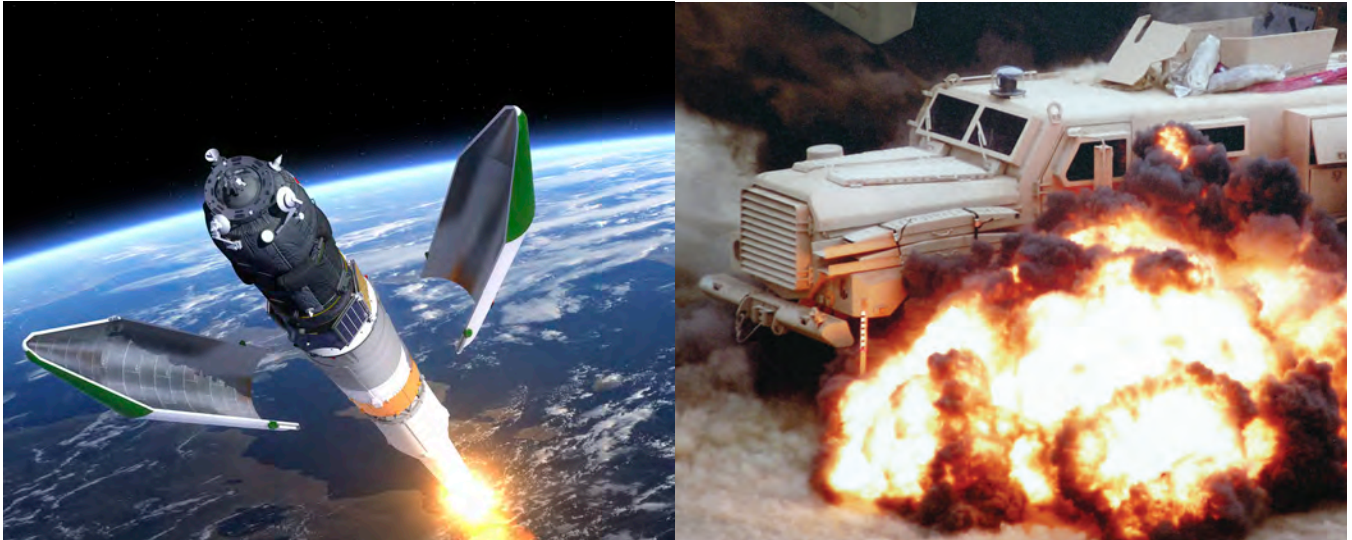
We can do better than this! 

The author can be contacted at: p.walter@tcu.edu.



WHITE PAPER #45

This WP explains in detail the types of accelerometers most suitable for measuring shock, particularly severe shock. It contains detailed test results and analysis from a laboratory comparison of PCB accelerometers versus its nearest competitor (Endevco). The evaluation tool used was a Hopkinson Bar. Shock levels were applied to 50,000 G. In addition to laboratory results, customer supplied test results are also presented. The types and levels of accelerations that can be successfully measured are shown to have been expanded.



Acceleration Sensing Technologies for Severe Mechanical Shock

Written By

Anthony Agnello

Jeffrey Dosch

Robert Metz

Robert Sill

Patrick Walter

Acceleration Sensing Technologies for Severe Mechanical Shock

Anthony Agnello; Jeffrey Dosch; Robert Metz; Robert Sill; Patrick Walter

PCB Piezotronics, Inc.

Depew, New York 14043-2495

Since there is no unique definition of “severe mechanical shock”, this paper first provides examples of the types of mechanical shock encompassed by this work. Next presented is a summary of lessons learned over the years, and/or pitfalls discovered, with acceleration sensing technologies used in past measurement attempts of these types of shock. Based on these lessons, a description of current sensing technology approaches and their integration into accelerometers is provided. Due to the uniqueness and severity of some of the shock environments being considered, often the ultimate success or failure of these approaches can only be evaluated in the actual test application. Nevertheless, a descriptor of laboratory evaluation techniques employed during sensor development is provided. Last, results from the application of some of these sensing technologies in actual field applications are illustrated.

INTRODUCTION

The term “severe mechanical shock”, as used here, encompasses the gun launch of projectiles and/or projectile barrel exit, high speed penetration events (earth, rocks, and structures), air blast loading of structures, missile-silo attack, jet engine blade severance, air drop impact, underwater detonation, torpedo impact, transportation vehicle crashes, pile driving, and more. Some subcategories of these shock environments are described in military standards [1] as follows:

Pyroshock – “refers to the localized intense mechanical transient response of materiel caused by the detonation of a pyrotechnic device on adjacent structures. A number of devices are capable of transmitting such intense transients to a materiel.” These devices include explosive bolts, separation nuts, pin pullers and pushers, bolt and cable cutters and pyro-activated operational hardware, flexible linear shape charges (FLSCs), mild detonating fuses (MDFs), explosive transfer lines, V-band (Marmon) clamps, and more.

Gunfire – “gunfire environment may be considered to be a high rate repetitive shock having the form of a substantial transient vibration produced by (1) an air-borne gun muzzle blast pressure wave impinging on the materiel at the gun firing rate, (2) a structure-borne repetitive shock transmitted through structure connecting the gun mechanism and the materiel, and/or a combination of (1) and (2).”

Ballistic Shock – “is a high-level shock that generally results from the impact of projectiles or ordnance on armored combat vehicles. Armored combat vehicles must survive the shocks resulting from large caliber non-perforating projectile impacts, mine blasts, and overhead artillery attacks, while still retaining their combat mission capabilities.”

Organizations such as NASA and the Institute of Environmental Science and Technology (IEST) have complementary standards [2, 3].

All of these described environmental inputs to the sensing accelerometer involve various combinations of acceleration levels, velocity changes, and spectral content. These inputs typically occur in more than one direction, however; each accelerometer is intended to isolate and respond to only one vector component of this input. While

high-G levels associated with large velocity changes are a challenge, the larger measurement challenge is associated with the combination of high-G levels and broad frequency spectra.

Reference 4 describes the basic physics associated with high amplitude, broad spectrum loading of structures. Referencing from that document, Figure 1 below shows the acceleration time response at the center of a specific, infinite (large in diameter) aluminum plate explosively loaded with TNT. This response would be maintained until relief waves from the plate's edges add complications.

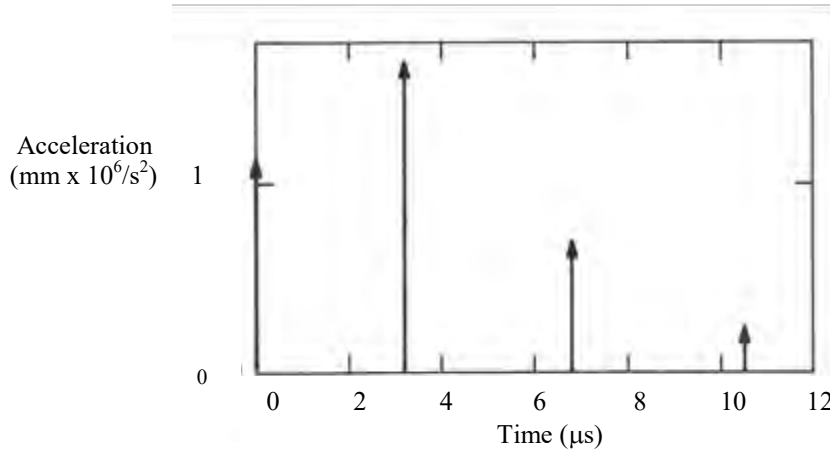


Figure 1: Acceleration Versus Time of Loaded Surface of Aluminum Plate Interacting with TNT

In a real, built-up structure, reflections from joints, interfaces, and interconnections would still further complicate this response. If we assume that an accelerometer responds as a simple, lightly-damped oscillator, Figure 2a shows its resonant response to a single impulse. Depending on the relative timing, the accelerometer's response to two similar impulses could be like Figure 2b, which results in near signal cancellation due to a 180 degree out of phase condition. Alternately, for three similar impulses, if timing were right, there could be reinforcement as in Figure 2c. In short, the amplitude of the response of an accelerometer during the material response phase of a complicated, built-up structure encountering complex or non-deterministic loading is very unpredictable.

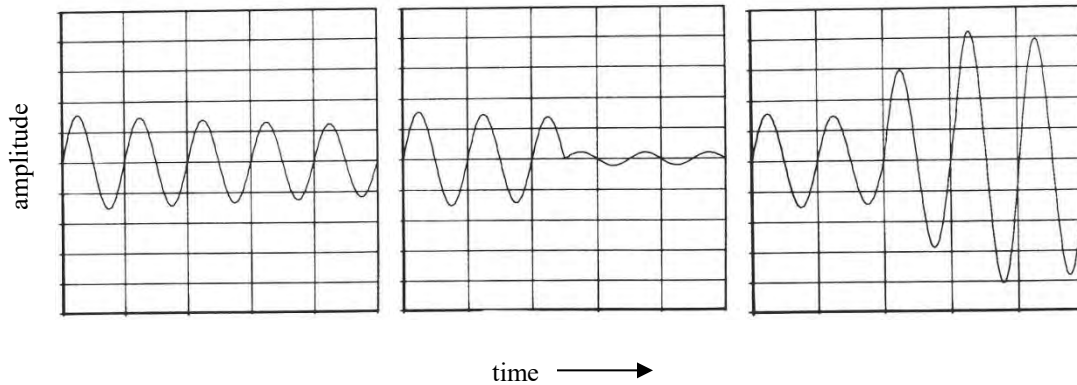


Figure 2a: Single Impulse

Figure 2b: Two Impulses

Figure 2c: Three Impulses

Figure 2: Response of Simple Spring-mass System to 1, 2, and 3 Impulses

The challenge is then to measure the time-history associated with the resultant vibratory modes of the structure (unit under test, UUT) at the location where the accelerometer is affixed concurrent with or after the material response of

the structure has dissipated. This challenge arises because of the unpredictability of the initial response of the accelerometer due to its resonant excitation, as illustrated in Figure 2, during this material response phase. This initial response will superpose on the UUT's later-time structural response and can cause accelerometer or instrumentation channel over ranging, problems associated with broad bandwidth input to the analog front portion of the instrumentation system (e.g., slew-rate limiting), accelerometer breakage, and more.

LESSONS LEARNED

A summary of lessons learned in applying various accelerometer technologies to measuring "severe mechanical shock" follows. Reference [4] is again the basis for this summary.

1950s to mid-1970s: The sensing technology used to measure severe mechanical shock over these decades was almost exclusively piezoelectric type materials, specifically ferroelectric ceramics. A frequent frustration was that accelerometers containing these ceramics often displayed a baseline shift or offset from their initial zero at shock termination. Reference [5] showed that this shift was an intrinsic property of these ferroelectric ceramics that could occur at stress levels as low as 100-150 psi.

Mid 1970s to 1983: Discrete semiconductor gages were integrated into accelerometer design (nomenclated piezoresistive or PR) for high-G, high-frequency shock. These devices operated on a Wheatstone bridge principal and the bonded, semiconductor gages themselves were impervious to zero shift. Their small size, approximately 1 gram, also made them compatible with high frequency response. An improved sensing and resultant measurement capability in "severe mechanical shock" environments was attained.

1983 to 2010: An all microelectromechanical (MEMS) sensing technology was integrated into a high-G shock accelerometer (Endevco Model 7270(A), B. Wilner) in 1983. Its total silicon flexure, with boron strain gages diffused into the silicon, achieved working ranges to 200,000 G and resonant frequencies to 1.2 MHz. However, loading of the type shown in Figure 1 still excited the resonance of the accelerometer. In addition, with such a wide measurement frequency bandwidth, attention had to also be focused on other modes of vibration (e.g., torsional) of its seismic element that could be excited. Last, its pure silicon flexure, with essentially no damping, resulted in a very high "Q" as compared to ferroelectric ceramic and bonded semiconductor technologies (10 to 20 times higher postulated). Thus, breakage at high frequencies often occurred. In addition, in the early 1990's, attempts began to internally mechanically isolate piezoelectric accelerometers in order to mitigate mechanical stress inputs and resultant zero-shift at high frequencies. In order to lessen the influence of the isolator resonance, these accelerometer designs were typically accompanied by a 2-pole filter integrated into the accelerometer housing.

As a byproduct of these lessons learned, accelerometer durability and measurement accuracy have improved. The status of current sensing technologies for severe mechanical shock is reported below.

CURRENT SENSING TECHNOLOGIES

Mechanically Isolated and Electrically Filtered Piezoelectrics:

Measurement accuracy and durability are important considerations when designing piezoelectric accelerometers for severe mechanical shock environments. Durability may be the more important of these two because the associated issues can cause measurement inaccuracies and, in extreme cases, complete data loss.

Mechanical isolation is commonly used with the sensing element (i.e., the piezoelectric ceramic and its attached mass) of an accelerometer to make the accelerometer more durable and less prone to zero shift. The isolator functions as a low-pass mechanical filter decoupling the sensing element from the accelerometer housing at high frequencies. In turn, this protects the element from undesirable, out-of-bandwidth, high frequencies and energy. Figure 3 compares the shock response of an accelerometer both with and without mechanical isolation during a metal-to-metal impact.

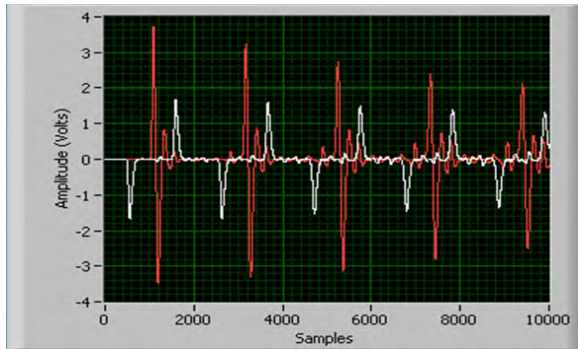


Figure 3a: Mechanically Isolated

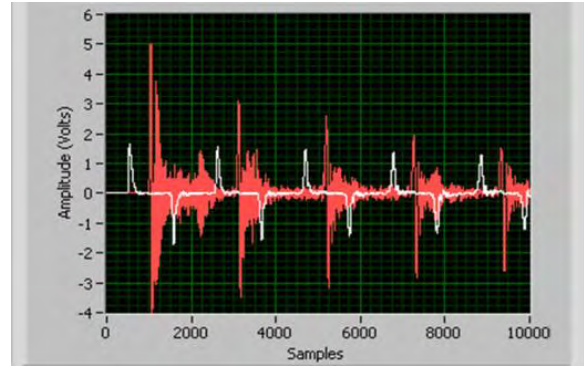


Figure 3b: Unisolated

Figure 3: Effect of Mechanical Isolation on Accelerometer Response

Mechanical isolation also reduces the amount of base strain transmitted into the sensing element. Base strain is often the root cause of measurement inaccuracies such as high transverse sensitivity, nonlinearity, and zero shift. It can be defined as any undesired output from the sensing element caused by deformation of the accelerometer's mounting surface. Since base strain can be more of an influence at higher energy levels, both nonlinearity and zero shift become larger error contributors with increasing amplitude. Figure 4 shows a finite element analysis (FEA) of an accelerometer with and without mechanical isolation. Note how the location of the maximum strain moves from the sensing element to the mechanical isolation.

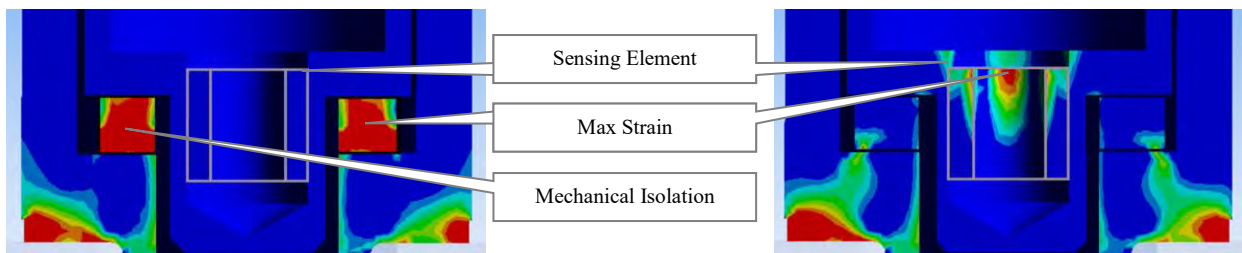


Figure 4a: Mechanically Isolated

Figure 4b: Unisolated

Figure 4: Effect of Mechanical Isolation on Base Strain

Material properties of the mechanical isolator must be carefully considered as they can cause additional measurement inaccuracies. Material that is too soft can create linearity issues because the material will deflect differently at high amplitudes that it does at lower amplitudes. Too soft of a material can also result in a sensing system with too low of a resonant frequency, negatively affecting the frequency response of the accelerometer below 10 kHz (shown in Figure 5a). Ten (10) kHz is a minimum design goal in all accelerometers intended to measure severe mechanical shock. Conversely, material that is too hard will not provide enough isolation to reduce the undesired out-of-bandwidth high frequencies and energy.

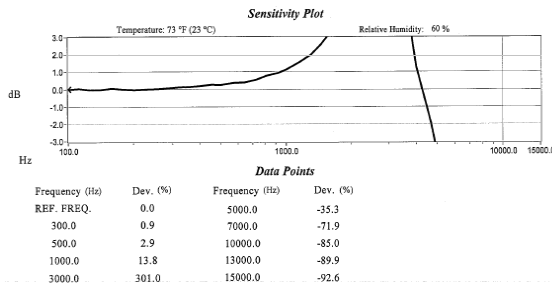


Figure 5a: Low System Resonant Frequency

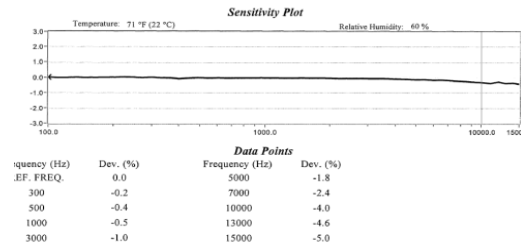


Figure 5b: Desired Frequency Response

Figure 5: Effect of Isolator on Accelerometer Frequency Response

The cutoff frequency of the isolator must be much lower than the accelerometer resonance to assure adequate high-frequency attenuation. An optimum relationship between stored energy and energy dissipation, or Q factor, for the isolator is desired to maximize the accelerometer's region of flat frequency response. An under damped system (high Q factor), as shown in red in Figure 6a, will oscillate at its resonant frequency and decay as energy is lost. Figure 6b shows a more optimally damped system.

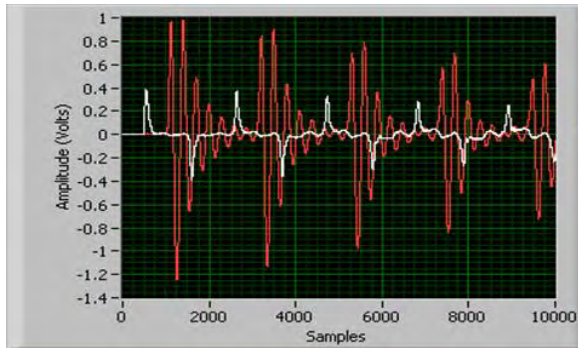


Figure 6a: Underdamped Accelerometer Response

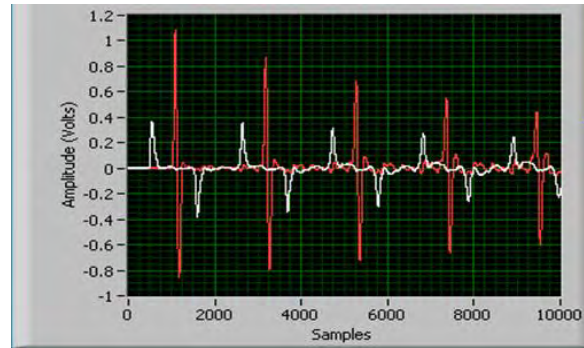


Figure 6b: Optimally Damped Accelerometer Response

Figure 6: Influence of Q Factor of Isolator on Accelerometer Response

Since optimal damping cannot be attained with a simple elastomeric material, nominal 2-pole low pass electrical filtering is also incorporated in the accelerometer to attenuate any residual resonant peak associated with the isolator. It further eliminates high frequencies and prevents overloading of subsequent signal conditioning. The electrical filter, configured around the ICP[®] circuit, is tailored to the mechanical isolator's resonant frequency so as to result in a sensor frequency response that is flat to > 10 kHz. Figure 7 shows a representative amplitude versus frequency response function for an accelerometer when the response of the mechanical isolator is combined with an electrical filter.

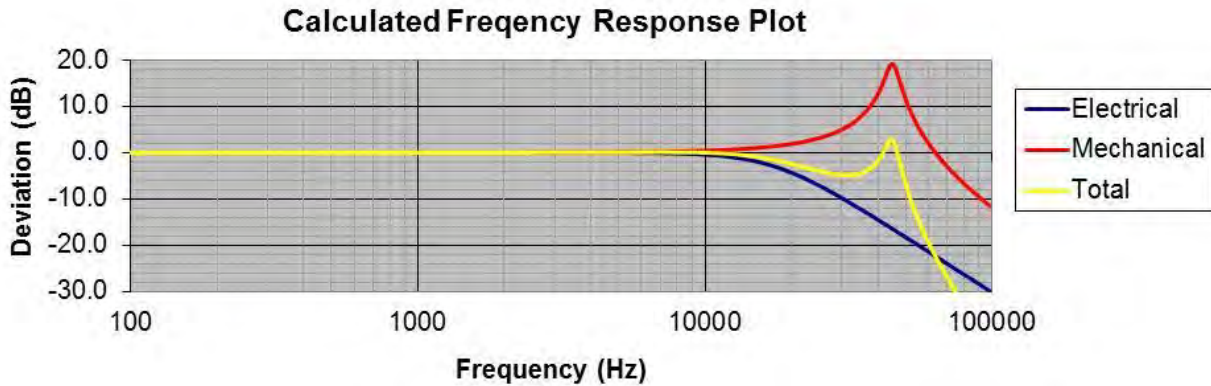


Figure 7: Mechanical Isolator Resonance and the Electrical Filter

Thermal properties of the isolation material must also be considered. Temperature changes can alter material properties of the isolator, which in turn will alter accelerometer performance. Thermal properties can constrain the useable temperature range of the accelerometer since calibrations are typically performed at room temperature. As the temperature increases, the mechanical isolation material may become softer, lowering the accelerometer's resonance and lessening its region of flat frequency response (Figure 5a).

Additional design considerations can further protect the sensing element from base strain, thus improving accelerometer performance. During an extremely severe mechanical shock, some strain may still be transmitted through the mechanical isolator. Grooves or undercuts can be added to the accelerometer housing to concentrate the area of the base strain at a location away from the sensing element, thus reducing its affects. Figure 8a & 8b shows a finite element analysis (FEA) of a housing before and after the addition of an undercut. Note how the location of the maximum strain moves from the sensing element to the undercut. Secondary rigid mechanical isolation can also be used to mitigate any base strain that has been transmitted through the primary mechanical isolator. Figure 8a & 8c shows a FEA of an accelerometer with and without secondary rigid mechanical isolation. Note the reduction in strain on the sensing element with the addition of the rigid isolation.

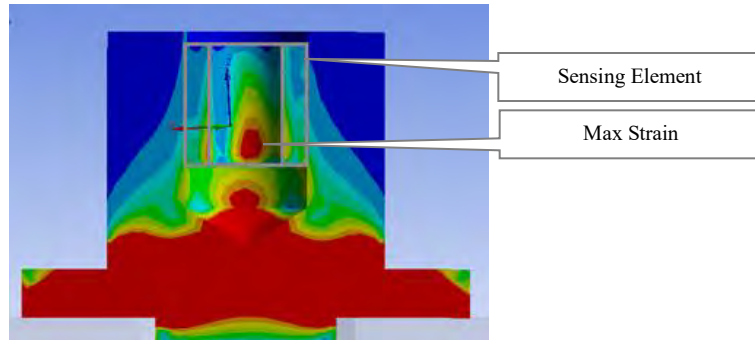


Figure 8a: Standard Housing

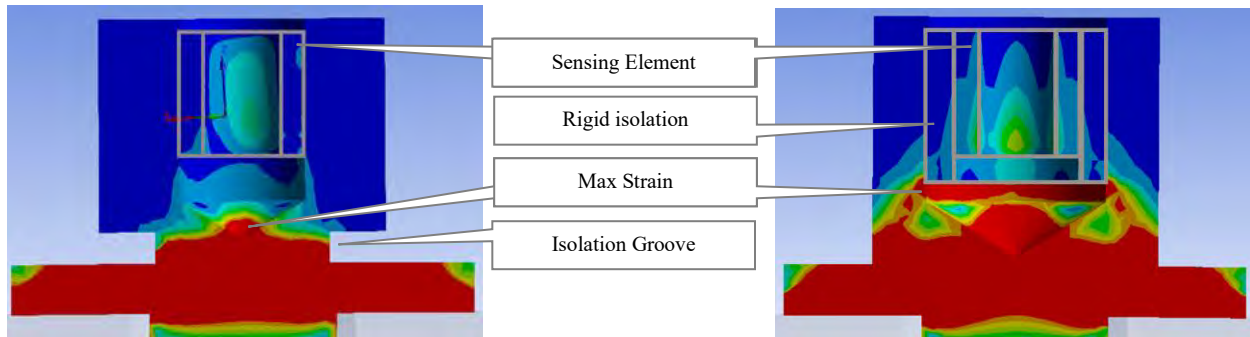


Figure 8b: Standard Housing

Figure 8c: Undercut Housing

Figure 8: Strain Concentration With and Without Undercuts

The type of piezoelectric material used in the sensing element is also an important design consideration. Ferroelectric ceramics are used in piezoelectric accelerometers because they have higher charge sensitivities than materials such as quartz. These materials are poled by high voltages during their manufacture to align their dipoles and induce a piezoelectric effect. Figure 9 shows the dipole alignment of a ferroelectric ceramic before and after poling.

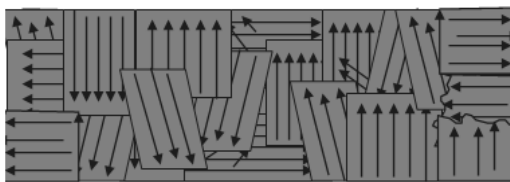


Figure 9a: Ferroelectric with Random Dipoles

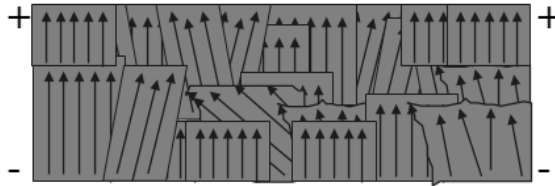


Figure 9b: Ferroelectric after Poling

Figure 9: Poling of Ferroelectric Material

Ferroelectrics can be susceptible to dipole realignment when overstressed, a phenomenon in which some of the dipoles switch back to random orientation. This realignment can cause the baseline shift or offset (called zero shift) shown in Figure 10. Mechanical isolation can help to eliminate the chance for baseline shift or offset caused by overstressing a ferroelectric ceramic sensing element. Depending on the coercive forces between the dipoles, various ferroelectric ceramics display differing amounts of zero shift.

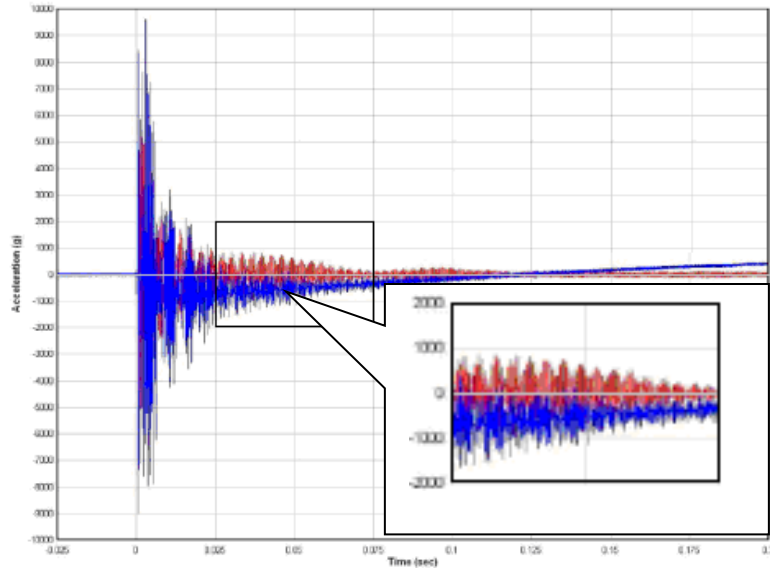


Figure 10: Accelerometer with Baseline Shift (Blue) and Without (Red)

The effect of internal wiring is another important design consideration. The size and type of wire used within the sensing element can be critical to the proper functioning of the accelerometer. Large, single strand wires can cause base strain by imparting side loads onto the element. Conversely, small, single strand wires can fatigue easier and result in a loss of output signal. Multi-strand wires add flexibility to help prevent fatigue while increasing sensor durability.

Epoxy can be used to over coat wires and to secure the various components of the sensing element; however, it must be used cautiously as it introduces other variables. Too much epoxy can cause base strain by exerting side loads onto the element. Conversely, if not enough epoxy is applied, structural integrity may be compromised. Cleanliness of areas where epoxy is applied is critical to bonding. Contaminates, especially machining oils, can cause the epoxy to debond. This can enable movement of the element components, resulting in zero shift and other signal output errors. Surface preparation (sandblasting, rough finish, etc.) all help promote epoxy adhesion.

In summary, the combined addition of mechanical isolation and electrical filtering has helped to make piezoelectric accelerometers more durable and reliable. These technologies, combined with other design lessons learned over the years, have helped to reduce undesired stresses in accelerometer sensing elements enhancing the probability of acquiring successful measurement of severe mechanical shock.

MEMS Technology:

There are two principal reasons that strain gauge technology can offer an attractive alternative to piezoelectric technology: 1) accurate response when integrating long duration events (requiring flat frequency response to essentially zero Hertz) and 2) minimal zero shift. Metal wire and foil type strain gauges were initially used, but, as mentioned in Ref [4], piezoresistance technology began to be used in the 1970's, evolving into MEMS technologies in the 1980s. The piezoresistance property of silicon strain gauges was found to be superior to that of foil gauges, with an orders-of-magnitude higher Gage Factor provided by boron-doped silicon. The first sensor assemblies used thermally-matched pairs of discrete doped silicon elements that were hand-epoxied and -wired to machined metal structures in a tension-compression bridge as depicted in Figure 11.

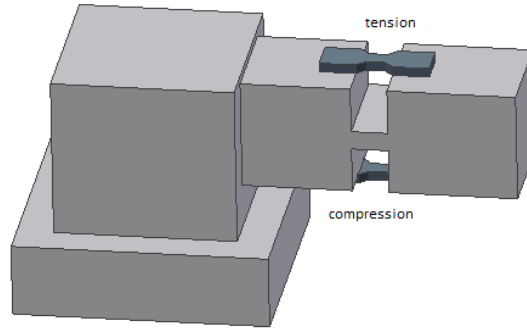


Figure 11: Silicon Strain Gages Monitoring Motion of Cantilevered Mass across Slot

The cost of this type assembly was high, and zero shift sometimes became an issue not due to the silicon gages but rather due to cracks and/or creep in the epoxy holding the gages to the structure. At times even outright failure of the epoxy occurred. These weaknesses, i.e., both the application time and fragility of the epoxy, were addressed by the use of MEMS manufacturing techniques to simultaneously form the entire sensor structure for hundreds of sensors from a silicon wafer. The mechanical flexural elements were joined together as originally grown with gages predoped in the single crystal silicon.

The semiconductor processing allowed extreme miniaturization, enabling hundreds if not thousands of sensors to result for the same wafer processing cost, affording a potential price decrease in per-unit completed accelerometer. This miniaturization also provided the advantage of increased performance efficiency. Smaller structures have higher stiffness-to-weight ratios. This means the resultant sensors have lower sensitivities and higher resonant frequencies if all their parts are proportionately smaller. Since the trend over time in mechanical shock testing has been towards measuring increasingly higher acceleration levels, it was not a disadvantage that the new, smaller sensors had lower sensitivities and much higher resonances. One unexpected disadvantage was that the single crystal silicon had virtually no internal damping, unlike the natural damping properties (though small) attributable to the epoxies that held the previous generation of manually assembled accelerometers (Figure 11) together.

A depiction of the most successful of the earliest MEMS sensors is given in Figure 12. Its size and efficient geometry provided extraordinarily high resonances, ranging from many hundreds of kilohertz to over a megahertz for the millimeter-sized chip. The sensor element was an assembly of a sensor chip attached to a pedestal. Although hundreds were made at a time from one wafer, each wafer needed to subsequently be diced and these individual parts hand assembled. Because the design mimicked the arrangement of the manually assembled, discrete assembly of Figure 11, with tension gauges above and compression gauges below, it required wire bonds on each side of the sensor chip. As mentioned previously, when completed the monolithic structure made of single crystal silicon possessed almost no internal damping.

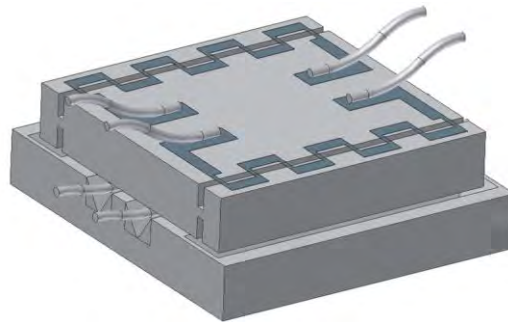


Figure 12: Early MEMS Sensor Developed for Severe Mechanical Shock

As will be discussed further in a later part of this paper, this lack of damping allowed very high levels of sensor resonant amplification. As one author (R. Sill) can attest as a member of that sensor development team, it was somewhat of a surprise to find that many shock inputs, even those with finite velocity change as opposed to pyrotechnic types, had sufficient energy in the megahertz range to excite its resonances. The result was frequent sensor failure from becoming overstressed. Therefore, some sensor damping was desired to reduce this resonant amplification.

Frictional dissipation of energy requires relative motion; however, the internal sensor displacements of the early MEMS shock accelerometers were practically at an atomic level. They were inadequate to facilitate any significant sensor damping. Although some early model, low-range, high-sensitivity piezoresistive sensors (made of large hand-assembled parts with relatively large displacements) utilized fluid damping with silicone oils, this was an impractical solution at extremely high g levels. In addition, the viscosity of oils was strongly affected by temperature, which meant the frequency response of sensors using oil damping was extremely temperature dependent. The viscosity of air, however, is much less temperature dependent. This fact was exploited in the next generation of MEMS shock sensors.

Squeeze film damping uses the motion of air “sloshing” between moving plates to dissipate energy. Similar to stiffness-to-weight ratios, as dimensions become very small the scale of viscous-to-inertial forces becomes larger. As dimensions between plates reduced to a few microns, early MEMS variable capacitance sensors for low g ranges could be optimally damped with just air. Key to that success was the comparatively large area of the plates of the capacitive elements and the very low stiffness of the flexures involved with these low G range devices. Contrasted with the geometry of the sensor in Figure 12, the next generation of MEMS shock sensors developed at PCB was designed to utilize air damping. This was accomplished by increasing the area of the sensor’s inertial mass, and decreasing the stiffness of its flexures. The section geometry of this new generation is shown in Figure 13. Both tension and compression gauges are more conveniently integrally doped on the top surface. The comparatively large cantilevers supporting the X-shaped inertial mass provide the area for damping. They are intentionally less efficient so the resonant frequency is as low as practical to allow adequate motion for squeeze film damping while still providing adequate sensitivity and frequency response. Not shown are the lid and base layers that surround the core, providing the gap for squeeze film damping, as well as over range stops and hermetic protection.

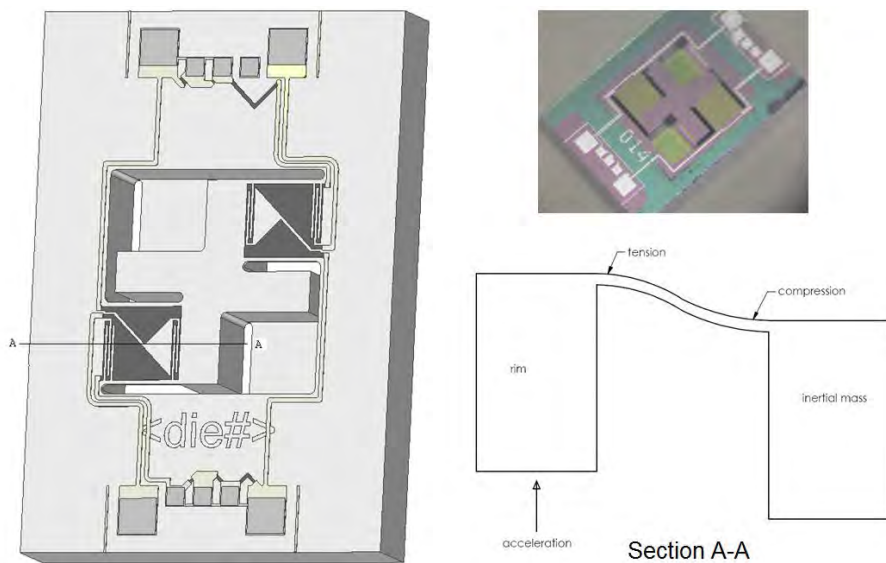


Figure 13: The Core Layer of PCB’s MEMS Lightly Damped Shock Sensor

The initial version of PCB's MEMS sensor was designed for a full range of 20kG. It was packaged in a variety of housings, including the Endevco 7270A's flat, two-screw package shown beside it in Figure 14. Because of its early development, identified previously to be 1983, the Endevco 7270 will subsequently be identified as the Legacy Sensor. The photograph shows the lightly damped PCB sensor prepared for a side-by-side comparison on a Hopkinson bar with the packaged Legacy Sensor depicted in Figure 12. This "breakaway" fixture was placed on the end of the bar to allow free flight for comparison of zero shift of the PCB 3991A1020K with an identically ranged Legacy Sensor. Between this fixture and the end was placed a quartz plate with electrodes, to serve as a force gauge reference. The test was performed by Dr. Danny Frew (then of Sandia National Laboratories) on the Hopkinson bar at Purdue University



Figure 14: PCB and Legacy Shock Accelerometer on Breakaway Fixture

Results of this Hopkinson bar test are shown in Figure 15. Most noticeable is the enormous resonant response of the essentially undamped Legacy Sensor. The lower resonant frequency value of the lightly damped PCB sensor resulted in some small oscillations observed during the main pulse, which quickly dissipated, unlike the undamped Legacy Sensor response. It is now believed that relaxation of mounting screw preload releases elastic energy from the screws in bursts short enough to mimic the impulse sequence depicted in Figure 2.[6]).

Good correlation during the initial pulse is shown among the three sensors in this Hopkinson bar test (Figure 15). The PCB sensor had low Q resonant amplification during this initial 10 kG pulse, and the 20kG Legacy Sensor showed an extremely high Q (ringing) response after the breakaway fixture detached from the bar. After separation, zero shift is observed on the output of the monitoring (yellow) piezoelectric quartz disk. The initial test pulse of Figure 15 was carefully crafted to reduce high frequency input in the Hopkinson bar.

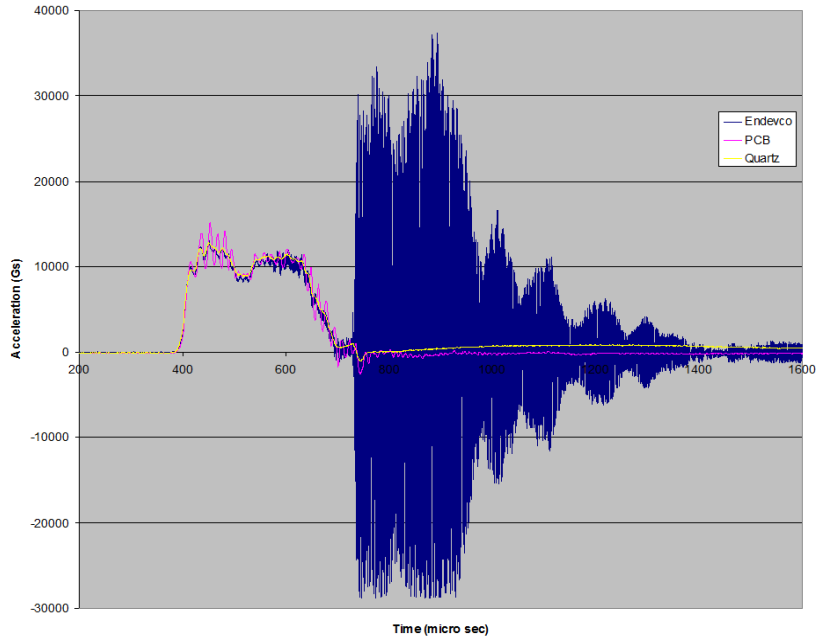


Figure 15: Comparative Hopkinson Bar with Breakaway Fixture Sensor Test Results

In contrast, another test was performed with the opposite intent, i.e., to maximize high frequency input. A mechanical hammer test applied approximately 100 blows over a two second interval, with each blow generating peaks of approximately 10kG as measured by the wideband data acquisition system (5MHz sampling with 2.5MHz antialias filters). The geometric arrangement of the sensors tested is shown in Figure 16. This depiction shows the size and relative separation of the PCB sensor alongside two mechanically filtered Legacy Sensors that were on the same test specimen. The point of impact was near the sensors, in a direction normal to the mounting surface, and therefore parallel to the sensitive axis of all of the sensors. The mechanically filtered package is traditionally used to prevent sensor failure due to over range from resonant amplification in the high Q Legacy Sensor during explosive events and metal-to-metal impacts.

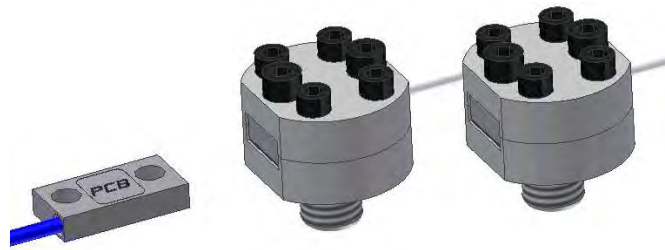


Figure 16: Relative Size and Separation of PCB and Isolated Legacy Sensors Used in Testing

Figure 17 shows the resultant FFT spectrum from the PCB 20KG sensor in Figure 16 when subjected to one of the 10kG hammer blows. A more revealing view of the high frequency components of the new sensor is shown and soon discussed in a logarithmic plot of these same data in Figure 19.

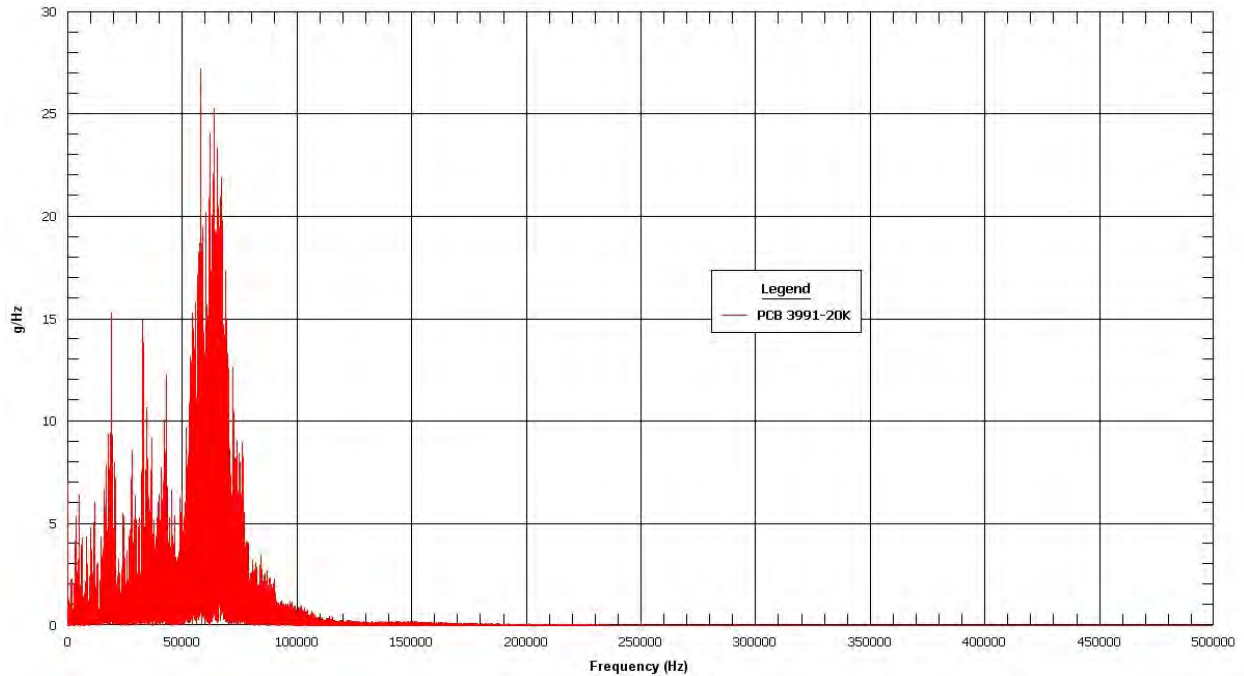


Figure 17: Representative FFT Spectrum from the PCB 20KG Sensor Subjected to a 10kG Hammer Blow

Figure 18 below shows the equivalent FFT spectrum from the undamped 20KG Legacy Sensor, in one of the isolated rubber mechanical mounts, subjected to the same 10kG hammer blow as the PCB sensor in the previous Figure 17.

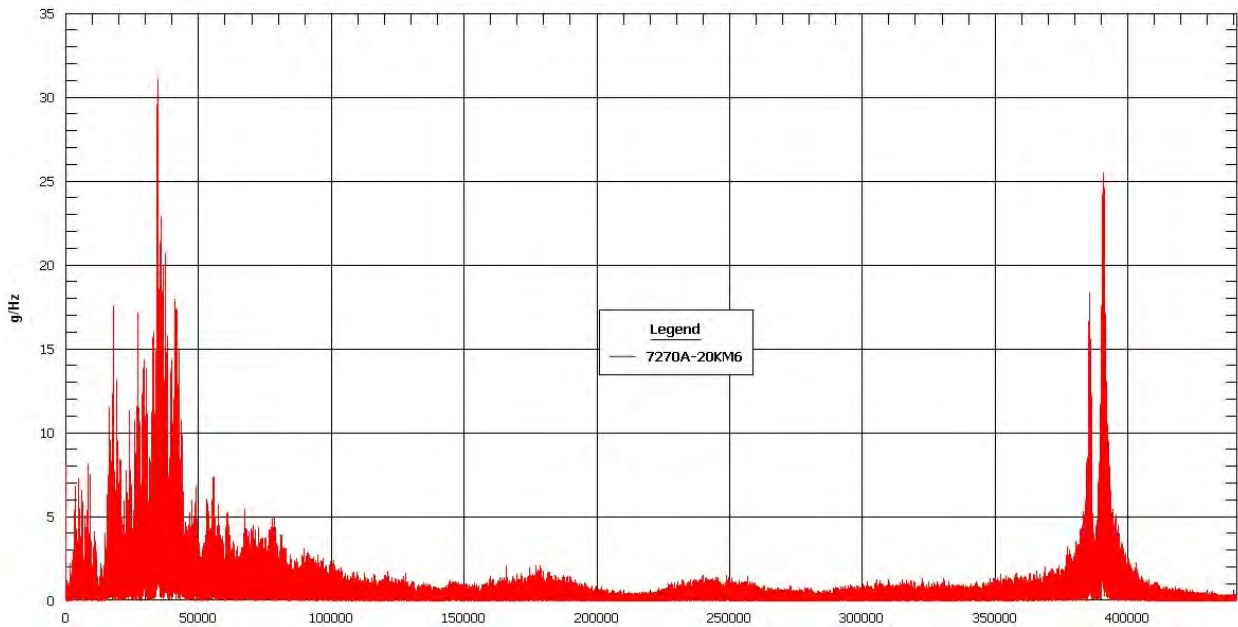


Figure 18: Comparative FFT Spectrum from the Legacy Sensor

Comparing the spectra of Figs. 16 and 17, as close as it is possible, note that both seem to match each other below about 20 kHz. The PCB sensor shows the amplified response of its lightly damped 65 kHz resonance in Figure 17.

The 30-40 kHz associated with the resonance of the rubber isolation in the commercial Legacy Sensor “M6” package is visible in Figure 18. The input is shown, remarkably, to include essentially white noise to 500 kHz or higher. High Q 380 kHz twin resonances associated with the 20kG Legacy Sensor are illustrated in spite of the mechanical isolation. (A similar plot of a 60kG Legacy Sensor displayed its resonances at 900 kHz.)

Figure 19 is an expanded logarithmic plot of the PCB sensor data from Figure 17. Overlaid is a theoretical single-degree-of-freedom response with a 65 kHz resonance and damping coefficient of ~ 0.05 . Assuming that the energy in the hammer tests is fairly “white” (i.e., uniform over all frequencies), as indicated by the response spectrum of the Legacy Sensor in Figure 18, the FFT magnitude of the input should approximately match the frequency response function of any sensor subjected to it. The roll off of the new PCB MEMS sensor past the resonance in Figure 19 has a much steeper decline than a perfect single degree of freedom response. This perhaps indicates that the squeeze film damping in the PCB sensor is more effective than expected. The conclusion that can be drawn from these data is that the light damping in the new MEMS sensors minimizes sensor overstress, thereby enhancing its ability to survive and measure severe mechanical shock measurements.

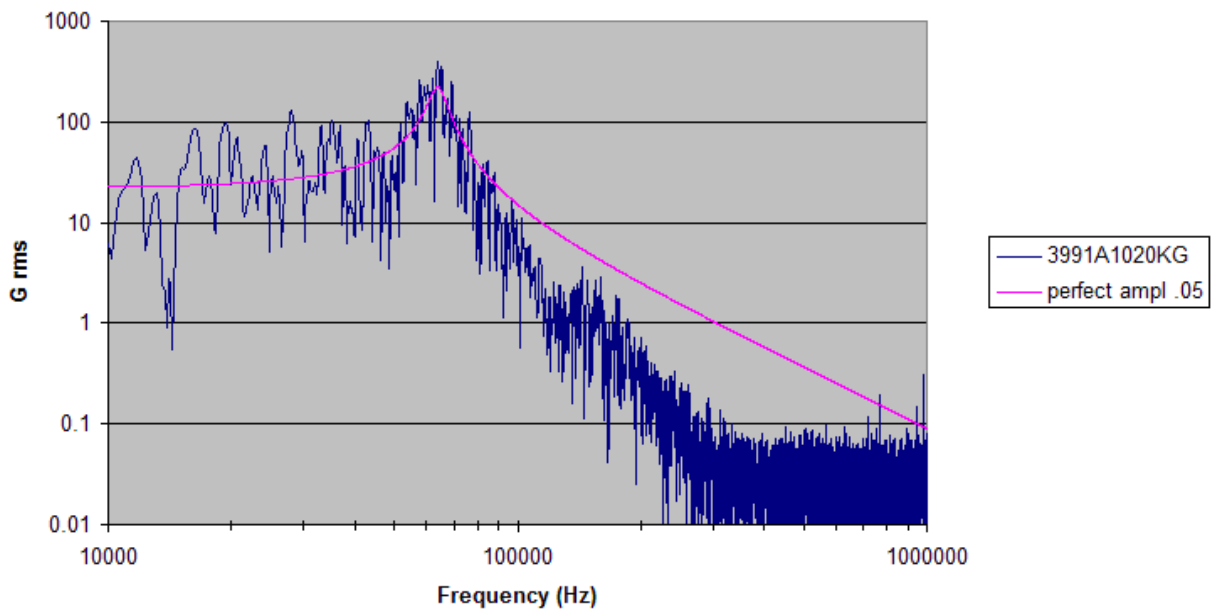


Figure 19: Logarithmic Plot of the PCB Sensor Data from Figure 17 with a Superposed Single-degree-of-freedom Second-order System with a 65 kHz Resonance and Damping Coefficient of ~ 0.05

LABORATORY EVALUATION TECHNIQUES AND RESULTS

A well-designed shock sensor will accurately report on-axis acceleration while rejecting all extraneous electrical, mechanical, and environmental inputs as it is subject to shock levels that would damage most ordinary sensors. In the field, these extraneous inputs will occur in combination. In the laboratory, acceptance tests are constructed to singly quantify the sensor’s influence to each input and then impose reasonable acceptance limits. Many of the acceptance tests performed on shock accelerometers are similar to tests performed on “ordinary” vibration accelerometers and include: vibration sensitivity, frequency response, base strain, transverse sensitivity, temperature coefficient of sensitivity, inherent noise, and immunity to electromagnetic interference. The only challenge with these “ordinary” acceptance tests is the acquisition of the very low level signal output from a high-range, low-sensitivity shock accelerometer. Other parameters such as zero-shift, shock survivability, and linearity require testing on a Hopkinson bar, a device capable of producing very high peak acceleration levels. In this section theory

and operation of the Hopkinson bar will be described followed by a discussion of the interpretation of Hopkinson bar data.

Hopkinson Bar Acceptance Test System

The Hopkinson bar test system can generate peak acceleration levels in excess of 100,000g. It consists of an instrumented titanium bar, a projectile and launch tube, signal conditioning, a PC based data acquisition system and signal processing software [7,8]. The accelerometer under test is mounted on one end of the bar and reference strain gages are mounted near the mid-point of the bar. Impact of the projectile against the bar launches a strain transient whose shape approximates a half sine. Referring to Figure 20 impact of the projectile starts a compressive wave at time $t = t_1$ which propagates to the right at the speed c_o , the speed of a longitudinal wave in a solid. At time $t = t_2$ the leading edge of wave has reached the strain gage. The wave continues to the right until it is reflected at the accelerometer boundary as a tensile strain wave travelling to the left. The time $t = t_3$ is after the wave has reflected at the accelerometer boundary. The stress wave continues to propagate, reflecting back-and-forth until dissipative forces completely attenuate the wave.

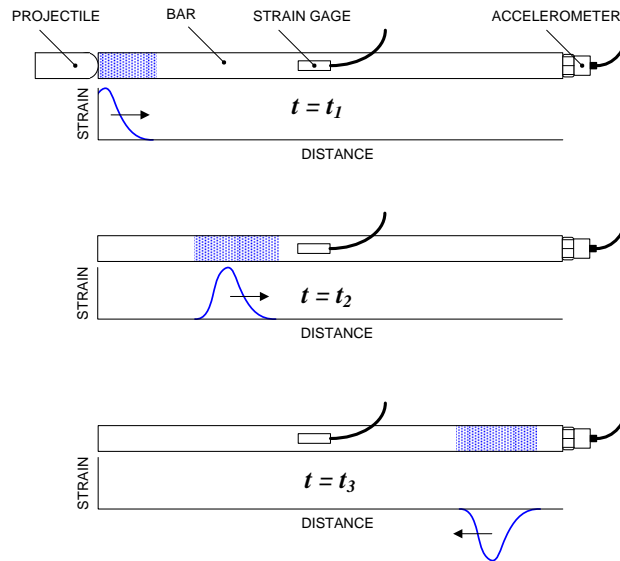


Figure 20: Three “Snapshots” of Propagating Strain Wave Generated by Projectile Impact Against Hopkinson Bar

Determining the bar's tip acceleration from the strain gage signal is straightforward. The velocity, v , at a point away from the ends of the rod is proportional to the reference strain, ϵ_r [2]:

$$v(t) = c_o \epsilon_r(t) \quad (1)$$

At the end of an unconstrained bar, the velocity is doubled and stress is zero. Thus, the reference velocity at the location of the accelerometer is:

$$v_r = 2c_o \epsilon_r \quad (2)$$

The reference acceleration is found by differentiating the above expression

$$a_r = 2c_o \frac{d\epsilon_r}{dt} \quad (3)$$

Equation (3) is exact for reflection of an ideal 1-dimensional strain wave in a long slender bar. This implies: dispersion and attenuation of the propagating stress wave is small, stress wave is a simple 1-D compression/tension wave, the compression wave is perfectly reflected at the accelerometer/bar boundary, and the stress-strain relationship is linearly elastic. These are reasonable assumption given the frequency of interest, the size of the accelerometer, and the diameter of the bar in a typical accelerometer test. Furthermore, at PCB the relationship between strain and velocity is calibrated directly using a laser vibrometer rather than depending on the assumptions inherent in Equation (2).

Typical time waveform of a piezoceramic shock sensor mounted on a Hopkinson bar is shown in Figure 21. Shown here are four reflections of the stress wave scaled to acceleration and integrated to velocity.

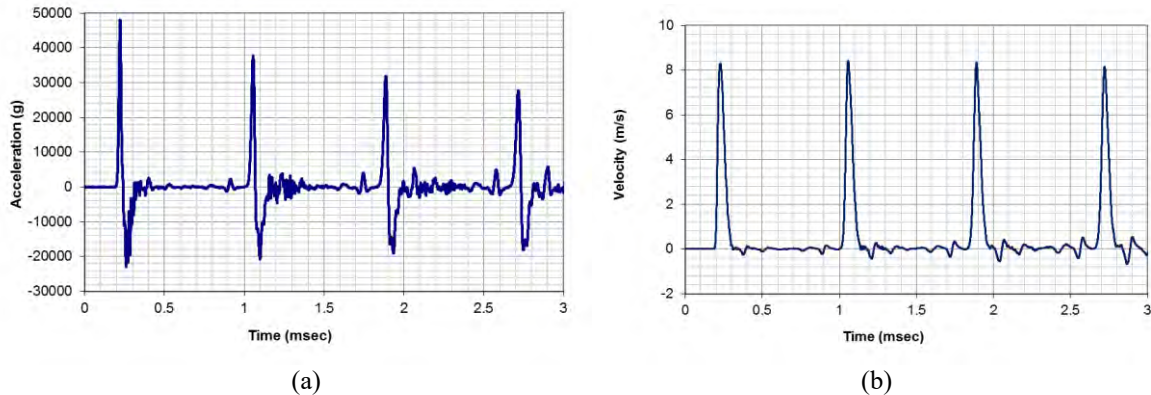


Figure 21: PCB Model 350C21 Output, Acceleration (a) and Integrated Velocity (b), from 50000g Hopkinson Bar Test.

Interpretation of Test Results

In interpreting Hopkinson bar acceptance test data, or any shock data for that matter, it is important to keep in mind that the sensor response depends on the input spectrum. One can have two shock inputs generated by a Hopkinson bar with equal peak accelerations but have very different frequency spectra and damage potential. The sensor response and associated metrics of zero-shift, frequency response, sensitivity, and other parameters depend implicitly on the shape of the shock waveform. Ideally the Hopkinson acceptance test will exercise the sensor through its acceleration range with an acceleration spectrum representative of the field application. And equally important, the waveform must be consistently controlled so that every sensor tested is subject to the same shock conditions. In the Hopkinson bar system, the waveform and peak level is controlled by maintaining control of a number of variables. The projectile material, hardness, diameter, length, and surface geometry have a strong influence on the frequency content. Projectiles must be monitored over time to ensure frequency spectrum does not change with use. Acceleration amplitude is controlled through projectile velocity, which is adjusted through air pressure in the launch tube. The shock amplitude and frequency spectrum cannot be controlled independently. High amplitude impacts are usually associated with higher frequency content. Increased high frequency content at high amplitude can sometime be alleviated through the use of a mitigator (material placed between projectile and bar) or by changing the projectile/bar as amplitude is increased. Lastly, the data window chosen for processing the response will significantly influence the response metrics. Response can be based on a single pulse, a number of reflected pulses, or through the use of a “fly-away” mounting fixture, a portion of the first pulse.

Zero-shift A zero-shift is a change in the sensor’s zero-g bias level while subject to shock. It is arguably the most important metric to be evaluated by the Hopkinson bar test. It could be said that the ability to survive shock and report data without zero-shift is what separates a shock sensor from an “ordinary” vibration accelerometer. Every accelerometer manufactured by PCB that is classified as a shock sensor will undergo testing to demonstrate acceptable zero-shift. For users of shock sensors the potential problem is that small shifts in the zero level will result in large errors when the time record is integrated to velocity or when transformed to a shock response

spectrum. Threshold for acceptable zero-shift is small and is most easily observed by integrating to velocity and a “classic” zero-shift will be easily seen as a ramp in the velocity record. At PCB, acceptable value for zero-shift is an internal metric, but it is very small, and not usually stated in the specification. The value for zero-shift is expressed as the percent change in the bias referenced to the peak acceleration level.

Frequency Response Accelerometer frequency response is usually and most accurately performed using sinusoidal vibration on a shaker against a back-to-back reference. In a shaker frequency response, the sensor is swept through the desired frequency range at relatively low acceleration levels ranging from 1g to 10g. To obtain response while subject to high acceleration levels, shock excitation must be used. A frequency response from the Hopkinson bar is obtained as follows. Accelerometer and strain data from the first pulse are obtained (data from subsequent reflections are ignored) and Fourier transforms are applied. The strain signal (proportional to velocity) is scaled to acceleration (g) in the frequency domain. The accelerometer sensitivity (mV/g) is obtained in the frequency domain as the ratio of the sensor output (Volts) and reference acceleration (g). An example of a shock sensor frequency response is shown in Figure 22. Responses were at obtained 5 shock impact levels from 10,000g to 50,000g.

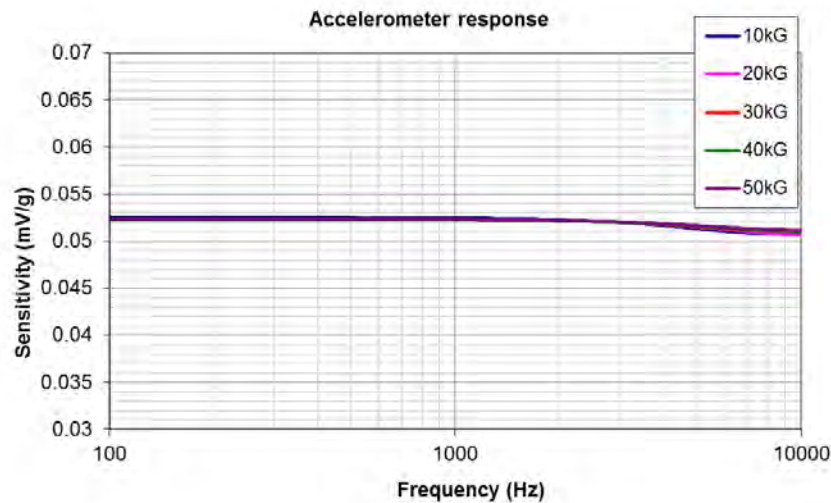


Figure 22: PCB Model 350C21 Piezoceramic Shock Sensor Frequency Response (Response at 5 Levels from 10,000g to 50,000g)

Sensitivity Sensitivity (mV/g) is found by taking the ratio of the sensor-under-test and strain gage reference. This can be performed in the frequency domain as in Figure 22. Or more commonly it is found by peak picking in the time domain. To minimize error when using peak picking methods it is important that the input does not contain high frequency that would excite sensor resonance.

Nonlinearity Nonlinearity is deviation of output from an expected linear input-output relationship. There are two common approaches to specify nonlinearity in shock sensors. Nonlinearity can be specified as the change in sensitivity with acceleration level, e.g. nonlinearity <2.5%/10000g. Alternatively nonlinearity can be expressed as maximum deviation from best fit straight line of the output as the sensor is shocked at 20% intervals up to full scale. For most piezoelectric and piezoresistive shock sensors the nonlinearity is small. An exception is that some older model mechanically isolated piezoelectric shock sensors can exhibit very large nonlinearity. An example of such a sensor is shown Figure 23. Integrated to velocity the time domain signal shows a series of steps which is the result of acceleration sensitivity being different in the positive direction compared to the negative. In the frequency domain two effects of the nonlinearity can be observed. There is increase in sensitivity with g-level and the resonant frequency of the mechanical isolator drops with acceleration level. Piezoelectric shock accelerometers with mechanical isolation can be manufactured with linear response as shown in the example of Figure 24. Here the velocity returns to zero after each impact and the frequency response is consistent with input level. Lastly, Figs. 24a

and 24b show the Hopkinson bar derived velocity and frequency response of a MEMS accelerometer (Figure 25, PCB Model 3501A1260KG). Response is linear in that velocity returns to zero after each impact (Fig 24a) and sensitivity does not change significantly with acceleration level (24b).

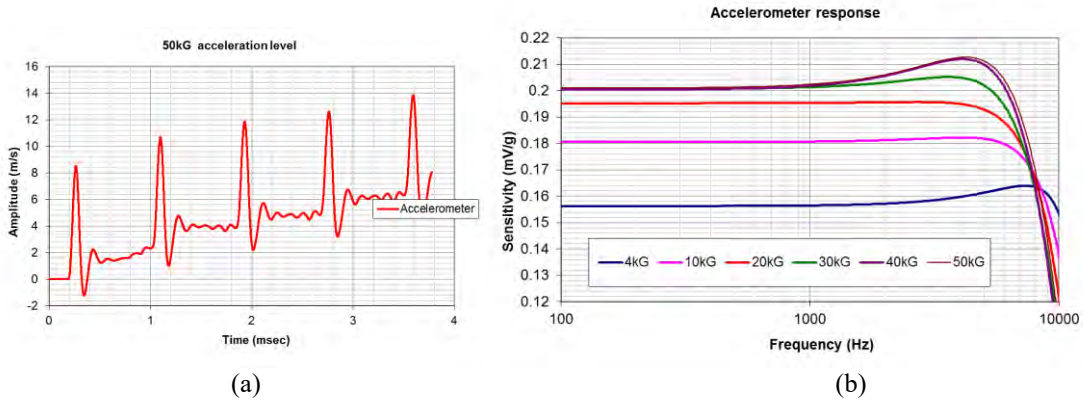


Figure 23: Shock Sensor Nonlinear Response. Integrated signal does not return to zero and shows step-wise behavior (a). Frequency response changes with acceleration input (b). Sensor is competitor's piezoceramic accelerometer with mechanical isolator.

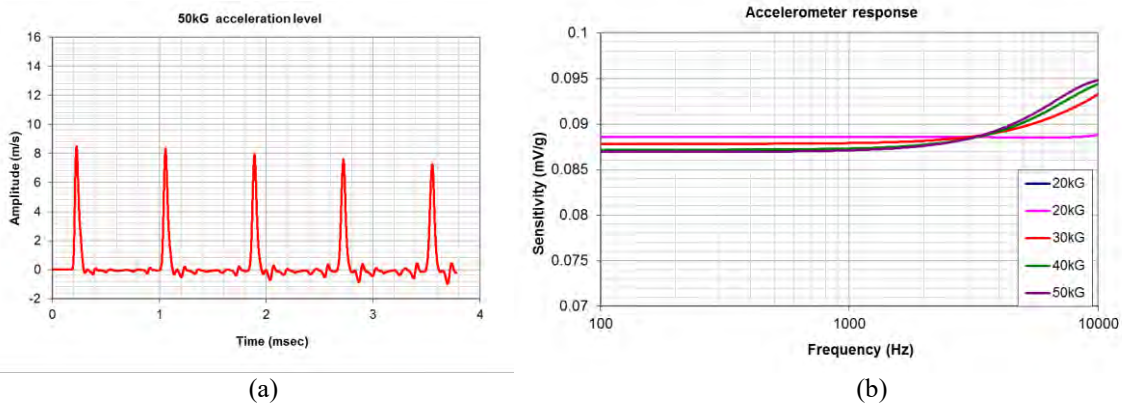


Figure 24: Linear Response from PCB Model 350D02 Having Mechanical Isolation. Velocity returns to zero after each impact (a). Frequency response is consistent with acceleration level (b).

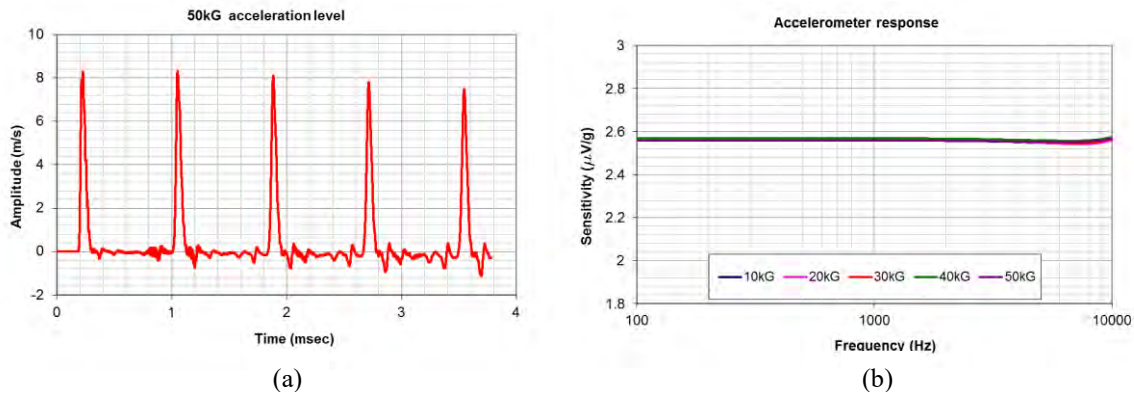


Figure 25: Linear Response from PCB Model 3501A1260KG MEMS Accelerometer: Velocity (a) and Frequency Response (b).

FIELD PERFORMANCE

The preceding discussion has described the development and laboratory evaluation of both mechanically isolated piezoelectric and MEMS accelerometers. Every application that involves severe mechanical shock is different and no single accelerometer solution is best suited for all. When zero-shift of piezoelectric accelerometers occurs, or accelerometer fragility becomes an issue, both of the aforementioned technologies offer a potential solution.

Both mechanically isolated piezoelectric and MEMS accelerometers have been successfully used to characterize severe mechanical shock such as described in the Introduction to this paper. Case studies will now be presented illustrating successful performance of both of these technologies under conditions of severe mechanical shock.

Penetration Tests with MEMS PR Accelerometers

Projectile penetration testing was performed at the US Army's Engineering Research and Development Laboratory (ERDC) in Vicksburg, MS. Two ruggedized data recorders, each with 3-channels capability, sampled the outputs of two triaxial configurations of both the lightly damped PCB Model 3991 and the Legacy Sensor. After the signals passed through 10kHz anti-alias filters the sampling rate was 75kHz. The penetrator was launched at ~1440 ft/s into unreinforced, unconfined, 6000 psi concrete. It stopped after 33 inches of penetration and experiencing a peak deceleration of 15kG. The physical configuration is shown in Figure 26.

The waveforms at upper left and right of Figure 27 show results from the axially directed sensors during launch and impact, respectively. The transverse data for the launch are portrayed in the lower graphs, showing the largest rattle when leaving the barrel. Both Legacy Sensors in the transverse directions display zero-shift. [10] The erroneous data may be caused from improper mounting such as a loose mounting screw, lack of epoxy, or cable motion. All of these mounting errors can lead to post-shock base strain that manifests itself as zero-shift.

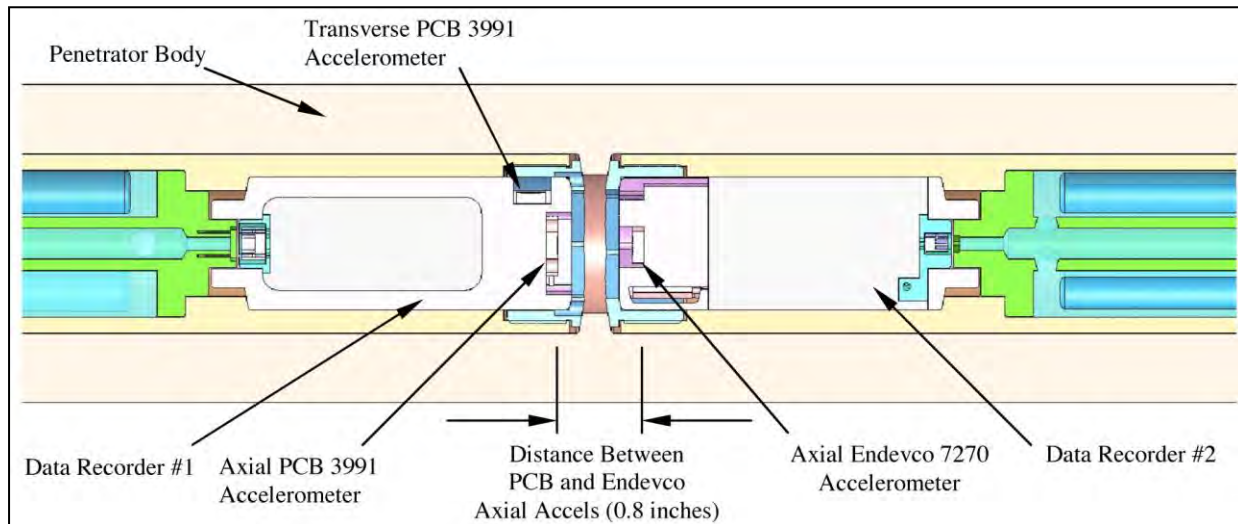


Figure 26: Placement of Sensors and Recorders. [10]

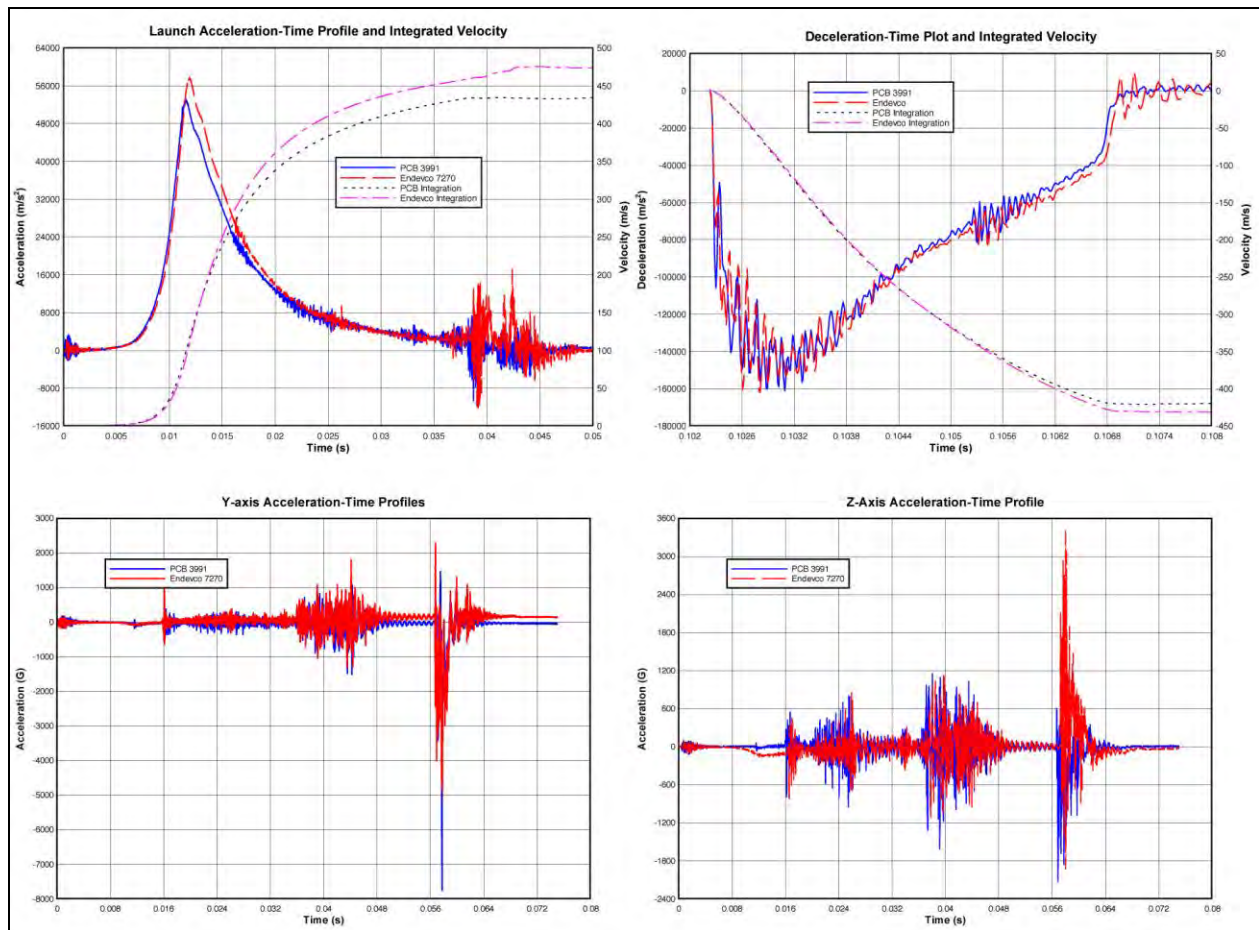


Figure 27: Comparative Waveforms of Triaxial Configured Sensors.

Pyroshock Tests Comparing Mechanically Isolated Piezoelectric and MEMS Accelerometers

When working with live pyrotechnics on full-scale test articles is not practical, other methods to simulate defined shock response spectra have been developed. Pyroshock simulation techniques may be arranged into two categories: mechanically excited and pyrotechnically excited. Short duration mechanical impacts on structures can produce a response similar to that produced by a pyrotechnic source. Mechanically excited simulations allow control of dominant frequencies up to about 10kHz. For tests that require frequency content perhaps to 20kHz, a pyrotechnically excited technique is usually more appropriate. In either technique, the use of piezoelectric shock accelerometers that lack mechanical isolation can create measurement errors in the velocity integral and SRS.

A question that always challenges the test engineer is which type measurement sensor to select? Three sensors were compared in this test; mechanically isolated and electrically filtered piezoelectric 50KG range PCB Model 350B02, 2% damped PCB MEMS 60KG range Model 3501A1260KG, and the undamped MEMS Legacy Sensor in a 60KG range. Figure 28a shows the location of the three sensors subject to a simulated pyroshock event.

The impact to the subject test structure, shown in Figure 28b, was achieved by a modified direct fastening powder actuated system, which is used to qualify components for spacecraft applications.



Figure 28a: Test arrangement of shock sensors.



Figure 28b: Fastener attachment during test.

Figure 28: Metal Impact Test

The mechanically isolated piezoelectric, damped MEMS and un-damped Legacy Sensor produced nearly equivalent test results. In this test it was shown that all three can potentially be used in some severe mechanical shock applications, including pyroshock. Figures 29, 30 and 31 document the time response and the SRS of the tested accelerometers. As Figure 32 shows, all three sensor types show close correlation in their SRS responses up to 20kHz. The case demonstrates that under controlled conditions, all three sensing technologies are suitable for the severe mechanical shock measurement.

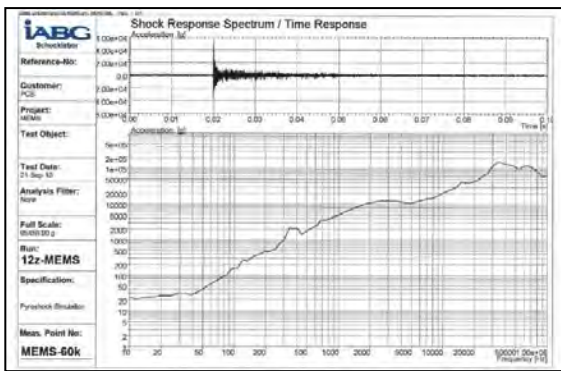


Figure 29: PCB 3501A1260KG DC Coupled, Time and SRS

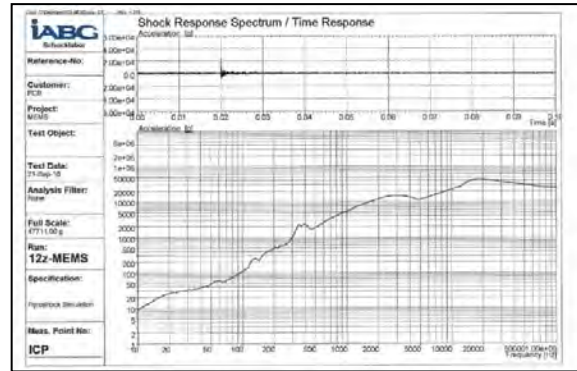


Figure 30: PCB 350B02 ICP[®] Coupled, Time and SRS

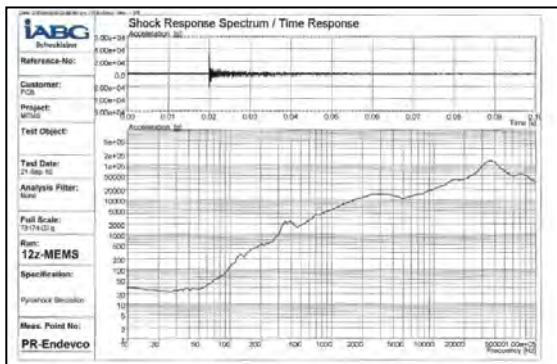


Figure 31: Legacy Sensor DC coupled, time and SRS

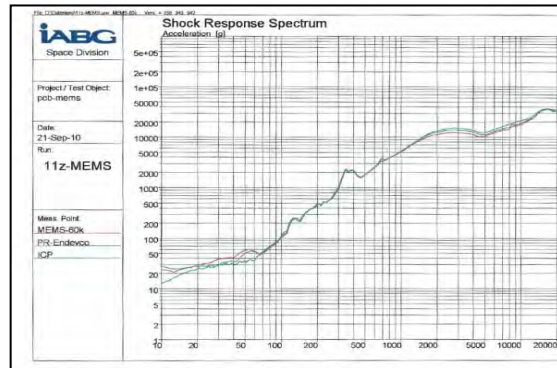


Figure 32: SRS Overlay of All Three Sensors

Pyroshock Tests with Mechanically Isolated and Non-isolated Piezoelectric Accelerometers

A pyroshock test pulse was performed on a tunable beam at MGA Research Corp., Akron, NY. Testing compared a mechanically isolated piezoelectric ceramic PCB 350C02 (50KG) and a non-isolated piezoelectric ceramic PCB 350B21 (100KG) shock accelerometer. The cantilever beam, Figure 33a, was clamped at one end of a massive base structure that imposed a nearly fixed-end condition on the beam. The shock accelerometers were mounted to the beam on a test plate located 3 inches apart and centered on the impact point. The sensors were impacted from below the beam by firing a projectile from an air gun beneath the beam. A close up of sensor installation is shown in Figure 33b.

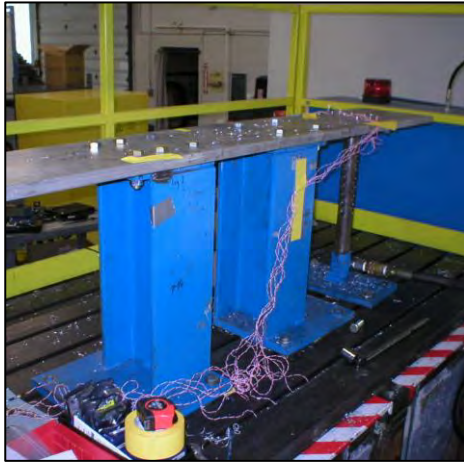


Figure 33a: Pyroshock Tunable Beam

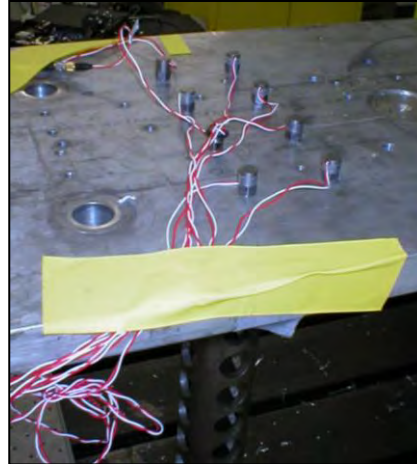


Figure 33b: Sensor Installation on Beam

Figure 33: Pyroshock Test Setup at MGA [11]

Figure 34 shows the shock acceleration time history. The 350C02 mechanically isolated piezoelectric accelerometer, considered the reference sensor for this test, shows a peak shock level of approximately 2400 g's. The non-isolated accelerometer 350B21 produced peak levels up to 7000 g's. The differences stem from the high Q factor at resonance for the 350B21. The two sensors differ in their waveform shape somewhat as the sensors were not collocated. The benefit of mechanical isolation is clear in terms of removing high Q factor resonant amplification and the related measurement errors of overstating the peak acceleration of a shock pulse.

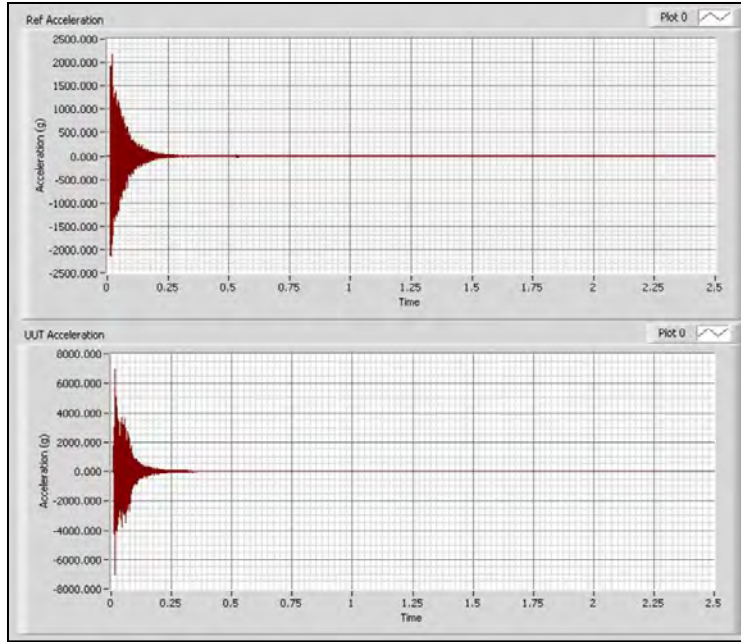


Figure 34: Acceleration Data from Tunable Beam Test, 350C02 (top) and 350B21 (bottom)

The associated SRSs in Figure 35 are rich with high frequency content, evident by its plateau not occurring until near 10 kHz. The ideal max positive and negative SRS that results from the shock pulse should be symmetrical. Evaluating the SRS data for the 350C02, good symmetry is observed across the entire frequency range of 10 Hz to 10 kHz. The non-isolated PCB 350B21 is producing an offset (zero shift) as indicated by the rise in the SRS below 100 Hz. The isolated piezoelectric appears to provides very good results with positive and negative symmetry and we may conclude that isolation is required in piezoelectric accelerometers for severe mechanical shock.

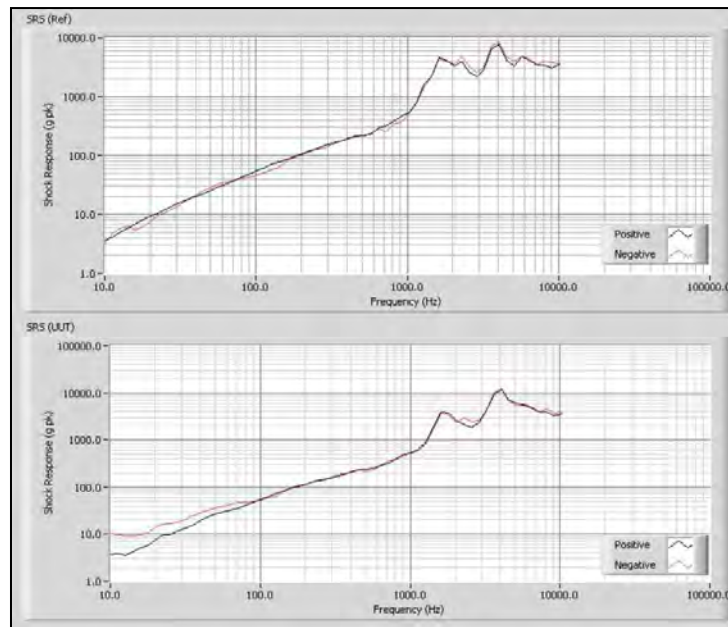


Figure 35: SRS Data from Tunable Beam Test, 350C02 (top) and 350B21 (bottom)

All of the aforementioned sensors have displayed the capability to measure severe mechanical shock. The data sets provided from real world applications show successful application of isolated and LP filtered piezoelectric accelerometers as well as MEMS accelerometers. The successful inclusion of a small amount of damping in MEMS accelerometers is improving their performance in severe shock environments. No two technologies will perform the same in every application due to the uniqueness of the individual environments. In addition to considering the basic accelerometer sensing technology, in every application detailed attention has to be paid to proper accelerometer mounting, cable/connector interface and assembly, cable tie-down, and more before a successful measurement can be initiated through the remainder of the measurement system.

CONCLUSIONS

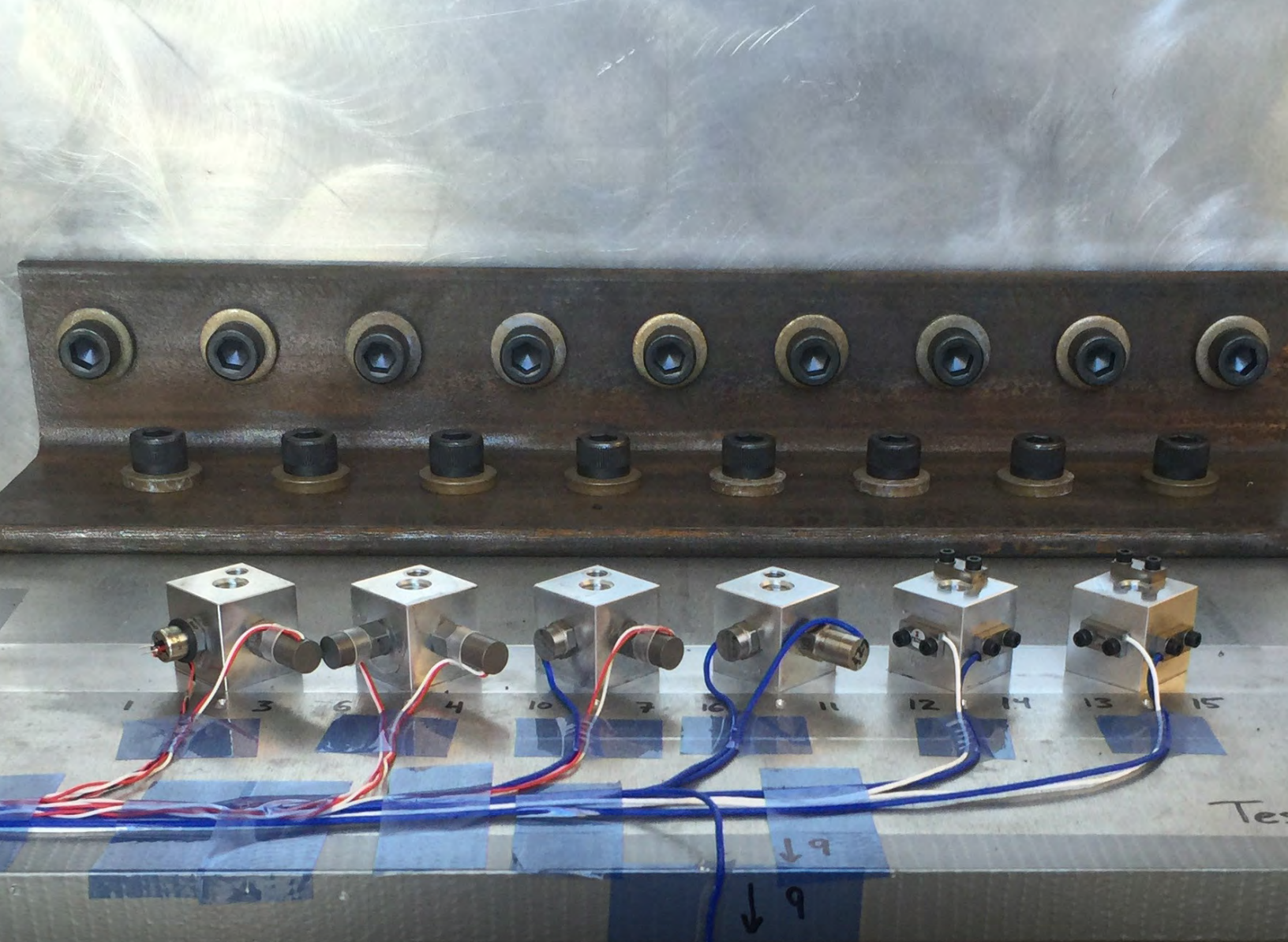
The measurement of severe mechanical shock has many associated challenges.

- The mechanical shock environment typically has significant motion in 6-degrees of freedom.
 - In early time (near $t = 0$) this motion is incapable of adequate modeling and therefore lacks definition.
- Extremely high frequencies accompany severe mechanical shock, and these high frequencies typically excite the resonant frequency of the accelerometer.
 - As a result, the accelerometer can easily be over ranged or driven nonlinear due to this resonance excitation.
- In highly energetic environments, accelerometers can be subjected to significant levels of kinetic energy.
- Base strain can be a problematic, extraneous input to the accelerometer.
 - Other deleterious environments may co-exist (thermal transients, ionized gases, etc.).
- Cable induced noise is always a potential concern.
- Over the years, research and experience has documented that under severe mechanical shock loading ferroelectric ceramic accelerometers often display a baseline shift or offset from their initial zero at shock termination.
 - Mechanical isolation of ferroelectric ceramic accelerometers, coupled with an internal 2-pole filter available in an ICP® circuit, is allowing piezoelectric accelerometers to operate successfully at higher G-levels than were previously achievable.
 - Good design practices are allowing their elastomeric isolation materials to perform in a dynamically linear fashion within the accelerometers.
- As an alternative technology to piezoelectric accelerometers, a new generation of MEMS shock accelerometers has been evolved. As opposed to existing legacy MEMS sensors, these designs incorporate:
 - squeeze film damping,
 - over range stops, and
 - hermetic protection.
- In order to investigate their performance, accelerometers designed to measure severe mechanical shock are subjected to very high acceleration levels on a Hopkinson Bar. Parameters evaluated include zero-shift, shock survivability, and linearity.
- In some situations, the frequency environments associated with severe mechanical shock may be so expansive, the acceleration levels so high, or the other directional inputs so severe that successful measurements simply cannot be obtained. In addition, there is no single accelerometer design that is a “magic bullet” optimum for every measurement challenge
 - *Advances in state of the art accelerometer design have resulted in improved technology options for severe mechanical shock. These technologies have been shown to be raising the limits as to the types and levels of accelerations that can be successfully measured.*

REFERENCES

[1] MIL-STD-810G, Department of Defense Test Method Standard: Environmental Engineering Considerations and Laboratory Tests, October 31, 2008.

- [2] IEST-RP-DTE032, Pyroshock Testing Techniques, October 2009.
- [3] NASA-STD-7003, Pyroshock Test Criteria, December 20, 2011.
- [4] Walter, Patrick L. "Lessons Learned in Applying Accelerometers to Nuclear Effects Testing", *The Shock and Vibration Digest*, Volume 15, Number 6, IOS Press, November 2008.
- [5] Plumlee, Ralph H., "Zero-Shift in Piezoelectric Accelerometers," Sandia National Laboratories Research Report, SC-RR-70-755, March 1971.
- [6] Dodson, Jacob C., Coker, Jordan, Glikin, Neil, Wolfson, Janet C., Foley, Jason R., "Energy Transmission Across Threaded Preloaded Interfaces", Proceedings 83rd Shock and Vibration Symposium (SAVE), New Orleans, LA, Nov 4-8, 2012.
- [7] Sill, R, "Shock Calibration of Accelerometers at Amplitude to 100,000g using Compression Waves", *Proceeding of the 29th International Instrument Symposium*, Albuquerque, NM, pp. 503-516, 1983.
- [8] Dosch, Jeffrey, Jin L, "Hopkinson Bar Acceptance Testing for Shock Accelerometers", *Sound and Vibration*, vol. 33 [2], pp. 16-21, February 1999.
- [9] Davies, R. "A Critical Study of the Hopkinson Pressure Bar," *Philosophical Transaction, Series A*. Royal Society of London, Vol 240, pp 352-375, 1948.
- [10] Sill, R. "Field Evaluations of a Damped MEMS Shock Sensor," 79th Shock and Vibration Symposium, Orlando, 2008.
- [11] Photo courtesy of MGA Research Corp., Akron, NY.



WHITE PAPER #60

This WP details accelerometer evaluation performed by PCB staff and consultants in a true pyro environment. Accelerations on the order of 15,000 G peak to 10,000 Hz were measured with indicated frequency content extending past 30 KHz. The stimuli were omnidirectional with regard to the sensing axis of the accelerometers under evaluation. Five tests on eight models of accelerometers were performed, and 11 channels of data were successfully recorded on every test. Among the models tested were those evaluated in WP45. Results were very good. Instrumentation system configuration used in the testing is presented along with the analysis performed.



Evaluation of Accelerometers for Pyroshock Performance in a Harsh Field Environment

Written By

Anthony Agnello & Robert Sill PCB Piezotronics, Inc., Depew, NY, USA
Patrick Walter Texas Christian University/PCB Consultant, Fort Worth, TX, USA
Strether Smith Independent Consultant, Cupertino, CA, USA

An evaluation of the performance of eight (8) different models of accelerometers in severe pyroshock environments has been planned, executed, and analyzed. These experiments showed that modern versions of accelerometers using both Mechanically Isolated Electrically Filtered Piezoelectric (MIEF-IEPE) and Micro Electromechanical Systems (MEMS) technology provided excellent results for excitations encountered in high-level pyrotechnic testing.

**Agnello, Anthony; Sill, Robert; Smith, Strether;
and Walter, Patrick**

Evaluation of Accelerometers for Pyroshock Performance in a Harsh Field Environment

Anthony Agnello and Robert Sill
PCB Piezotronics, Inc.
Depew, NY 14043

Patrick Walter
Texas Christian University/PCB Consultant
Fort Worth, TX 76129

Strether Smith
Independent Consultant
Cupertino, CA 95014

A series of experiments has been performed to evaluate the performance of eleven accelerometers commonly used in high level pyrotechnic shock tests. They included both mechanically isolated and electronically filtered piezoelectric and silicon (MEMS) based devices manufactured by Meggitt's Endevco Corporation and PCB Piezotronics. All had a range of 50KG or higher.

Five tests at different levels (quantity of explosive) emulated some of the more severe amplitude and frequency excitation that might be expected in laboratory-or field-based experiments. The higher level tests produced significant plastic deformation in the fixture. Accelerations on the order of 15 KG peak to 10,000 Hz were measured with indicated frequency content extending past 30 KHz.

The majority of the modern accelerometers performed far better than the authors expected. All exhibited some zero shift, which averaged between 0.02% and 0.25% of the peak-peak shock level accelerometer for the five tests. One outlier had an average offset of 0.94%. However, even these small errors severely compromised the SRS calculations at lower frequencies.

The technique used to reduce the effect of these offset errors is also presented to validate test results.

INTRODUCTION

If data quality is poor when measuring mechanical shock, it is common to blame the accelerometer. However, there are other contributors to this lack of success that need to be considered. These include: poor mounting surface for the accelerometer, improper accelerometer coupling (surface finish, torque, grease), large transverse acceleration inputs, cable issues (cable tie down, shielding, bend radii, stiffness, connector pin chatter, etc.), improper signal conditioning and data acquisition (over ranging, slew rate limiting, signal/noise, improper grounding, wrong input/output characteristics, ...), extraneous environmental inputs coupling into the measurement system, and many more. In addition, at times the environment that is attempted to be measured may be just too harsh for the accelerometer to operate in reliably.

During development testing of high-G accelerometers the main evaluation tool used by the accelerometer manufacturer is the Hopkinson Bar¹. Testing performed on this bar can achieve levels of over 100 KG and frequencies above 10 KHz, however, by design the motion it produces is essentially 1-dimensional. Comparative testing of a group of severe shock (high-G) accelerometers, primarily using a Hopkinson Bar, has been reported previously².

This work documents field testing performed at National Test Systems (NTS), Santa Clarita, CA. The test environment provided, described in detail below, was a series of explosive pyrotechnic events.

Two accelerometers types were tested:

1. Mechanically Isolated and Electrical Filtered Piezoelectric technology (denoted MIEF- IEPE) and
2. Micro ElectroMechanical Systems technology (denoted MEMS).

The MIEF- IEPE accelerometers had an internal elastomeric matrix to isolate the piezoelectric element from the high stresses encountered at their resonance excitation. An internal electrical filter reduced the effects of this isolation on frequency response up to and including 10 KHz.

The MEMS accelerometers had sculptured silicon dice manufactured with precision tolerances to effect over range stops and provide a small amount of damping (0.02 to 0.04 typical). They had nominal resonances of approximately 150 KHz. The one exception was the Model 7270, which had a damping ratio well below 0.01 and no mechanical stops. This was a byproduct of its resonance being approximately 600 KHz.

Reference 2 provides a detailed description of both technologies.

Both accelerometer types are referenced as those suited for pyroshock measurement in MIL STD 810G³.

In the following sequential sections of this paper are: (1) a description of the test environment, (2) identification of the accelerometer models tested, (3) a description of the instrumentation system, (4) top-level observations based on the accelerometer time-histories, (5) a description of the analysis performed with results, and (6) conclusions based on this analysis.

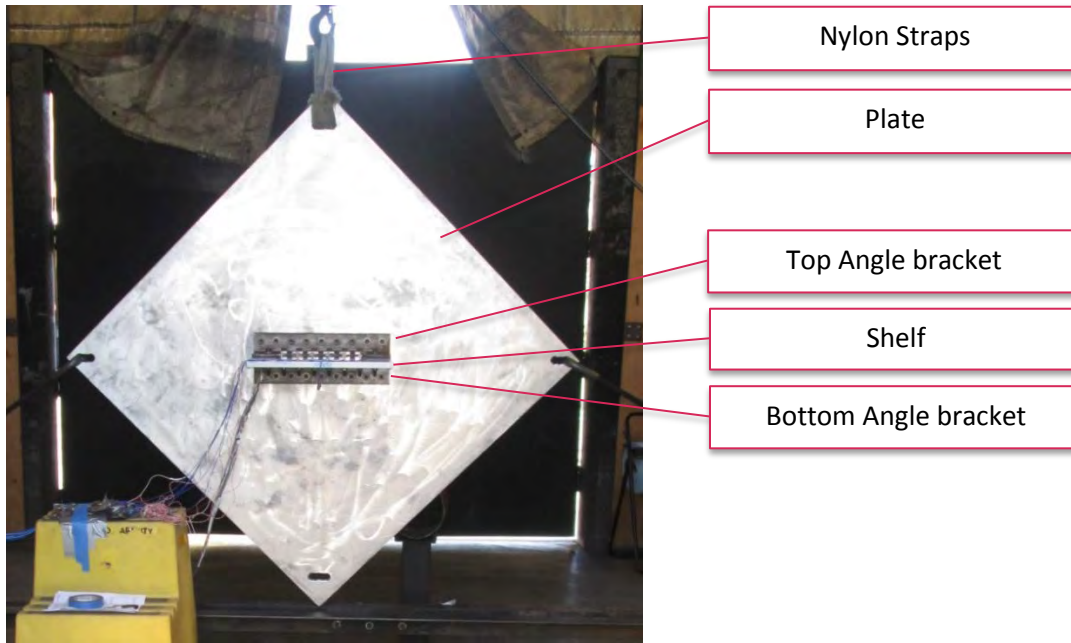
Test Environment

The 5 tests conducted (identified as Tests 2 - 6 since Test 1 was a simple hammer tap performed to verify setup) were pyrotechnic shocks using increasing levels of explosive.

The test fixture is shown in Figure 1. The primary structure was a *48 x 48 x 1 inch 6061* aluminum plate shown suspended with heavy nylon straps in the corners. An *18 x 12 x 0.75 inch 6061* aluminum shelf was mounted on the front side of the plate using two *3/8"* thick steel angle brackets. Each angle bracket was secured to the plate using nine *3/8-16* grade 8 bolts. The shelf was secured through both angle brackets using eight *3/8-16* grade 8 bolts. Bolt torque was checked before and after each test to assure consistency.

The accelerometers were mounted on 6061 aluminum 1" cube adaptor blocks, that were also secured to the shelf using *3/8-16* grade 8 bolts. The accelerometers were torqued before each test and checked afterwards against recommended values. The six blocks were oriented 45° normal to the shock axis in an attempt to keep the X & Y inputs approximately equivalent (Figure 2). The intent of this mounting orientation was to assess each accelerometer's performance in its sensing axis while it concurrently encountering a significant transverse acceleration in this same X-Y plane. Measurements discussed later also showed a significant Z-axis acceleration occurring.

The mounting surfaces of the plate and triaxial adaptor blocks were machined with a roughness of ≤ 8 Ra and a flatness of ≤ 0.001 ". Coupling grease was also applied to these surfaces to obtain optimal contact and shock transmissibility through each surface.



Nylon Straps

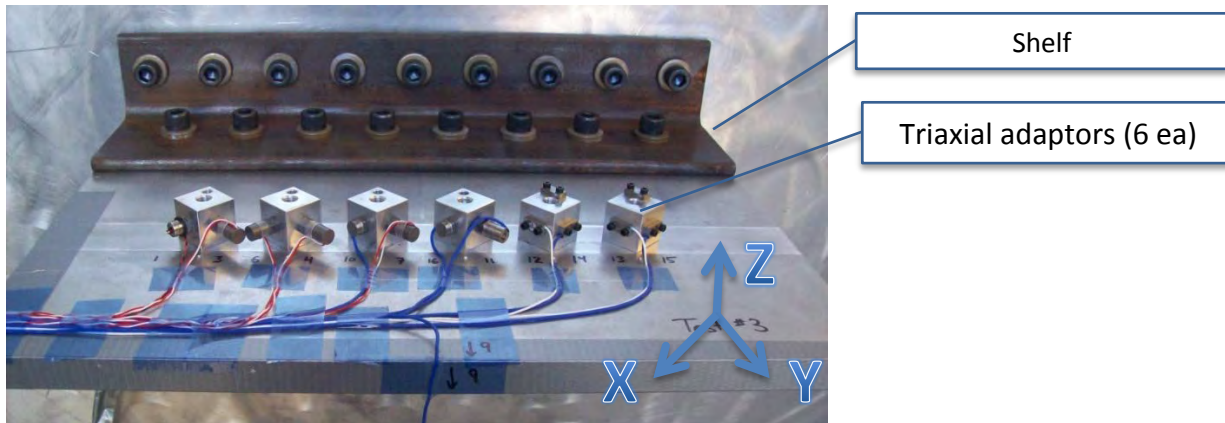
Plate

Top Angle bracket

Shelf

Bottom Angle bracket

Figure 1. Test Setup



Shelf

Triaxial adaptors (6 ea)

Figure 2. Mounting Blocks 1-6 (moving left to right) with Test Accelerometers (note: Z-axis accelerometers shown here were used in Test 6 only)

The explosives were mounted in an isosceles triangle configuration (Figure 3) on the back side of the plate, equal distances from the location of the center of the shelf. The excitation varied from three 2' coils of 15 grain/foot detonating cord to three 25' coils of 18 grain/foot detonating cord in five tests.

- Test 2: Three 2' coils of 15 grain/foot detonating cord
- Test 3: Three 5' coils of 15 grain/foot detonating cord
- Test 4: Three 10' coils of 15 grain/foot detonating cord
- Test 5: Three 20' coils of 15 grain/foot detonating cord
- Test 6: Three 25' coils of 18 grain/foot detonating cord

Increased explosive charge did not result in a proportional increase in shock amplitude. Test 6, consisting of three 25' coils of 18 grain/foot detonating cord, reached nominal peak acceleration amplitudes of only a factor of three (3) relative to Test 2. Two reasons are opined for this lack of proportionality. First, the explosive energy is largely

reflected from the rear surface of the plate. Second, with increased explosive quantity more energy was absorbed by inelastic plate deformation. Figure 4 is a picture (typical) of the plate deformation in front of one of the three coils of explosive after Test 6. By comparison, Test 2 resulted in almost no deformation to this same plate.

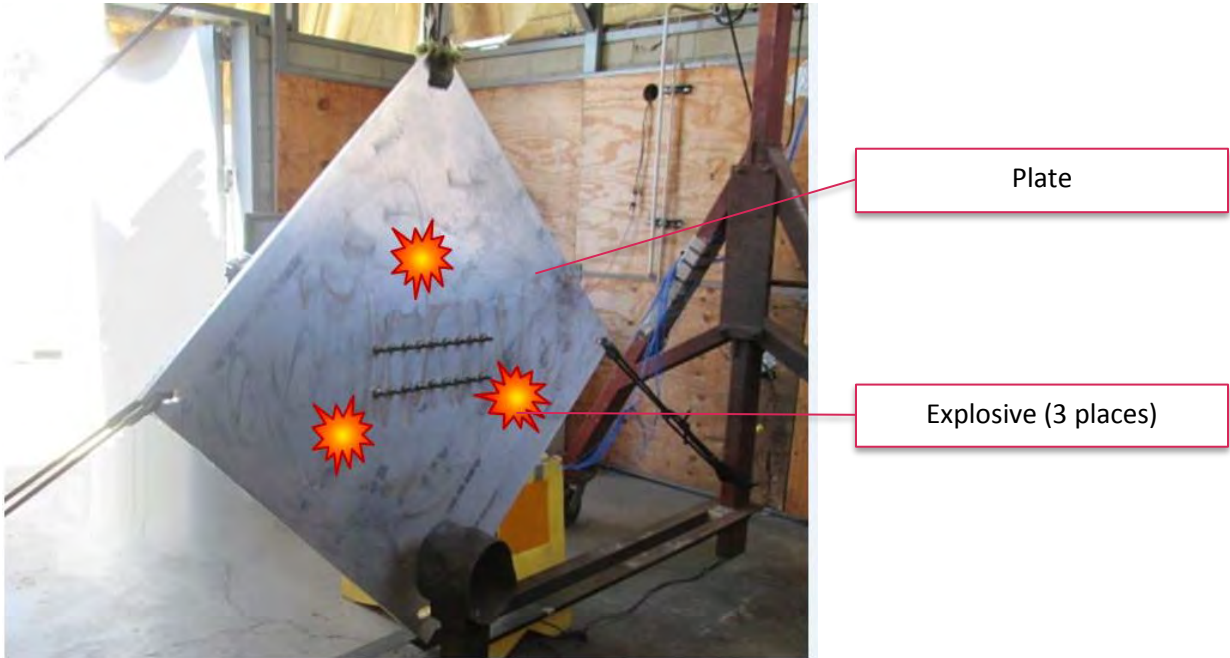


Figure 3. Explosive Loading Configuration Relative to Plate/Shelf

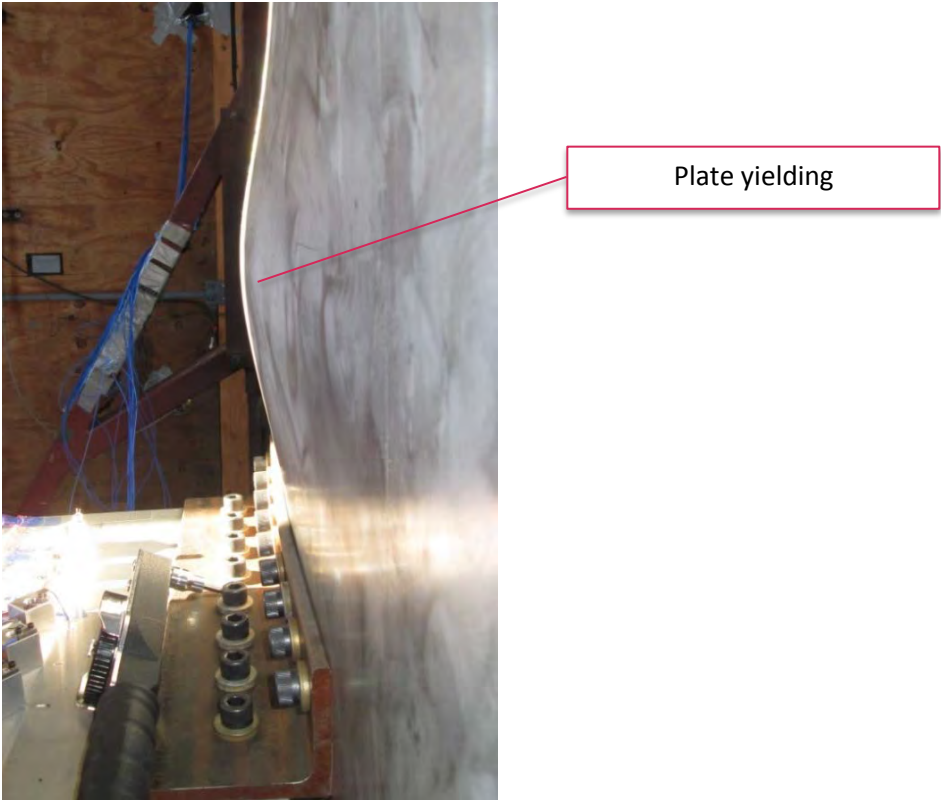


Figure 4. Local Plate Yielding

All of the accelerometers compared during these tests are listed below. They were randomly selected production models. All of them are commercially marketed for pyroshock measurement as defined in MIL STD 810G³.

For Tests 2 through 5 only the X (denoted Left) and Y (denoted Right) orientations on each block were actively occupied. Each block had 2 accelerometers located on it whose comparison was of particular interest to those supporting the testing. Figure 2, as noted, portrays the configuration for Test 6 during which additional active accelerometers were placed on the blocks in the Z (Vertical) direction. Recall Test 6 possessed the largest quantity of explosive loading. The below table details accelerometer placement for Test 2. In Test 3 the Block 2 Y accelerometer was switched to the Block 2 X position and the Y position then became occupied by a PCB Model 350B01. This X -Y configuration remained fixed for the remainder of all testing, i.e., Tests 3-6. Block 4 Y was occupied by a prototype accelerometer not commercially available so its results are not portrayed.

Manufacturer	Model	S/N	Technology	Block/Location	Channel Number
ENDEVCO	7255A	CF75	ISOL PE	1/Left	1
PCB	350B01	52322	ISOL PE	1/Right	3
ENDEVCO	7255A	CF78	ISOL PE	2/Left	2
PCB	350D02	50292	ISOL PE		6
PCB	350D02	50292	ISOL PE	2/Right	6
PCB	350B01	52323	ISOL PE		4
PCB	3501B	5805	MEMS	3/Left	10
PCB	350D02	50293	ISOL PE	3/Right	7
PCB	3501B	5806	MEMS	4/Left	16
N/A	N/A	N/A	N/A	4/Right	N/A
ENDEVCO	7270A	40423	MEMS	5/Left	12
PCB	3991B	3823	MEMS	5/Right	14
ENDEVCO	7280A	41800	MEMS	6/Left	13
PCB	3991B	3824	MEMS	6/Right	15

Note:

*Models 7255, 350D02, 350B01 are MIEF- IEPE technology
Models 3501B, 3991, 7270, 7280 are MEMS technology*

Prior to any pyro testing, the sensitivities of all of the accelerometers (including the effect of their 40' cables) were determined through a precise calibration process and these values were used in testing.

Instrumentation System Configuration

As noted, 40 feet of cable was required for each accelerometer to reach from the test bay to the test control and recording room. Each accelerometer type (MIEF-IEPE and MEMS) required different cables. After the signal from an accelerometer was transmitted through its cable, it passed through an appropriate amplifier and low pass filter and terminated into a data acquisition system.

Due to cable length the cable capacitance added additional filtering. This additional filtering was measured and considered in the design of the instrumentation system.

During testing, the cables were secured and adequate strain relief was provided (Figure 2). This assured the integrity of the cable and minimized the generation of any cable noise. Placebo accelerometers were also mounted, powered, and monitored on the test shelf to measure the instrumentation system noise floor.

When mounted, all MIEF- IEPE accelerometers were torqued to 4 ft lbs and all MEMS accelerometers were torqued to 8 in lbs. Mounting block surface preparation and cable tie down were described previously. Both accelerometer types had nominally flat frequency response to 10 KHz.

Above 10 KHz the frequency response of the isolated and internally filtered piezoelectric technologies is limited by the combination of their contained elastomeric material and their 2-pole internal electrical filter. 10 ma of drive current was provided to this accelerometer type to power the internal electronics and assure there were no additional frequency limitations below 10 KHz due to cable capacitance.

A PCB Y481A03 system was used to condition the isolated/filtered piezoelectric devices. MEMS accelerometers were conditioned with a PCB 482C27.

ICP©: PCB Y481A03 16



MEMS: PCB 482C27



Figure 5: Respective Signal Conditioning Used in all Calibration/Testing

Both signal conditioners had flat frequency response to 100 KHz. They were operated in the ac couple mode. For the MIEF- IEPE accelerometers the ac coupling removed the internal accelerometer bias voltage. The accelerometers themselves were -3 dB attenuated at nominally 2 Hz. For the MEMS accelerometers the ac coupling

removed bridge offset to enable symmetric operation around 0 volts. The ac coupling in both conditioners was low enough in frequency to assure data integrity above 10 Hz. Full scale amplifier output for both was 20 V pk - pk.

The conditioner gain was set to provide an expected maximum full scale signal of 4 V pk - pk (2.0 V 0 - pk). The gains were set to provide 7 KG 0 - pk full scale for Test 2, 14 KG for Test 3, and 21 KG for Tests 4, 5, and 6.

These ranges were conservatively selected to cover any expected transducer resonant response without amplifier saturation. Maximum signal full scale level recorded up to 10 KHz (Test 6) was nominally 15 KG. This level provided assurance that all accelerometers and analog signal conditioning operated within their linear range.

To allow direct comparison of accelerometer performance between types and models all signals needed to be frequency constrained to 10 KHz. The amplifier outputs were input to a Precision Filters PF-1UA-16FA-HP4F/LP4FP-Z low-pass 4-pole filter in "Pulse" mode. This filter provided excellent phase linearity and maintained amplitude response flat within 5% to 10 KHz. Signal content is attenuated by 95% (~ 26 dB at 94 KHz). This filter, plus filtering occurring due to capacitance in the cable run from the MEMS, attenuated any response at the resonances of the MEMS accelerometers by more than 50 dB. Thus, both MEMS and MIEF-IEPE channels could be ranged the same in terms of V/G.

The resulting signal was digitized with a DSPCon Piranha III data acquisition system. This system digitized the signal with a resolution of 16 bits over a range of +/- 2.5 volts and sampled at a rate of 1.2 million samples/second. Signal attenuation at the Nyquist frequency was so great as to eliminate any aliasing considerations. *In 2 instances the data acquisition system front end over ranged slightly and these records are identified and were processed but not evaluated.*

Macroscopic Data Observations in the Time Domain

This test provided a unique opportunity to compare a variety of sensor designs under crafted explosive pyrotechnic conditions. The following is provided as a global overview before a more intense data examination.

The time-domain plots when overlaying all sensors in each of the tests show a surprising degree of envelope uniformity. Viewed at high time resolution, however, the actual lack of correlation, and the difference between the responses of the various designs and locations is apparent. An example is shown in a view of the first 500 microseconds of Test #2 in Figure 6.

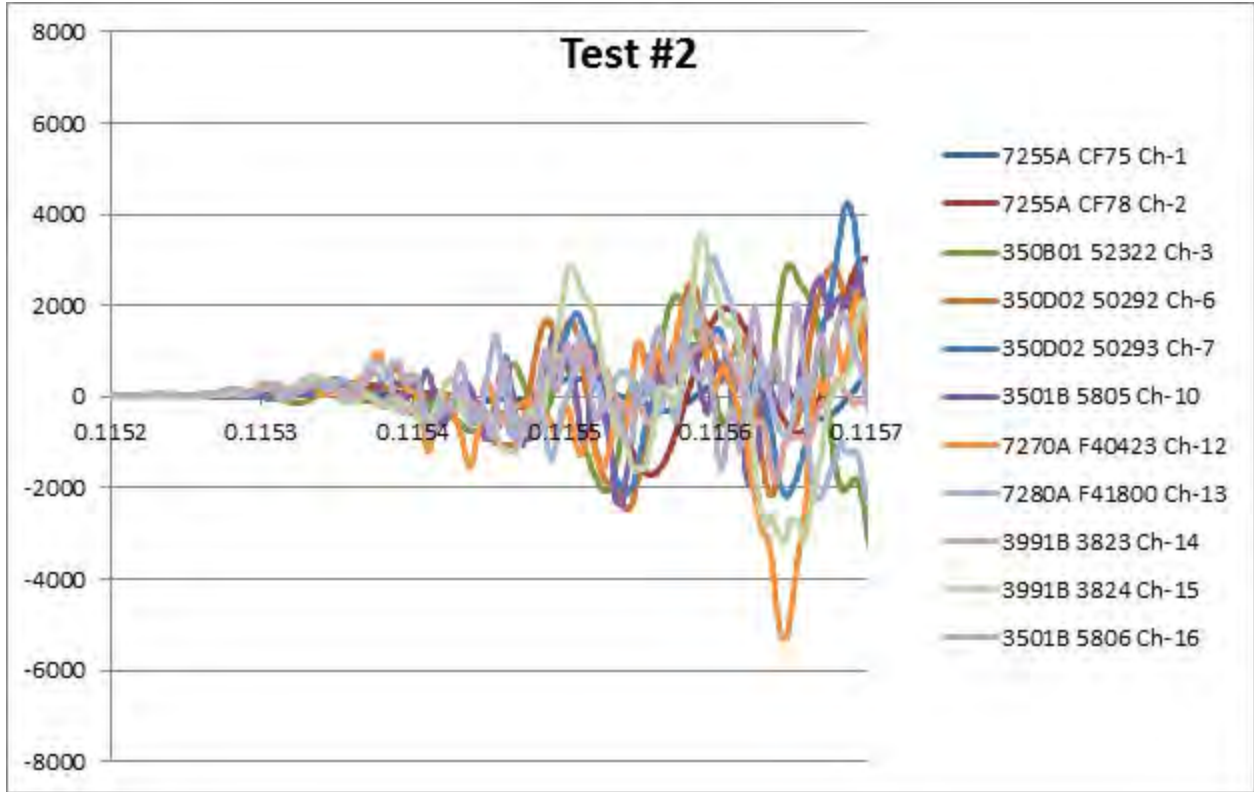


Figure 6: Initial 500 microseconds of Test #2 (G vs. time)

Figure 7 shows the results of averaging the left (X) and right (Y)-facing faces of the 45-degree angled blocks. During Test 6 additional sensors were attached on the tops of blocks (Z-axis), with sensitive axes normal to the plate. The average of the Z axis channels was very similar to the average of the Y axis for Test 6 (*the points are on top of one another*). Figure 7 provides an indication of the severity of the testing as suggested by the omnidirectional nature of the shock inputs encountered by the accelerometers.

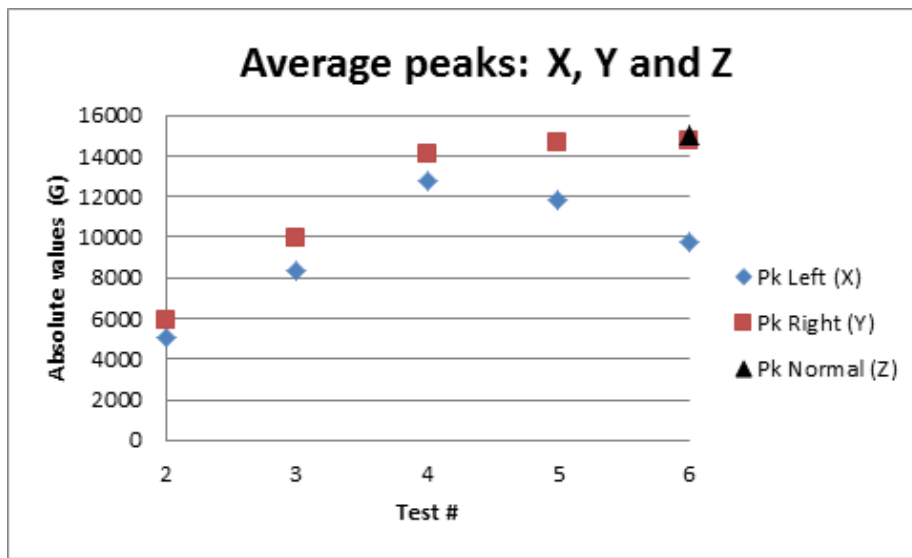


Figure 7: Averages of Peaks in the Three Axes (G vs. time)

Figures 8, 9, 10, 11, and 13 show general conformance of responses between accelerometers/locations for individual tests.

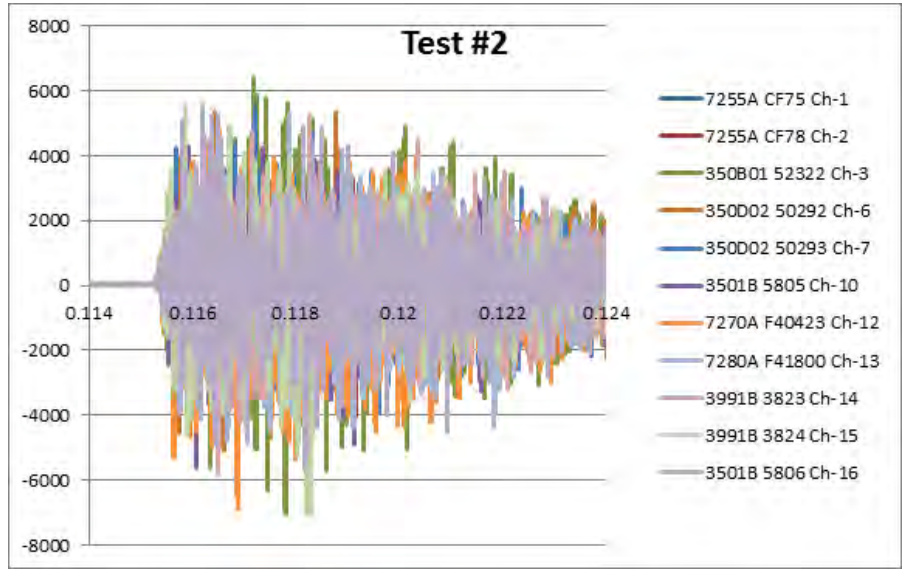


Figure 8: Time History of all Channels for Test #2 (G vs. time)

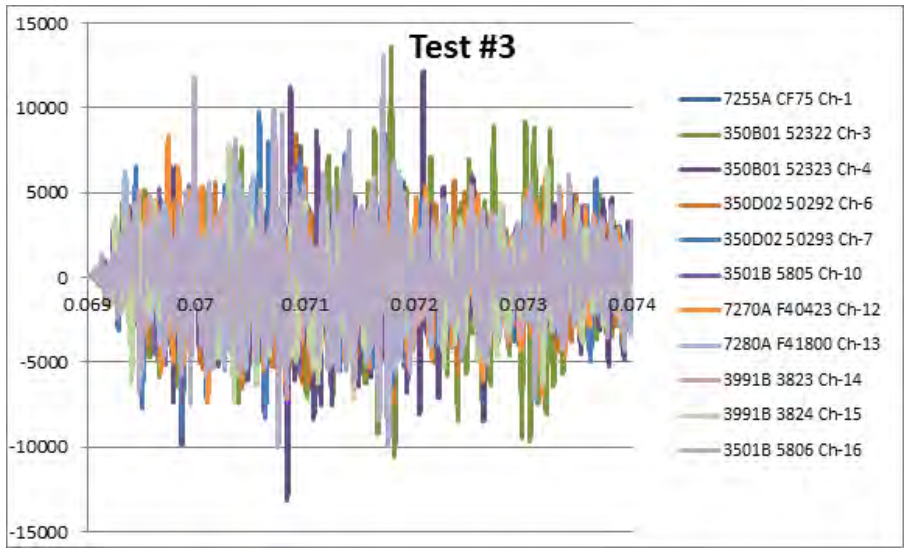


Figure 9: Time History of all Channels for Test #3 (G vs. time).

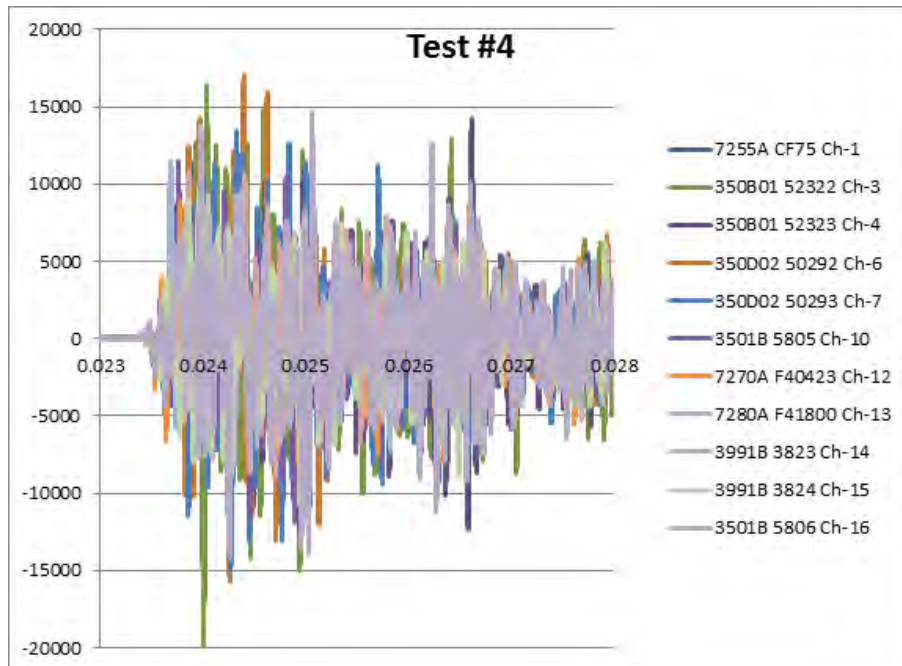


Figure 10: Time History of all Channels for Test #4 (G vs. time)

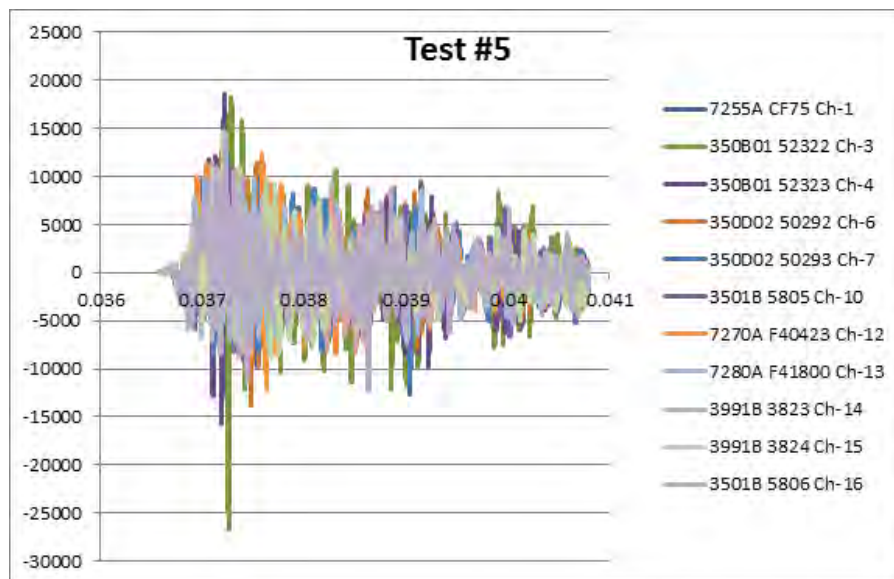


Figure 11: Time History of all Channels for Test #5 (G vs. time) .

The largest quantity of explosive was employed in Test #6. As noted, in this test an additional four accelerometers were placed in the Z axis on the top of the mounting blocks. As seen in Figure 12, they detected the shelf resonance, estimated at 940 Hz, with a pk-pk displacement of ~2 mm. All four sensors were tightly correlated after the second period of oscillation and provide additional credence to the omnidirectional nature of the input shock.

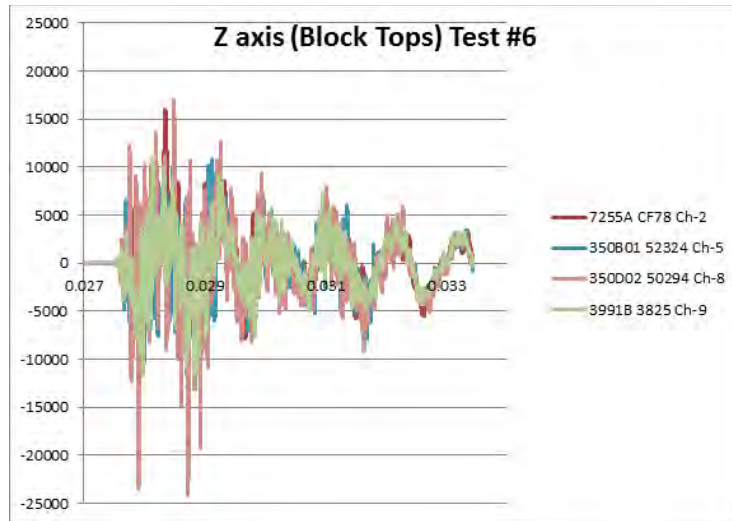


Figure 12: Time History of Z axis Sensors in Test #6 (G vs. time) .

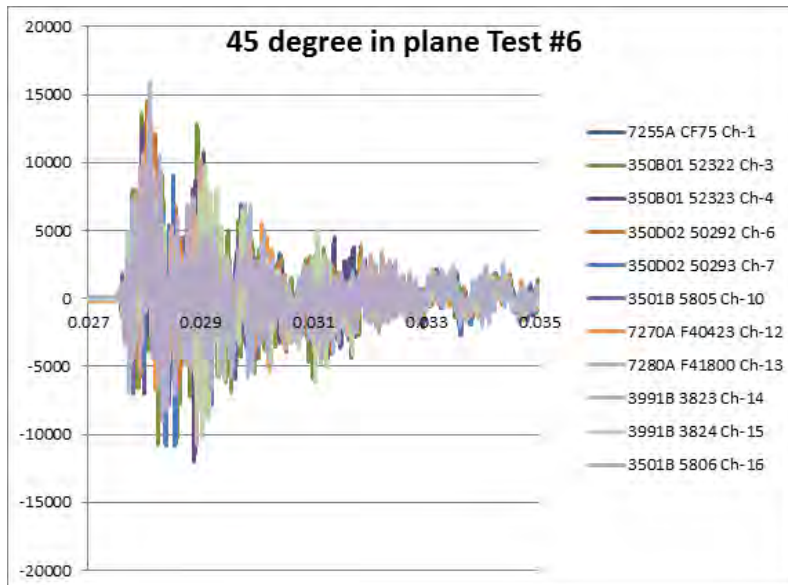


Figure 13: Time History of X and Y Axes Sensors in Test #6 (G vs. time)

Following are six plots decomposing Figure 13 by comparing the output of the two sensors on each of the six blocks (Test 6).

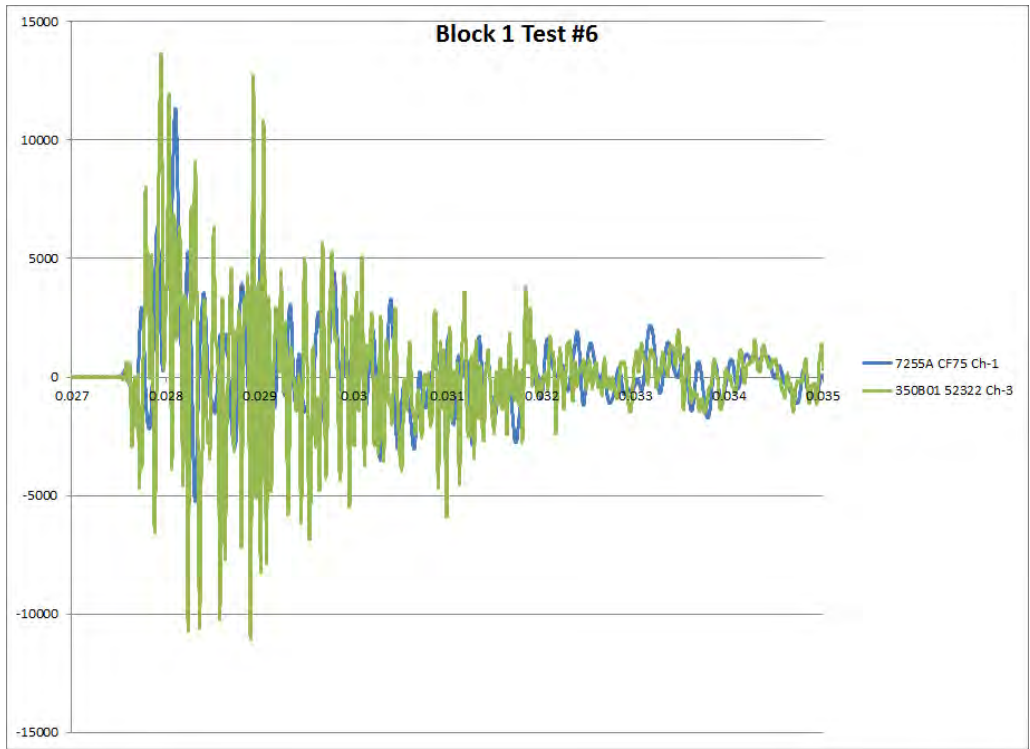


Figure14: Block 1 Test #6, S/N CF75 and 52322

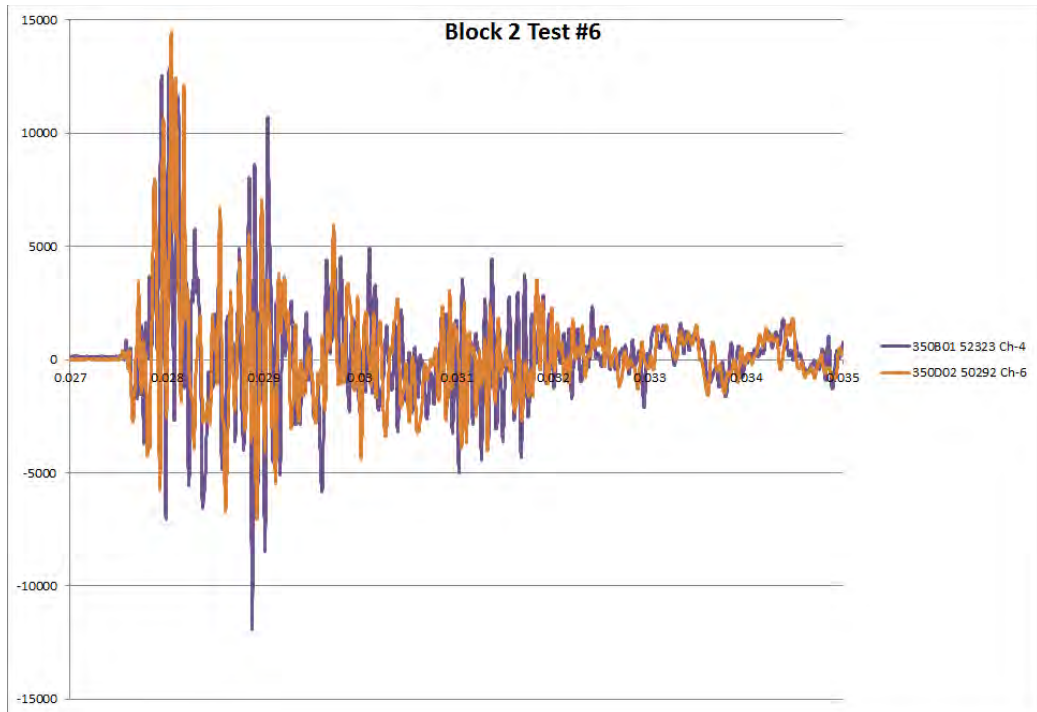


Figure15: Block 2 Test #6, S/N 52323 and 50292

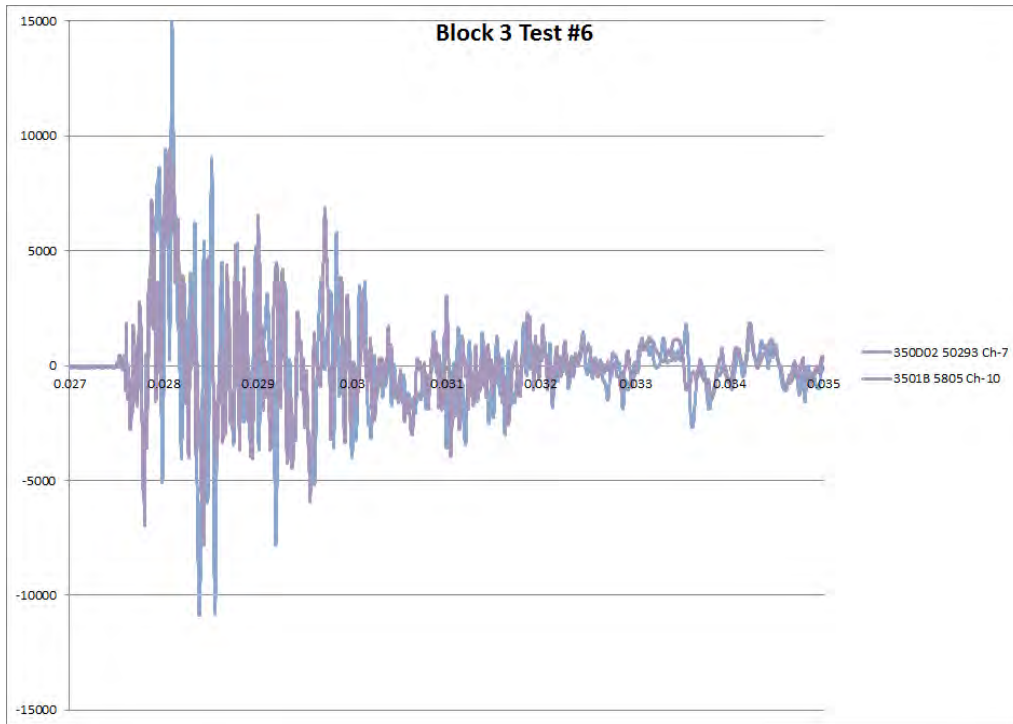


Figure 16: Block 3 Test #6, S/N 50293 and 5805

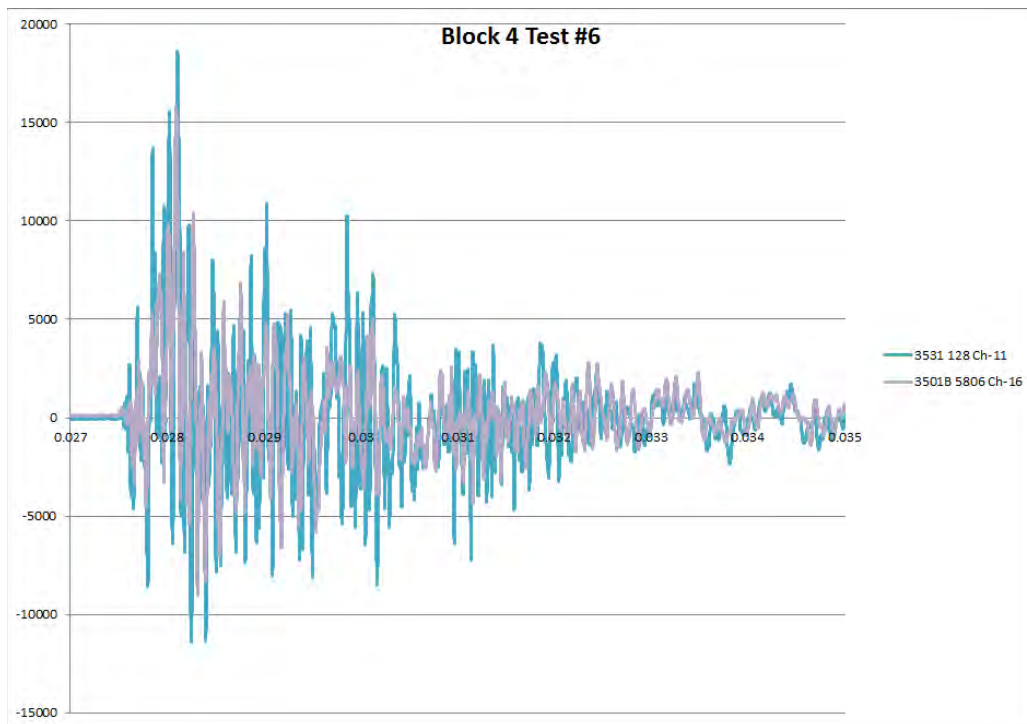


Figure 17: Block 4 Test #6, S/N 128 (prototype unit) and 5806

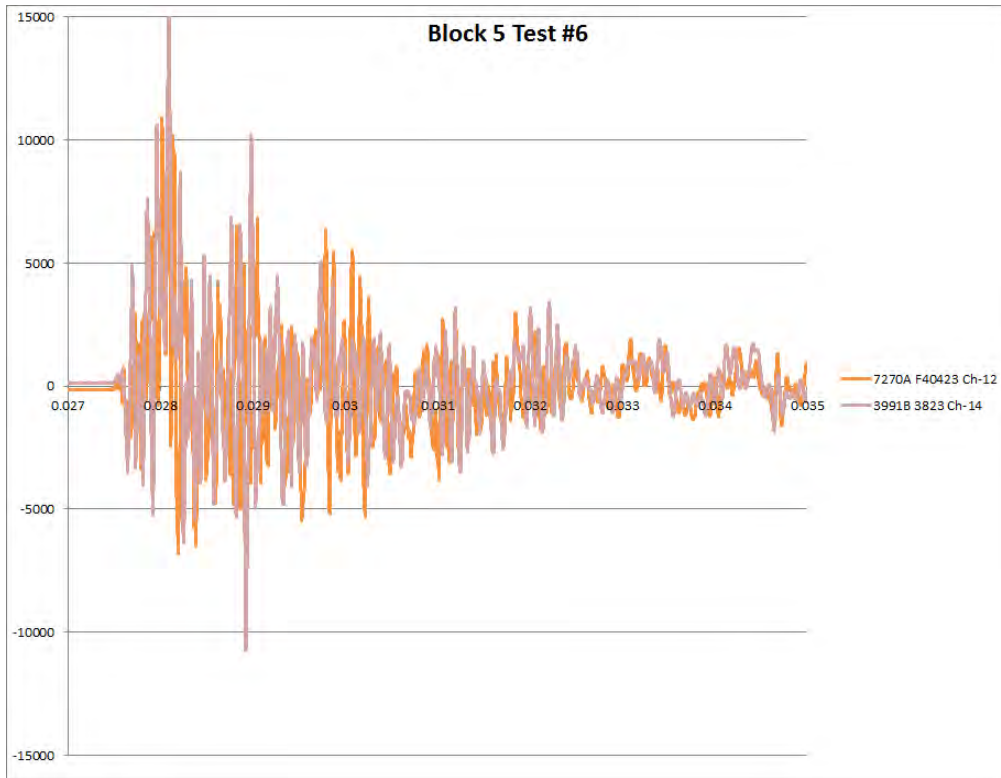


Figure 18: Block 5 Test #6, S/N F40423 and 3823

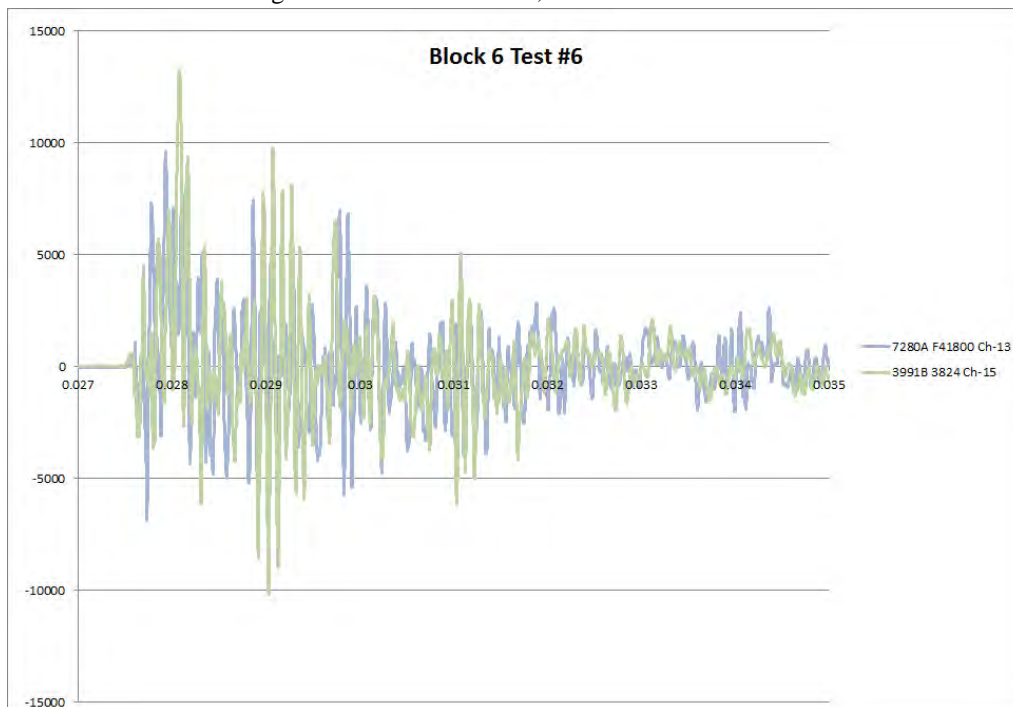


Figure 19: Block 6 Test #6, S/N F41800 and 3824

The preceding six time histories show that while some uniqueness exists, the X-Y accelerometers on each block generally follow the same profile.

Data Analysis and Results

The following procedure was used to analyze all of the data records:

1. A 0.3 second time history starting .001 seconds before the first evidence of motion was extracted from each experimental record.
2. The noise baseline immediately in front of the shock was averaged and the result was subtracted from the whole record.
3. The first 0.05 second of the record was plotted as shown upper left frame of Figure 20.
4. The integral (velocity) of the full period was calculated and the first 0.05 seconds plotted in the lower left frame.
 - a. The slope of the integral between .03 and .05 seconds was calculated by linear regression and is listed as the acceleration offset below the plots. This was then “normalized” by division by the peak-peak acceleration.
5. The Shock Response Spectrum (SRS) was calculated using the Smallwood algorithm⁵ from 10 Hz. to 10 KHz. for the full 300 millisecond period. The positive (solid) and negative (dotted) SRS curves are plotted in the upper right frame.
6. The RMS Fourier Spectrum was calculated for the full period and plotted from 10 Hz. to 100 KHz. in the lower right.

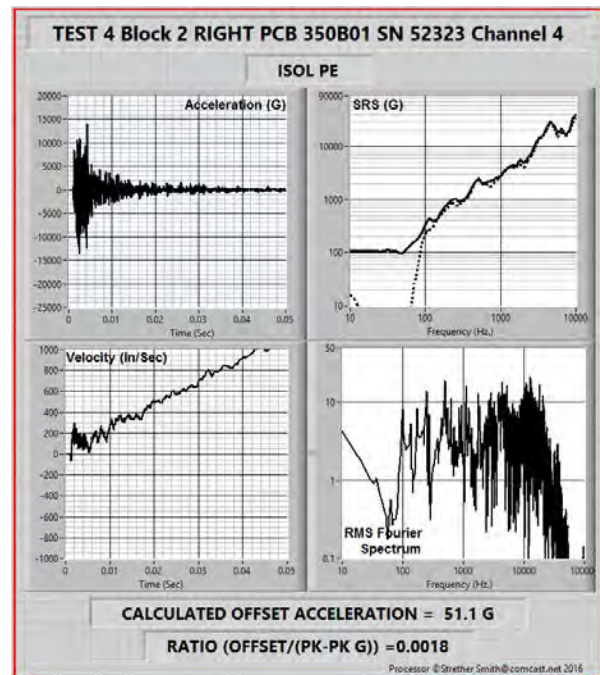


Figure 20. Typical Raw Data Analysis Plot

All of the test results are can be found in the Appendix in the back of the report.

Discussion of the Raw Results:

One of the remarkable findings of this study was that the acceleration offsets were as small as they are. For most of the records (all of the “good” accelerometers) the offsets were less than 0.25% of the Peak-to-Peak acceleration response.

However, even these tiny errors cause enormous discrepancies in the analyses that are normally performed.

For pyrotechnic shock tests, it is known that the velocity should be zero at the beginning and end of the test. Inspection of the velocity trace in Figure 20 (and in the Appendix for other channels) shows a very different result.

Any error in indicated velocity has serious consequences when assessing the damage potential of the measured signals. For example, the low-frequency portion of the acceleration Shock Response Spectrum (SRS) is seriously compromised by these experimental errors, even if they are very small.

The sensitivity of the SRS to these errors makes it a good diagnostic for assessing the tools that might be used to reduce the problem. Ideally, the SRS of a pyroshock waveform will have as a minimum these two characteristics:

- At low frequency (well below any structural mode activity) the slope of the SRS plotted in log-log form will be +2 (12dB/Octave).
- The positive and negative SRS results will be the same.

These SRS criteria, when combined with the fact that the velocity should be zero at the end of the test, give us an excellent set of criteria against which to assess any data correction attempt.

Correction Strategy:

Several methods have been proposed to reduce the effect of these experimental errors: High-pass filtering (References 6, 7) and wavelet correction (Reference 8).

This paper uses a third method based on the subtraction of velocity errors.

The strategy used is a refinement of the technique described in Reference 9. It uses the fact that we have a very good estimate of the velocity after the dynamics have settled down; the velocity must be very close to zero. Hence, any residual velocity must be an error.

The correction procedure is:

- Integrate the raw data to obtain velocity.
- Characterize the velocity error.
- Subtract the velocity error from the raw velocity.
- Differentiate the corrected velocity to find the corrected acceleration.

Of course, the challenge is to characterize the velocity error accurately. A correction curve, made up of three parts, is used:

- Zero, at the beginning of the transient.
- A low-order polynomial for the end (most of) the transient.
- A cubic spline to join the two.

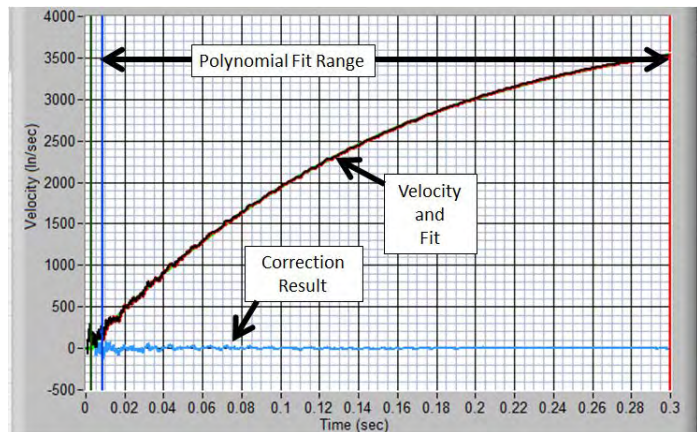


Figure 21. Full Analysis Period Fit

Figure 21 shows the correction for the full analysis time period. Details of the correction curve are shown in the expanded view of the shock start in Figure 22.

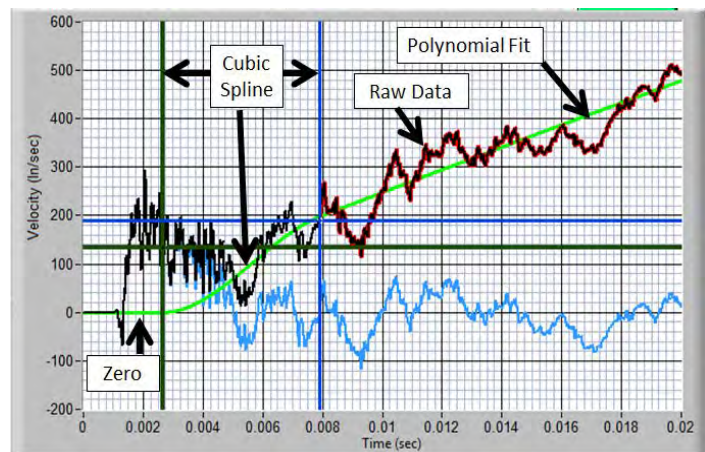


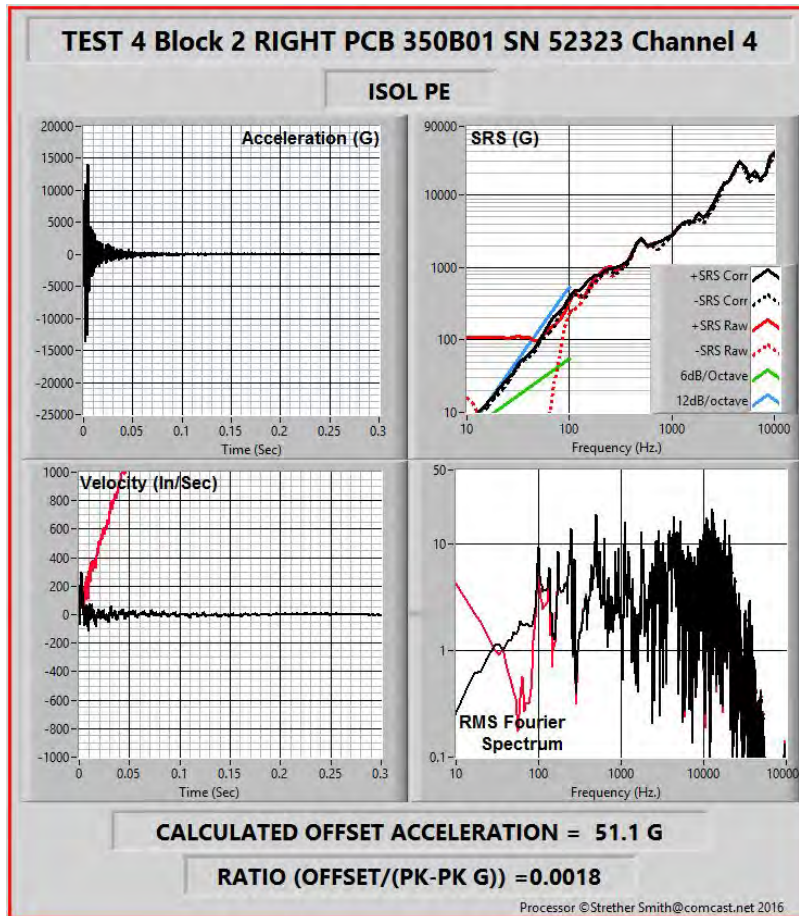
Figure 22. Analysis Curve Fit Detail

The “tuning” parameters are:

- The degree of the polynomial (usually 3rd or less).
- The start of the polynomial.
- The start of the spline.

In most cases, the parameters can be set once and used for all of the channels in a test. In a few cases, manual adjustment may be required.

The results for the example data set are shown in Figure 23.



It can be seen that:

- After the initial pulse, the velocity is very close to zero.
- The positive and negative SRS curves are essentially identical.
- The slope of the SRS at low frequency is very close to 12 dB/octave.

Examination of the results from all of the channels in the Appendix will show that the correction is generally very good for most of the channels.

Figure 23. Example Data Set Results

Tabulated Results:

As reported, five tests were performed and 11 channels of data were successfully recorded on every test. Eight (8) models of accelerometers were tested. Thus, on some tests a given model would be represented by more than one unit. On Test 2, two data channels were slightly over ranged at the input to the data acquisition system. To maintain objectivity in the analysis process, these two channels were denoted as CHANNEL SATURATION even though the amount of over ranging was slight. The response of one unit in Test 5 was intermittent after the shock ended. It was denoted INTERMITTENT. Its time history also appeared a bit unusual.

As a minimum, an assessment of test results can consider the calculated SRSs, the Fourier spectra of the signals, the symmetry of the positive and negative SRSs, and the resultant measured zero offsets. Some of these considerations are interrelated. In trying to perform an impartial assessment the authors decided they could only achieve consensus agreement using the criteria of GOOD, BAD, and QUESTIONABLE for each recorded data channel. ALL authors had to collectively agree to make a definitive call.

Recognizing that this test was coordinated by PCB Piezotronics Inc., and involved a competitor's accelerometers, independent consultants were invited to participate. In addition, every recorded and processed test result is presented in the Appendix (55 records) for viewing and assessment by other interested parties.

PYROSHOCK ACCELEROMETER EVALUATION RESULTS									
Manufacturer	Model	S/N	Technology	Block/Location	Test 2	Test 3	Test 4	Test 5	Test 6
ENDEVCO	7255A	CF75	ISOL PE	1/Left	BAD	BAD	BAD	BAD	BAD
PCB	350B01	52322	ISOL PE	1/Right	CHANNEL SATURATED	GOOD	GOOD	GOOD	GOOD
ENDEVCO	7255A	CF78	ISOL PE	2/Left	BAD				
PCB	350D02	50292	ISOL PE			GOOD	GOOD	GOOD	GOOD
PCB	350D02	50292	ISOL PE	2/Right	GOOD				
PCB	350B01	52323	ISOL PE			GOOD	GOOD	GOOD	GOOD
PCB	3501B	5805	MEMS	3/Left	BAD	BAD	GOOD	GOOD	GOOD
PCB	350D02	50293	ISOL PE	3/Right	GOOD	GOOD	GOOD	GOOD	GOOD
PCB	3501B	5806	MEMS	4/Left	BAD	BAD	GOOD	GOOD	GOOD
				4/Right	*****	*****	*****	*****	*****
ENDEVCO	7270A	40423	MEMS	5/Left	GOOD	QUESTIONABLE	GOOD	GOOD	GOOD
PCB	3991B	3823	MEMS	5/Right	QUESTIONABLE	QUESTIONABLE	GOOD	GOOD	GOOD
ENDEVCO	7280A	41800	MEMS	6/Left	GOOD	GOOD	GOOD	INTERMITTENT	BAD
PCB	3991B	3824	MEMS	6/Right	CHANNEL SATURATED	QUESTIONABLE	GOOD	GOOD	GOOD

Conclusions

- An evaluation of the performance of eight (8) different models of accelerometers in severe pyroshock environments has been planned, executed, and analyzed. This effort was characterized by:
 - Omnidirectional shock inputs to tens of thousands of Gs of almost equal magnitudes in all directions,
 - Matched transfer characteristics on all data channels with verified flat amplitude and linear phase to 10 KHz (the upper normal SRS analysis frequency),
 - Distortion free data return on 53 of 55 recorded data channels, and a
 - Consistent data analysis process.
- Analysis indicates that the MIEF-IEPE type shock accelerometers provided GOOD results and performed at least as well as the MEMS type in all testing, with the exception of two units characterized as BAD via nonlinear behavior consistent with prior work as described in Reference 2 (see Tabulated Results, Endevco Model 7255).
- Given the potential sources of zero shift in acceleration records *identified in the report Introduction*, test results were much better than anticipated. Based on the “as recorded” data, a maximum acceleration offset (i.e., zero shift) of less than 0.25% referenced to the pk-pk value was recorded across all results marked “GOOD” (see Appendix).

Since all test results are published in the back of this report, interested individuals can draw their own comparative conclusions.

These experiments showed that modern versions of accelerometers using both MIEF-IEPE and MEMS technology provided excellent results for excitations encountered in high-level pyrotechnic testing.

This finding should be recognized in future test specifications and standards.

References

1. Dosch, Jeffrey, Lin Jing, "Hopkinson Bar Acceptance Testing for Shock Accelerometers", Sound and Vibration, February 1999.
2. Agnello, Anthony, Dosch, Jeffrey, Metz, Robert, Sill, Robert, Walter, Patrick, "Acceleration Sensing Technologies for Severe Mechanical Shock", Sound and Vibration, pp. 9-18, February 2014.
3. MIL-STD-810G, DEPARTMENT OF DEFENSE TEST METHOD STANDARD: ENVIRONMENTAL ENGINEERING CONSIDERATIONS AND LABORATORY TESTS (31 OCT 2008).
4. Walter, Patrick L., "Lessons learned in applying accelerometers to nuclear effects testing", Shock and Vibration, (14), pp. 1-11, 2007.
5. Smallwood, David: "An Improved Recursive Formula for Calculating Shock Response Spectra" 51st Shock and Vibration Bulletin, 1980.
6. Smallwood, David O., and Jerome S. Cap, "Salvaging Pyrotechnic Data with Minor Overloads and Offsets," *Journal of the Institute of Environmental Sciences and Technology*, Vol. 42, No. 3, pp. 27-35.
7. Smith, Strether, and Bill Hollowell, "Techniques for the Normalization of Shock Data," *Proceedings of the 62nd Shock and Vibration Symposium*, Springfield VA, 1991.
8. An improved wavelet correction for zero shifted accelerometer data, Timothy S. Edwards, Shock and Vibration 10, 159-167, IOS Press, 2003.
9. Smith, Strether, TEST DATA ANOMALIES—When Tweaking's OK, Sensors Magazine, December 2003.

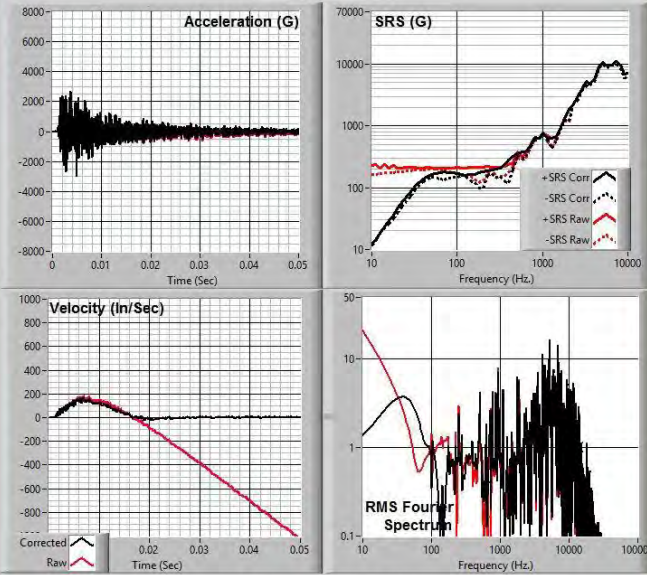
Acknowledgement

Appreciation is expressed to Mr. Bob Metz, PCB, for supporting this activity and maintaining hands off to allow an objective data analysis process. Appreciation is similarly expressed to Mr. Lou Zagst, PCB, for coordination of the test interface with NTS. Special gratitude is provided to Mr. John Czajkowski for permitting access to National Test Systems (NTS) excellent test facility in Santa Clarita, CA. Mr. Steve Fulton and Mr. Dave Williams are awarded many thanks for their dedicated support during this true ordnance pyroshock test series.

APPENDIX

TEST 2 Block 1 LEFT ENDEVCO 7255 SN CF75 Channel 1

ISOL PE



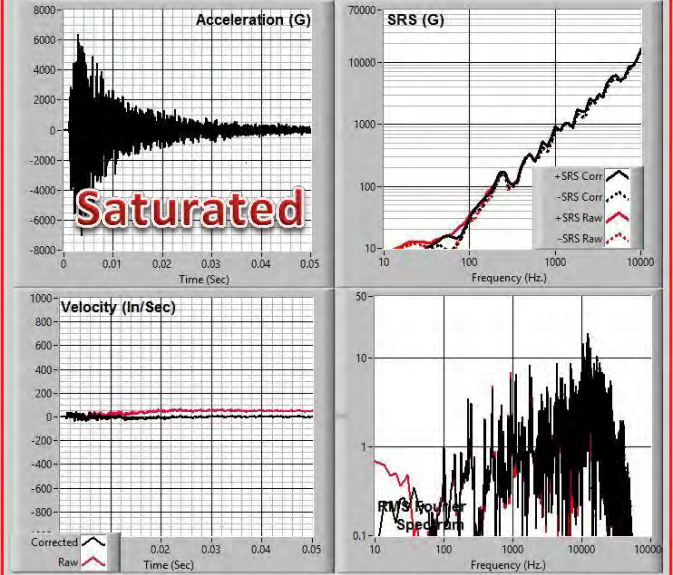
CALCULATED OFFSET ACCELERATION = -83.5 G

RATIO (OFFSET/(PK-PK G)) = -0.0147

Processor ©Strether Smith@comcast.net 2016

TEST 2 Block 1 RIGHT PCB 350B01 SN 52322 Channel 3

ISOL PE



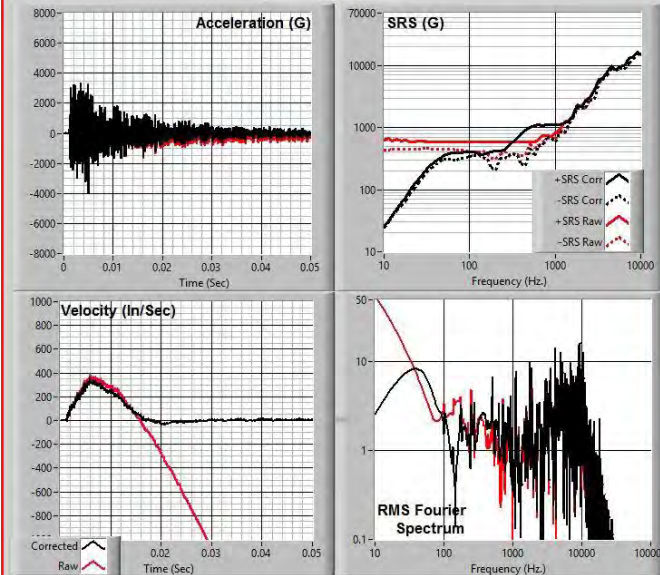
CALCULATED OFFSET ACCELERATION = -1.0 G

RATIO (OFFSET/(PK-PK G)) = -0.0001

Processor ©Strether Smith@comcast.net 2016

TEST 2 Block 2 LEFT ENDEVCO 7255 SN CF78 Channel 2

ISOL PE



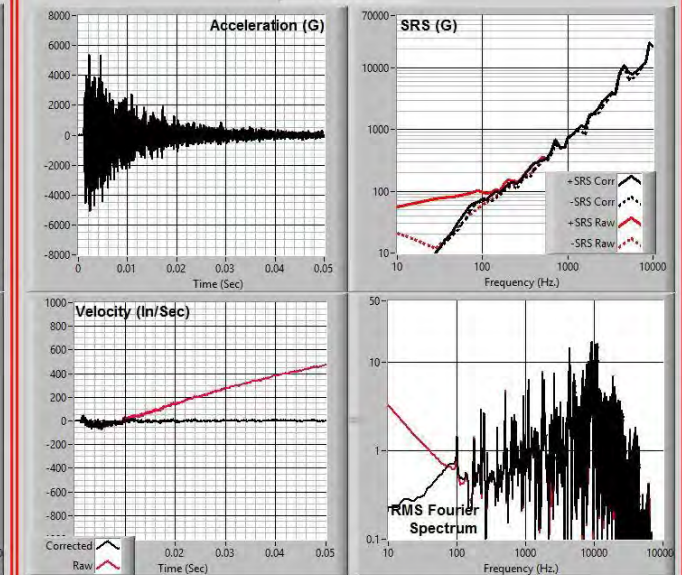
CALCULATED OFFSET ACCELERATION = -226.1 G

RATIO (OFFSET/(PK-PK G)) = -0.0307

Processor ©Strether Smith@comcast.net 2016

TEST 2 Block 2 RIGHT PCB 350D02 SN 50292 Channel 6

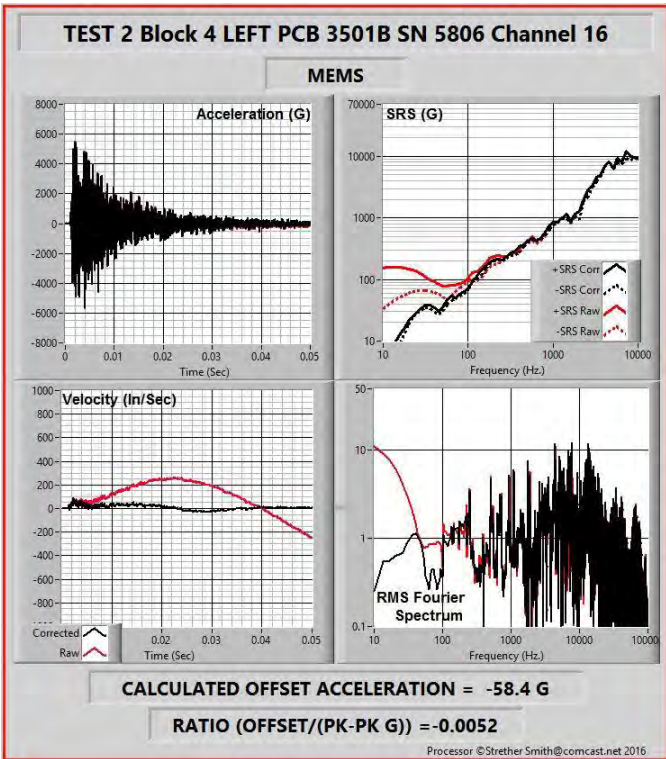
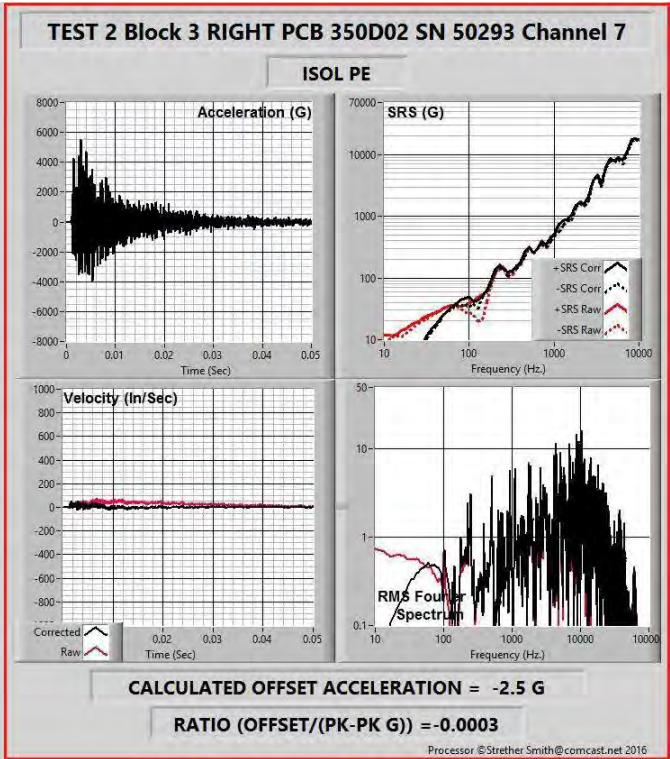
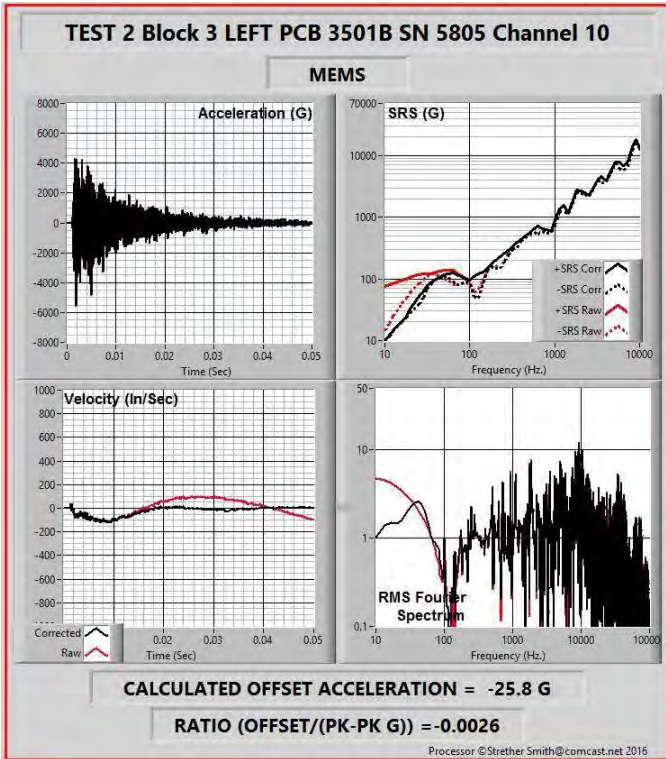
ISOL PE



CALCULATED OFFSET ACCELERATION = 25.8 G

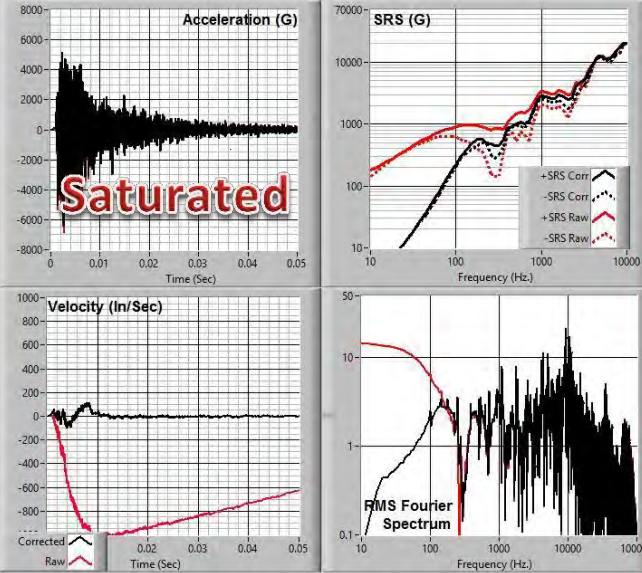
RATIO (OFFSET/(PK-PK G)) = 0.0025

Processor ©Strether Smith@comcast.net 2016



TEST 2 Block 5 LEFT ENDEVCO 7270 SN 40423 Channel 12

MEMS



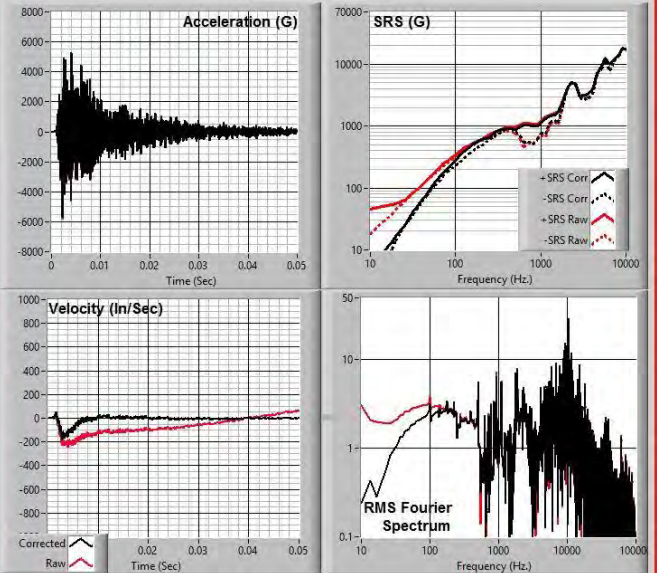
CALCULATED OFFSET ACCELERATION = 28.1 G

RATIO (OFFSET/(PK-PK G)) = 0.0024

Processor ©Strether Smith@comcast.net 2016

TEST 2 Block 5 RIGHT PCB 3991 SN 3823 Channel 14

MEMS



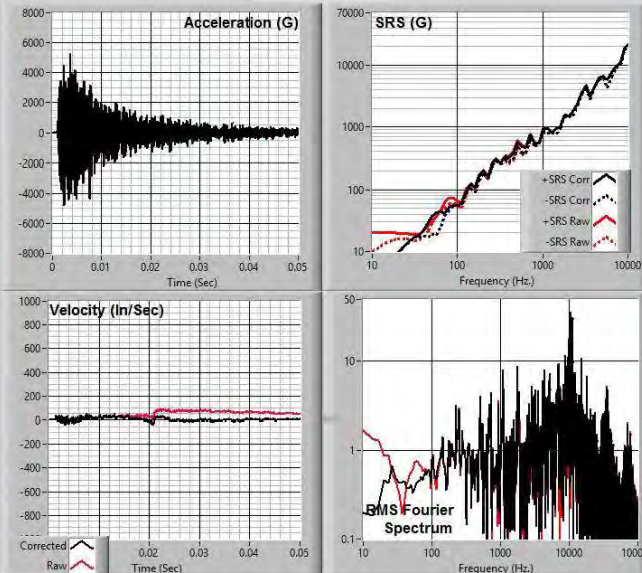
CALCULATED OFFSET ACCELERATION = 16.0 G

RATIO (OFFSET/(PK-PK G)) = 0.0014

Processor ©Strether Smith@comcast.net 2016

TEST 2 Block 6 LEFT ENDEVCO 7280 SN 41800 Channel 13

MEMS



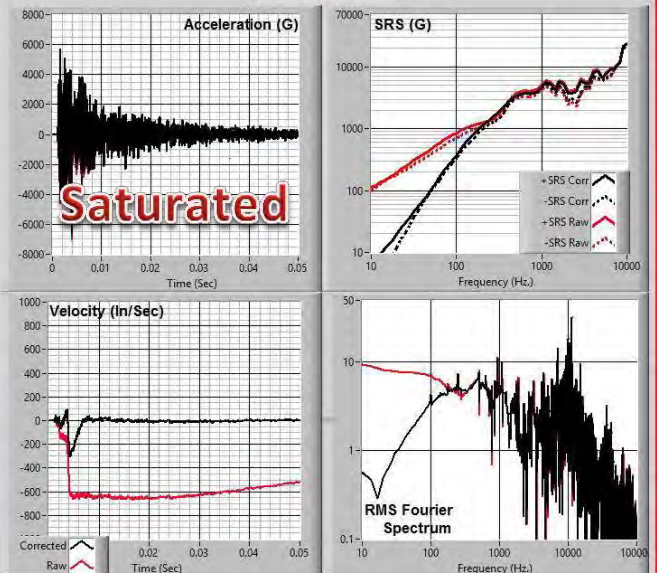
CALCULATED OFFSET ACCELERATION = -3.5 G

RATIO (OFFSET/(PK-PK G)) = -0.0003

Processor ©Strether Smith@comcast.net 2016

TEST 2 Block 6 RIGHT PCB 3991 SN 3824 Channel 15

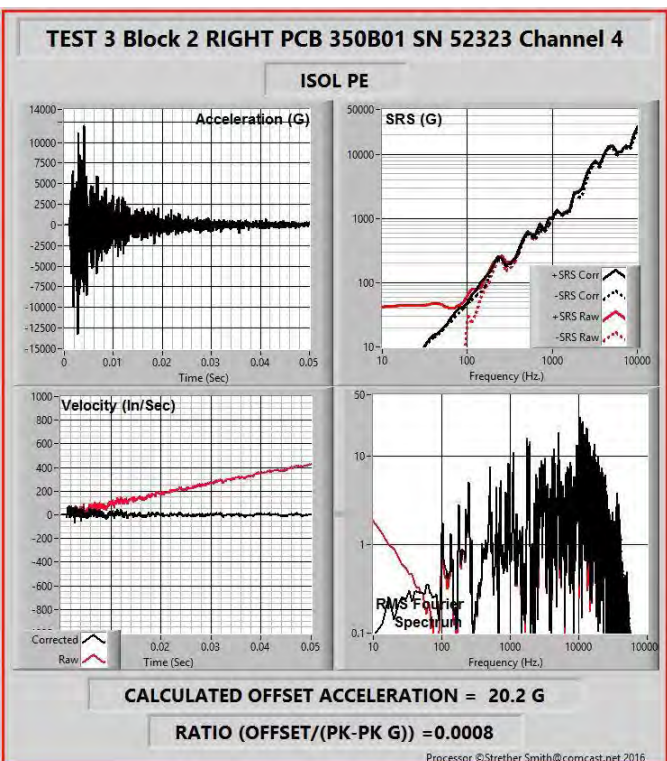
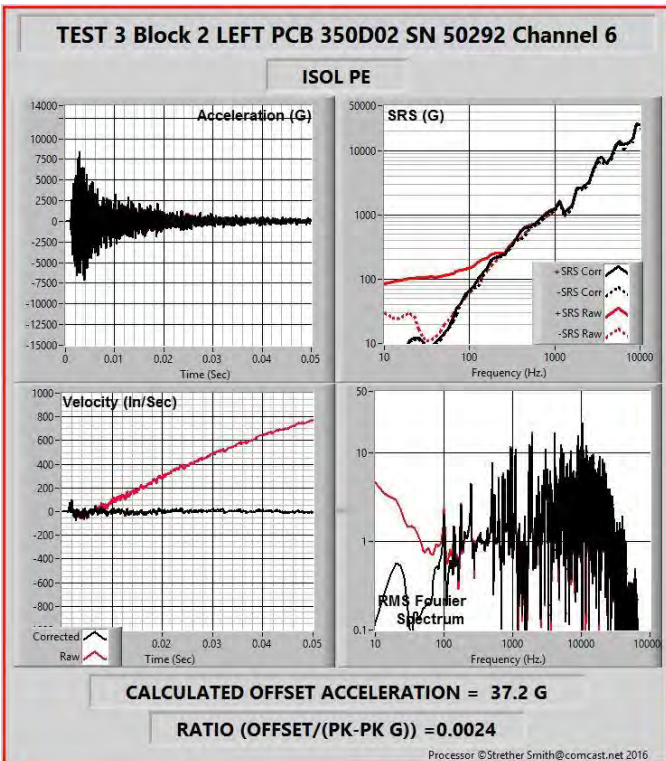
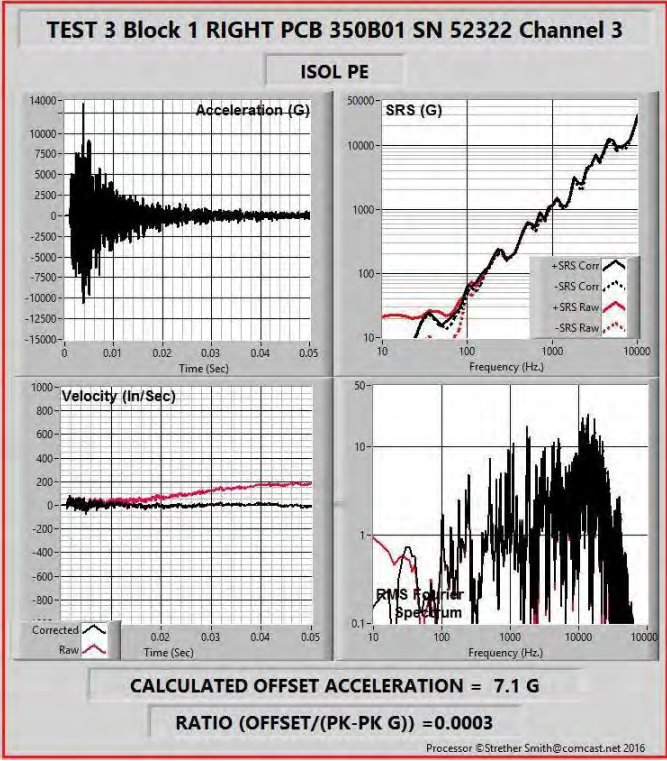
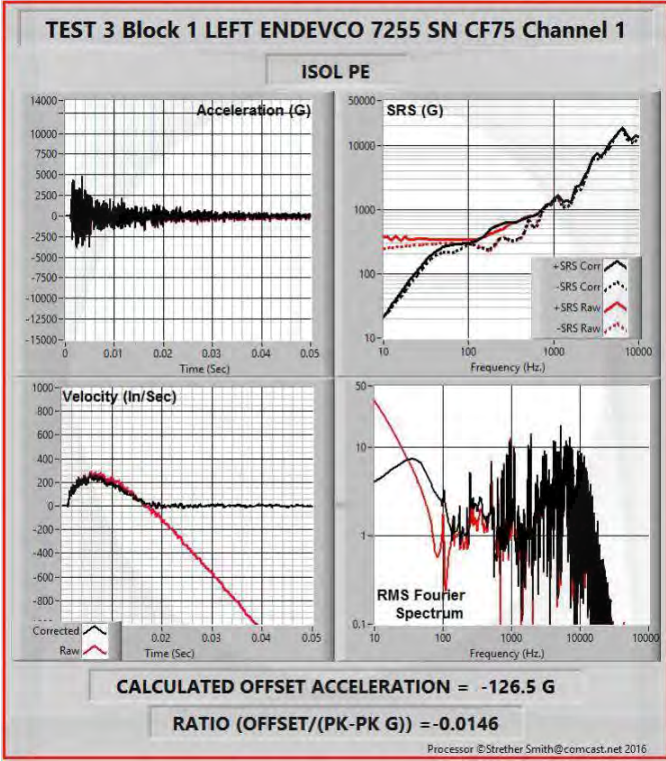
MEMS

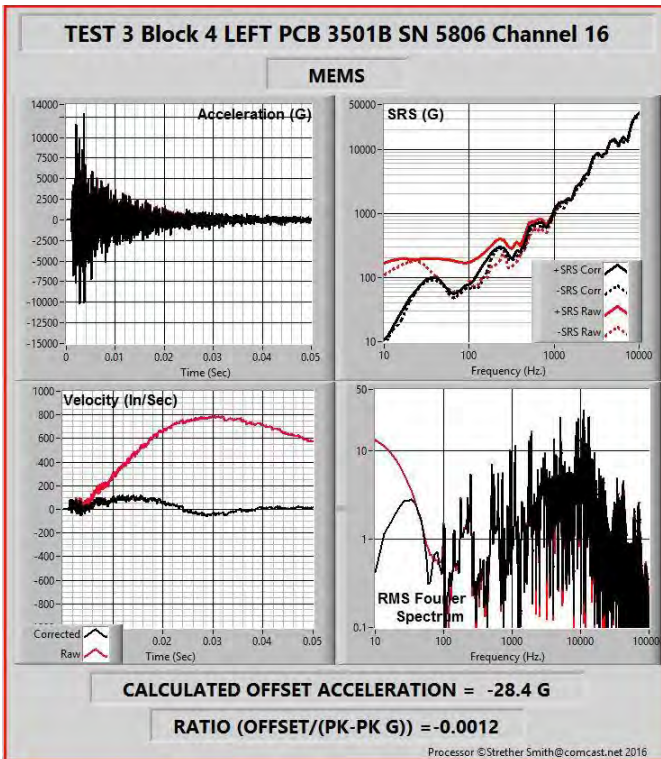
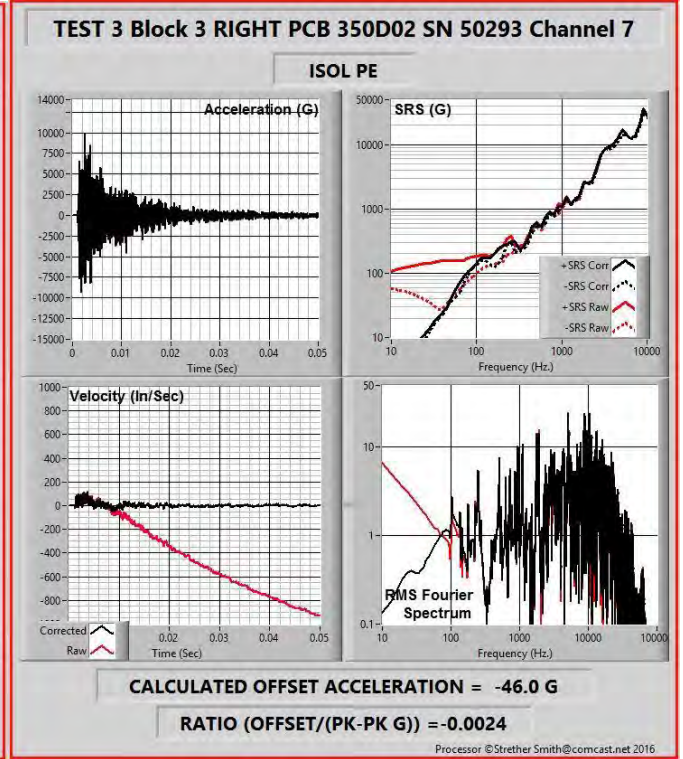
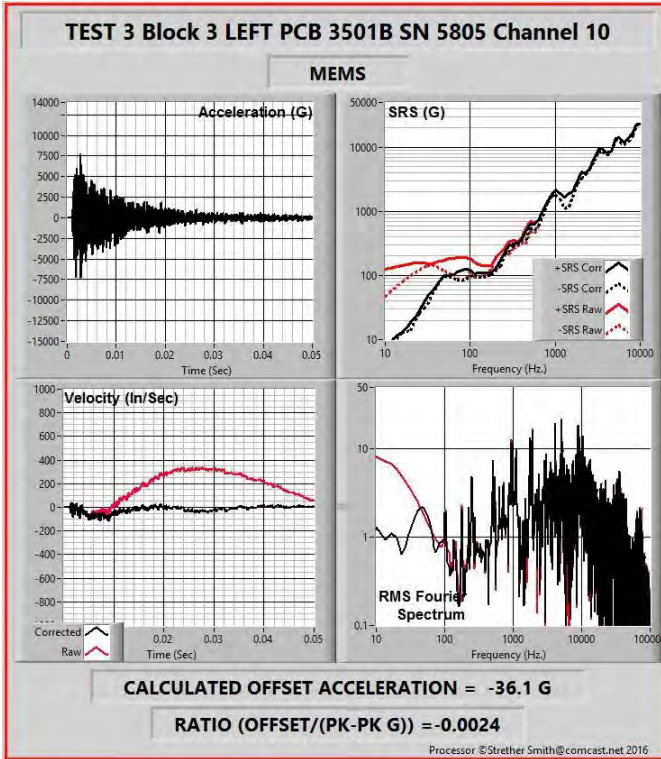


CALCULATED OFFSET ACCELERATION = 14.3 G

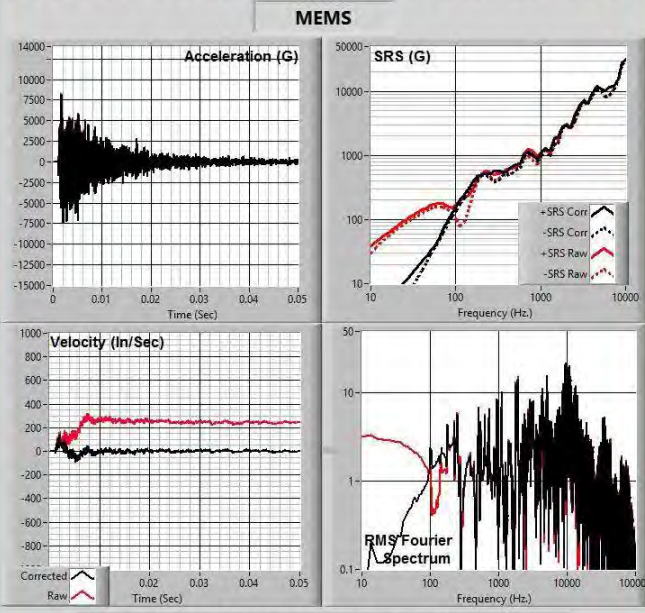
RATIO (OFFSET/(PK-PK G)) = 0.0011

Processor ©Strether Smith@comcast.net 2016





TEST 3 Block 5 LEFT ENDEVCO 7270 SN 40423 Channel 12

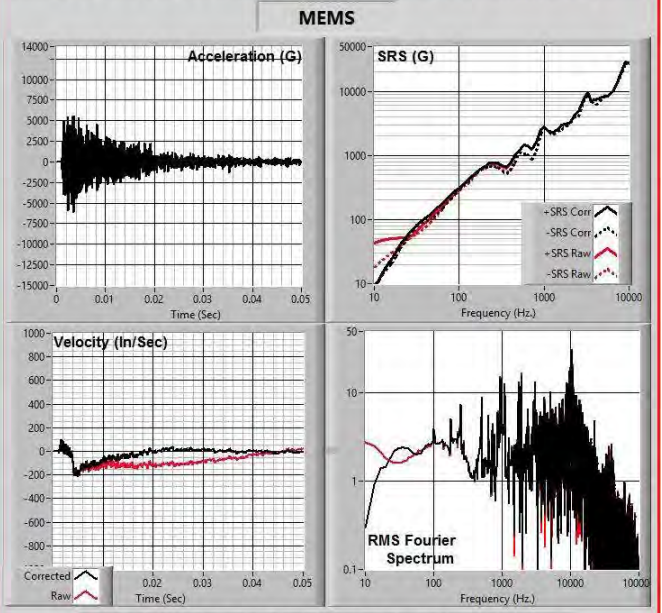


CALCULATED OFFSET ACCELERATION = -0.3 G

RATIO (OFFSET/(PK-PK G)) = -0.0000

Processor ©Strether Smith@comcast.net 2016

TEST 3 Block 5 RIGHT PCB 3991 SN 3823 Channel 14

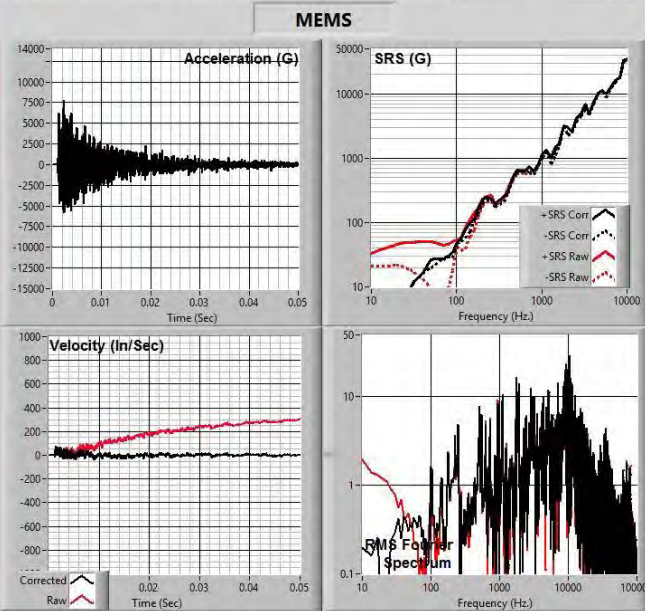


CALCULATED OFFSET ACCELERATION = 14.4 G

RATIO (OFFSET/(PK-PK G)) = 0.0012

Processor ©Strether Smith@comcast.net 2016

TEST 3 Block 6 LEFT ENDEVCO 7280 SN 41800 Channel 13

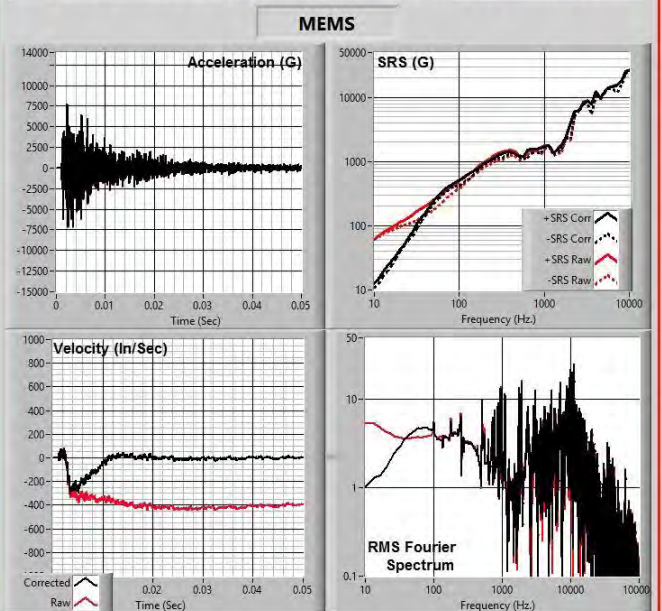


CALCULATED OFFSET ACCELERATION = 8.0 G

RATIO (OFFSET/(PK-PK G)) = 0.0006

Processor ©Strether Smith@comcast.net 2016

TEST 3 Block 6 RIGHT PCB 3991 SN 3824 Channel 15



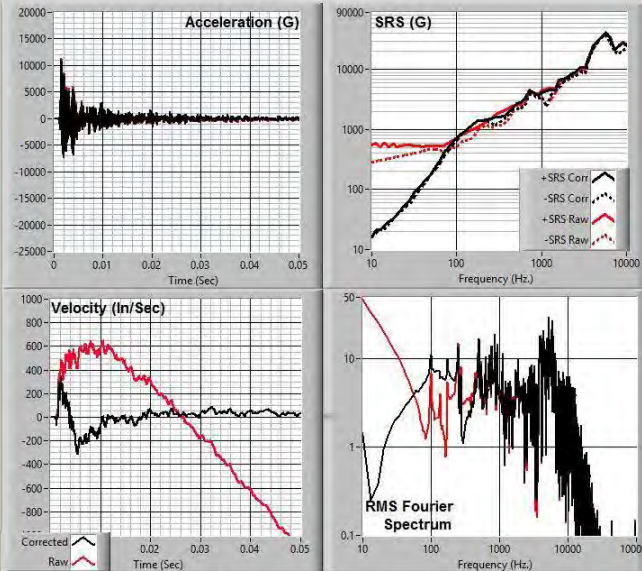
CALCULATED OFFSET ACCELERATION = 4.0 G

RATIO (OFFSET/(PK-PK G)) = 0.0003

Processor ©Strether Smith@comcast.net 2016

TEST 4 Block 1 LEFT ENDEVCO 7255 SN CF75 Channel 1

ISOL PE



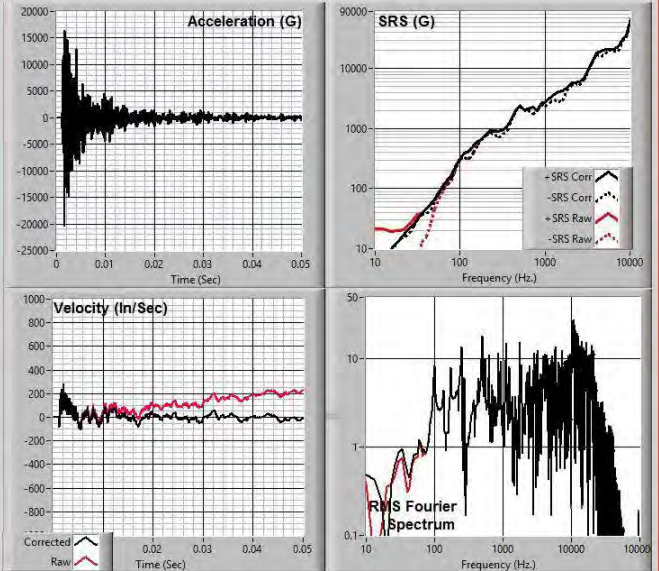
CALCULATED OFFSET ACCELERATION = -127.8 G

RATIO (OFFSET/(PK-PK G)) = -0.0070

Processor ©Strether Smith@comcast.net 2016

TEST 4 Block 1 RIGHT PCB 350B01 SN 52322 Channel 3

ISOL PE



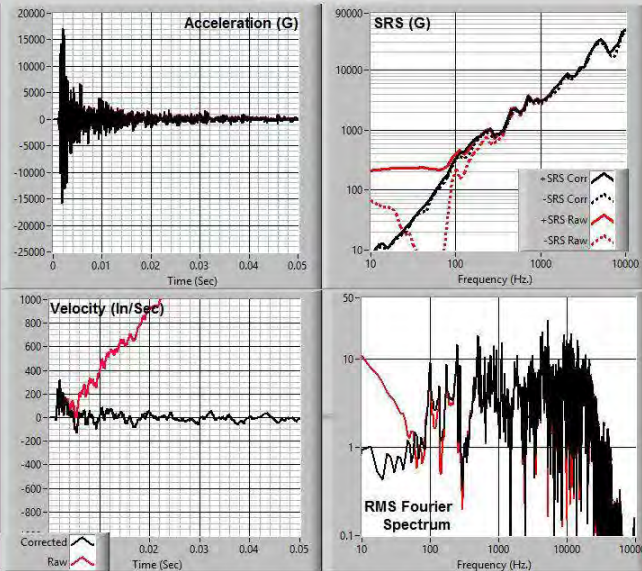
CALCULATED OFFSET ACCELERATION = 9.4 G

RATIO (OFFSET/(PK-PK G)) = 0.0003

Processor ©Strether Smith@comcast.net 2016

TEST 4 Block 2 LEFT PCB 350D02 SN 50292 Channel 6

ISOL PE



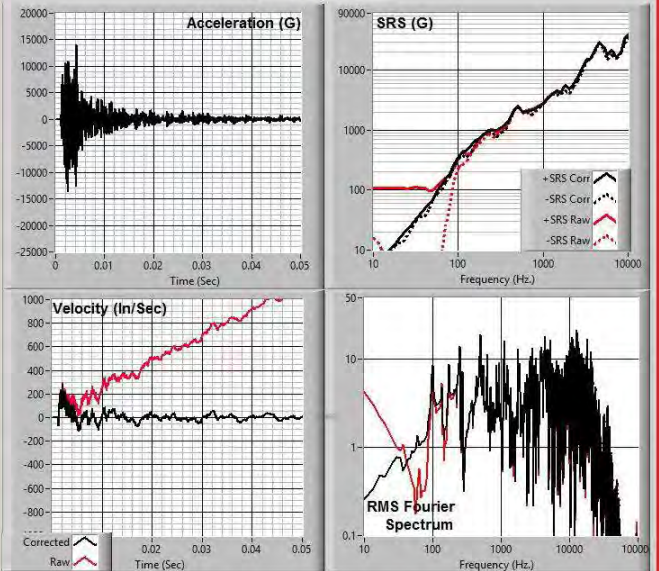
CALCULATED OFFSET ACCELERATION = 94.8 G

RATIO (OFFSET/(PK-PK G)) = 0.0029

Processor ©Strether Smith@comcast.net 2016

TEST 4 Block 2 RIGHT PCB 350B01 SN 52323 Channel 4

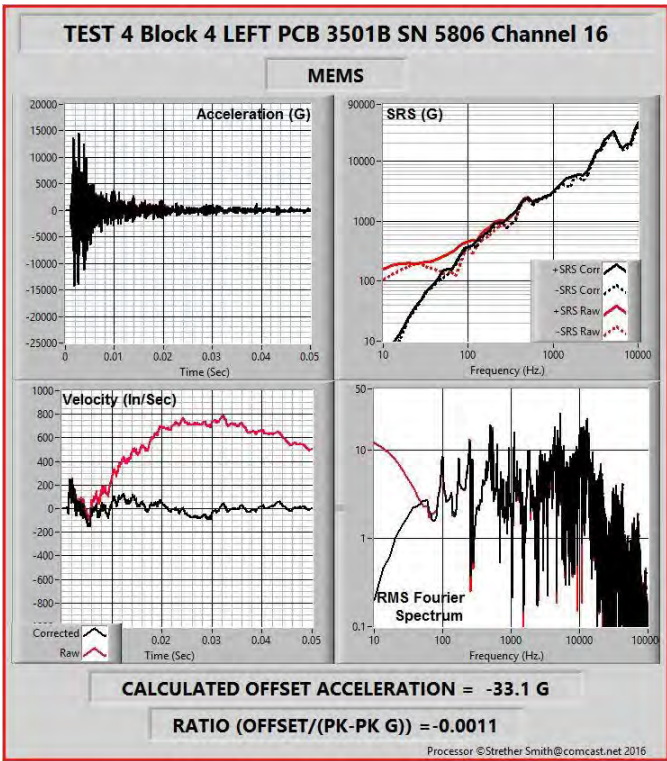
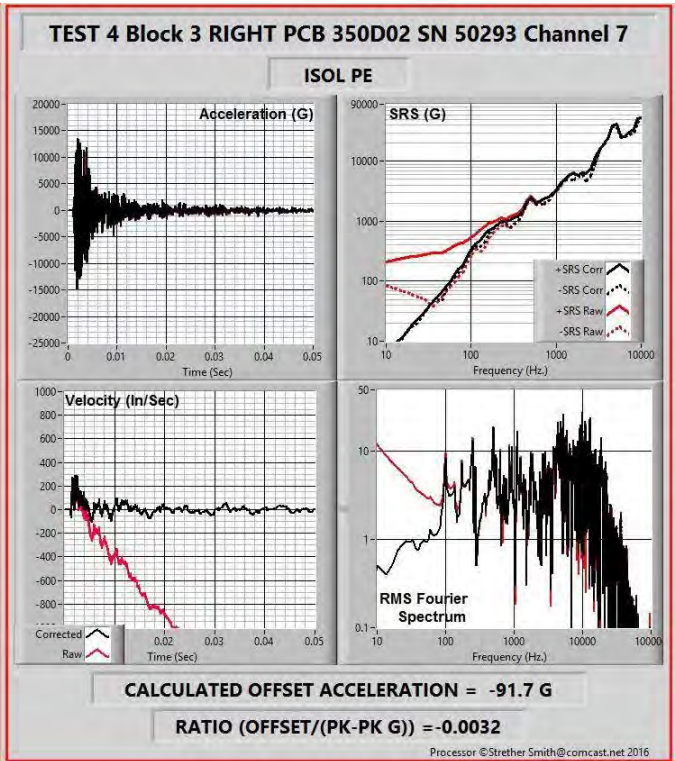
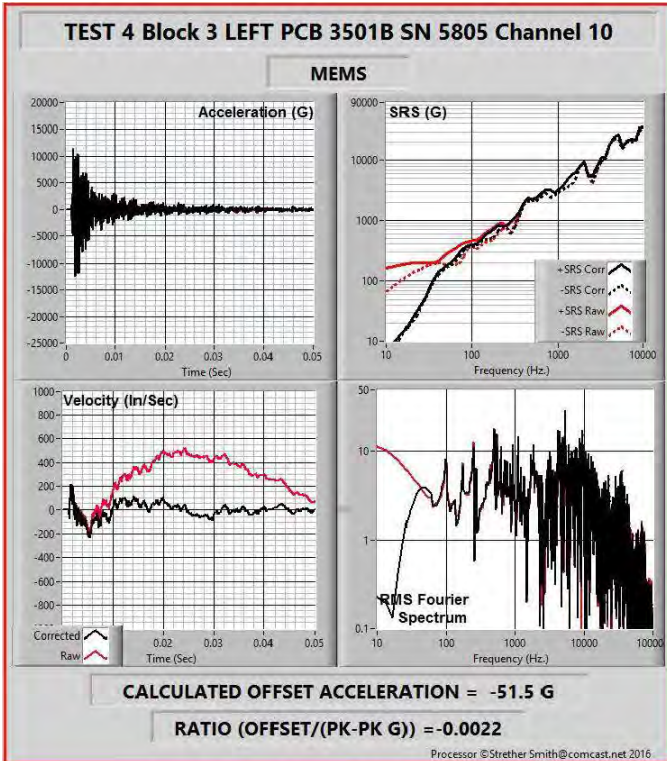
ISOL PE



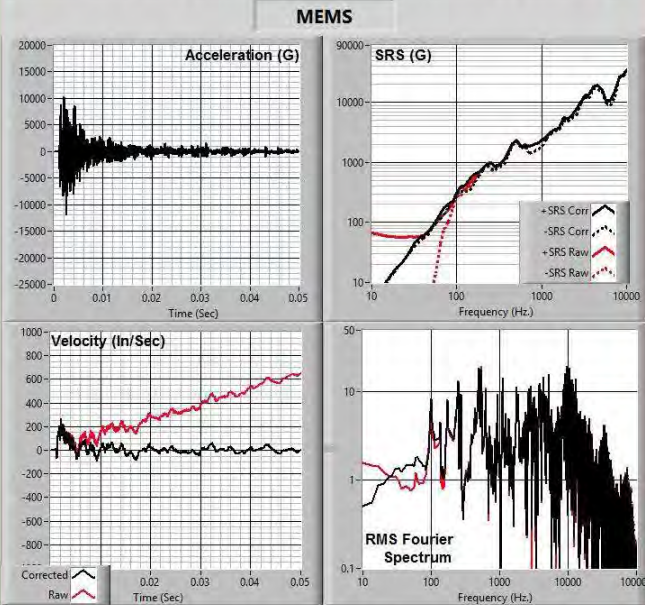
CALCULATED OFFSET ACCELERATION = 51.1 G

RATIO (OFFSET/(PK-PK G)) = 0.0018

Processor ©Strether Smith@comcast.net 2016



TEST 4 Block 5 LEFT ENDEVCO 7270 SN 40423 Channel 12

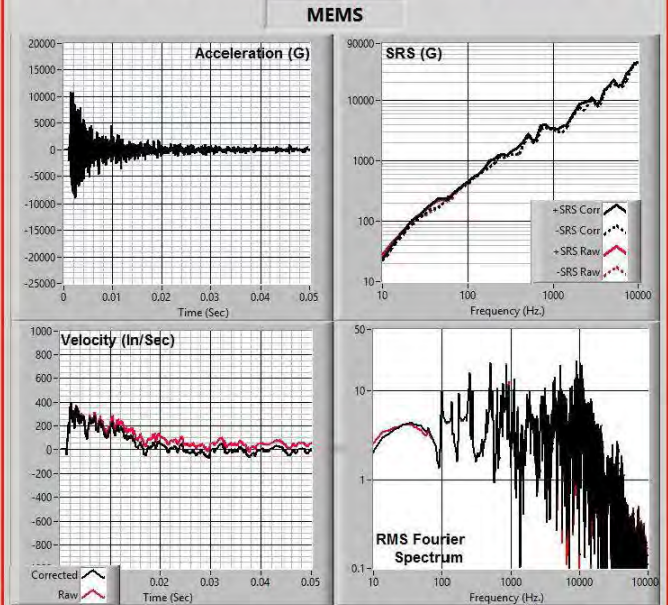


CALCULATED OFFSET ACCELERATION = 32.4 G

RATIO (OFFSET/(PK-PK G)) = 0.0015

Processor ©Strether Smith@comcast.net 2016

TEST 4 Block 5 RIGHT PCB 3991 SN 3823 Channel 14

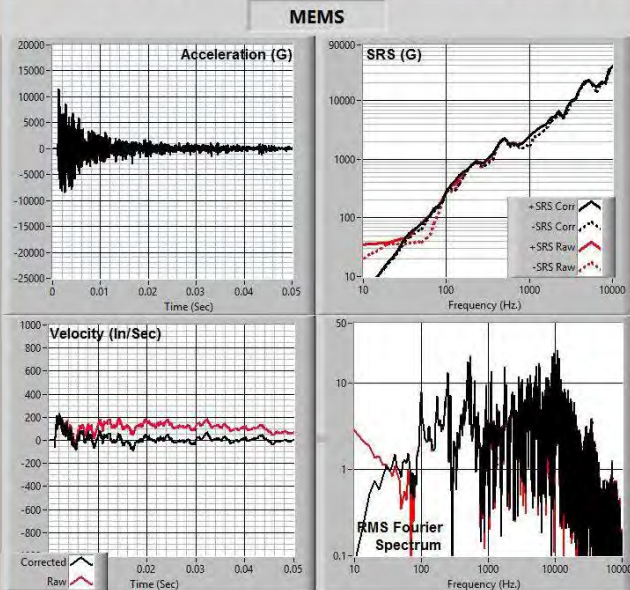


CALCULATED OFFSET ACCELERATION = -1.4 G

RATIO (OFFSET/(PK-PK G)) = -0.0001

Processor ©Strether Smith@comcast.net 2016

TEST 4 Block 6 LEFT ENDEVCO 7280 SN 41800 Channel 13

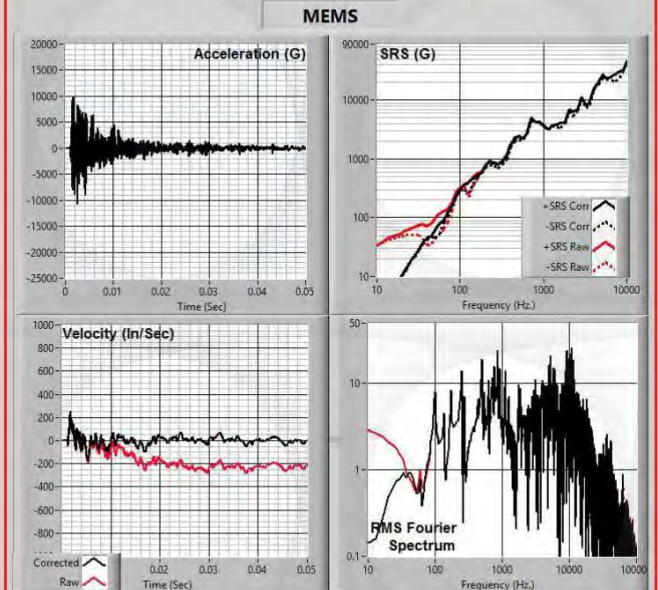


CALCULATED OFFSET ACCELERATION = -11.1 G

RATIO (OFFSET/(PK-PK G)) = -0.0006

Processor ©Strether Smith@comcast.net 2016

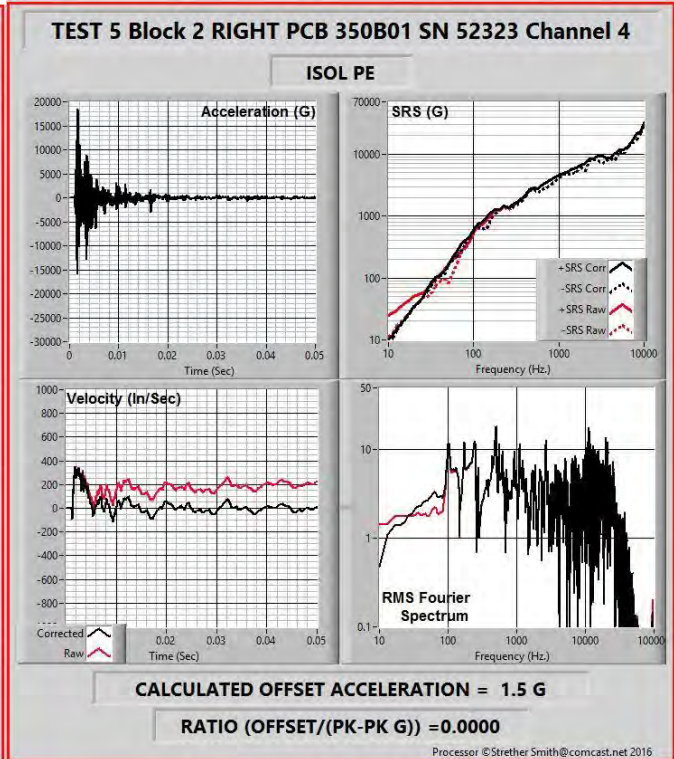
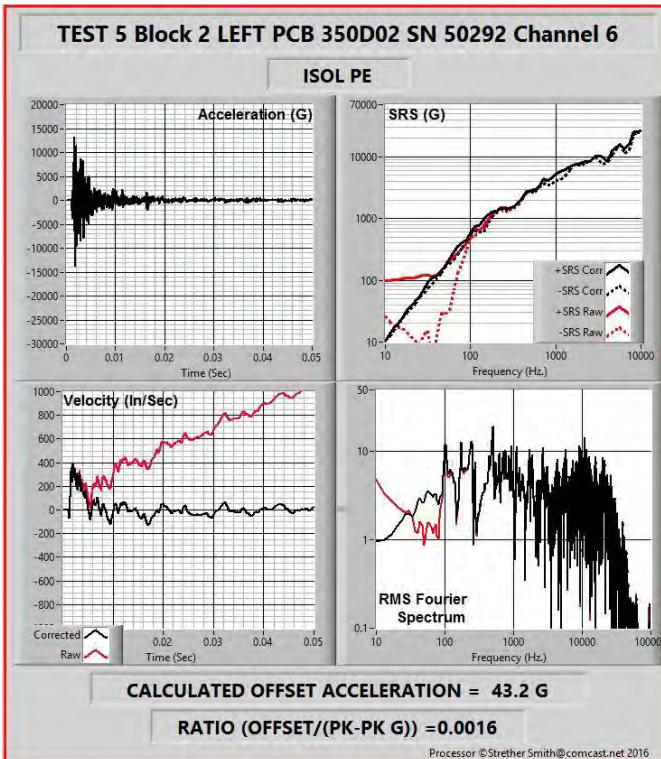
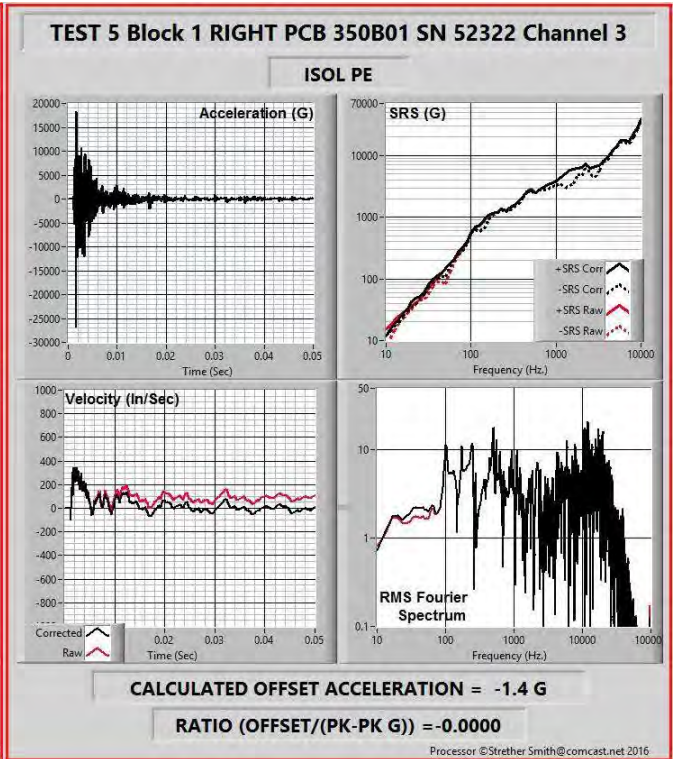
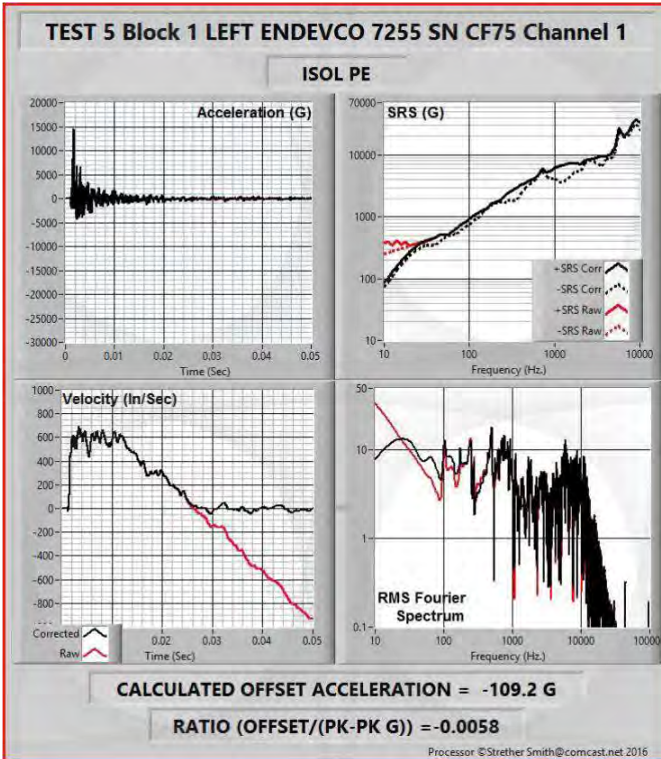
TEST 4 Block 6 RIGHT PCB 3991 SN 3824 Channel 15



CALCULATED OFFSET ACCELERATION = -1.3 G

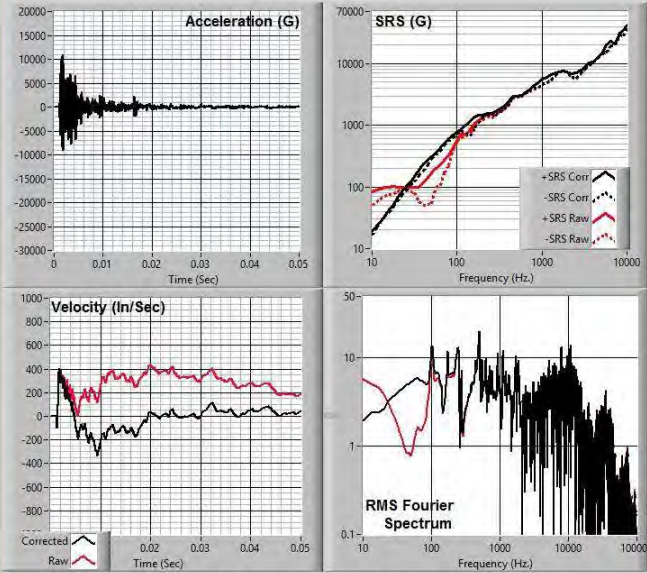
RATIO (OFFSET/(PK-PK G)) = -0.0001

Processor ©Strether Smith@comcast.net 2016



TEST 5 Block 3 LEFT PCB 3501B SN 5805 Channel 10

MEMS



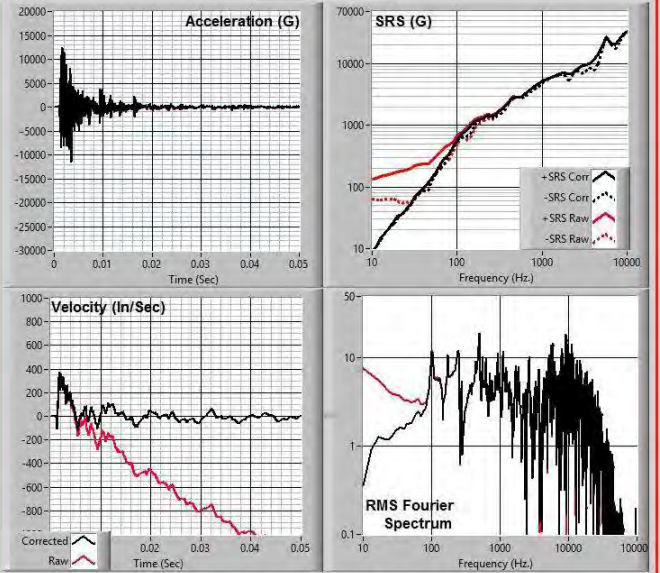
CALCULATED OFFSET ACCELERATION = -25.1 G

RATIO (OFFSET/(PK-PK G)) = -0.0013

Processor ©Strether Smith@comcast.net 2016

TEST 5 Block 3 RIGHT PCB 350D02 SN 50293 Channel 7

ISOL PE



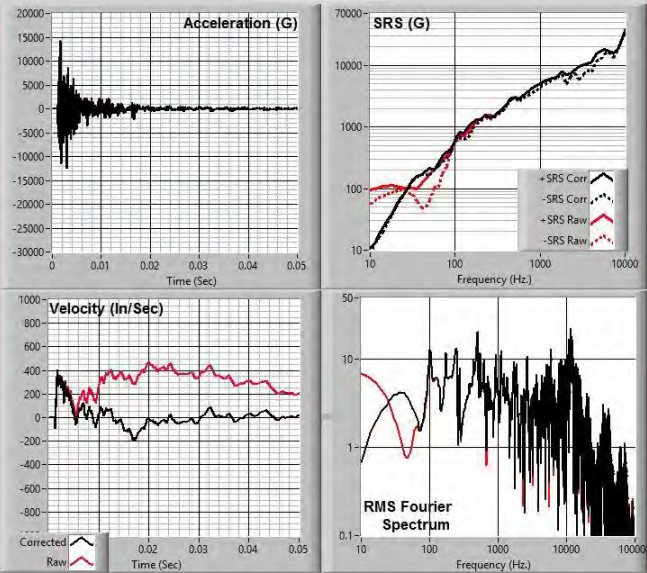
CALCULATED OFFSET ACCELERATION = -54.8 G

RATIO (OFFSET/(PK-PK G)) = -0.0023

Processor ©Strether Smith@comcast.net 2016

TEST 5 Block 4 LEFT PCB 3501B SN 5806 Channel 16

MEMS



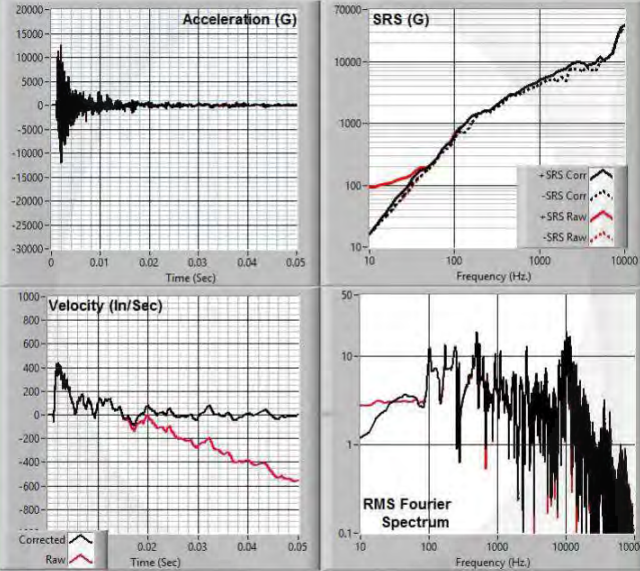
CALCULATED OFFSET ACCELERATION = -27.7 G

RATIO (OFFSET/(PK-PK G)) = -0.0010

Processor ©Strether Smith@comcast.net 2016

TEST 5 Block 5 LEFT ENDEVCO 7270 SN 40423 Channel 12

MEMS



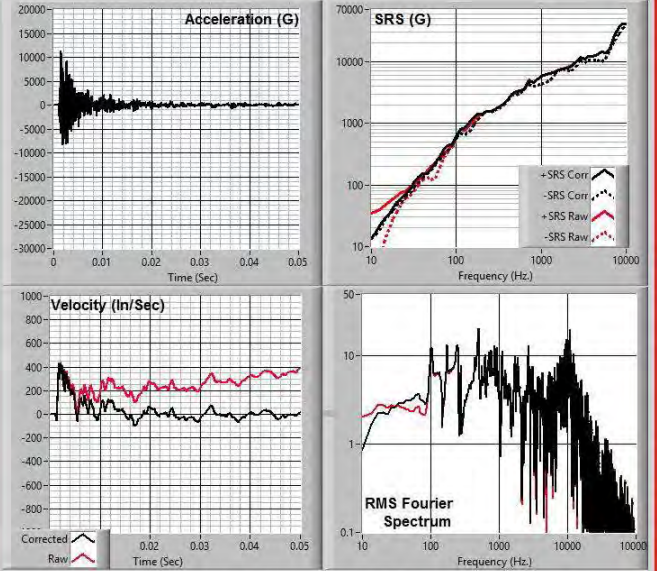
CALCULATED OFFSET ACCELERATION = -46.2 G

RATIO (OFFSET/(PK-PK G)) = -0.0019

Processor ©Strether Smith@comcast.net.2016

TEST 5 Block 5 RIGHT PCB 3991 SN 3823 Channel 14

MEMS



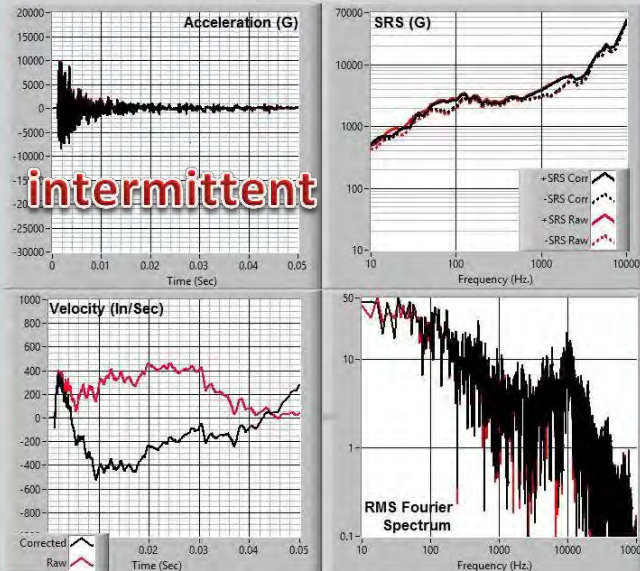
CALCULATED OFFSET ACCELERATION = 13.1 G

RATIO (OFFSET/(PK-PK G)) = 0.0007

Processor ©Strether Smith@comcast.net.2016

TEST 5 Block 6 LEFT ENDEVCO 7280 SN 41800 Channel 13

MEMS



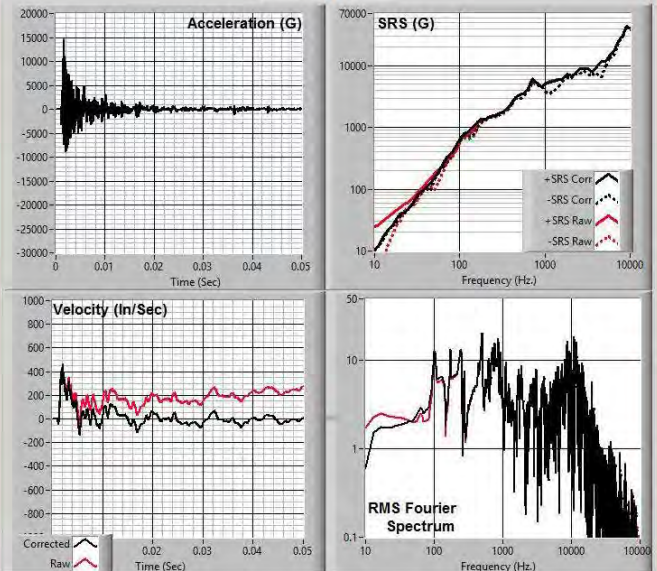
CALCULATED OFFSET ACCELERATION = -41.0 G

RATIO (OFFSET/(PK-PK G)) = -0.0022

Processor ©Strether Smith@comcast.net.2016

TEST 5 Block 6 RIGHT PCB 3991 SN 3824 Channel 15

MEMS



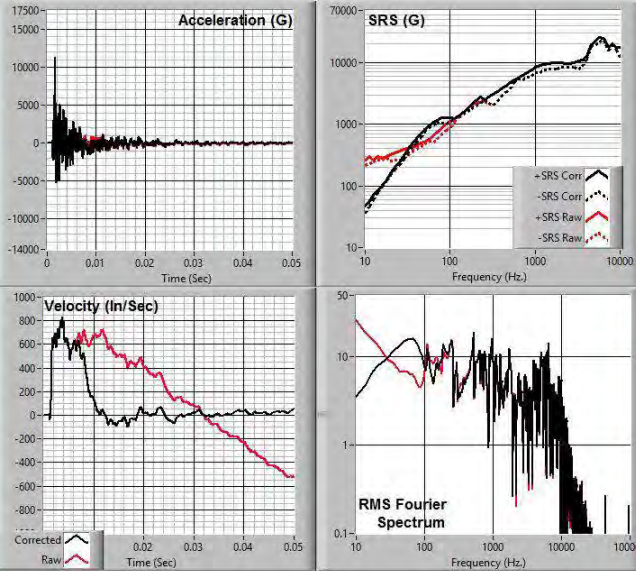
CALCULATED OFFSET ACCELERATION = 7.5 G

RATIO (OFFSET/(PK-PK G)) = 0.0003

Processor ©Strether Smith@comcast.net.2016

TEST 6 Block 1 LEFT ENDEVCO 7255 SN CF75 Channel 1

ISOL PE



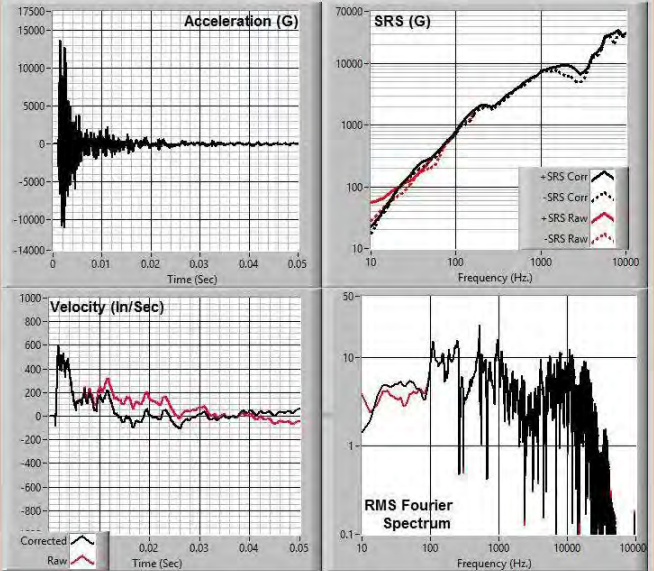
CALCULATED OFFSET ACCELERATION = -80.0 G

RATIO (OFFSET/(PK-PK G)) = -0.0048

Processor ©Strether Smith@comcast.net 2016

TEST 6 Block 1 RIGHT PCB 350B01 SN 52322 Channel 3

ISOL PE



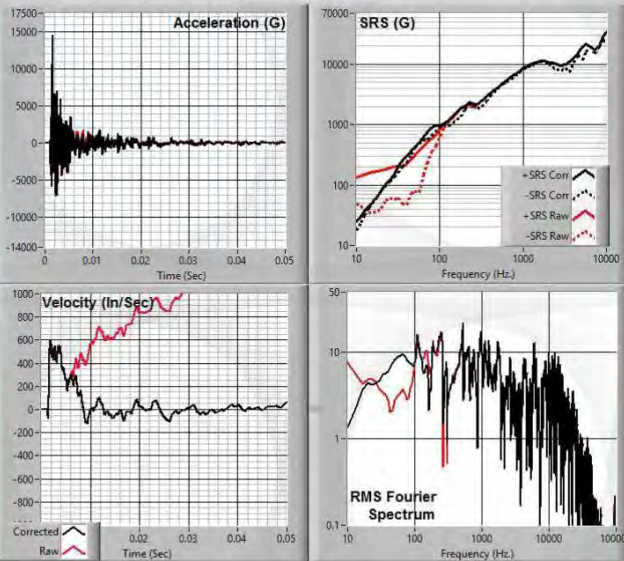
CALCULATED OFFSET ACCELERATION = -13.8 G

RATIO (OFFSET/(PK-PK G)) = -0.0006

Processor ©Strether Smith@comcast.net 2016

TEST 6 Block 2 LEFT PCB 350D02 SN 50292 Channel 6

ISOL PE



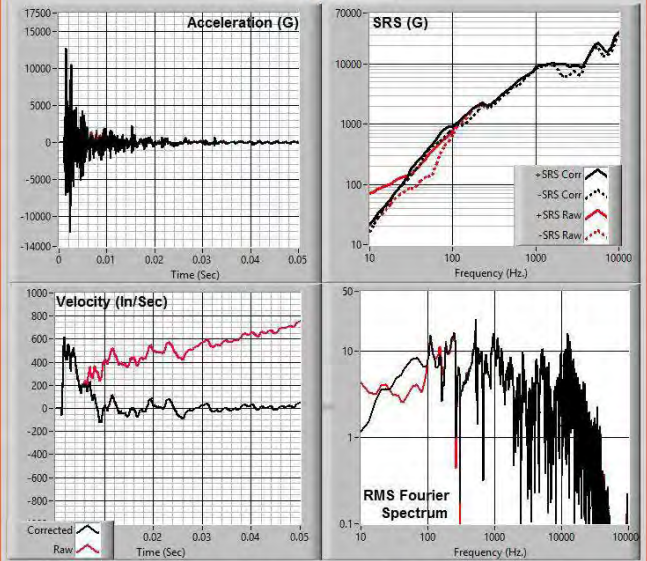
CALCULATED OFFSET ACCELERATION = 56.7 G

RATIO (OFFSET/(PK-PK G)) = 0.0026

Processor ©Strether Smith@comcast.net 2016

TEST 6 Block 2 RIGHT PCB 350B01 SN 52323 Channel 4

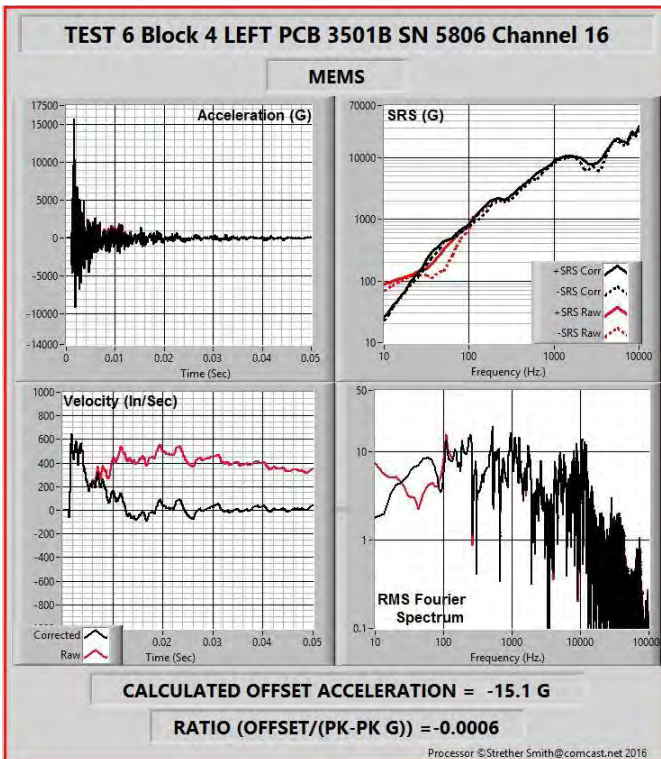
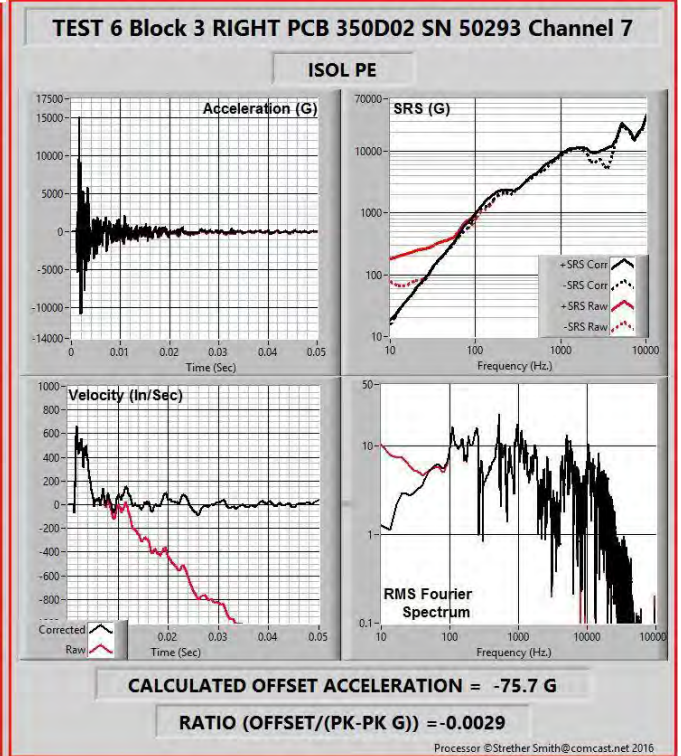
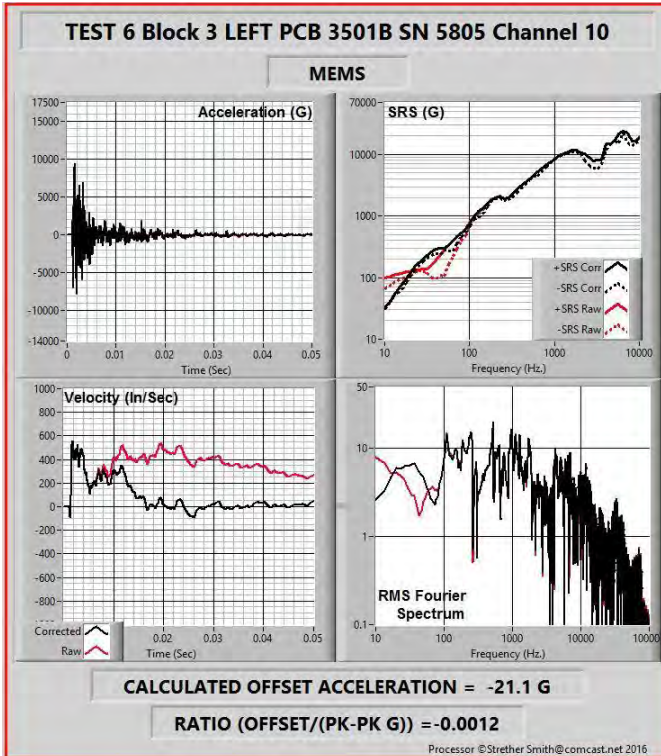
ISOL PE



CALCULATED OFFSET ACCELERATION = 24.5 G

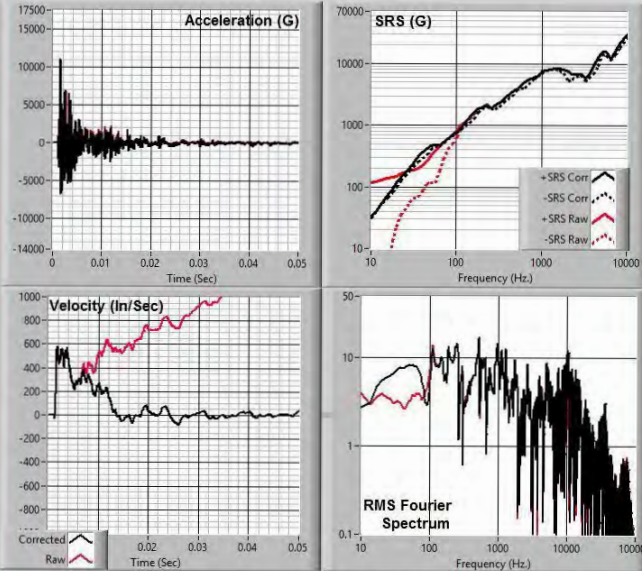
RATIO (OFFSET/(PK-PK G)) = 0.0010

Processor ©Strether Smith@comcast.net 2016



TEST 6 Block 5 LEFT ENDEVCO 7270 SN 40423 Channel 12

MEMS



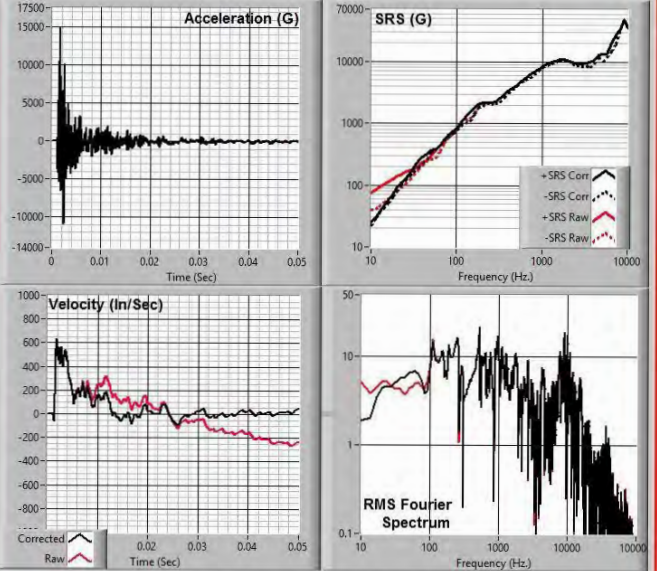
CALCULATED OFFSET ACCELERATION = 61.1 G

RATIO (OFFSET/(PK-PK G)) = 0.0034

Processor ©Strether Smith@comcast.net 2016

TEST 6 Block 5 RIGHT PCB 3991 SN 3823 Channel 14

MEMS



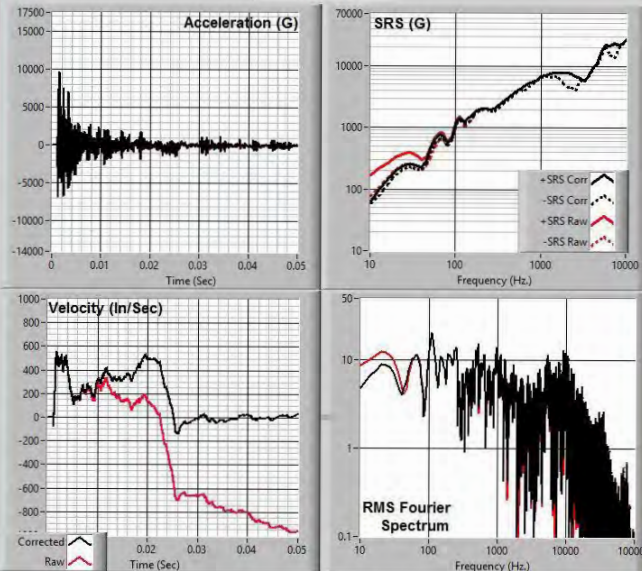
CALCULATED OFFSET ACCELERATION = -24.3 G

RATIO (OFFSET/(PK-PK G)) = -0.0009

Processor ©Strether Smith@comcast.net 2016

TEST 6 Block 6 LEFT ENDEVCO 7280 SN 41800 Channel 13

MEMS



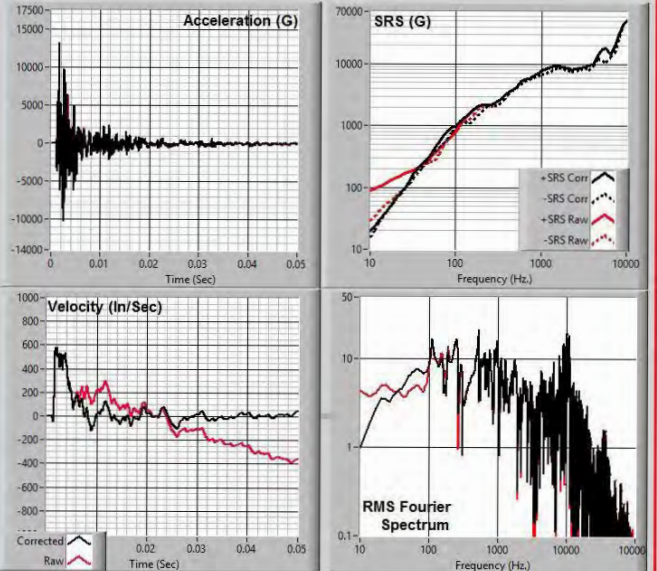
CALCULATED OFFSET ACCELERATION = -40.7 G

RATIO (OFFSET/(PK-PK G)) = -0.0025

Processor ©Strether Smith@comcast.net 2016

TEST 6 Block 6 RIGHT PCB 3991 SN 3824 Channel 15

MEMS



CALCULATED OFFSET ACCELERATION = -33.0 G

RATIO (OFFSET/(PK-PK G)) = -0.0014

Processor ©Strether Smith@comcast.net 2016



WHITE PAPER #61

This WP details the potential sources of zero shifts in pyroshock measurements. These shifts bias the low frequency shock response spectrum (SRS). Among these sources are included the accelerometer mounting, cable effects, over ranging of the amplifier, slew rate limitations, and more. Examples are provided, which illustrate these effects.



Causes of Zero Offset in Acceleration Data Acquired While Measuring Severe Shock

Written By

Anthony Agnello, PCB Piezotronics

Jeff Dosch, PCB Piezotronics

Robert Sill, PCB Piezotronics

Strether Smith, Independent Consultant

Patrick Walter, Texas Christian University

Causes of Zero Offset in Acceleration Data Acquired While Measuring Severe Shock

Anthony Agnello, PCB Piezotronics
Jeff Dosch, PCB Piezotronics
Robert Sill, PCB Piezotronics
Strether Smith, Independent Consultant
Patrick Walter, Texas Christian University

Abstract

One of the most frustrating aspects of the measurement of severe pyroshock events is the acceleration offset that almost invariably occurs. Dependent on its magnitude, this can result in large, low-frequency errors in both shock response spectra (SRS) and velocity-based damage analyses. Fortunately, recent developments in accelerometer technology, signal conditioning, and data acquisition systems have reduced these errors significantly. Best practices, have been demonstrated to produce offset errors less than 0.25% of Peak-Peak value in measured near-field pyrotechnic accelerations: a remarkable achievement.

This paper will discuss the sensing technologies that have come together to minimize these offsets. More important, it will document the many other potential contributors to them. Included among these are accelerometer mounting issues, cable and connector sources, signal conditioning amplitude range/bandwidth, and digitizing errors (e.g. aliasing), and more.

Introduction

Pyroshock is the decaying, oscillatory response of a structure to high-amplitude and high-frequency mechanical excitation (e.g., explosives, metal to metal impact). The frequencies that comprise this oscillatory response can extend to many thousands of Hertz and beyond. A detailed discussion of the process is presented in Reference 1.

An offset in the recorded acceleration-time record characterizing the pyroshock event can preclude its integral (velocity) from returning to zero. This failure of the recorded acceleration record to integrate to zero is typically viewed as an unfavorable metric on data quality.

A small step in the acceleration record when integrated results in a ramp in velocity. Velocity errors can also result from signal clipping and nonlinearity. For the purposes of this paper, a zero shift is any acceleration artifact that corrupts the velocity record and low-frequency shock response spectrum.

Whenever these errors are found, the performance of the accelerometer measuring the event is automatically questioned. However, there are many other sources of offset in the data error path. To obtain good results, all these contributors must be properly addressed.

Advances in Accelerometer Technology

References 2 and 3 provide a history of the evolution of accelerometer technology. Accelerometers are complex-dynamic systems that have resonances associated with their housing, connector, mount, seismic sensing element, and more. If properly designed and mounted, the lowest resonance of their seismic element (f_n) limits the range of frequencies over which their sensitivity can be treated as constant (typically $f_n/5$). Thus, accelerometers historically used to measure pyroshock have been approximated in terms of a simple, lightly-damped oscillator model.

In 1960 Endevco introduced a 100,000 G piezoelectric (PE) accelerometer with a resonance of 80 KHz. Although pyroshock does not normally approach 100,000 G, out of band energy in the early-time material response always excites the resonance of the accelerometer. Thus, early accelerometers attempting to measure pyroshock had to remain linear over a large amplitude range so that their out of band frequencies could be removed by low-pass filtering. This process yielded desired pyroshock characterization to frequencies up to 10 KHz. However, it was noted that this resonance excitation typically imparted a high enough stress into the piezoelectric ceramic element of the accelerometer to induce an offset (zero-shift) in the data. An extensive investigation [4] in 1971 determined this offset

was due to an inherent limitation in ferroelectric ceramics that were available at that time attributable to dipole reorientation under stress.

As a byproduct of Lawrence Livermore sponsored work performed by Endevco in 1970, the Model 2266 radiation tolerant piezoresistive (PR) accelerometer was introduced with diffused gages (4-wire resistive bridge) in ranges to 30,000 G. Application of this model accelerometer in underground nuclear test environments showed it to perform with less zero shift than had been observed with PE accelerometers. A nonradiation hardened PR accelerometer (Model 2264) soon followed for pyro testing. Again, less zero shift in pyroshock environments was observed by users. Based on this success, in 1983 Endevco introduced the Model 7270A piezoresistive accelerometer in the form of a MEMS device with a resonant frequency of up to 1.2 MHz. It was, and still is, manufactured in ranges to 200,000 G.

The 7270A captured a large portion of the pyroshock market. However, a deficiency was found due to the high amplification of its flexure at resonance because it had almost no damping. Despite its extremely high resonant frequency, it was susceptible to breakage due to out-of-band energy. To compensate for this deficiency, an isolated holder was developed [5] to protect it at high frequencies. While it improved reliability, the isolator's size and mass could potentially modify high-frequency structural response.

Between 2008 and 2010 PCB introduced its MEMS-based PR accelerometers (Models 3991 and 3501) in ranges to 60 KG. These accelerometer models were designed with lower resonant frequencies than the 7270A to enable them to incorporate light damping and mechanical stops. Soon after, Endevco introduced the similar 7280A MEMS accelerometer series. Both PCB's and Endevco's developments improved on the fragility associated with the 7270A.

Having abandoned "hard mounted" piezoelectric accelerometer development for pyroshock based on the knowledge gained in Reference 4, in 1988 Endevco developed a Model 7255A Isotron™ (IEPE) accelerometer. It had a range of 50 KG with built-in mechanical isolation and a 2-pole electrical filter. Although this idea was technically sound, testing over the years has shown this model to be nonlinear. PCB improved the mechanical-isolation strategy, and the release of its models 350CO2 (CY 2005) and 350DO2 (CY 2012) effectively solved the nonlinearity problem.

This design approach uses mechanical isolation to reduce the resonant amplification in the piezoelectric element greatly improving the zero-shift issue. The electronic filter compensates for the transfer function of the elastomeric isolator. Thus, the accelerometer can be thought of as a two-degree of freedom system with the higher frequency resonance of the contained PE element suppressed by a combination of mechanical isolation and electrical filtering.

The single-axis accelerometers from Endevco and PCB appropriate for pyroshock including near field are shown in Table 1 and Figure 1.

Endevco 7270A	60 KG	200mV FS	$f_n \sim 600$ KHz	1.5 grams
PCB 3991/3501	60 KG	200 mV FS	$f_n \sim 130$ KHz	1.5 grams
Endevco 7280A/AM4	60 KG	200 mV FS	$f_n \sim 130$ KHz	1.5 grams
PCB 350DO2	50 KG	5000 mV FS	f_n suppressed	4.5 grams

Table 1. Comparison of Characteristics of Comparable Range Pyroshock Accelerometers



Figure 1. Physical Envelope of Pyroshock Accelerometers, left to right: 7270 A (form also standard for 3991 and 7280A), 3991/3501 with surface mount, 350DO2

Recent Comparative Pyroshock Tests and Results

In CY 2016 a carefully planned sequence of “live pyro” tests was performed to compare the performance of candidate accelerometers. These included those models listed in Table 1 along with a few others. Details of this test and the results can be found as reference 6.

As occurs in most pyro testing, none of the acceleration records were free of zero shift and hence did not integrate to zero. However:

One of the remarkable findings of the study was that the acceleration offsets were remarkably small. For most of the records, the offsets were less than 0.25% of the Peak-to-Peak acceleration response. The minimum offset in all testing was 0.02% of the Peak-Peak response. For the MEMS devices, this value corresponded to 20 microvolts.

Even these tiny errors cause enormous discrepancies in the calculated SRS at frequencies below 100 Hz.

In the more severe tests in this sequence, Peak-to-Peak measured pyroshock was 30 KG. Across five tests, valid data was recorded on 53 of 55 recorded channels. This was a remarkably high data return in such an energetic environment and a testimony to the quality of the testing performed.

In the collective authors’ opinion, these results were as good as could be expected. They represent a threshold as to how well pyroshock data can be recorded today. (All of the small offsets were corrected by post processing and yielded valid test results.)

As noted in the Introduction, although the accelerometer performance is usually indicted, many other contributors can be responsible for these small data offsets. The following attempts to identify all the potential sources in the measurement system that can cause these small offsets

Offset Sources Associated with the Accelerometer

Often the offset error from the accelerometer is a result of improper use and not an inherent defect in the accelerometer. Common usage errors include use of the sensor beyond its specified range, inadequate mounting torque, poor mounting surface, inadequate cable strain relief, or insufficient supply current (for ICP® type signal conditioning).

Fundamentally a physical cause of offset error is the transmission of undesired stress into the sensing element [9]. The challenge in accelerometer design is an accelerometer that responds only to acceleration along its sensing axis while rejecting all other mechanical, thermal, and electrical inputs. Pyroshock is a complex environment with acceleration along all axes, large dynamic strain transmitted through the sensor mounting surface, and large inertial forces applied to cable connections.

Zero shift in PR sensors is not inherent to the silicon structure itself (Figure 2a). Rather, it is the result of residual stresses transmitted through various interfaces in the sensor die and packaging (Figure 2b). Silicon is a crystalline linearly elastic material without hysteretic characteristics that might cause a non-return to zero. Piezoresistive gage areas are created by implanting dopants into the silicon resulting in a unitary crystalline structure. When subject to shock below its fracture strength, the silicon structure in isolation cannot permanently deform. However, PR accelerometers can zero shift when shock induced residual stresses are transmitted into the active gage area of the silicon sensing structure. These stresses originate at stressed interfaces such as die bond layers, die packaging, wiring, or at the sensor mounting interface. In designing a PR accelerometer for pyroshock, it is the goal to minimize transmission of residual stress into the active gage area of the silicon structure. Out-of-band high-frequency content and subsequent sensor resonant ringing is another potential source of zero offset resulting in bad data or even permanent damage to the sensor. A successful design strategy to eliminate this influence is a controlled gap between the moving sensing element and the core/lid. The controlled gap provides both viscous air damping and overrange stops that engage when the sensor is subject to shock beyond its specified range.

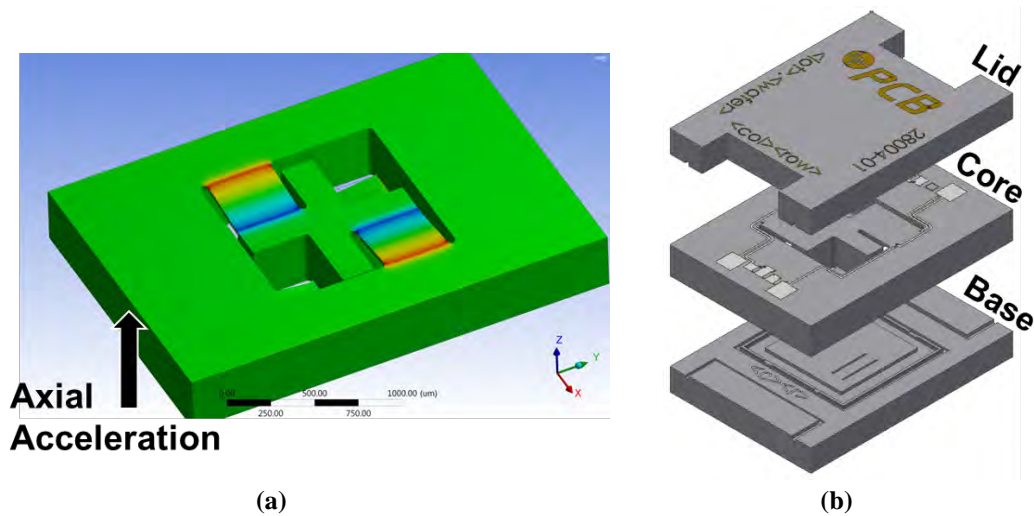


Figure 2. Piezoresistive MEMS element (a) and die package (b). Red color on the element indicates an area of high strain and good location for the implanted piezoresistive gage.

Residual stress is also a cause of zero shift in PE accelerometers. Isolation from this residual stress is a challenge because of the large active volume of the piezoceramic element. A typical piezoceramic sensing element may be an annular cylinder with diameter x height of 2 mm x 3 mm (Figure 3). Piezoelectric charge will be generated if stress is applied to any part of this volume. This contrasts with PR silicon element in which the active gages are small structures of approximately 0.1 mm in length.

With PE accelerometers, dipole realignment is an additional source of zero-shift for certain piezoceramic materials [4]. A successful design strategy for PE accelerometers is the incorporation of a built-in mechanical isolator and use of special piezoceramics that do not exhibit the dipole switching phenomenon. The mechanical isolator serves two functions. It filters out of band high-frequency energy and reduces strain transmission into the piezoceramic element. The isolator must be designed to be linear over the sensor operating range so that isolator nonlinearity is not a cause of offset error.

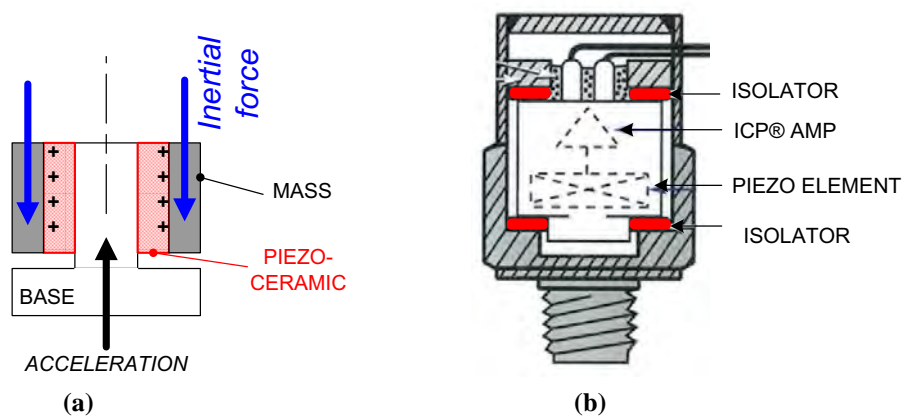


Figure 3. Piezoceramic element (a) and packaged sensor (b). Mechanical isolator isolates both the piezoceramic element and ICP® amplifier from out-of-band energy.

Even the best-designed accelerometer will exhibit zero shift when subject to over range. When an accelerometer is subject to acceleration beyond its specified range, the output may become nonlinear, its signal may clip, and under severe conditions the sensor may suffer permanent damage. This error is insidious in that when overrange occurs, the actual peak acceleration level is not always observable in the acquired data record. This may be because the overrange acceleration occurred in a direction transverse to the sensing axis or the bandwidth of the sensor/measuring chain is insufficient to detect it. Pyroshock can have significant high-frequency content, extending to the megaHertz range and this high-frequency energy is typically filtered out by any number of components in the measuring chain.

For undamped PR accelerometers, there is the possibility that high-frequency pyroshock energy may induce excessive sensor ringing. The peak amplitude of the ringing may extend into the nonlinear operating range of the accelerometer or, in cases of sufficient magnitude, fracture the silicon sensing element. Silicon is an extremely low loss material and sensing elements fabricated without intentional damping can have Q (quality factor) well more than 1000. For undamped PR sensors, a mechanical isolator can greatly improve sensor survivability. Good data can be obtained as long as the isolator itself does not introduce signal nonlinearity. Alternatively, “lightly damped” PR sensors with Q values of approximately 30 have been demonstrated to provide improved linearity and survivability without the need for an additional isolator.

Examples of accelerometer offset due to “misuse” are demonstrated using PCB’s Hopkinson Bar Calibration System (Figures 4 through 11). The Hopkinson bar is an ideal demonstration platform as the test variables can be well controlled. The sensor under test is mounted on one end of a long slender bar and impacted by a projectile at the opposite end [10]. This produces a stress transient that propagates back and forth in the bar as a series of pulses with peak acceleration levels that can exceed 100,000 G. Integration of the acceleration record (integrated to velocity) produce a series of half sine shock pulses that theoretically returns to zero velocity after each pulse. A metric for “a bad” data record that contains accelerometer offset error is velocity that does not return to zero after the acceleration pulse.

In the first example (Figure 4), an ICP® piezoelectric accelerometer (PCB Model 350D02, contains integral mechanical filter) is mounted to the end of the Hopkinson bar with a 0.003-inch-thick piece of flat solder underneath it, mimicking a surface imperfection such as a thread burr that might be found in field application. With a good mounting surface, the velocity is well behaved, returning to zero after each acceleration pulse (Figure 4b). With debris on the mounting surface, the velocity does return to zero between impacts.

The second example demonstrates the importance of choosing a PE accelerometer with a well-designed mechanical isolator (Figure 5). The integral mechanical isolator must be linear over the full shock acceleration range and the isolator’s resonance must be well-beyond the frequency band of interest. In this demonstration, the PCB Model 350D02’s velocity properly returns to zero after each impact (Figure 5b). In contrast, the mechanical isolator in the legacy model is not properly designed for the shock environment, exhibiting non-linearity and in-band resonance resulting in zero offset (Figure 5c).

The third example demonstrates the importance of reliable cable connections (Figure 6). Arguably the cable connection is the weak link in the measuring chain and first suspect when bad data is obtained. In this example a 10-32 microdot connector connects the coaxial signal conditioner cable (blue) to the twin lead sensor cable (red and white). The connector assembly is tied down to the Hopkinson bar mimicking cable motion that might be encountered in the field during a shock event. With connector’s knurled nuts fully engaged the sensor does not exhibit zero offset (Figure 6b). When one of the nuts is not fully engaged there is movement between the connector pin and socket resulting in zero shift (Figure 6c). It should be noted that the poorly engaged connector only exhibits brief intermittency during the highest levels of shock. Under most conditions the sensor would test acceptably. Because of the intermittent nature, this is something that would be difficult to diagnose in the field.

The fourth example demonstrates the importance of sufficient supply current when ICP® type sensors are used with long cables (Figure 7). Supply current sufficient to drive cable capacitance is required to avoid signal slew distortion [8]. To conserve battery life, most ICP® battery conditioners are set to 2 mA. Of the data acquisition systems that have integral ICP® signal conditioning, many have supply current limited to only 4 mA. In this example, the sensor has a 4000 pF load equivalent to 130 feet of 30 pF/foot cable between sensor and signal conditioner. The sensor does not exhibit zero offset with 10 mA supply current (Figure 7b) but does when supply current is 2 mA (Figure 7c).

The fifth example demonstrates the importance of using the recommended mounting torque (Figures 8 and 9). With proper mounting torque, the sensor does not exhibit zero offset (Figures 8b and 9b). With inadequate mounting torque, the sensor exhibits zero offset (Figures 8c and 9c) as well as ringing (Figure 8c).

The sixth and last example demonstrates the importance of the signal conditioner with gain properly chosen as to not over range (Figure 10). In this example the signal gain is sufficient to clip the peak accelerometer signal, resulting in zero offset in the velocity record (Figure 10c). Clipping in the signal conditioner is insidious in that the clipping in the accelerometer record may be masked by subsequent low pass filter stages.

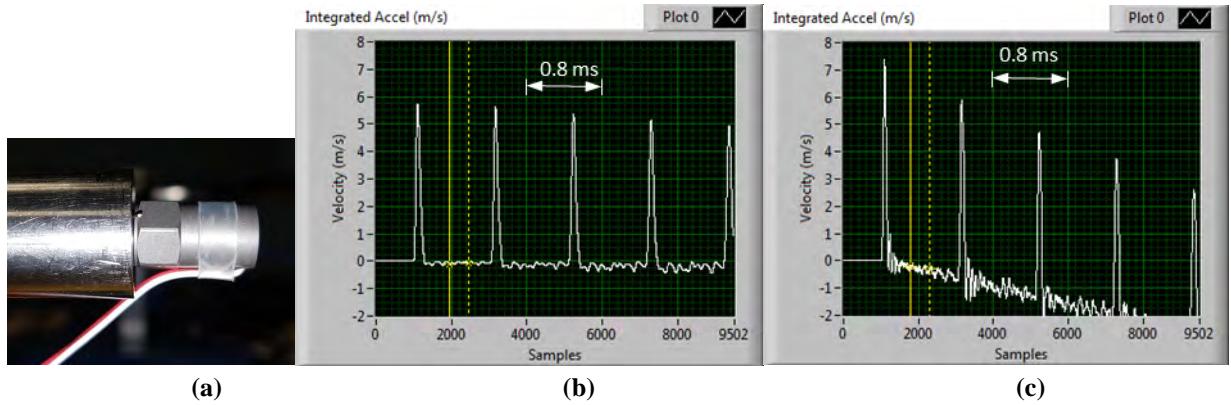


Figure 4. Shock at 25,000G peak with varying surface conditions. PCB Model 350D02 ICP® PE sensor on Hopkinson bar (a); integration to velocity with good mounting surface (b); and integration to velocity with 0.003-inch-thick debris on the mating surface at (c).

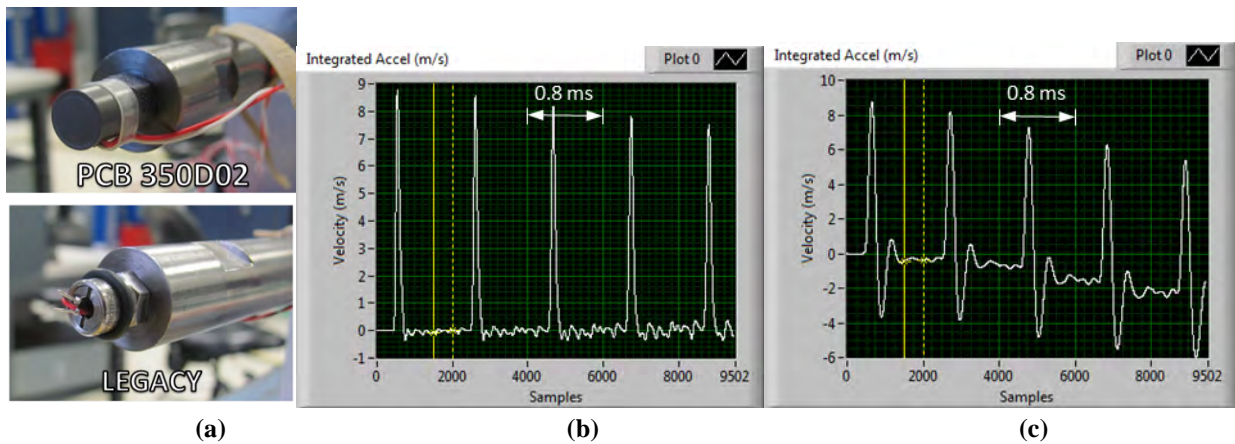


Figure 5. Shock at 50,000G peak with varying sensor models. PE sensor models with integrated mechanical isolators mounted on Hopkinson bar (a); integration to velocity of PCB Model 350D02 PE sensor (b); and integration to velocity of legacy PE sensor (c).

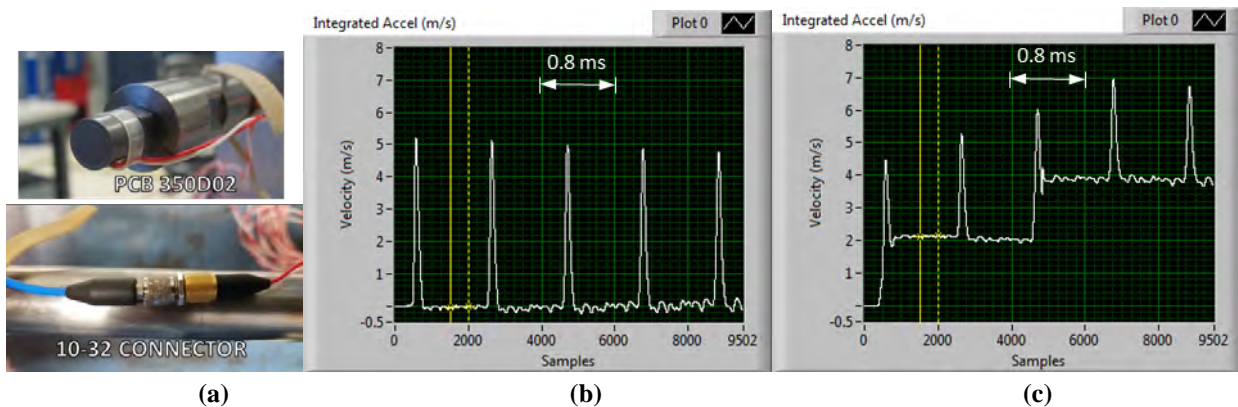


Figure 6. Shock at 28,000G peak with varying connection integrity. PCB Model 350D02 sensor mounted to end and cable/connector attached to the side of Hopkinson bar (a); integration to velocity with connector nuts tight (b); and integration to velocity with one of the nuts not fully engaged (c).

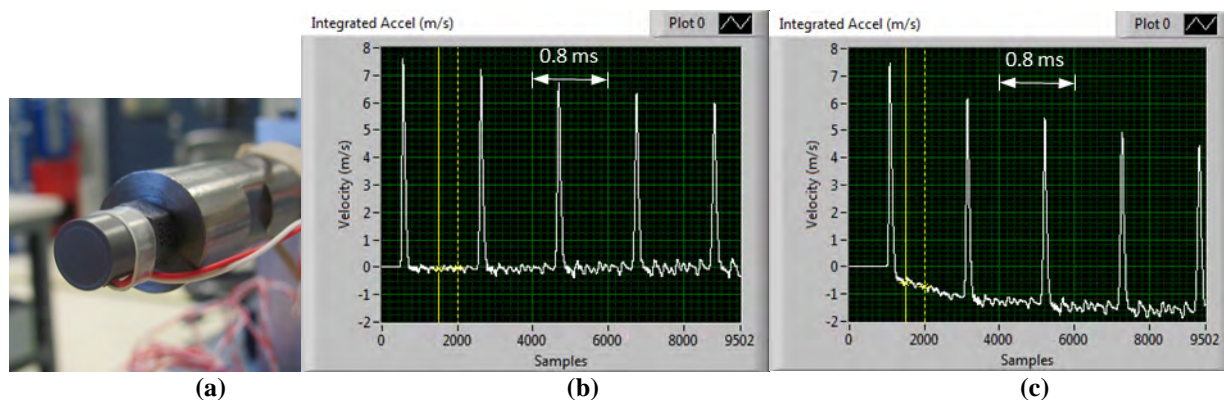


Figure 7. Shock at 60,000G peak with 130-foot long coaxial cable (4000 pF capacitance) and varying ICP® supply current. PCB Model 350B21 ICP® PE on Hopkinson bar (a); integration to velocity with 10 mA supply current (b); and integration to velocity with 2 mA supply current (c).

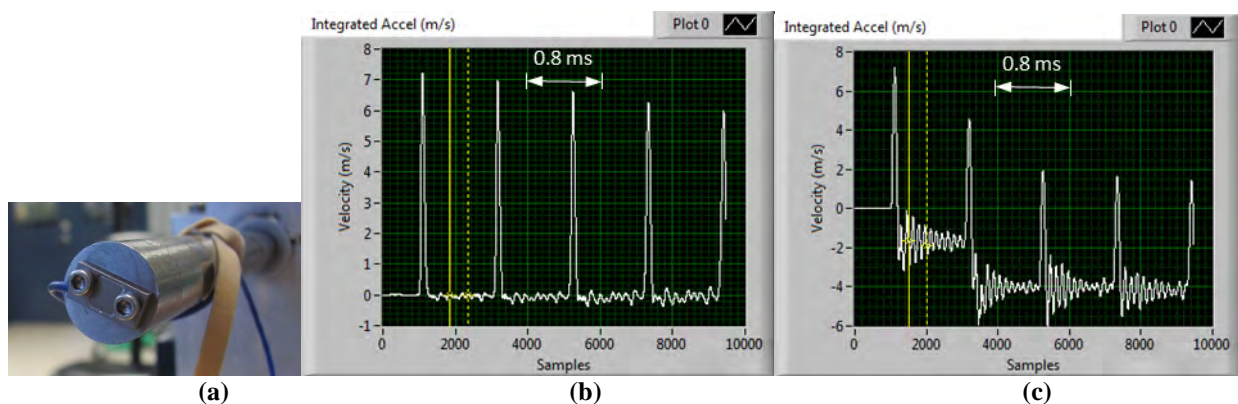


Figure 8. Shock at 50,000G peak with varying mounting torque. PCB Model 3991-60KG PR MEMS sensor mounted to Hopkinson bar (a); integration to velocity with proper mounting torque (b); and integration to velocity with inadequate torque on one of the two screws (c).

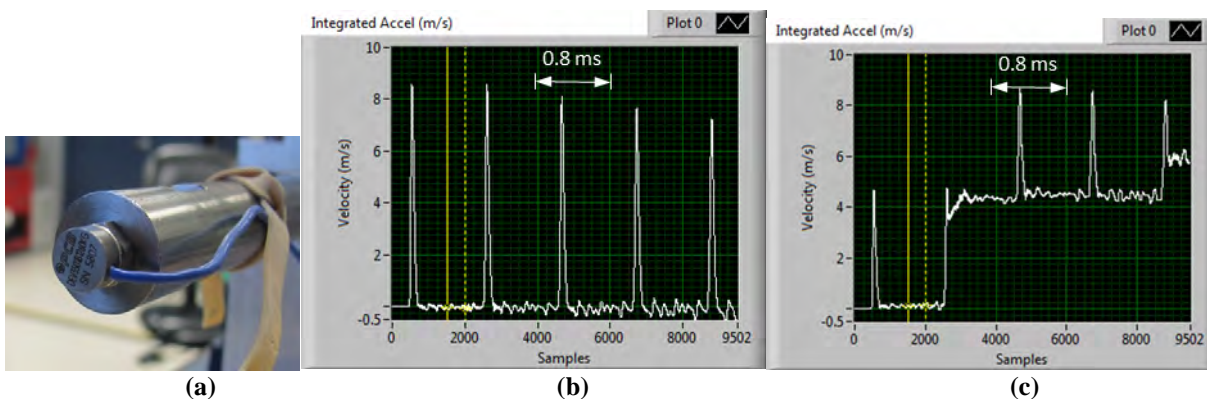


Figure 9. Shock at 50,000G peak with varying mounting torque. PCB Model 3501-50KG PR MEMS sensor mounted to Hopkinson bar (a); integration to velocity with proper mounting torque (b); and integration to velocity with inadequate torque (c).

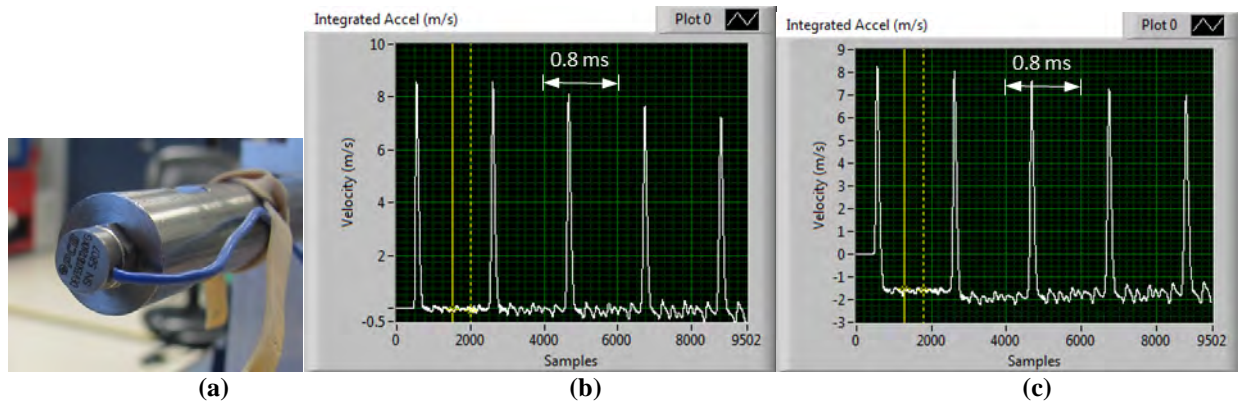


Figure 10. Shock at 60,000G with varying conditioner gain. PCB Model 3501-60KG PR MEMS sensor mounted to Hopkinson bar (a); integration to velocity with adequate ranging of signal conditioner gain (b); integration to velocity with excessive gain causing clipping in signal conditioner (c).

Offset Sources Associated with the Cable

The accelerometer cable can modify the signal passing through it by introducing both unintended filtering and/or internally generated noise. Noise generation within the cable is identified by the term triboelectric effect. This effect will subsequently be discussed after first considering the potential for filtering introduced by the cable.

When using ICP® type accelerometers to measure mechanical shock at frequencies of 10,000 Hz or higher, as noted previously, the capacitance associated with the cable may require higher drive currents than the typically supplied 2-4 milliamp. If required, this increased current would be necessary to eliminate signal amplitude distortion attributable to the cable capacitance. The technical and mathematical justification for increasing current with cable capacitance is provided in reference 7. Readily available charts (reference 8) provide this frequency vs. current relationship for varying values of cable capacitance.

For MEMS accelerometers, the cable capacitance and any additive line resistance, coupled with the resistive bridge source resistance, will result in a low pass RC filter. For example, 5000Ω source impedance (typical for some MEMS sensors) driving 60 feet of coax (e.g., RG58 = 25 pF/foot) will result in -3dB attenuation at 21,000 Hz.

Independent of ICP® or MEMS accelerometer type, early filtering in the cable can result in a data offset by masking the fact that a given accelerometer has exceeded its linear range.

Triboelectric effects result in random noise generation in cables and this noise does not have to be statistically symmetric. Thus, it can result in small zero offsets when averaged. This effect is important to understand when dealing with bridge type sensors providing millivolt level signals or accelerometers without contained electronics (non ICP®). For this effect to occur there must be cable motion. The triboelectric effect (also known as *triboelectric charging*) is a type of contact electrification in which certain materials become electrically charged after they come into contact with a different material and then become separated (such as through rubbing). The polarity and strength of the charges produced differ according to the material types, surface roughness, temperature, strain magnitude, and other parameters. Thus, this effect is not very predictable, and only broad generalizations can be made about it. Since all instrumentation cables are combinations of metal conductors, inner dielectrics, metal shields, and outer jackets of differing materials, it would be expected that any motion of the cable would result in some triboelectric effect (signal generation). This motion can be attributed to cable vibration or, in mechanical impact environments where cables are taped or securely tied down, cable compaction due to traveling stress waves underneath them. The greater the relative motion between the cable constituents, the more charge that is generated. Figure 11 shows one example of this charge generation within a coaxial cable.

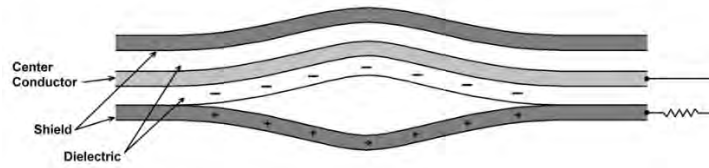


Figure 11. Charge Buildup Due to Cable Motion

Offset Sources and Other Errors Associated with the Signal Conditioning and Data Acquisition Systems (DAQs)

When performing pyroshock testing the objective is normally to provide a good estimate of the shock response spectrum at frequencies up to 10KHz. As noted in the introduction to this paper, the failure of a recorded pyroshock pulse to integrate to zero results in low-frequency errors in the SRS causing data quality to be questioned.

Additional data acquisition faults that may produce offsets and resultant velocity errors include the following bulleted items:

- Zero offset-and low-frequency drift.
 - Small offset errors will seriously affect analysis results.
- Measurement over-range problems.
 - Signal saturation will distort the results and may affect offsets.
 - Signal slew-rate-capability exceedance will cause offsets.
- Inadequate alias protection and sample rate/time resolution.
 - Aliasing of the signal will corrupt all frequencies including the offset (0 Hz).
 - SRS analysis specifications (to be discussed) set the requirement for minimum sample rate.

To provide data to explore the data acquisition challenges, an experiment was performed by Mark Remelman [13] using Spectral Dynamics' explosive test fixture. Two accelerometers, Endevco 7270-20K and PCB 350D02, were tested in a back-to-back configuration and the signals were measured using a Spectral Dynamics VIDAS data acquisition system sampling at 5,000,000 samples/second.

The data from the 7270 will be used to demonstrate the effect of the errors listed above. The voltage response has gain applied to make it's time history peak = 1 volt as shown in Figure 12. Pertinent derived parameters are:

- Upper Left Frame: The voltage output (normalized to 1 V).
- Middle Left Frame: Slew rate in Volts/ μ Second
- Lower Left Frame: The integral, proportional to velocity, which (correctly) approaches zero after the shock.
- Upper Right Frame: The positive (solid) and negative (dotted) Shock Response Spectrum. The two curves agree well.
- Lower Right Frame: The RMS Spectrum that shows:
 - Significant signal energy out to 700 KHz.
 - The transducer resonance at 415 KHz.

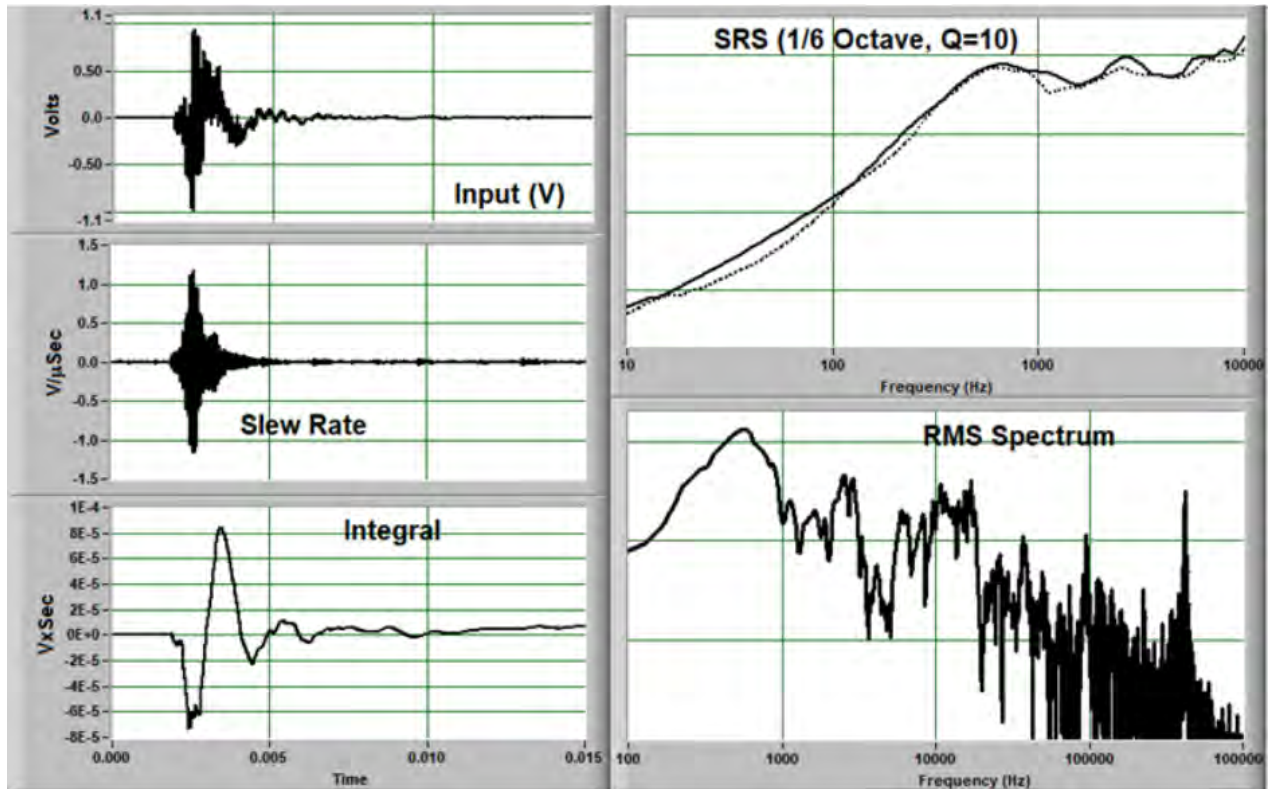


Figure 12. Shock Response Measured with an Endevco 7270
Scaled to 1 Volt Peak

The following four examples use analytically-generated errors to demonstrate their effects on this data set.

1. The Effect of Offset

Figure 13 shows the effect of adding an offset of 1% of the peak value to the data. The integral and low-frequency shock response spectrum (RED) are significantly compromised. In Figures 13-16, BLACK represents the original signal (Figure 12).

In the real world, offsets in the measured data typically occur. The output from MEMS devices can contain offsets due to bridge unbalance and/or any dc acceleration component. The signal conditioning and data acquisition system will also introduce small offsets. All of these must be corrected.

As has been noted, this error is typically dealt with in data post processing.

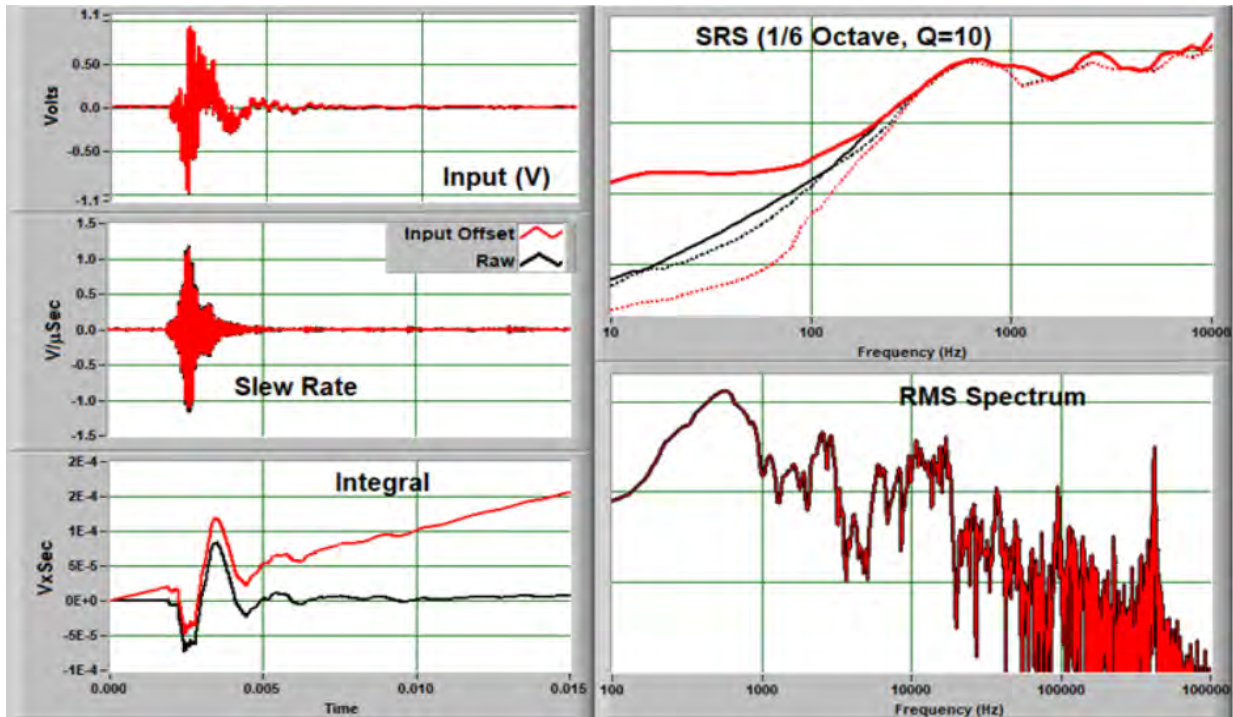


Figure 13. Effect of 1% Offset

2. The Effect of Amplitude Clipping

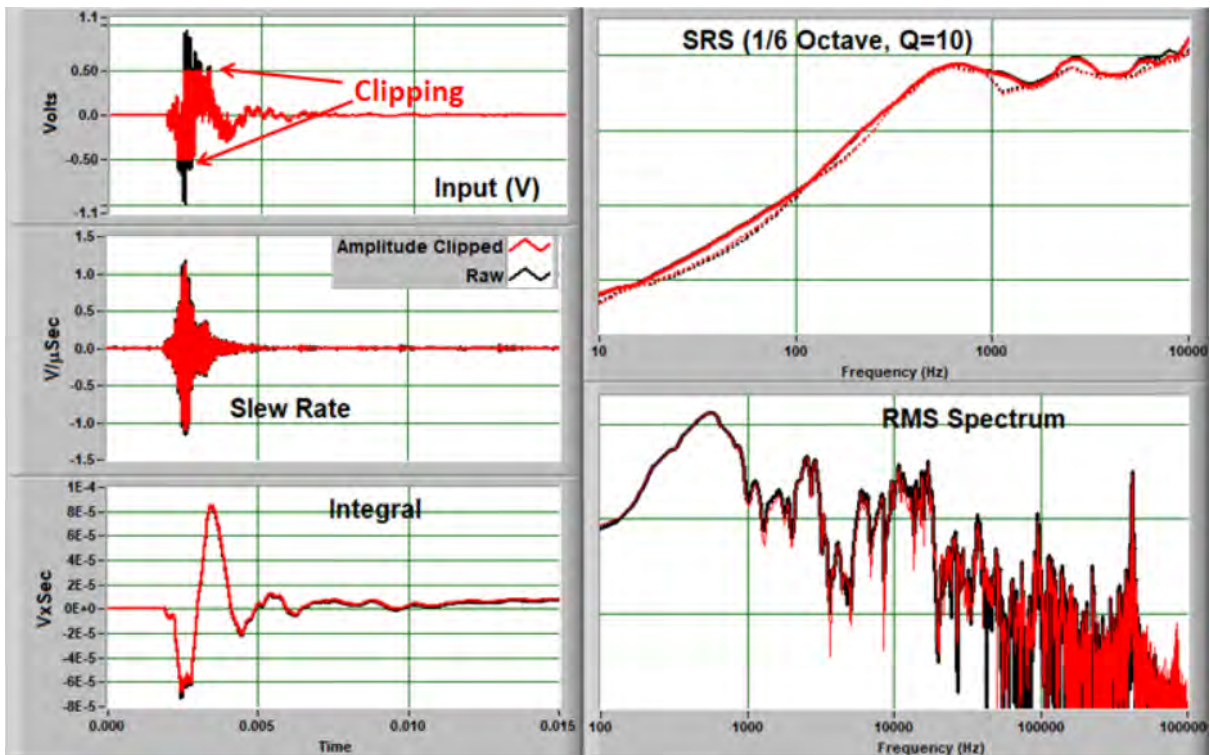


Figure 14. The Effect of 50% Amplitude Clipping

Surprisingly, even drastic clipping, like that shown in Figure 14, does not produce significant offsets (or significant discrepancies in other indications). Only the time record shows the (obvious) error.

Ones sided clipping (as seen in the example in Figure 10) may show more significant errors.

In any case, this data set is corrupt, and the test must be rerun with a wider input range.

3. The Effect of Slew Rate Clipping

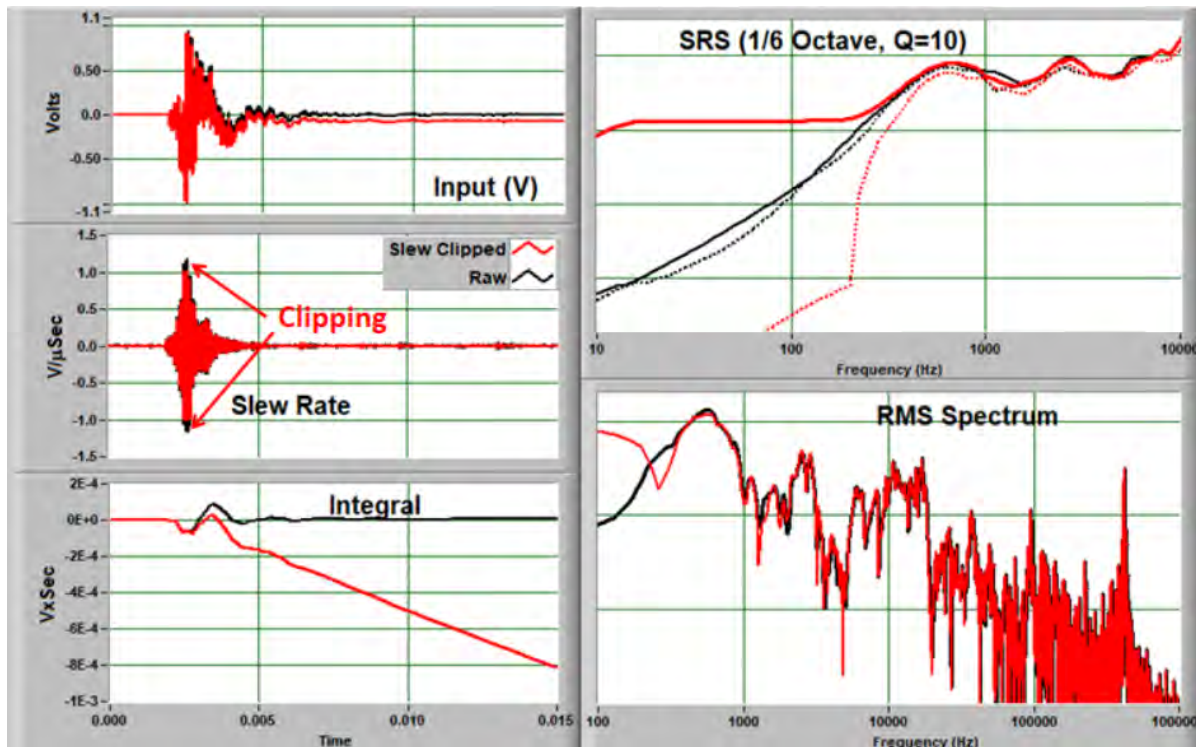


Figure 15. The Effect of Slew-Rate Clipping

Figure 15 shows the effect of a very small clipping on the slew rate. If the amplifier processing this signal is limited to $1 \text{ V}/\mu\text{Second}$, there are significant offsets. The offset starts at the peak of the slew rate which is also near the peak of the shock. Hence, it looks like an offset error that might be produced by the transducer (discussed above).

Slew rate is an increasingly important consideration when using essentially undamped accelerometers with their associated very high resonant frequencies (e.g. Model 7270). A detailed study of the record in Figure 12 was performed by one of the authors (S. Smith) of this paper. It concluded that when applying gain to the 7270 to acquire the equivalent signal levels as the 350DO2 to 10 KHz, the slew rate demands on the signal conditioning channel for the 7270 in this instance were 15 times greater than that required for the 350 DO2.

4. The Effect of Aliasing

Aliasing errors corrupt the entire frequency range. If energy is aliased to near zero frequency, offsets will occur as shown in Figure 16.

In this case, the sampled signal in Figure 12 has its digitization rate decimated to 40 KS/S without appropriate anti-aliasing filtering. Thus, all the signal energy content above 20 KHz (i.e., the Nyquist frequency) is folded to lower frequencies. Specifically, data frequency content between 20 KHz and 40 KHz is moved to between 0 and 20 KHz, which results in offset components. In fact, this folding occurs multiple times [12].

Again, this error starts near the shock peak, so it looks like a transducer-shock offset.

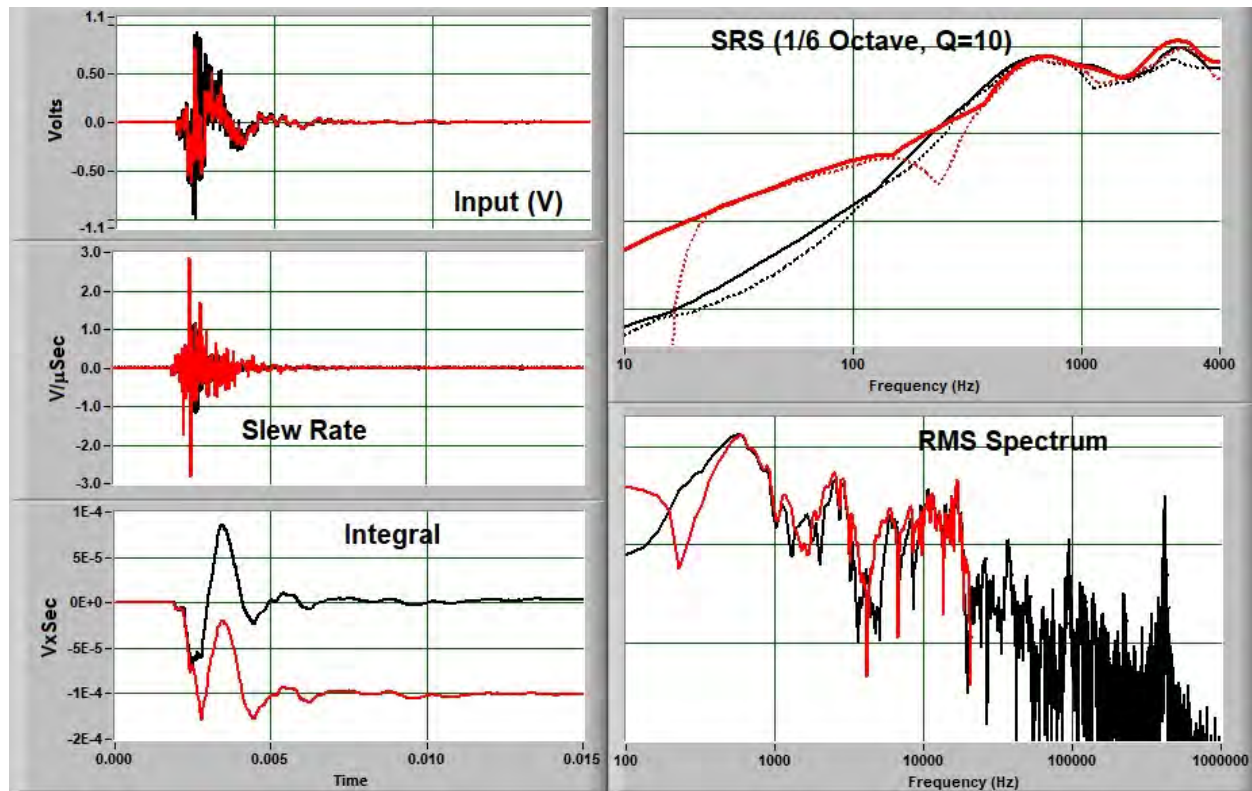


Figure 16. The Effect of Aliasing

Basic Data Acquisition System Requirements

Classical Shock Response Spectrum (SRS) analysis practice requires a minimum of 10 points/cycle at the maximum SRS analysis frequency (normally 10KHz.) which leads to a minimum sample rate of 100KS/S. With this sample rate, appropriate data systems can provide an acquisition bandwidth of 30KHz. Acquisition of ten points/cycle assures that the SRS magnitude estimate (peak SRS band response) will be within 5% of the truth.

Summary and Conclusions

Prior testing in harsh field environments (e.g., pyrotechnic shock) has demonstrated that, for properly designed instrumentation systems, signal offsets from accelerometers can be limited to an extremely small magnitude. The following list summarizes the potential offset contributors that have been discussed in this work.

- Accelerometer related:
 - Residual stress externally induced in the accelerometer during the shock event can result in signal offset. This applies to both MEMS (piezoresistive, i.e., PR) and piezoelectric (PE) accelerometers.
 - Dipole realignment that results in an offset can occur in select ferroelectric ceramic accelerometers. This offset can be minimized or eliminated by assuring that the piezoelectric element operates at low stress levels. The newer design mechanically-isolated, electrically-filtered piezoelectric accelerometers solve this problem.
 - Improper accelerometer mounting torque and/or inadequate mounting surface preparation, as illustrated by examples in this paper, can readily induce stress in the sensing element of the accelerometer resulting in signal offsets.

- Cable related:
 - Motion-related cable interconnect issues can result in offsets in recorded signals through inadvertent electrical grounding and/or intermittency between the cable center pin and its mating receptacle.
 - Triboelectric effects generated within the cable due to vibration or mechanical impact can produce asymmetric acceleration baseline noise resulting in offsets.
- Nonlinearities at any location in the instrumentation system:
 - Improper selection of gain in the signal-conditioning amplifier allowing the data channel to over range will result in a zero offset.
 - Subsequent filtering in the instrumentation system can obscure the fact that this over range condition has occurred. This filtering can even occur attributable to capacitance in interconnect cables.
 - Improper isolator design in a mechanically isolated accelerometer can result in nonlinearities with resultant signal zero offset.
 - Undamped legacy MEMS accelerometers (Endevco 7270A) are particularly susceptible to over range situations due to their high Q. This occurs when the accelerometer resonance is excited by out of band energy. MEMS accelerometers are now available with slightly more damping (Q=30 or less) to help lessen this resonance response. The mechanically-isolated, electrically-filtered PE accelerometers largely eliminate this out of band energy.
 - Slew rate limitations in the electronics are another potential source of nonlinearities and resultant base line offsets.
 - For ICP circuits, inadequate supply current when driving long cables at high frequencies can result in signal slew distortion.
 - The extremely high resonant frequencies (> 500 KHz) of the undamped legacy MEMS accelerometers (Endevco 7270A) can readily create offsets in recorded signals due to slew rate limitations in their signal conditioning electronics.
- Aliasing:
 - Inadequate sampling rate relative to the spectral content of the signal can result in high frequencies in the spectrum being “folded” down to lower frequencies, which can result in a zero offset.

As noted in the introduction to this paper, the recorded signal emanates from an accelerometer and thus it is often blamed for any offsets occurring in the data. However, as has been demonstrated, these offsets can and do occur in all components of the instrumentation system. Critical attention to all these potential contributors is required to make adequate pyroshock measurements. Hopefully the references provided below will also provide additional contributory guidance.

References:

1. MIL STD 810 Issue G, MIL-STD-810G – Part 19 (Pyroshock) Method 517, 2015.
2. Walter, Patrick L., History of the Development of the Accelerometer, 50 Years of Shock and Vibration Technology, SAVIAC SVM-15, ed. Henry C. Pusey, pp. 376-385, 1996.
3. Walter, Patrick L., The History of the Accelerometer, *Sound and Vibration*, pp. 84-92, January 2007.
4. Plumlee, R. H., Zero-Shift in Piezoelectric Accelerometers, Sandia National Laboratories Research Report, SC-RR-70-755, March 1971.
5. Bateman, V. T., Bell, R. G., and Davie, N. T., Evaluation of Shock Isolation Techniques for a Piezoresistive Accelerometer, Proceeding 60th Shock and Vibration Symposium, hosted David Taylor Research Center, Underwater Explosions Research Division, Portsmouth, Virginia, November 1989.
6. Agnello, Anthony, Sill, Robert, Smith, Strether, and Walter, Patrick, Evaluation of Accelerometers for Pyroshock Performance in a Harsh Field Environment, Proceedings 87th Shock and Vibration Symposium, New Orleans, LA, October 2016 (also available as PCB Piezotronics White Paper No. 60).

7. Walter, Patrick L., The instrumentation cable: critical but often neglected, *Test Engineering and Management*, pp. 8-11, December/January 2014-2015.
8. High Frequency Response of ICP® Sensors, http://www.pcb.com/Resources/Technical-information/tech_signal.
9. Agnello, A., Dosch, J., Metz, R., Sill, R., and Walter, P., Acceleration Sensing Technologies for Severe Mechanical Shock, *Sound & Vibration*, February 2014.
10. Dosch, Jeffrey, Lin Jing, "Hopkinson Bar Acceptance Testing for Shock Accelerometers," *Sound and Vibration*, Vol. 33 Issue 2, pp 16-21, February 1999.
11. Smith, Strether, "Acquiring and Analyzing Pyrotechnic Test Data the Right Way" *Sound and Vibration Magazine*, September 2008.
12. Edwards, Timothy S., Effects of Aliasing on Numerical Integration, *Mechanical Systems and Signal Processing*, Volume 21, Issue 1, January 2007, Pages 165-176.
13. Thanks to Mark Remelman of Spectral Dynamics for providing the basic time history.



WHITE PAPER #85

This WP discusses signal modification attributable to the electrical impedance of cables for MEMS (Micro-Electro-Mechanical-Systems) Shock Accelerometers. No matter how well designed, an instrumentation system can only correctly condition and record signals from transducers if these signals are transmitted with fidelity via the cable interfacing the transducer to the system. For MEMS (Micro-Electro-Mechanical-Systems) piezoresistive (PR) shock accelerometers, the two main cable concerns are signal modification due to: (1) additive triboelectric noise generated within the cables and/or (2) unknown or unaccounted for electrical impedance characteristics of the cable. Small diameter, lightweight, (e.g. AWG 36) integral, 4-conductor, shielded cables are required for interconnection to the 1.4 grams or less accelerometers in order to avoid mass loading of the article under test. These cables are specially design for the shock environment, and the WP provides some useful calculations to help the end user estimate their signal loss for these specific cables types and lengths.



MEMS Shock Accelerometers

Signal Modification Attributable to the Electrical Impedance of Their Cables

Written By

Patrick L. Walter, PCB Piezotronics

Alan Szary, Precision Filters, Inc.

James Woernley, Precision Filters Inc.

**MEMS SHOCK ACCELEROMETER SIGNAL MODIFICATION ATTRIBUTABLE TO THE
ELECTRICAL IMPEDANCE OF THEIR CABLES**

FINAL: March 2021

**Patrick L. Walter
Measurement Consultant, PCB Piezotronics
Professor Emeritus, TCU Engineering
Fort Worth, TX 76129**

**Alan Szary
VP Engineering & Business Development, Precision Filters, Inc.
Ithaca, NY 14850**

**James Woernley
Application Engineer, Precision Filters Inc.
Ithaca, NY 14850**

ABSTRACT

No matter how well designed, an instrumentation system can only correctly condition and record signals from transducers if these signals are transmitted with fidelity via the cable interfacing the transducer to the system. For MEMS (Micro-Electro-Mechanical-Systems) piezoresistive (PR) shock accelerometers, the two main cable concerns are signal modification due to: (1) additive triboelectric noise generated within the cables and/or (2) unknown or unaccounted for electrical impedance characteristics of the cable. Small diameter, lightweight, (e.g. AWG 36) integral, 4-conductor, shielded cables are required for interconnection to the 1.4 grams or less accelerometers. Larger diameter attachment cables would degrade the structural performance of the accelerometer. The effects of triboelectric noise within these small diameter cables has been documented and solutions provided.⁴ The subject of this research is the influence of the electrical impedance of the cable on the gamut of MEMS accelerometers designed to operate in severe shock environments. This influence is primarily a function of the combined cable/MEMS element high frequency RC time constant. Challenges exist in determining this time constant, and a method is proposed for accurately predicting system frequency limitations posed by *individual* cable and sensor characteristics. Electrical bench testing has verified the accuracy of these predictions. A hardware solution, *AC Shunt Calibration*, is provided to determine in-situ instrumentation system frequency constraints accurately and efficiently prior to test initiation.⁶ Last, mechanical shock testing was performed and was shown to correlate with results of the electrical bench testing.

INTRODUCTION

In 2019, PCB Piezotronics executed an agreement with Meggitt PLC (MGGT.L) to purchase the assets of its Endevco sensor business. Not surprisingly, the sensor product lines of Endevco, established in 1947, and PCB, established in 1967, overlapped in many areas. In the aerospace and defense (A&D) sector, the strong suit of both companies lay in manufacturing accelerometers to measure severe mechanical shock. Examples of these shocks are encountered in structures exposed to impact and explosive loading. PCB had previously developed a line of mechanically isolated piezoelectric accelerometers with incorporated electronics (ICP®) and low-pass filters (e.g., model 350DO2). These had been verified to yield excellent shock reproduction at frequencies up to 10 KHz at acceleration levels up to and exceeding 10's of thousands of Gs.¹ The significant overlap in products was between the two companies' MEMS (PR) based accelerometers. Micro-Electro-Mechanical Systems, or MEMS, represent a technology that evolved from the semiconductor device fabrication market. It can be defined as miniaturized mechanical and electro-mechanical elements (i.e., devices and structures) that are made using the techniques of microfabrication. The critical dimensions of MEMS devices can vary from well below one micron, on the lower end of the dimensional spectrum, up to several millimeters. The competitive MEMS-based accelerometer models for severe shock, with ranges of 20,000 G or above, are listed in the first two filled columns of TABLE 1 below.




MEMS (PR) ACCELEROMETERS FOR SEVERE SHOCK							
MODEL							
ENDEVCO 7270A	RANGES (KG)	MINIMUM Rout OHMS	MAXIMUM Rout OHMS	SUPPLY VOLTS V	F.S. OUT (NOMINAL) (mV)	RESONANT FREQUENCY (KHZ)	USEABLE FREQUENCY (KHZ)
	20	350	950	12 MAX	200 typical @ 10V	350	50
	60	350	950	12 MAX	200 typical @ 10V	700	100
	200	350	950	12 MAX	200 typical @ 10V	1,200	150
					DAMPING < 0.007 CRITICAL NO MECHANICAL STOPS		
ENDEVCO 7280A	RANGES (KG)	MINIMUM Rout ohms	MAXIMUM Rout ohms	SUPPLY VOLTS V	F.S. OUT (NOMINAL) (mV)	RESONANT FREQUENCY (KHZ)	USEABLE FREQUENCY (KHZ)
	20	4000	9000	12 MAX	300 typical @ 10V	100	10
	60	4000	9000	12 MAX	300 typical @ 10V	130	13
					DAMPING < 0.04 CRITICAL MECHANICAL STOPS		
PCB 3991	RANGES (KG)	MINIMUM Rout ohms	MAXIMUM Rout ohms	SUPPLY VOLTS V	F.S. OUT (NOMINAL) (mV)	RESONANT FREQUENCY (KHZ)	USEABLE FREQUENCY (KHZ)
	20	4000	8000	15 MAX	200 typical @ 10V	>60	10
	60	4000	8000	15 MAX	200 typical @ 10V	> 120	20 (1dB)
					DAMPING < 0.04 CRITICAL MECHANICAL STOPS		

TABLE 1: Competitive Endevco and PCB MEMS (PR) Shock Accelerometer Models (current 2019)

A first review of the individual data sheets for the three accelerometer models pictured in TABLE 1 indicates few differences between them. They all have the same geometric form factors, weigh approximately 1.4 grams, mount with 2 each 4-40 screws, require torques of 8 +/- 2 inch-pounds, have integral 4-wire stranded 36 AWG insulated conductors with an outer cable shield and jacket, and have nominally the same sensitivity with comparable supply voltages. A detailed test series performed at National Test Systems (NTS) compared representative models of MEMS based accelerometers under conditions of severe shock.² Based on shock response spectrum (SRS) analysis of their measured signals, they performed comparably.

TABLE 1 presents a subset of specifications allowing a more detailed comparison. Note the output resistances of the accelerometers vary in the extreme by a ratio of 26:1 (9,000 ohms to 350 ohms) across the different models. In addition, the useable frequency capabilities specified across the 3 models/ranges vary by a factor of 15:1 (150 KHz to 10 KHz). Last, again note the cable is an integral feature of the accelerometer. The cable can be provided in any length that the customer requests. To the extent that the cable can be modeled in terms of its parallel line capacitance and series resistance, it has the potential to modify (i.e. filter) the accelerometers' output signal. To a first-order approximation, the "cutoff" or -3dB limitation induced by this filtering is controlled by the accelerometers' output resistance (R) and cable capacitance (C). The reciprocal of this product (RC = seconds) is the filter's -3 dB frequency (ω_c) in radians/second. RC is defined here as the **high frequency** time constant τ . If ω_c is divided by 2 pi (2π) the value of the filter cutoff frequency (f_c) in Hz is $[0.159/(RC)]$. The complete description of this 1st order filter, normalized to its "cutoff" frequency, is presented in Figure 1. Note that the filter can attenuate the high frequencies encountered in severe shock while also phase shifting them (e.g., 45 degrees at $\omega/\omega_c = 1$). Both plots are solely a function of the RC product; that is, the **high frequency** time constant τ controls the frequency content that passes through the cable. Recall that R varies between and within accelerometer models and C varies with cable length. The fact that R varies widely within a model is primarily associated with differences between the silicon wafers and their contained dies resulting from the microfabrication process.

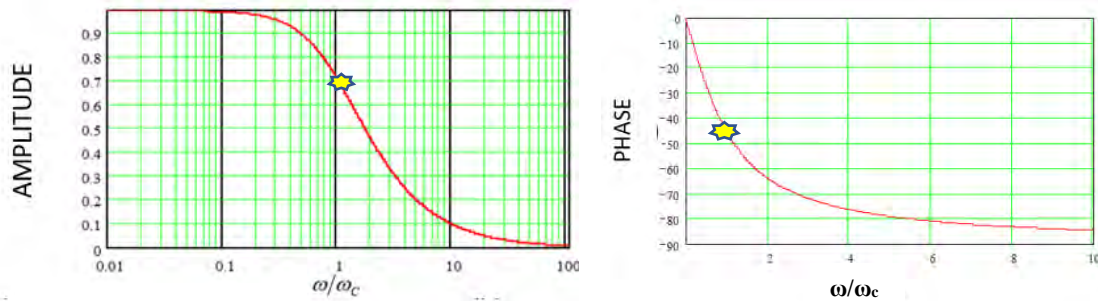


Figure 1: Amplitude (Left) and Phase (Right - in degrees) Plots vs their Normalized Frequency Response for a 1st Order Low-pass Filter (RC = τ)

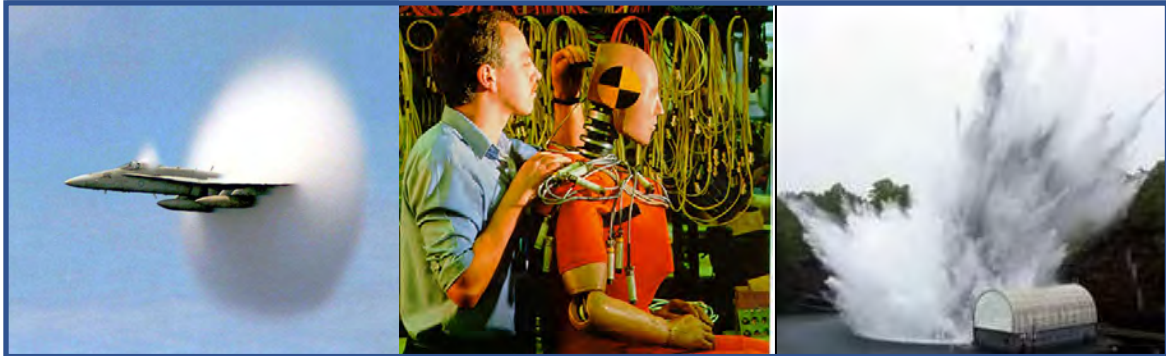
Predictive models will subsequently be developed and validated in this work to enable specification of the high frequency limitation in a measured shock pulse due to the RC product τ (time constant) of the accelerometer/cable combination.

SEVERE SHOCK

Severe shock, as defined here, possesses at least two of the following three (3) attributes: a broad frequency spectrum, high acceleration levels, and high energy. Examples that satisfy these criteria follow:



Penetrating a Concrete Target



Sonic Boom

Crash Testing

Navy Barge Shock

Figure 2. Examples of Severe Shock

In the environments of Figure 2, critical components must often survive and remain functional during and even after the event. It is imperative to measure the shock these components encounter during the event. For safety considerations, this often involves running long cables to a “hardened” instrumentation room (Fig. 3A). Alternately, a hardened and versatile “junction box” (Fig. 3B) may be a permanent part of the test facility. In this case, sensor cables are transitioned at the “box” to already existing facility cables, which are extended far enough to eliminate the need for a hardened instrumentation room. Thus, whether due to damage during a test or the requirement for additional length, accelerometer cables often are spliced to various other cable extensions.



Figure 3A. Hardened Instrumentation Room

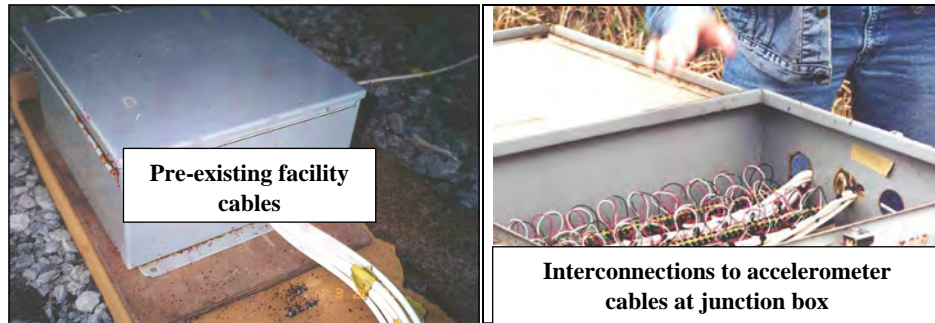


Figure 3B. Hardened Junction Box Showing Cable Transitions

Figure 3. Cable Runs Become Lengthy in Severe Shock Environments

The necessary steps to design an instrumentation system to measure and record these shocks are defined in reference 3. Step 5 references the cable.

“5. *The sensor’s cable must be carefully selected.* The cable has resistance, capacitance, and inductance. If its influences are not understood and accounted for, it can attenuate signals and induce unwanted filtering. It can also be a signal source attributable to cable induced triboelectric effects. In addition, if not properly shielded, it can also couple undesired electromagnetic and electrostatic fields into the signal. Wear, bend radius, and thermal capabilities are but a few additional cable selection considerations.”

Reference 4 discusses how the cable capacitance and resistance can limit the signal fidelity of MEMS PR sensors. Unlike ICP® shock measurements, with low output impedance where long cable runs are typically co-axial and cable capacitance is easily measured, the cables supporting MEMS sensors are more complex. As noted previously, MEMS sensors require as a minimum 4 conductors, each in its own insulated jacket, an outer conductive shield, and a final insulated jacket over the assembly. In addition, operating into a differential amplifier (typical), the electrical grounding of the shield must be properly managed.

***PROBLEM MODELING**

To investigate how the time constant of the accelerometer/cable combination can constrain the upper frequency limitation of the measurement, a basis is needed for comparison (i.e., a recognized standard). Since many of these severe shocks are associated with military applications, an existing military standard (MIL-STD-810H (METHODS 516.8 and 517.3 ANNEX A)) will be referenced for instrumentation requirements over the measurement passband of interest. *For single shocks, MIL-STD-810H requires a pass-band flatness of +/- 1 dB and phase linearity to within +/- 5 degrees across the frequency bandwidth of interest (0 - f_{max}). If f_{max} is not specified, a default value of 10 KHz is recommended.* Keep in mind, other government agencies (NASA, DOE, ...), organizations, companies, and individuals are free to generate their own requirements.

Figure 4 (left) shows the Bode plots (Amplitude and Phase Vs. Frequency) for an idealized shock accelerometer model. The model’s initial 180 degree phase offset simply reflects that fact that an accelerometer’s mass motion relative to its base acceleration occurs in an opposing direction. As expected, the model predicts this. The phase shift at the accelerometer’s natural frequency is always + 90 degrees [-90 - (-180)] = +90. The Bode plots for an idealized RC low-pass filter cable model that it interfaces with are shown in Figure 4 (right). The abscissa for each plot shown (4 total) is normalized to the -3dB frequency of the low-pass cable model. Note that the natural frequency (f_n) of the accelerometer in these plots is five times the cable -3dB frequency. For example, if this was to represent a PCB 3991A-20K model/range, with an f_n of 70 KHz, f_{-3dB} would be 14 KHz ($f_n/5$).

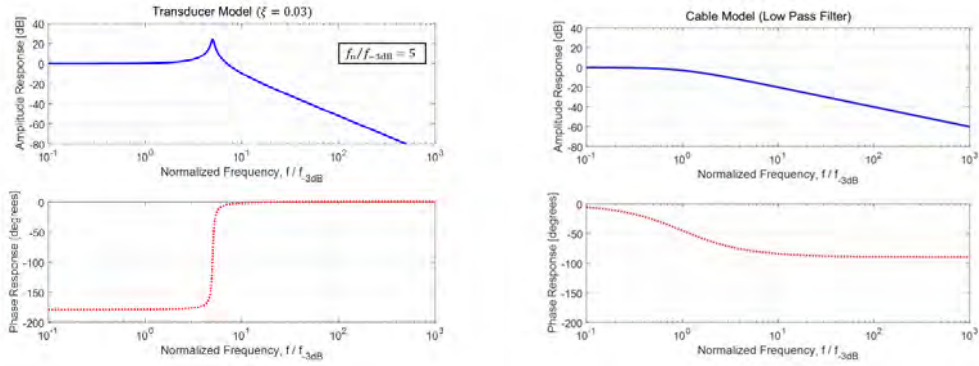


Figure 4. Idealized Accelerometer Model Left and Idealized Low-pass Cable Model Right

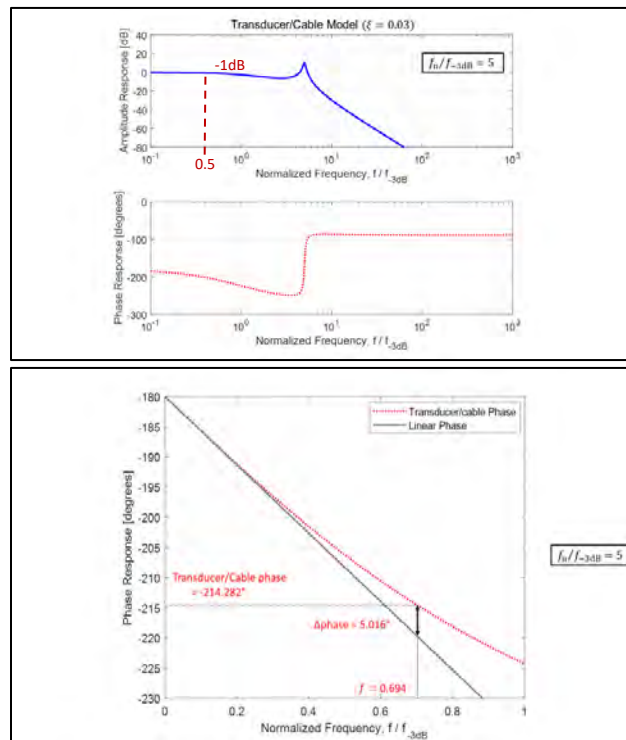


Figure 5. Idealized Combined Accelerometer/Cable Model (top) and Assessment of Model Phase Nonlinearity (bottom)

Figure 5 (top) combines the accelerometer model and the cable model of Figure 4. To accomplish this, the individual amplitude responses must be multiplied and the phase responses added. Based on the projection of the initial phase slope in Figure 5 (bottom), 5 degrees phase nonlinearity for the combined model occurs at 0.694 f_{-3dB} . For the PCB 3991A-20K example used earlier, this corresponds to about 9.7 KHz (14 KHz x 0.694). However, from Figure 5 (top), -1 dB amplitude attenuation occurs at about 7 KHz (14 KHz x ~ 0.5 f_{-3dB}). Thus, the referenced MIL STD constrains the useable frequency response of the accelerometer/cable combination to ~ 7 KHz (7 < 9.7). Note, the manufacturer’s specification for useable frequency response for the 3991A-20 K is 10 KHz (Table 1). Also, of note in this example, the low-pass filtering effect due to the cable attenuates the output signal amplitude at $f_n = 70$ KHz by 12 dB.

Figure 6 (next) shows that if hypothetically the natural frequency of this accelerometer were increased by a factor of 10 ($f_n/f_{-3dB} = 50$), while the same $RC = \tau$ lowpass accelerometer/cable time constant was maintained, no improvement in useable frequency response would occur. In addition, the low-pass filtering effect due to the cable attenuates the output signal amplitude at f_n (now = 10 x 70 or 700 KHz) by 34dB. The output signal amplitude at f_n would be 10 dB below the static (0 Hz) response of the accelerometer model.

It is not unusual in severe shock for the natural frequency of the MEMS element to be structurally excited and superposed on the desired low frequency signal (below 10 KHz here). The signal attenuation observed at f_n in both preceding examples ($f_n/f_{-3dB} = 5$ & 50) has advantages and disadvantages. For example, this attenuation might preclude the linear range of the signal conditioning amplifier from being exceeded at or around f_n . Signal overrange and/or “clipping” is a nonlinear process resulting in the generation of false data frequencies in the recorded data. Conversely, if the MEMS element is overstressed or breaks, the cause of breakage could be obscured by this signal attenuation at f_n .

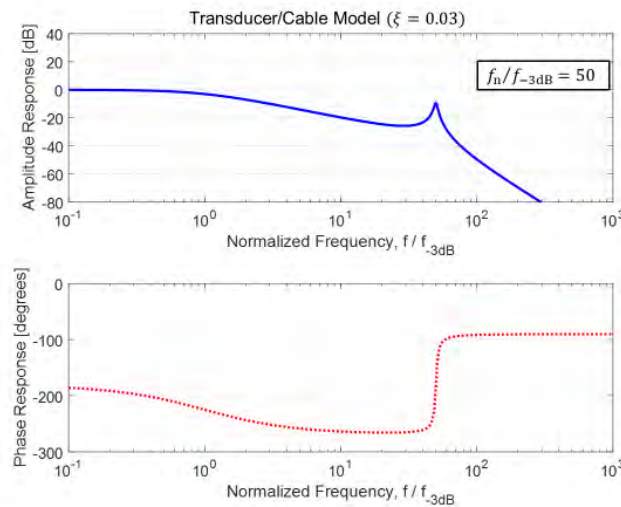


Figure 6: Idealized Combined Accelerometer/Cable Model $f_n/f_{-3dB} = 50$

After modeling the two (2) preceding values of f_n/f_{-3dB} , a parametric study was performed by varying f_n/f_{-3dB} continuously, as in Figure 7. Results in Figure 7 clearly show that as f_n/f_{-3dB} gets below a value of approximately 3, any useable gain in frequency response becomes limited by the 5-degree phase nonlinearity requirement. A conservative value in test planning would be to keep $f_n/f_{-3dB} > 3$ and limit useable frequency response of the cable/accelerometer system to no more than 0.51 (51%) of f_{-3dB} .

While cable selection considerations have been discussed before⁴ and equations presented, this research represents the first detailed study on the frequency constraints cables place on MEMS accelerometers. The experimental model verification that follows will validate these constraints as well as identify additional limitations posed when considering the cable resistance alone. While all 3 accelerometer models come in the package configurations shown in TABLE 1, other package configurations exist (Figure 8). In Figure 8, the only manufacturer’s specification difference between the 3991 and 3501 (e.g.) in equivalent acceleration ranges is mounting preference.

**The contribution of Professor Tristan Tayag, Texas Christian University, in model development and computational validation for the preceding section is gratefully acknowledged.*

EXPERIMENTAL MODEL VERIFICATION

Three **20 KG** (20,000 G range) accelerometers in the same mechanical configuration as the 3501 (1/4-28 thread) were made available for testing from PCB – one of each model. They are tracked by Model and S/N. The output resistance unique to each accelerometer Rout (R_o) is also provided in ohms (Ω).

PCB 3501B1220 KG	S/N 11009	$R_o = 6543 \Omega$
Endevco 7270A-20KM4	S/N 11053	$R_o = 577 \Omega$
Endevco 7280AM4-20K	S/N 11417	$R_o = 4674 \Omega$

The individual calibration sheets provided by the manufacturer with each Model and S/N are available in Appendix A.

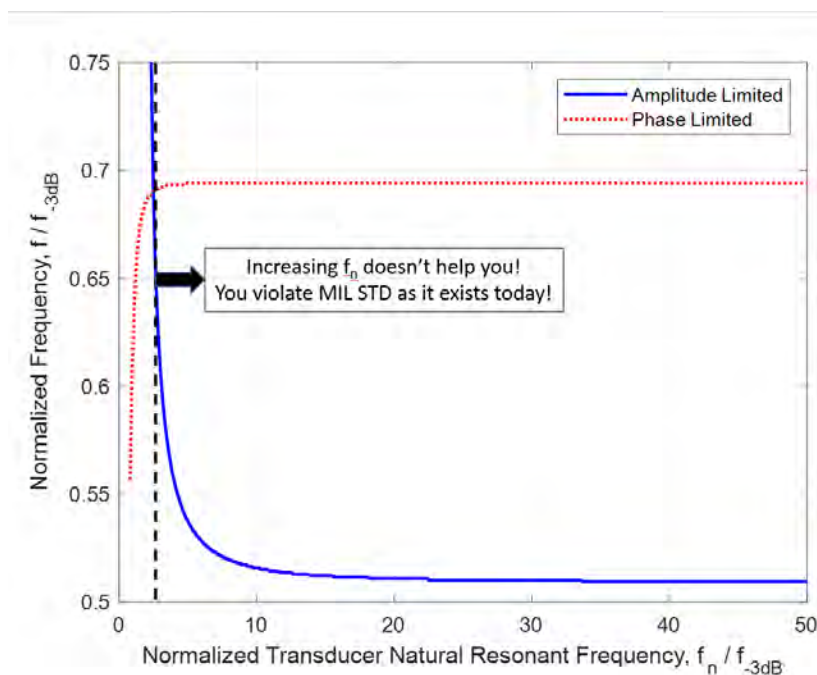


Figure 7: Limitations in Useable f/f_{-3dB} As a Function of f_n/f_{-3dB}



Figure 8. PCB 3991 (top) and 3501 (1/4-28 mounting thread bottom)

Each of the three (3) accelerometers was delivered with 10 feet of manufacturer provided integral cable. The cable delivered on the 3501 was the PCB Model 096, which had been reported on previously⁴ and was selected as the standard MEMS shock cable for testing. At an appropriate point in an individual test sequence, each accelerometer under evaluation had an additional 153 feet of 096 cable spliced to its existing cable. Any accelerometer/cable time constant (RC) determination could then be normalized to the same cable capacitance and illustrate the effect of system RC product on the maximum useable data content. For this reason, all initial data will be presented as having been acquired through 163 feet of PCB Model 096

cable, which is a close approximation. The 163-foot figure resulted as a byproduct of a request for 150 feet, with 153 feet shipped to splice onto the 10-foot integral cables provided.

With hardware available for testing, numerous issues associated with the influence of the cable impedance must be further understood. Specific issues include:

1. Loss of high frequency data content due to unaccounted filtering effects associated with the cable;
2. Signal attenuation at all frequencies due to cable line resistance;
3. Individuality of hardware:
 - a. The output resistance across the various accelerometer models of interest were noted in the specifications to vary by 26:1;
 - b. The cable capacitance and line resistance vary with cable type, cable length, number of conductors, conductor diameter, and “field” repairs resulting in more than one type of cable spliced to another, and more;
4. In-situ electrical characterization of the cable/accelerometer system’s output frequency capability immediately before initiating any field test.

DETERMINATION AND VERIFICATION OF APPLICABLE CABLE CAPACITANCE AND SENSOR OUTPUT RESISTANCE

As shown above, the “cutoff” or -3 dB limit of the combined cable/accelerometer MEMS sensing element is controlled by its output resistance R and cable capacitance C according to $f_{-3dB} = (2\pi RC)^{-1}$. Methods for determining the applicable R and C to compute f_{-3dB} are developed below, along with a procedure to validate the predicted roll-off through direct measurements using standard bench-top instruments. Finally, a method for in-situ, pre-test characterization of actual cable roll-off in a measurement system with a properly equipped signal conditioner is described, based on Precision Filters proprietary *AC Shunt Calibration* technique. Reference 6 (Szary *et al.*) provides additional details to support this section of the report.

Determining applicable cable capacitance (C):

A standard 4-wire connection from a MEMS PR shock accelerometer to a signal conditioner is shown in Figure 9. The 4-wire cable connects (+) and (-) excitation supply to the bridge inputs, and the (+) and (-) signal outputs to the signal conditioner’s differential input. The shield of the cable is connected to ground at the signal conditioner and shields the internal conductors from electrostatic noise.

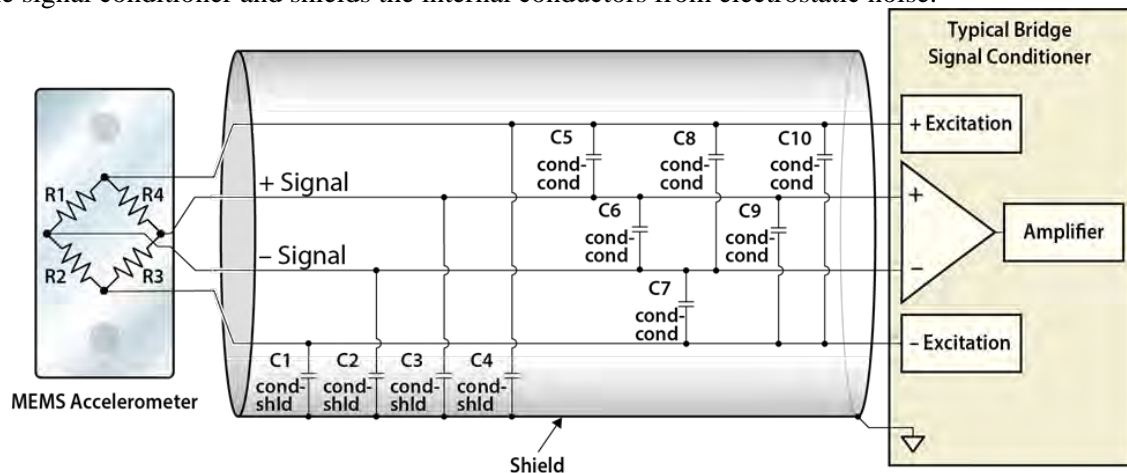


Figure 9. Diagram of a measurement system with a MEMS sensor, 4-wire cable, and signal conditioner. All conductor-shield and conductor-conductor capacitances are shown.

To quantify the cable roll-off two key points must be understood:

1. Every conductor within the cable has a deterministic capacitance to the cable shield, denoted here as $C_{cond-shld}$. For a properly designed non-paired multi-conductor cable, the assumption is made that all conductor-to-shield capacitances are equal. In Figure 9, these capacitances are numbered C_1-C_4 .
2. Every conductor within the cable also has a deterministic capacitance to every other conductor, denoted here as $C_{cond-cond}$. Again, the assumption is made that in a properly constructed non-paired cable the conductor-to-conductor capacitances are equal. In Figure 9, these capacitances are numbered C_5-C_{10} .

Previous work by Precision Filters⁶ describes how to determine correct values for $C_{cond-shld}$ and $C_{cond-cond}$ and shows how the model in Figure 9 can be reduced to a single relation for the total cable capacitance, C_{total} , required for the determination of cable roll-off in a full bridge circuit:

$$C_{total} = C_{cond-shld} + 4C_{cond-cond}$$

Determining the applicable resistance (R):

The balanced symmetry of the bridge circuit shown in Figure 9 allows analysis of the roll-off on only the (+) signal output, since the roll-off on the (-) signal output will be equivalent. Figure 10 shows a simplified drawing of the (+) signal output from the MEMS accelerometer.

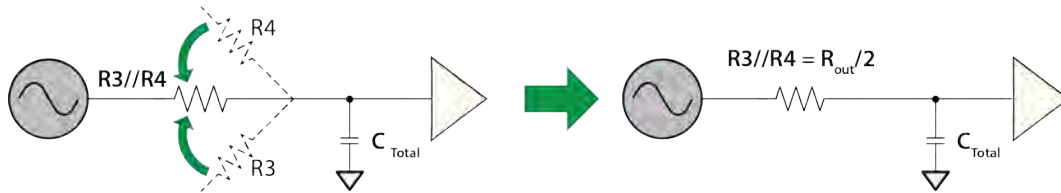


Figure 10. Simplified model of the bridge circuit (+) signal output in the MEMS accelerometer. The measured output resistance, R_{out} , reported on manufacturer calibration sheets is related to $R_3//R_4$ as shown.

The resistance acting on the cable capacitance C_{total} is the parallel combination of R_3 and R_4 , commonly denoted $R_3//R_4$. As discussed earlier, output resistance varies widely from sensor to sensor due to lot-to-lot variation in sensor production. Fortunately, most accelerometer calibration certificates report an output resistance, R_{out} that represents the exact measured resistance between the bridge corners for a given accelerometer. As shown in Figure 10, this output resistance equates to twice $R_3//R_4$, and thus provides an accurate approximation of the bridge output resistance that can be used to estimate cable roll-off in a full bridge with 4 active arms.

An additional contributor to cable roll-off with low impedance sensors is the series resistance of the cable. In cases where a cable is extremely long or of very small diameter, this series resistance cannot be ignored. Since the cable series resistance is distributed over the entire length of the cable, its effect on cable roll-off cannot be analyzed using the full value as a lumped element at the location of the sensor. Bench-top measurements with different lengths and types of cable have shown that the cable series resistance at the location of the sensor is well-approximated as $(1/3)*R_{cbl}$, where R_{cbl} is the total distributed resistance of each of the two wires. This resistance must be added to $R_{out}/2$ for an accurate determination of the cable roll-off.

Using values determined for C_{total} and R_{out} , our simplified model for the sensor-cable pair can be used to estimate the cable roll-off frequency, f_{-3dB} (Figure 11). Of note here, while cable inductance does have an effect at higher frequencies, predictions of cable roll-off at f_{-3dB} and below are shown to be better than 5% accurate even without considering cable inductance. Cable inductance is therefore not included in the analysis that follows.

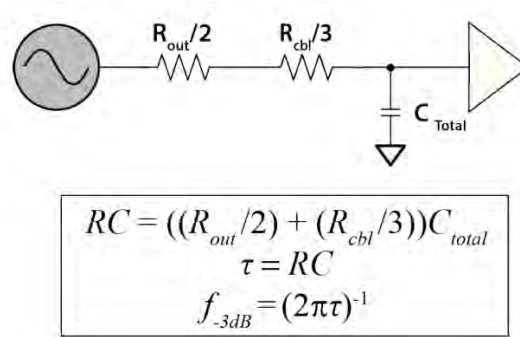


Figure 11. Summary diagram (top) and formulation (bottom) of the sensor-cable roll-off estimation method. Note that RC is defined as the time constant, τ , introduced earlier.

Application:

The methodology outlined above can be used to estimate the -3 dB cable roll-off for any sensor-cable pair. Here cable roll-off is predicted for the three test accelerometers (listed by model, S/N and R_0) at the top of page 8. Assumptions are that each sensor is paired with 163 feet of cable: 10 feet of integral 096 low noise 4-conductor cable connected to 153 feet of PCB model 096 extension cable. Capacitance measurements are made in accordance with the methodology developed by Precision Filters⁶ and converted to a total capacitance using the method outlined above. The output resistance, R_{out} , was obtained from factory calibration certificates for each sensor. The cable series resistance was obtained from measurements on the PCB 096 cable (0.42 ohms per foot). The resulting estimates (Predicted f_{-3dB}) are summarized in TABLE 2.

Experimental Verification:

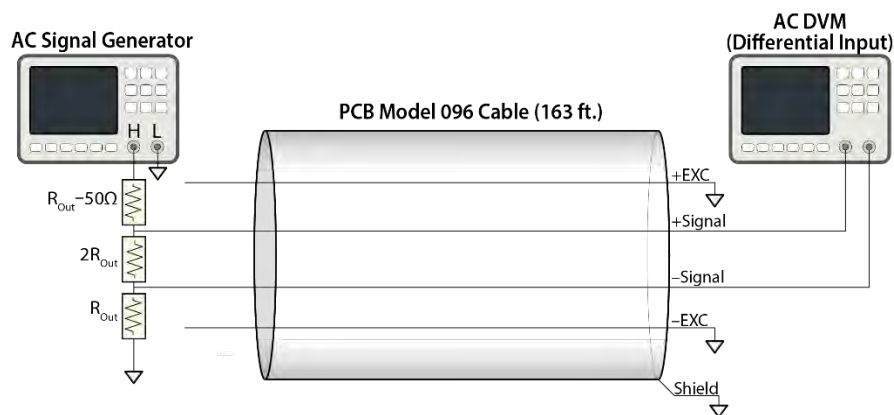


Figure 12: Bench-top setup used to obtain measurements of sensor-cable roll-off for comparison with values predicted using the model summarized in Figure 11. The procedure is described in more detail in Reference 6.

To check the accuracy of cable roll-off estimates, the laboratory procedure described by Precision Filters was used to obtain measurements of roll-off for each sensor-cable pair in Table 2 (Figure 12). The setup paired the same type and length of PCB cable with resistors that matched the output resistance of each MEMS sensor.

For this setup to accurately represent actual test conditions, the following requirements must be met:

- The cable shield is grounded so as to be equivalent to the run-time condition.
- (+) and (-) excitation lines are connected to ground at the signal conditioner side of the cable to simulate the same low impedance to ground as the constant voltage excitation supply.
- A differential signal is applied to (+) signal and (-) signal wires through a differential attenuator made up of discrete resistors equal to R_{out} and $2*R_{out}$ where R_{out} is the output resistance from the calibration certificate of the selected accelerometer.
- If the signal generator has non-zero output impedance (typically 50 ohms, as shown in Figure 12), this resistance should be taken into account by subtracting from the upper bridge-simulating resistor for improved accuracy of the roll-off measurement.

With these requirements satisfied, the f_{-3dB} frequency can be determined by sweeping the signal generator from 100 Hz to 100 kHz (Figure 13). The results (*Measured f_{-3dB}*) are given in TABLE 2. Measured values for each sensor differ from the predicted values by less than 2%.

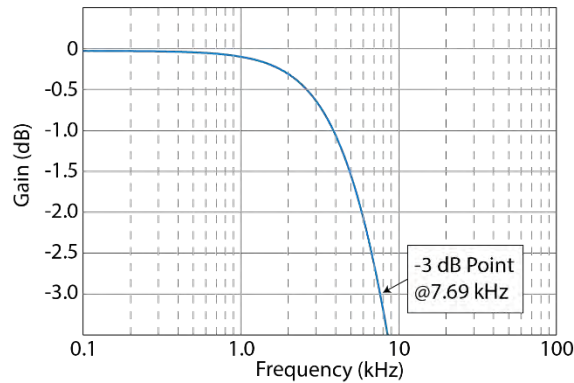


Figure 13. Results of the bench-top experiment described in Figure 12 for the PCB 3501

Sensor Model	Sensor SN#	Sensor $R_{out}/2$ (ohms)	Cable $(1/3)*R_{cbl}$ (ohms)	Cable C_{total} (pF)	Predicted f_{-3dB} (kHz)	Measured f_{-3dB} (kHz)
PCB 3501B1220KG	11009	3,272	22.8	6,152	7.85	7.69
Endevco 7270A-20KM4	11053	289	22.8	6,152	83.0	82.7
Endevco 7280AM4-20K	11417	2,337	22.8	6,152	11.0	11.0

TABLE 2. Predicted and measured values for the sensor-cable roll-off (f_{-3dB}) of three MEMS accelerometers. Note that R_{out} values for each sensor are taken directly from the manufacturers' calibration certificates.

AC Shunt Calibration for In-situ Cable Roll-off Determination

The experimental verification of cable roll-off predictions using the method described above is often impractical for measurements in the field. Common practice is to specify an accelerometer with a predetermined length of lead wire that is integral to the delivered accelerometer assembly. Often the lead wire installed by the manufacturer is very fine 32-36 gage wire. Cutting and re-splicing this wire for the purpose of conducting the above measurement would be undesirable. Additionally, conducting a sensitive measurement in a harsh environment with specialized equipment is logistically difficult. For this reason, Precision Filters has developed a proprietary technology called *AC Shunt Calibration*¹⁰ which enables the direct measurement of cable roll-off from the convenience of the instrumentation room. In AC shunt calibration, an AC current is injected into the R_1/R_2 bridge corner (Figure 14). This current interacts with the actual output resistance of the bridge corner to produce a sensor-based test signal V_{test} that is equal to $I \cdot R_{out}/2$. As the frequency of the test signal is increased, the interaction of the actual cable capacitance and the sensor's actual output resistance produces a very similar frequency response as that produced by the MEMS element within the active sensor.

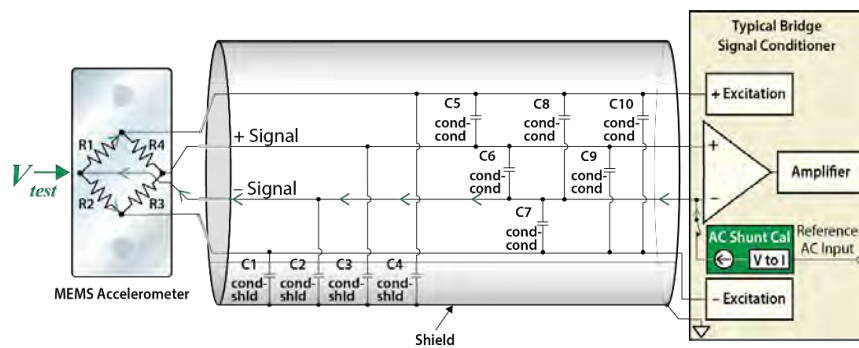


Figure 14. Diagram of the measurement system shown in Figure 9 configured for AC Shunt Calibration. The simulated test signal generated within the MEMS sensing element is V_{test} .

The Precision Filters AC Shunt Calibration technique¹⁰ was used to measure the cable roll-off for the same sensor-cable pairs in Table 2. The results (Figure 15) are consistent with the predicted and laboratory measured values. For comparison, the red traces in the graphs show the dramatic difference in cable response with only the 10 feet of factory installed cable.

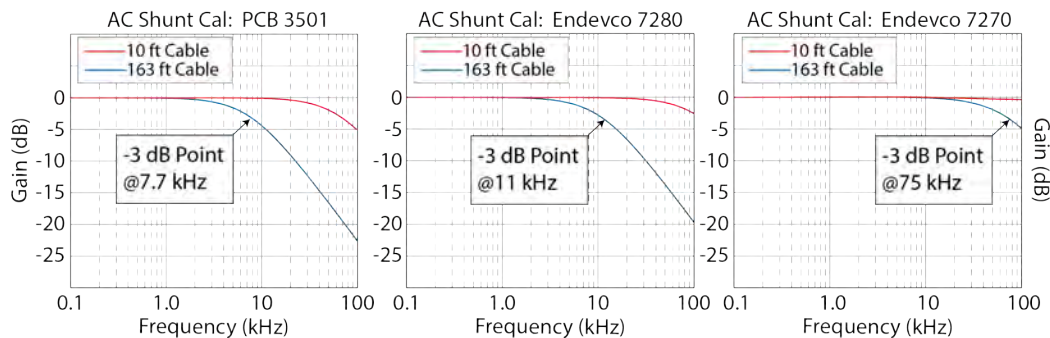


Figure 15. Results of AC shunt calibration tests on the sensor-cable pairs showing good agreement with data summarized in TABLE 2.

MECHANICAL SHOCK TEST VERIFICATION

As supplied (and verified by their specifications in TABLE 1), all three (3) of the above MEMS accelerometer models were certified to have a flat frequency response to a minimum of 10 KHz. Applying the results and discussion associated with Figure 7, the 163 feet of cable constrain the maximum useable frequency response of the accelerometers to 51% of their -3dB frequencies. Calculating 51% of the -3dB frequencies in Figure 15 (7.7 KHz, 11 KHz, and 75 KHz)] results in a maximum upper frequency limit of acceptable performance of 3.9 KHz, 5.6 KHz, and 38 KHz respectively. These maximum limits are based on the experimentally verified -3dB frequencies and the requirements of MIL-STD-810H. If the default frequency requirement of 10 KHz is accepted, two (2) of the accelerometers are immediately disqualified from consideration for shock application. The resistive output impedance of the MEMS element, interfaced to the electrical impedance of the cable, controls this *maximum* upper frequency limit of performance.

A question that should arise is: What if a shorter length (less than 163 feet) of the 096 cable had been used? The frequency response would be improved for each of the individual accelerometers. However, again note that among these accelerometer models, the output resistance in the extreme varies by a factor of 26:1. If another accelerometer of any model that by chance possessed a higher Rout were acquired, more frequency response might be lost than would be gained, even with a shorter length of cable. Dependent on cable type, a different cable might improve or lessen this maximum frequency limit.

While the specific length of cable tested was arbitrary, the need for long cables or cable extensions can best be illustrated (Figure 16 below) by the importance, expense, and hazards associated with severe shock tests, particularly at the systems level. To achieve reliability in complex systems, a finite number of full-scale system level shock tests are performed. The localized shock input to critical components that must survive and function during these tests is measured. Once system level testing enables determination of the input to these components, reliability at the systems level can subsequently be maintained through certification testing at the component level. All component testing is notably only as good as the system level shock measurements upon which it is based.



Figure 16 Example of Systems Level Testing

Assuming the electrical bench testing results of Figure 15 are correct, under mechanical shock the time-domain performance of the accelerometers should improve across the specific accelerometers/models from left to right. A laboratory shock capability was constructed to evaluate this premise. The design requirements that this laboratory shock capability had to satisfy were:

1. Capable of generating highly repeatable shock pulses;
2. Capable of generating shock pulses with significant frequency content to 10 KHz while still being “rich” in frequency content above that frequency;

3. Capable of generating significant shock amplitudes (multiple 1000s of Gs) to provide an adequate signal level to measure while not overranging or damaging the accelerometers (*note: All MEMS accelerometers evaluated produced about 50 mV output at 5,000 G*);
4. Capable of providing identical time/frequency signatures concurrently to both a reference accelerometer and the specific MEMS accelerometer being compared. The reference accelerometer selected was a 350D02 Mechanically-Isolated & Electrically Filtered ICP® accelerometer;^{1,2}
 - Its Full Scale Range of 50 KG would assure its survivability;
 - Although higher in Full Scale Range, its sensitivity was still 10 times greater than the test MEMS units;
 - Its increased sensitivity allowed its frequency response to be verified under vibration calibration as flat (essentially constant) and plotted to 10 KHz as displayed in Appendix A (A.2).

A versed sine or haversine pulse is frequently specified for component shock verification. Fourier Transforms were iteratively calculated to determine that a 100 to 125 microsecond duration haversine shock pulse would contain significant spectral content to 10 KHz enabling test to test comparison. Based on this analysis, a ballistic type pendulum was designed where two (2) identical, large, chrome-steel ball bearings on rigid moment arms would be rotated through equal angles and impacted in a co-linear manner. The controlled geometry of the bearings assured symmetry of impact. Their mechanical properties allowed them to remain undamaged during repeated impacts (Figure 17).

To extract rigid body motion from the bearings, the following minimum Design Constraints were placed on the bearings:

1. Their lowest resonant frequency had to be at or above 50 KHz;
2. Their mass had to be large compared to that of their rigidly attached accelerometers; and
3. The bearings themselves had to be isolated from the dynamics of their moment arm.
 - a. An elastomeric interface between the bearings and the moment arm accomplished this.

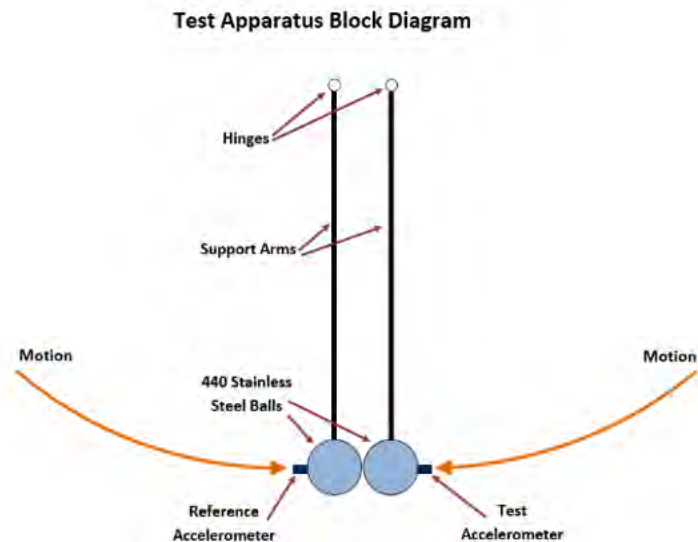


Figure 17. Illustration of the Ballistic Pendulum Used in Shock Testing

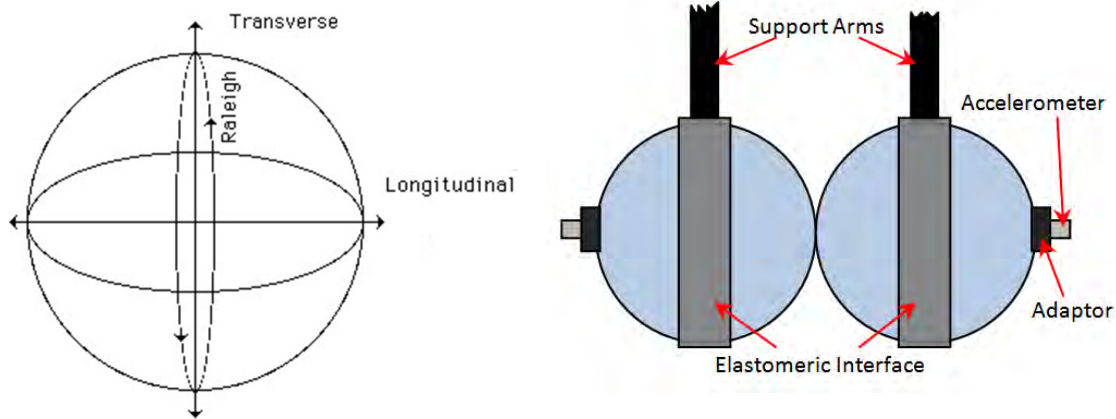


Figure 18. Wave Propagation in Solid Sphere (left). Longitudinal shown is P-Wave. Accelerometers on bearings (right) are rigidly mounted and elastomeric mounts that isolate the bearing from their support arms are pictorially shown.

Based on classical theory of wave propagation in elastic spheres,⁷ a 2.0-inch diameter steel ball bearing would have a round-trip transit time for its P or Longitudinal wave (Figure 18) of 0.0000204 seconds. This corresponds to a resonant frequency of ~50 KHz. A structure can be considered a “rigid” body to one-fifth of its lowest resonant frequency (e.g., 50 KHz/5 = 10 KHz). Thus, the 2-inch diameter bearing should satisfy the preceding Design Constraint #1. The weight of each ball bearing is 527 grams, the adapter and accelerometer combined is 3.2 grams. This satisfies Design Constraint #2 (527 >> 3.2 grams). Design Constraint #3 will be shown to be satisfied by the following qualification of the pendulum employed in the ‘Ballistic Pendulum Qualification Testing’ section of this report. The remainder of testing performed employs mechanical shock testing specifically to validate TABLE 2 and Figure 15. The following comments apply to all testing:

- ✓ The signal conditioning amplifiers used in testing were certified to have a -3dB frequency of 250 KHz. When testing the 7270A-20KM4, an amplifier with a -3dB frequency of 500 KHz was used. All acquired data were digitized at a rate of 1 million samples/second.
- ✓ The term **Wideband** in the context used below implies the only frequency limitation in the data are those imposed by the cable between the accelerometer and the signal conditioning.
- ✓ The term **Filtered** in the context used below denotes that an eighth-order linear-phase analog filter (PFI LP8P) was introduced in the front end of the signal conditioning. The filter was configured to have 1 dB attenuation at 10 KHz* and subsequently attain a slope of -160 dB/decade (48 dB/octave). Its purpose was both to satisfy the signal conditioning requirement of MIL-STD-810H and enable time domain data comparison against the Reference Sensor to 10 KHz. See Appendix B for the PFI LP8FP filter specifications.⁹

* This would be a reasonable filter setting with an assumption that there was no additional attenuation due to cable roll-off.

Ballistic Pendulum Qualification Testing

The intent of this testing was to assess the capability of the ballistic pendulum to deliver concurrent and repeatable deceleration shock pulses to both captured ball bearings over a frequency span up to and including 10 KHz. A PCB Model 350D02 accelerometer was rigidly adapted to the surface of each bearing, and both pulses were recorded on impact. 10 milliamps of current was provided to the ICP circuit of each accelerometer. Again note, the calibration data in Appendix A.2 showed both accelerometers have “flat” or constant frequency response to 10 KHz. As in all bench testing, care was taken not to tightly coil or kink the cables. 350D02 S/N 63666 was designated as the Reference Sensor and its response is indicated *red* in all comparative recorded shock data plots.

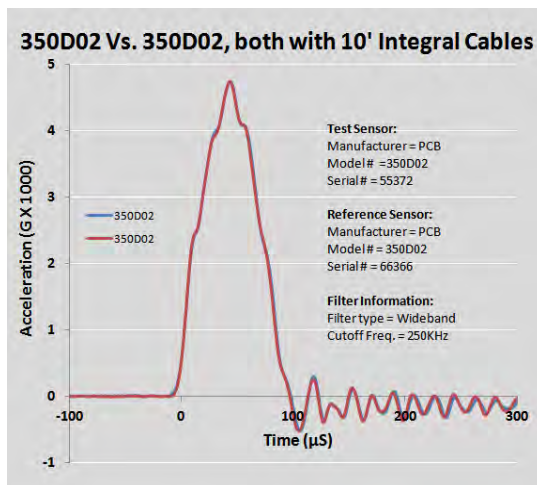
Note: To account for the time delay caused by the 350D02’s internal 2 pole filter, its output time axis was shifted 10 µseconds to properly align it with all comparative tests sensor data plots below (Plots 4-18).

[Plot #1] Wideband data were recorded multiple times, and what looks like a single trace is really two accelerometer traces (red and blue) on top of one another. If we look between the 200 and 300 µsec time markers we see approximately 5 cycles of a sine wave corresponding to a frequency of 50 - 53 KHz. Since the two accelerometer signatures correlate, this could verify the validity of the 50 KHz calculation of the resonant frequency of each ball bearing. Accelerometer performance cannot be verified traceable to national standards above 20 KHz.

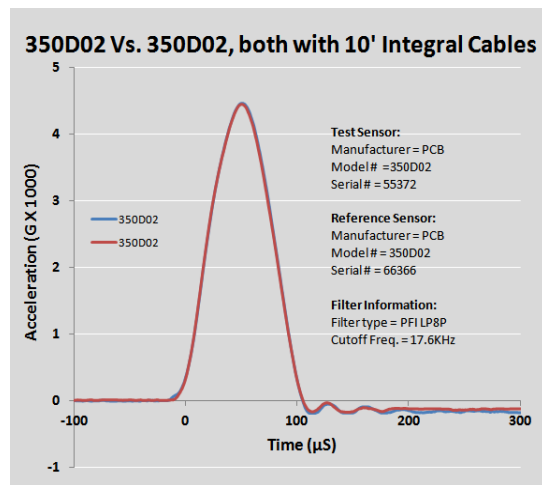
[Plot #2] The PFI LP8P Filter was inserted into the signal path and testing was repeated. Excellent correlation in the time-domain was noted. Both acceleration traces again lay on top of one another. The “ripple” after the pulse termination is understood and is an artifact of the filter.

[Plot #3] Observe that the Fourier Spectra magnitude of the pulses in plot #2 superpose almost exactly to 10 KHz. Above 10 KHz the analog filter progressively contributes to the attenuation of the two spectra. Significant frequency content to 10 KHz (and above) was achieved in testing (~ 100 µsec pulse width). Note, all testing displayed in plots #1, #2 and #3 was performed with only the 10 feet of attached cable supplied by the manufacturer.

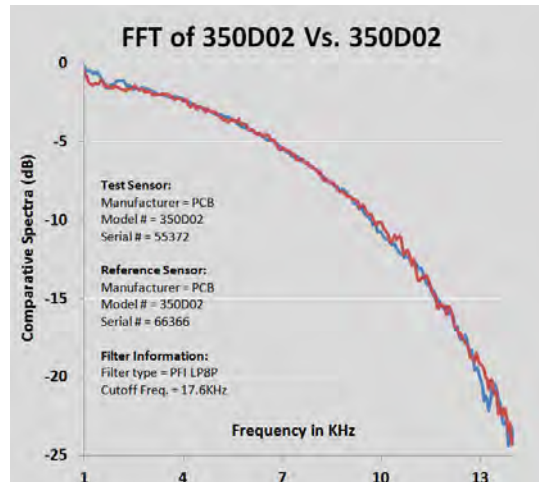
Conclusion: *All ballistic pendulum test system design goals were achieved. Performance assessment of the various MEMS accelerometer models could proceed.*



Plot #1



Plot #2



Plot #3

7270A Performance Assessment

Accelerometer Rout = 577 Ohms, Cable Length 10' and 163'

Previous discussion based on Figure 15 concluded that the specific 7270A-20KM4 supplied (Output Resistance of 577Ω) should satisfy the 10 KHz requirement of the MIL-STD both with and without the additional 153 feet of cable. Test results follow:

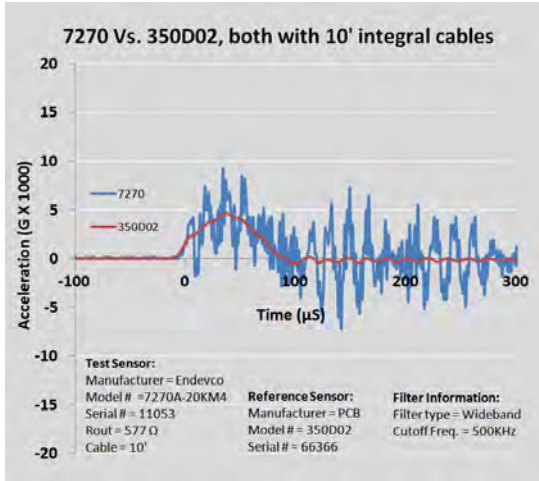
[Plot #4] Outcome of shock testing with 10 feet of cable and Wideband recording are shown. Note the higher indicated G output and frequencies in the signature (blue) of the 7270A.

[Plot #5] A portion of the recorded signal between 50 and 100 μsec is time expanded. The observed 20 cycles of oscillation divided by the 50 μsec time interval calculate to approximately 400 KHz. As a plausible explanation, the nominal resonant frequency of this model/range was specified to be 350 KHz (see TABLE 1).

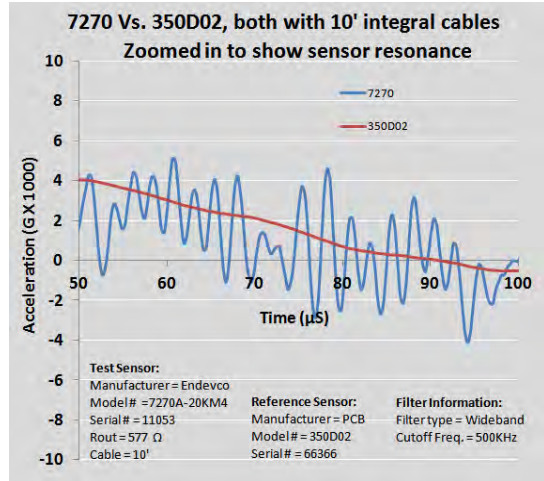
[Plot #6] The PFI LP8P filtered data shows excellent correlation in the time domain indicating both Test and Reference Sensor agreement to 10 KHz.

[Plot #7] Recorded Wideband, note that the 153 feet of added cable causes the 400 KHz resonance to be eliminated from the data. The input signal to the accelerometer cable is closely approximated by Plot #4, but the complex impedance of the cable eliminated any indication that the resonant frequency of the accelerometer has been excited. Note that a modulation frequency is visible in Plot #7 and, under closer examination, is slightly apparent in Plot #4. This modulated or beat* frequency is shown here to be about 10 KHz and is the difference (explained later) between two other frequencies $|f_1 - f_2|$.

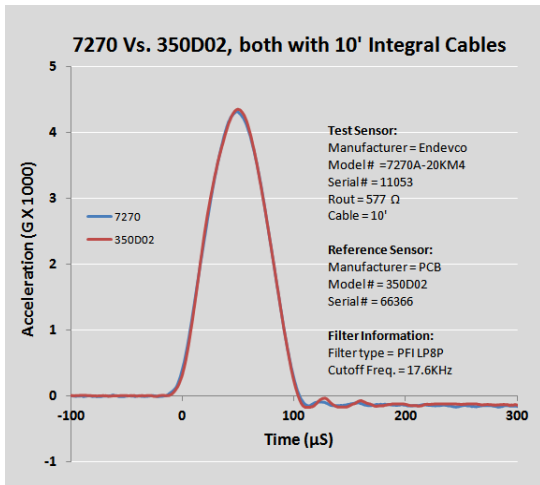
[Plot #8] Continuing comparison shock testing with the added 153 feet of cable shows the Test and Reference Sensors both correlate in time and, therefore frequency to 10 KHz. The PFI LP8P filter was again inserted into the signal path. The complex impedance of the cable has not constrained acquisition of accurate 10 KHz shock data.



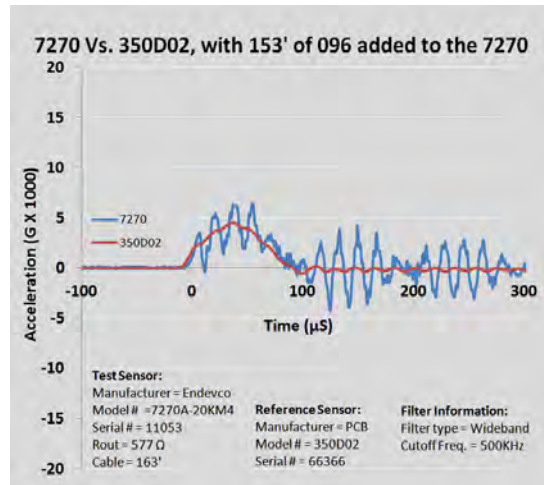
Plot #4



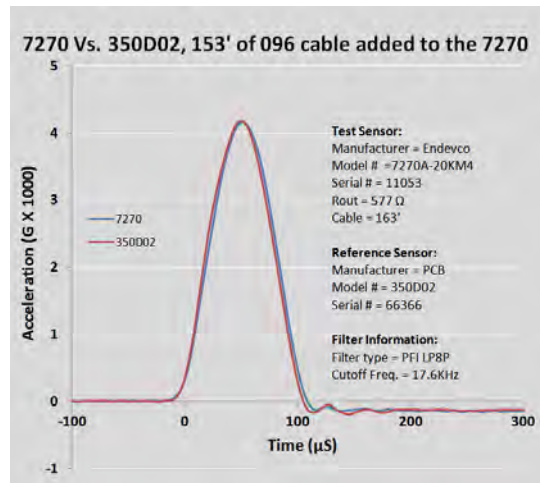
Plot #5



Plot #6



Plot #7



Plot #8

7270A Supply Voltage Assessment

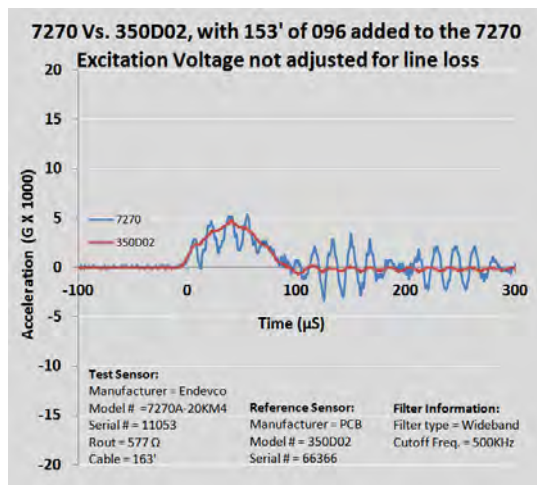
Accelerometer Rout = 577 Ohms, Change in Cable Length 153'

In all prior testing, 10 VDC Voltage was supplied to the Test Sensor. The 10 VDC supply voltage was measured as it was in the original calibration process, at the input to the 10-foot cable. If additional cable was attached, the 10VDC was still controlled at the splice connecting the two cables, i.e. at the same location.

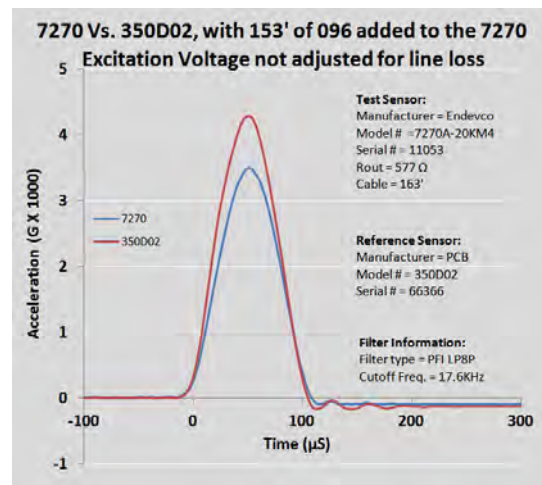
[Plot #9] The shock pulses displayed were recorded Wideband with the 10 VDC supply to the 7270A controlled at the excitation source, as opposed to the splice where the additional 153 feet of added 096 cable was connected. When filtered previously these shock pulses superposed. Testing in plot #10 below assesses if this superposition still exists.

[Plot #10] When Filtered, both pulses are observed to be similar in waveform, but the Test Sensor is 18% smaller in amplitude. This attenuation occurred since the 10 VDC supply voltage was controlled at the source of the 153' of additional cable as opposed to the location where it was spliced. 12.2 VDC at the cable source, in this instance, would have resulted in 10 VDC at the splice. The resistive and reactive impedance components of the cable still mitigate the higher frequencies from the Test Sensor (7270A). The resistance of the cable alone decreases the DC supply voltage to the Test Sensor uniformly lessening its output - *in this case by 18%!*

Conclusion: *The lower resistance of the 7270A (Output Resistance of 577Ω in this case) results in less frequency attenuation due to complex cable impedance. However, this lower resistance makes it more susceptible to line loss decreasing its supply voltage.*



Plot #9



Plot #10

7280AM4 Performance Assessment

Accelerometer Rout = 4674 Ohms, Cable Length 10' and 163'

Previous discussion based on Figure 15 concluded the specific 7280A supplied (Output Resistance of 4674 Ω) should satisfy the 10 KHz requirement of the MIL-STD without (but not with) the additional 153 feet of cable. Test results follow:

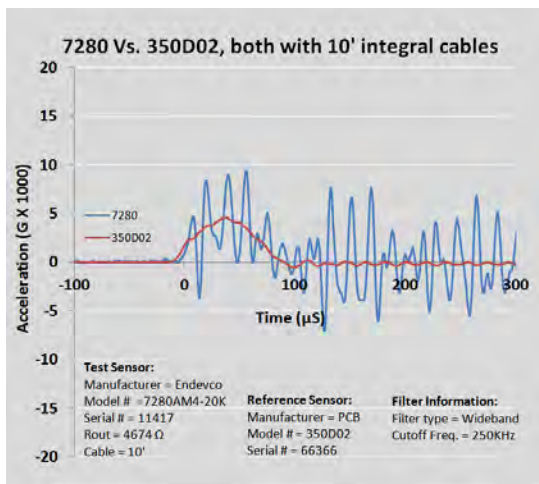
[Plot #11] The Wideband shock pulse comparison with 10 feet of cable is shown. TABLE I specifies the resonant frequency of the 7280A to be 100 KHz. The Test Sensor frequency observed in the record may be a bit lower than this value, but within tolerance.

[Plot #12] As predicted, the PFI LP8P Filtered data (10 feet of cable) shows excellent correlation in the time domain indicating both Test and Reference Sensor agreement to 10 KHz.

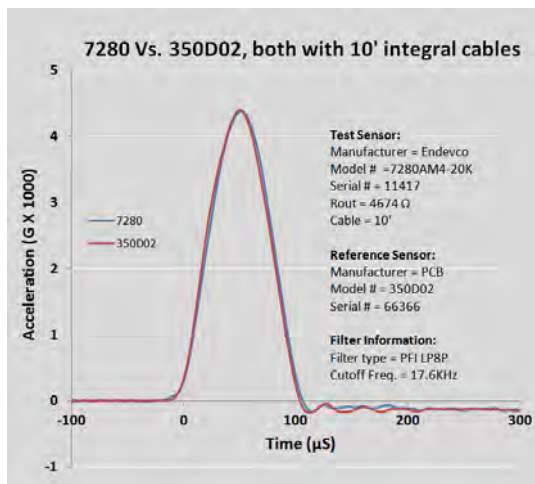
[Plot #13] The Wideband shock pulse comparison with the addition of 153 feet of cable is shown. Note that the Test Sensor resonance was severely attenuated. The input signal to the accelerometer cable is closely approximated by plot #11, but the complex impedance of the cable has greatly attenuated the resonant frequency response. The supply voltage had been increased to 10.27 VDC to account for resistive line loss. The higher resistance of the 7280A vs the 7270A required a lesser supply voltage increase.

[Plot #14] Continuing comparison shock testing with the added 153 feet of cable shows the Test and Reference Sensors do not correlate in time and, therefore, not in frequency content, to 10 KHz. The PFI LP8P filter was again inserted into the signal path. The complex impedance of the cable has constrained acquisition of adequate 10 KHz shock data. The reduced amplitude and time-shifted Test Sensor pulse peak, along with its increased pulse duration, are directly attributable to the high frequency RC filtering of the cable/sensing element combination.

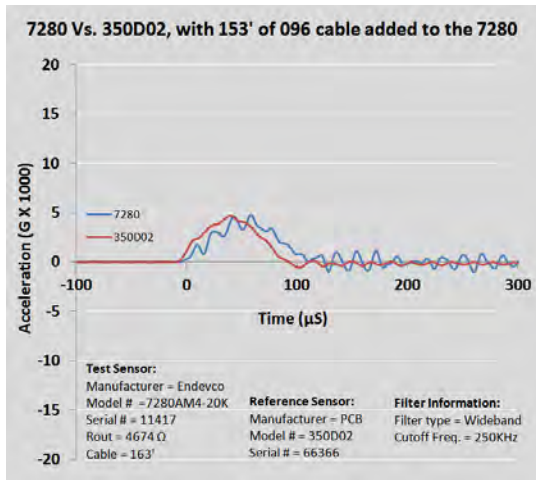
Conclusion: *The higher resistance of the 7280A (Output Resistance of 4674 Ω in this case) results in increased high frequency attenuation due to the complex cable impedance. Conversely, this higher resistance makes it less susceptible to resistive line loss decreasing its supply voltage.*



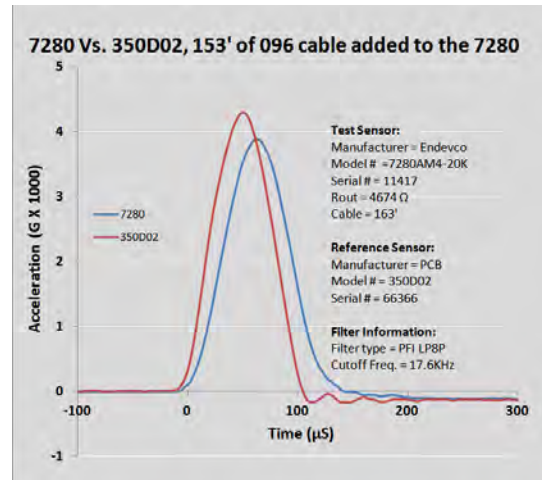
Plot #11



Plot #12



Plot #13



Plot #14

3501B Performance Assessment

Accelerometer Rout = 6543 Ohms, Cable Length 10' and 163'

Previous discussion based on Figure 15 concluded the specific 3501B supplied (Output Resistance of 6543 Ω) should satisfy the 10 KHz requirement of the MIL-STD without (but not with) the additional 153 feet of cable. Test results follow:

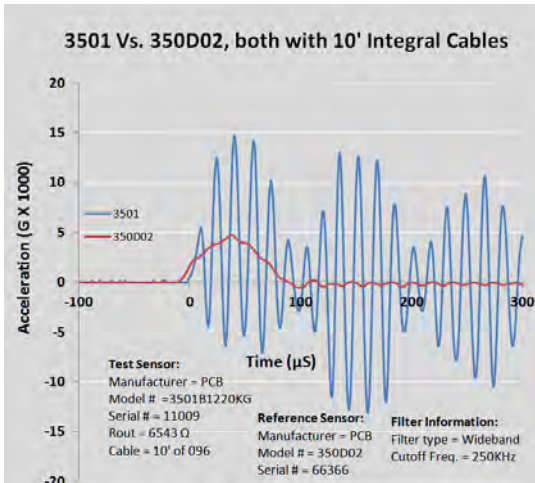
[Plot #15] The Wideband shock pulse comparison with 10 feet of cable is shown. TABLE I specifies the resonant frequency of the 3501B to be > 60 KHz. The Test Sensor frequency observed in the record is just slightly over this value (6+ cycles in ~ 100 µsec). Note again the beat* frequency | f₁-f₂ |.

[Plot #16] As predicted, the PFI LP8P filtered data (10 feet of cable) shows excellent correlation in the time domain indicating both Test and Reference Sensor agreement to 10 KHz.

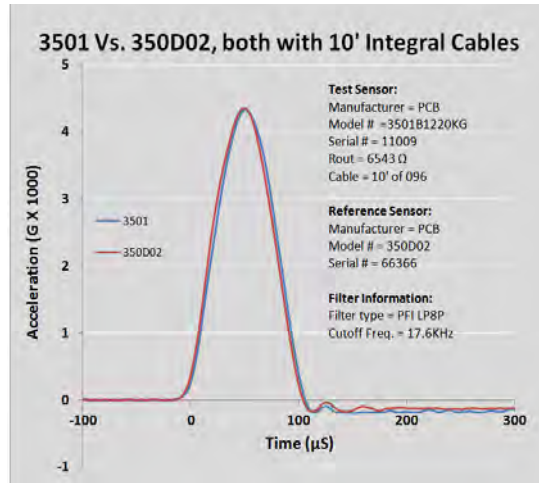
[Plot #17] The Wideband shock pulse comparison with the addition of 153 feet of is shown. Note that the Test Sensor resonance was severely attenuated. The input signal to the accelerometer cable is closely approximated by plot #15, but the complex impedance of the cable has attenuated the resonant frequency response by 4:1. The supply voltage had been increased to 10.21 VDC to account for resistive line loss. The higher resistance of the 3501B vs the 7280A vs the 7270 A required the least supply voltage increase.

[Plot #18] Continuing comparison shock testing with the added 153 feet of cable shows the Test and Reference Sensors do not correlate in time and, therefore, not in frequency content, to 10 KHz. The PFI LP8P filter was again inserted into the signal path. The complex impedance of the cable constrained acquisition of adequate 10 KHz shock data. The reduced amplitude and time-shifted Test Sensor pulse peak, along with its increased pulse duration, are directly attributable to the high frequency RC filtering of the cable/sensing element combination. The highest degree of time domain distortion correlates with the predictions of Figure 15

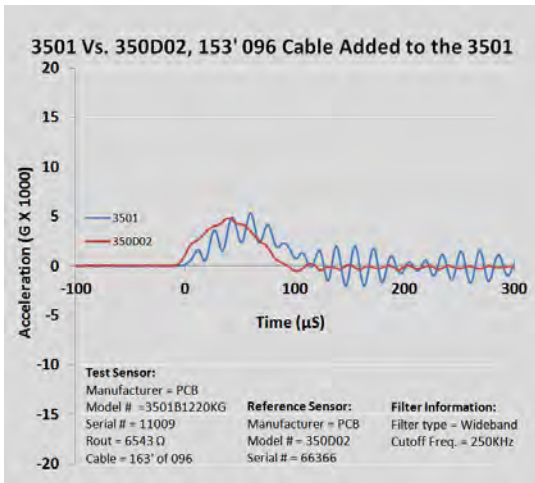
Conclusion: *The higher resistance of the 3501B (Output Resistance of 6543 Ω in this case) results in the greatest high frequency attenuation due to the complex cable impedance. Conversely, its higher resistance makes it the least of the 3 Test Sensors tested susceptible to resistive line loss decreasing its supply voltage.*



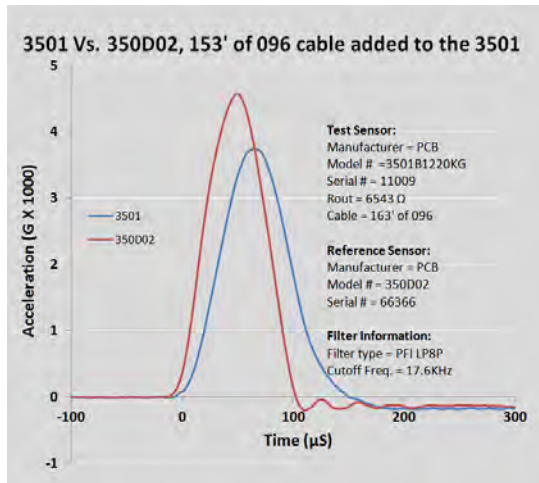
Plot #15



Plot #16



Plot #17



Plot #18

**note. The plots display a 10 KHz modulation in the Wideband data. The fact that it is present for all three MEMS sensors indicates that it is caused by a higher structural resonance in the bearing/mount assembly (see Figure 17). With a bearing resonance of 50 KHz, a second structural resonance of 60 KHz would create this beat frequency or modulation | 60-50|. Following this logic, this could explain why the resonant frequency (~ 60 KHz) of the 3501(see Plot #15) is accentuated. This discussion is provided only to provide clarity to the data. The beat frequency is irrelevant to the preceding analysis.*

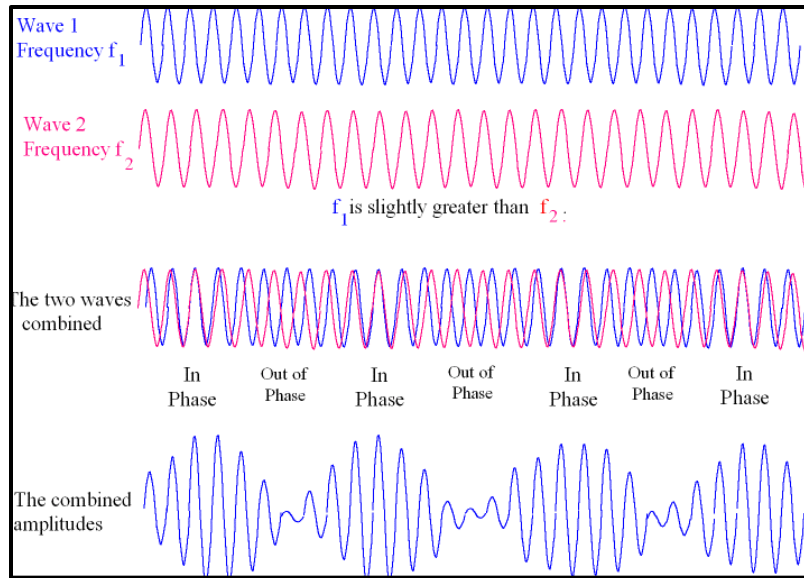


Figure 19. Explanation of a Beat Frequency

OTHER OBSERVATIONS

Not all cables are created equal

Cable properties can vary significantly from model to model due to differences in: conductor diameter, type, number, and material; jacketed coating material and thickness; shielding material (braided copper, aluminum, and nickel as well as foils) and thickness (single or double shielded); and conductor weaving (straight wire or twisted).



Figure 20. Examples of different cable types.

Moreover, the properties of a hybrid cable – constructed by splicing two different cables to achieve a longer run – can vary significantly along its length (see Figure 3). While each aspect of cable design has an intended purpose, their combined effect on the electrical characteristics that determine cable roll-off is less clear. To illustrate, we compare the effect of three different cables, each a 150 ft parallel 4-wire braided shield sequentially spliced onto the PCB 3501B (SN# 11009 as described in TABLE 2), on the frequency response of the cable-sensor pair.

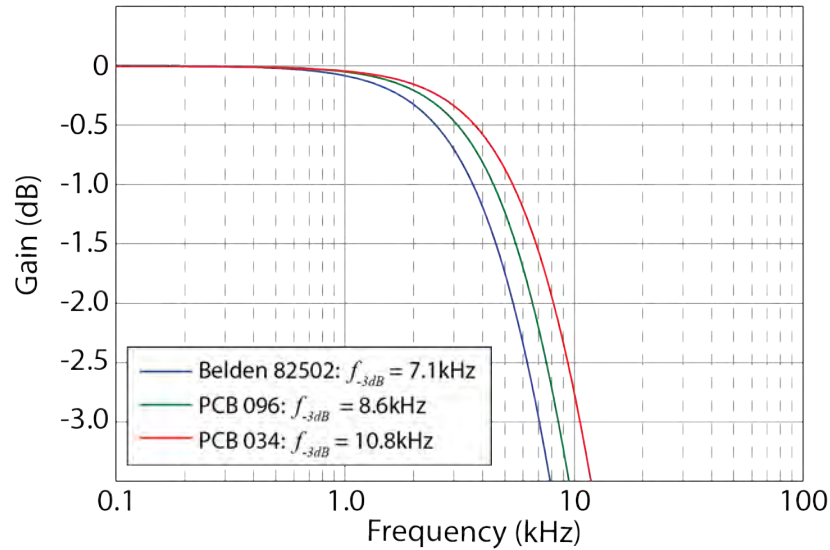


Figure 21. Variation of cable roll-off using the PCB 3501B (SN#11009 as described in TABLE 2) accelerometer and 150 feet of various cable types.

To understand the large variation in minus 3dB frequency (f_{-3dB}) in Figure 21, the electrical characteristics relevant to cable roll-off are tabulated below (TABLE 3) for each cable type along with the expected roll-off predicted by the equation in Figure 11. The closeness of the predicted roll-off to measured values lends support to the methodology of reference #6 and reinforces the notion that *not all cables are created equal*.

Cable Type	Cable C_{total}	Cable Series Resistance	Predicted f_{-3dB} (PCB 3501 $R_{out}/2=3,272\Omega$)	Measured f_{-3dB}
Belden 82502	45.9 pF/ft	0.024 Ω /ft	7.06kHz	7.1kHz
PCB 096	37.7 pF/ft*	0.420 Ω /ft	8.55kHz	8.6kHz
PCB 034	28.1 pF/ft	0.293 Ω /ft	11.5kHz	10.8kHz

TABLE 3. Cable electrical characteristics applied to the equation of Figure 11 and resultant predicted and measured results.

**Note: Graphite matrix in 096 cable, used to minimize triboelectric noise,⁴ slightly increases conductor to shield capacitance while virtually eliminating conductor to conductor capacitance.*

Having established agreement to actual measured response, the calculations of Figure 11 can be extended to infer useful information and guide the test planner to make key decisions in sensor, cable, and logistical issues. TABLE 4 charts the maximum frequency achievable to limit cable roll-off to -1dB for various lengths of these same cables with each of the sensors described in the top of page 8. Alternatively, TABLE 5 charts the maximum allowable cable length (ft) for -1dB cable roll-off at 10 kHz for these sensor/cable pairs.

<i>F</i>(max) for -1dB Cable Roll-Off (kHz)									
Cable Type	Cable length = 50 ft			Cable length = 100 ft			Cable length = 150 ft		
	PCB 3501*	Endevco 7270*	Endevco 7280*	PCB 3501*	Endevco 7270*	Endevco 7280*	PCB 3501*	Endevco 7270*	Endevco 7280*
Belden 82502	10.8	122	15.1	5.40	61.0	7.56	3.60	40.6	5.04
PCB 096	13.1	145	18.3	6.55	71.0	9.15	4.35	46.2	6.08
PCB 034	17.6	196	24.6	8.79	96.5	12.3	5.85	63.3	8.18

TABLE 4. *F*max (kHz) based on -1dB cable roll-off for various cable/sensor pairs.

**Note: refers only to specific sensors described on top of page 8.*

Max Cable Length for < -1dB Roll-Off @10kHz (ft)			
Cable Type	PCB 3501*	Endevco 7270*	Endevco 7280*
	Belden 82502	53	600
PCB 096	65	580	91
PCB 034	87	785	122

TABLE 5. Maximum cable length (ft) for -1dB cable roll-off at 10 kHz for various cable/sensor pairs. **Note: refers only to specific sensors described on top of page 8.*

Cable Series Resistance:

In addition to cable roll-off, the cable series resistance related to IR drops on the sensor excitation wiring must be accounted for. The low-mass cabling required for shock accelerometers necessarily consists of small gage (AWG), high-resistance wire. Depending on the ratio of cable resistance to the input resistance of the accelerometer, the IR drop on the excitation wiring could reduce the excitation delivered to the sensing element, causing a reduction in overall sensor sensitivity. Unlike cable roll-off that is only apparent at higher frequencies, reduced sensitivity due to IR drops in the excitation wiring affects all data frequencies. Reputable sensor manufacturers are aware of this desensitization and clearly state that sensor sensitivity presented on a calibration certificate assumes proper excitation at the signal conditioner end of the sensor’s integral cable (i.e., IR drops of the integral cable are accounted for). If additional cable length is added to the factory provided integral cable, the test planer must guarantee proper excitation at the location of the splice. The roll-off measurements presented in Figure 21 were taken while maintaining proper 10V excitation at the location of the splice using a calibrated DVM. TABLE 6 shows the reduced sensitivity that would be expected if the same sensor/cable pairs summarized in TABLES 4 and 5 were employed without correcting the excitation at the location of the splice.

Sensor desensitization caused by cable resistance (%)									
Cable Type	Cable length = 50 ft			Cable length = 100 ft			Cable length = 150 ft		
	PCB 3501*	Endevco 7270*	Endevco 7280*	PCB 3501*	Endevco 7270*	Endevco 7280*	PCB 3501*	Endevco 7270*	Endevco 7280*
Belden 82502	0.0	0.4	0.1	0.1	0.8	0.1	0.1	1.2	0.2
PCB 096	0.7	6.9	0.9	1.3	12.9	1.8	2.0	18.1	2.6
PCB 034	0.5	4.9	0.6	0.9	9.3	1.2	1.4	13.4	1.9

TABLE 6. Sensor desensitization vs extension cable length without excitation correction at the splice. ** Note: refers only to specific sensors described on top of page 8.*

It should be noted that if the low-impedance 7270 is selected to drive the capacitance of the long cable for optimal roll-off response, a nominal 18% desensitization error at all frequencies will occur. This tradeoff between improved frequency response (requiring low sensor resistance) and low sensitivity to cable series resistance (requiring high sensor resistance) represents the conflicting requirements, which is the unfortunate trade space the test planer of shock measurement is forced to negotiate. Thankfully, if the decision is made to extend cable frequency response by using low resistance sensors, methods exist to mitigate the potentially large desensitization errors. These methods are described below:

- 1) As was done for the measurements presented in this report, the excitation voltage at the splice can be measured with a DVM. The output of the excitation supply can then be manually increased as necessary until the voltage at the splice is correct. This method is acceptable as long as additional errors caused by resistance changes due to varying temperatures are within acceptable limits.
- 2) The resistance of the excitation wire can be estimated by cable manufacturers' published specifications. This total resistance can be used against the sensors input impedance to calculate the IR drop on the extension wire. Excitation can then be increased by this nominal amount. With relatively high-gage, low-resistance extension wire or when temperature changes in the test environment are known to be minimal, this technique may provide acceptable results. However, care must be taken to ensure that published specifications for cable resistance are accurate and valid for the cable temperature at test time.
- 3) The "Remote Sense" feature of high-performance bridge conditioner front ends uses an additional set of wires to control the excitation actually delivered to the bridge element or any predetermined location along the bridge wiring. The excitation supply automatically and continuously adjusts the excitation to maintain the correct level at the point where the additional "excitation sense" lines are connected to the primary excitation lines. If a 6-wire connection is possible from the splice location to the signal conditioner, then the remote sense method is preferred since it allows for precise and continuous control at all operating temperatures. The 6-wire remote sense technique is by no means a new or novel one, A description of the remote sense technique was documented as long ago as 1964 in the Tech note titled "*System Considerations for Bridge Circuit Transducers*," written by Peter R. Perino for Statham instruments⁸. For details on how to determine total cable capacitance and roll-off for a 6-wire section of a hybrid (spliced) cable, see Szary *et al.*⁶

Issues created by large variation of sensor characteristics within the same model

The microfabrication process involved in the manufacture of MEMS based accelerometers results in relatively well-behaved Wheatstone bridge sensing elements with controlled sensitivity and unstrained (zero G) bridge balance. However, an inherently large unit to unit variation exists in the bridge resistance properties of the final accelerometer assembly. This was clearly shown in TABLE 1 of this report where output resistance of various range sensors of the same model varied by *a factor of more than 2 to 1*. The test planner must be aware of this large resistance variation and its effect on the roll-off and desensitization characteristics of the cable/sensor pair. Swapping of sensors during test and/or field repair of damaged cables further complicate this process. Methodologies such as 6 wire remote excitation sense⁸ and PFI's AC shunt cal⁹ technique can be very helpful in managing these issues.

TABLE 7 (below) quantifies how the unit-to-unit variations in resistance impacts the maximum allowable cable length to comply with the default (10 KHz) frequency specified in MIL-STD 810H Annex A. TABLE 8 similarly quantifies how the unit-to-unit variations in accelerometer sensor input resistance impacts the accelerometer sensitivity at all frequencies.

Two examples will illustrate the application of TABLES 7 and 8. The examples will provide assessment across the *total range* of possible output resistances for each model. Recall, the goal is to achieve flat frequency response within +/- 1 dB to 10 KHz while managing any decrease in the accelerometer's sensitivity.

Variation in Max Cable Length for < -1dB Roll-Off @10kHz (ft)			
Cable Type	PCB 3501 (Max Rout/Min Rout)	Endevco 7270 (Max Rout/Min Rout)	Endevco 7280 (Max Rout/Min Rout)
Belden 82502	44/88	369/966	39/88
PCB 096	53/106	403/762	47/106
PCB 034	72/143	544/1042	64/143

TABLE 7. Variation of max cable length for -1dB cable roll-off at 10 kHz for various cable/sensor pairs based on variations in Rout as shown in TABLE 1.

Variation in sensor desensitization caused by sensor input resistance (%)									
Cable Type	Added Cable length = 50 ft			Added Cable length = 100 ft			Added Cable length = 150 ft		
	PCB 3501	Endevco 7270	Endevco 7280	PCB 3501	Endevco 7270	Endevco 7280	PCB 3501	Endevco 7270	Endevco 7280
Belden 82502	0/0.1	0.3/0.7	0/0.1	0.1/0.1	0.5/1.4	0.1/0.1	0.1/0.2	0.8/2.0	0.1/0.2
PCB 096	0.5/1.0	4.2/10.7	0.5/1.0	1.0/2.1	8.1/19.4	0.9/2.1	1.6/3.1	11.7/26.5	1.4/3.1
PCB 034	0.4/0.7	3.0/7.7	0.3/0.7	0.7/1.4	5.8/14.3	0.6/1.4	1.1/2.2	8.5/20.1	1.0/2.2

TABLE 8. Range of errors possible due to additional spliced cable (assumes length of sensor's integral cable to be negligible).

Examples Based on Default Requirement of 10 KHz:

Example 1: Consider an Endevco 7280A model accelerometer possessing the lowest specified output impedance for that model of 4000Ω. Assume that we are using Belden 82502 cable. Per TABLE 7, according to the methods and calculations presented in this paper, one can satisfy the default frequency requirements of the referenced MIL-STD with up to 88 feet of this cable. Assessing TABLE 8, the same accelerometer's sensitivity is decreased by less than 0.1% due to its high output resistance. Thus, for 88 ft of this Belden cable, compliance can be assured for this most optimal 4000Ω output impedance with the default 10 KHz requirement of the MIL-STD. However, the output impedance of the 7280A model can vary between 4000 and 9000 ohms. *If a random selection among 7280A's resulted in an output resistance of 9000 ohms, any cable length over 39 feet (per TABLE 7) would not satisfy the 10KHz requirement.*

Example 2: Consider whether the selection of an Endevco 7270A model accelerometer with the addition of 100 feet of spliced PCB 034 cable will satisfy the default 10kHz frequency requirement of the referenced MIL-STD. Per TABLE 7, it is clear that any randomly selected 7270A would easily meet this requirement with regard to pass-band flatness. *However, assessing TABLE 8, if sensor supply voltage is not corrected at the cable splice the desensitization created by the choice of 7270A's would create a uniform error at all frequencies of between 5.8 and 14.3 percent.*

SUMMARY

The completion of this work required cooperation between a sensor developer/manufacturer, a developer/manufacturer of precision analog signal conditioning, and a supporting university over a one-year period. Although separated by significant distances and the travel and interaction protocols of COVID-19, the communications technology of today enabled a detailed research, test, and analysis activity to be carefully implemented. The result was additional knowledge and guidance that should be incorporated into the specification and standards for instrumentation systems intended to measure severe shock. This guidance is of particular importance as it impacts the qualification testing of aerospace and defense (A&D) systems expected to operate and function under conditions of severe shock. Accurately measured shock inputs to critical components in the full-scale development testing phase of A&D systems provide the basis for qualification of subsequent production builds of these components. In turn, properly qualified components ensure the reliability of any full-scale system over its projected storage and usage lifetime.

To acquire critical high-frequency shock information to support A&D system reliability, a measurement system must be designed to operate within its linear range while providing an overall frequency response function (amplitude and phase characteristics) compatible with established test objectives. The order sequence of the individual measurement system components is also important.

The initial component in the measurement system is the accelerometer, which contains the MEMS sensing element. The structural dynamics of the accelerometer housing, the method and quality of attachment of this housing to the unit under test (UUT), the interface of the MEMS element to the housing, and the mechanical interface of the cable to the MEMS element combine to define the initial frequency response function in the measurement system.⁵ This response function is defined by the structural dynamics of the accelerometer assembly in its mounted configuration.

The next frequency response function in the measurement system, which was the subject of this work, is that associated with the accelerometer cable. The individuality of the cable is largely ignored for analysis as a separate component in the measurement chain. This work has proven that two accelerometers of the same model and range can have greatly differing frequency response functions attributable to differences in both the output resistance of their MEMS sensing elements and the distributed electrical impedances of their cables.

Measurement system standards for severe shock are typically specified around wideband differential amplifiers, data sampling rates of 1 MHz or higher, and sophisticated antialiasing filters. This work has definitively proven that oftentimes the high frequency information that these systems are designed to accommodate never exits the accelerometer cable. Methods both to analytically and experimentally characterize cables in the laboratory, as well as hardware to enable characterization in the field, have been described.⁶ *The cable is the too often ignored, but critically important, component in the measurement system.*^{4,6}

Acknowledgement: The predictive modeling of the sensor/cable frequency response combination in this report was performed within Precision Filters, Inc. and coordinated by Alan Szary, V.P engineering. *For derivation and verification of the predictive equations, the reader is strongly encouraged to acquire Reference 6.* James Woernley, PFI engineer, was tireless in acquiring shock data to illustrate the necessity to characterize the measurement system pretest to assure meaningful test data is acquired. Bob Metz,

Director of Aerospace and Development at PCB, supported this activity throughout with funding and hardware. I express my gratitude to all of them.

I personally dedicate this work to James Lally (deceased), co-founder (with his brother Robert) and CEO emeritus of PCB, and Prof. Peter K Stein (deceased), Arizona State University, both former Lifetime Achievement Award winners in S&V, who dedicated their careers to advancing measurement science.

Patrick L. Walter
Sandia National Labs (retired)
TCU Engineering Dept. (retired)

References:

1. Agnello, Anthony; Dosch, Jeff; Metz, Robert; Sill, Robert; and Walter, Patrick; *Acceleration Sensing Technologies for Severe Mechanical Shock*, PCB Piezotronics, Inc. White Paper #45
 - also published in: *Sound and Vibration*, pp. 8-19, February 2014.
2. Agnello, Anthony; Smith, Strether; Sill, Robert; and Walter, Patrick; *Evaluation of Accelerometers for Pyroshock Performance in a Harsh Field Environment*, PCB Piezotronics, Inc. White Paper #60.
3. Walter, Patrick L., *Acquiring Meaningful Test Data on Purpose*, *Sound and Vibration*, editorial, pp.2-3, March 2016.
4. Walter, Patrick L., *The Instrumentation Cable: Critical but Often Neglected*, PCB Piezotronics, Inc. Tech Note-33 (TN-33), 2015.
5. Walter, Patrick L., *How High in Frequency are Accelerometer Measurements Meaningful*, PCB Piezotronics, Inc. Tech Note-25 (TN-25), 2009.
6. Szary, Alan, et al., *Methods and Procedures for Predicting Cable Roll-off in Sensor Measurements, Part1: Full Bridge measurements*, Precision Filters. Inc. White Paper, 2020.
7. Lamb, H.A., *On the Oscillations of a Viscous Spheroid*, London Mathematical Society, pp. 51-70, Nov. 1, 1881.
8. Perino, Peter R., *System Considerations for Bridge Circuit Transducers*, Statham Instrumentation Notes, 1964.
9. Precision Filters Inc. LP8FP Specification sheet, (P8477 Rev C)
10. AC shunt Cal technique described in 28124 Specification sheet (P8465 Rev F), Pg. 4, Precision Filters Inc.

APPENDIX A.1

MEMS Test Accelerometer Calibration Certificates

~ Calibration Certificate ~

Model Number: 3501B1210KG
Serial Number: 11009
Manufacturer: PCB
Description: Piezoresistive Accelerometer
Method: ISO 16063-22

Test Data

Sensitivity @ Ref. Level: 9.148 $\mu\text{V/g}$ (0.933 $\mu\text{V}/\text{m/s}^2$)	Excitation Voltage: 10.00 Volts
Reference Input Level: 5000 g (49033.2 m/s^2)	Offset Voltage: 1.0 mV
Pulse Duration: 0.25 msec	Input Resistance: 6241 Ohms
Temperature: 73°F (23°C)	Output Resistance: 6543 Ohms
	Humidity: 42 % RH

Condition of Unit

As Found: n/a

As Left: New Unit, In Tolerance

Notes

- This calibration is the result of averaging 3 shock pulses at the reference level. Calibration traceable to primary method which has been proficiency validated interlaboratory comparison to NIST project number 822271196.
- This certificate shall not be reproduced, except in full, without written approval from PCB Piezotronics, Inc.
- Calibration is performed in compliance with ISO 9001, ISO 10012-1, ANSI/ISO/IEC J240-1-1994, and ISO 17025.
- See Manufacturer's Specification Sheet for a detailed listing of performance specifications.
- Measurement uncertainty (95% confidence level with coverage factor of 2) for amplitudes 20 to 2,000 g's pk; $\pm 1.9\%$ and for amplitudes $> 2k$ to 10k g's; $\pm 2.6\%$.

Technician: John Pattison (JP 1174) **Cal Date:** 4/20/2020
Station: CAL139

3425 Walden Avenue • Dayton, New York 14043
 Tel: 888-684-6913 • Fax: 716-895-3886 • www.pcb.com

Cal ID: CAL139-362035959

Calibration Certificate

Document number: 160668
Description: 4 Arm PR accelerometer
Manufacturer: ENDEVCO
Model Number: 7276A-20KIM
Serial Number: 11093

Sensitivity: 6.732 $\mu\text{V/g}$
 0.8904 $\mu\text{V}/\text{m/s}^2$

Pulse Duration: 0.123 ms
Shock Level: 5130 g
 50305 m/s^2

Excitation: 10.0 V

Temperature (°C): 23 (°F): 71
Relative Humidity (%): 41
Input Resistance (ohms): 577
Output Resistance (ohms): 577
ZMO (mV): 26.8

Notes:

Figure number: _____
Uncertainty estimate (95% confidence, k=2):
 +/- 1.7 % 100.0 < a <= 2000.0 g
 +/- 2.5 % 2000.0 < a <= 10000.0 g

Traceability:
 Ref Manufacturer: ENDEVCO
 Ref Model number: 2270
 Ref Serial number: 14117
 Traceability #: NIST 863/290325-15

Equipment and procedures used:
 Console S/N: AC35
 Exciter name: POP
 Test Name: FINAL POP REV E

By: _____
 CANDO, VICTORIA
 Test Date: 4/17/2020 8:25 AM
 Print Date: 4/17/2020
 MDC - HRM
 3/17 11.7

CALIBRATION CERT #1182-02

This instrument was tested using comparison calibrations of Endevco's Automated Accelerometer Calibration System (AACCS) PN 6837. This calibration is traceable to the National Metrology Institute (NMI, NIST, PTB, etc.) and is in accordance with ISO/IEC 17025:2005 and ANSI/ISO/IEC J240-1-1994 (MIL-STD-4883a). Test procedure follows CL-TP-004, Transverse Sensitivity, when provided; was calibrated with uncertainty at 0.25% of output. This certificate shall not be reproduced, except in full, without written approval of PCB Piezotronics of NC, Inc. 09/09/Endevco

~ Calibration Certificate ~

Model Number: 7280A314-20K
 Serial Number: 11417
 Manufacturer: ENDEVCO
 Description: Piezoresistive Accelerometer
 Method: ISO 10603-22

Test Data

Sensitivity @ Ref. Level: 21.080 $\mu\text{V/g}$ (2.150 $\mu\text{V/ms}^2$)	Excitation Voltage: 10.04 Volts
Reference Input Level: 5000 g (4903.2 ms^{-2})	Offset Voltage: 5.7 mV
Pulse Duration: 0.21 msec	Input Resistance: 4662 Ohms
Temperature: 73°F (23°C)	Output Resistance: 4668 Ohms
	Humidity: 50 % RH

Reference SUT

Condition of Unit

As Found: In Tolerance
 As Left: In Tolerance

Notes

1. This calibration is the result of averaging 3 shock pulses at the reference level. Calibration is N.I.S.T. Traceable through Project 6843-0000008831.
2. This certificate shall not be reproduced, except in full, without written approval from PCB Piezotronics, Inc.
3. Calibration is performed in compliance with ISO 10012-1, ANSI/NCSL Z540.3 and ISO 17025.
4. See Manufacturer's Specification Sheet for a detailed listing of performance specifications.
5. Measurement uncertainty (95% confidence level with coverage factor of 2) for amplitudes 20 to 2,000 g's pk: ± 1.9% and for amplitudes > 2k to 10kg pk: ± 2.6%

Technician: Jeffrey Mattison Cal Date: 11/11/2020
 Station: CAL79

Page 1 of 1

3625 HAZELTON DRIVE • TORONTO, ON M2H 4S3
 TEL: 888-684-6013 • FAX: 718-681-3886 • www.pcb.com

Cal ID: CAL79-348791-1923-0

APPENDIX A.2

Mechanically-Isolated & Electrically-Filtered ICP® Reference Accelerometer Calibration Certificates

~ Calibration Certificate ~
Per ISO 10053-21

Model Number: 350D02
Serial Number: 55372
Description: ICP® Shock Sensor
Manufacturer: PCB Method: Back-to-Back Comparison AT401-3

Calibration Data

Sensitivity @ 100 Hz: 0.104 mV/g Output Bias: 10.2 VDC
(0.0106 mV/m/s²) Transverse Sensitivity: 3.0 %

Sensitivity Plot

Temperature: 70 °F (21 °C) Relative Humidity: 72 %

Frequency (Hz)	Dev. (%)	Frequency (Hz)	Dev. (%)
REF. FREQ.	0.0	5000	-0.3
300	-0.1	7000	-0.5
500	-0.3	10000	-0.8
1000	-0.2		
3000	-0.2		

Condition of Unit

As Found: In Tolerance
As Left: In Tolerance

Notes

1. Calibration is NIST Traceable thru Project 683/287323 and PTB Traceable thru Project 17014.
2. This certificate shall not be reproduced, except in full, without written approval from PCB Piezotronics, Inc.
3. Calibration is performed in compliance with ISO 9001, ISO 10012-1, ANSI Z540.3 and ISO 17025.
4. See Manufacturer's Specification Sheet for a detailed listing of performance specifications.
5. Measurement uncertainty (95% confidence level with coverage factor of 2) for frequency ranges tested during calibration are as follows: 5-9 Hz; +/- 2.0%, 10-99 Hz; +/- 1.5%, 100-1999 Hz; +/- 1.0%, 2-10 kHz; +/- 2.5%.

Technician: Ronald Stevens Date: 6/23/2017

PCB PIEZOTRONICS
VIBRATION DIVISION
3425 WALDEN AVENUE DEPEW, NY 14043
TEL: 888-684-0013 FAX: 716-651-3888 www.pcb.com

~ Calibration Certificate ~
Per ISO 10053-21

Model Number: 350D02
Serial Number: 66366
Description: ICP® Shock Sensor
Manufacturer: PCB Method: Back-to-Back Comparison AT401-3

Calibration Data

Sensitivity @ 100 Hz: 0.104 mV/g Output Bias: 11.5 VDC
(0.0106 mV/m/s²) Transverse Sensitivity: 1.9 %

Sensitivity Plot

Temperature: 72 °F (22 °C) Relative Humidity: 31 %

Frequency (Hz)	Dev. (%)	Frequency (Hz)	Dev. (%)
REF. FREQ.	0.0	5000	0.3
300	-0.1	7000	-0.4
500	-0.8	10000	-0.1
1000	0.3		
3000	0.1		

Condition of Unit

As Found: n/a
As Left: New Unit, In Tolerance

Notes

1. Calibration is NIST Traceable thru Project 683/287323 and PTB Traceable thru Project 17014.
2. This certificate shall not be reproduced, except in full, without written approval from PCB Piezotronics, Inc.
3. Calibration is performed in compliance with ISO 10012-1, ANSI Z540.3 and ISO 17025.
4. See Manufacturer's Specification Sheet for a detailed listing of performance specifications.
5. Measurement uncertainty (95% confidence level with coverage factor of 2) for frequency ranges tested during calibration are as follows: 5-9 Hz; +/- 2.0%, 10-99 Hz; +/- 1.5%, 100-1999 Hz; +/- 1.0%, 2-10 kHz; +/- 2.5%, 10-15 kHz; +/- 5%.

Technician: Mary Warren Date: 3/23/2020

PCB PIEZOTRONICS
VIBRATION DIVISION
3425 WALDEN AVENUE DEPEW, NY 14043
TEL: 888-684-0013 FAX: 716-651-3888 www.pcb.com

APPENDIX B

PFI LP8FP Filter Specification

LP8F & LP8P

8-POLE, 8-ZERO FLAT/PULSE LOW-PASS FILTER



DESCRIPTION

The LP8F and LP8P 8-pole, 8-zero Low-Pass filters together provide the user with the versatility to address applications in either the time or frequency domain. The choice of LP8F or LP8P is programmable in most Precision Filters products that offer this filter characteristic.

The LP8F is specified to have outstanding pass-band flatness and very sharp roll-off characteristics. The pass-band characteristic is nearly identical to an 8-pole Butterworth yet the LP8F has a much sharper roll-off. The LP8F is a good choice as an anti-aliasing filter and for applications such as spectral analysis. The LP8P has excellent transient response and phase linearity making it an ideal filter for time domain applications including transient (shock) measurements and time domain waveform analysis. The LP8P has frequency domain characteristics superior to the 8-pole Bessel filter. Like the Bessel, the LP8P has a broadly rounded amplitude response that is a consequence of the LP8P's linear phase property.

Cascade an HP8F with an LP8F to form a band-pass filter. If the filters are set with the -0.1 dB frequencies overlapping, the resulting band-pass filter will have 0.2 dB of insertion loss and will provide more than 80 dB of attenuation below $0.487 F_c$ and above $2.05 F_c$.

SPECIFICATIONS

	LP8F Maximally Flat Low- Pass Filter	LP8P Constant Time Delay Low-Pass Filter
Cutoff Frequency Amplitude	-3.01 dB	-3.01 dB
DC Gain	0.00 dB	0.00 dB
Pass-Band Ripple	0.00 dB	0.00 dB
Stop-Band Frequency:	1.7479 F_c	3.4688 F_c
Cutoff Frequency Phase	-360.0°	-161.9°
Phase Distortion (DC to F_c)	<102.0°	<0.05°
Zero Frequency Group Delay	0.7197/ F_c	0.4496/ F_c
Percent Overshoot	18.9%	1.1%
1% Settling Time	4.03/ F_c	1.25/ F_c
0.1 % Settling Time	7.02/ F_c	2.25/ F_c
-0.1 dB Frequency	0.8527 F_c	0.1792 F_c
-1 dB Frequency	0.9438 F_c	0.5685 F_c
-2 dB Frequency	0.9774 F_c	0.8088 F_c
-3.01 dB Frequency	1.0000 F_c	1.0000 F_c
-20 dB Frequency	1.2152 F_c	2.2342 F_c
-40 dB Frequency	1.4443 F_c	2.7556 F_c
-60 dB Frequency	1.6391 F_c	3.2016 F_c
-80 dB Frequency	1.7479 F_c	3.4688 F_c

